IPP-Report

Marco Sertoli

Local Effects of ECRH on Argon Transport at ASDEX Upgrade

Local Effects of ECRH
on Argon Transport at ASDEX Upgrade

Der Fakultät für Physik
der Ludwig-Maximilians-Universität München
zur Erlangung des akademischen Grades eines
Doktors der Naturwissenschaften (Dr. rer. nat.)
vorgelegte Dissertation

von

Marco Sertoli

München, den 24 März 2010

Abstract

Future deuterium-tritium magnetically confined fusion power plants will most probably rely on high-Z Plasma Facing Components (PFCs) such as tungsten. This choice is determined by the necessity of low erosion of the first wall materials (to guarantee a long lifetime of the wall components) and by the need to avoid the too high tritium wall retention of typical carbon based PFCs. The experience gathered at the ASDEX Upgrade (AUG) tokamak has demonstrated the possibility of reliable and high performance plasma operation with a full tungsten-coated first wall. The observed accumulation of tungsten which can lead to excessive radiation losses is mitigated with the use of Electron Cyclotron Resonance Heating (ECRH). Although this impurity control method is routinely performed at AUG, the underlying physics principles are still not clear. This thesis aims on providing further knowledge on the effects of ECRH on the transport of impurities inside the core plasma. The transport of argon has been therefore investigated in-depth in purely ECR heated L-mode (low-confinement) discharges. Studies on impurity transport in centrally ECR heated nitrogen-seeded H-mode (high-confinement) discharges have also been performed.

To this scope, a new crystal X-ray spectrometer of the Johann type has been installed on AUG for argon concentration and ion temperature measurements. New methods for the experimental determination of the total argon density through the integrated use of this diagnostic and of the Soft X-Ray (SXR) diode arrays have been developed. This gives the possibility of evaluating the full profiles of the argon transport coefficients from the linear flux-gradient dependency of local argon density. In comparison to classical χ^2-minimization methods, the approach proposed here delivers transport coefficients intrinsically independent of the modelling of periodic relaxation mechanisms such as those tied to sawtooth MHD (Magneto-Hydro-Dynamic) activity. Moreover, the good spatial resolution of the results enables the observation of local structures in the profiles of the transport coefficients which were previously undetectable.

Results from ECR heated L-mode discharges partly confirm the enhancement of diffusivity and the rise of an outward convection observed in previous studies. On the other hand, the results presented in this thesis show that the effect of ECRH is much more localized around the deposition radius than what was previously thought. These results are found in promising qualitative agreement with turbulence simulations. The new method has been also tested against χ^2-minimization and found reliable within the error estimates.

Experimental results on the impurity transport in nitrogen seeded H-modes show a cyclic behaviour of impurity transport connected to the occurrence of MHD instabilities. In presence of strong $m/n = 1/1$ MHD mode activity the rise of a strong outward convection is found to drive impurities out of the centre of the plasma. The effect if sensibly larger than what observed in ECRH heated L-modes. Since the main plasma parameters do not exhibit large variations, it is very probable that this outward convection is not of turbulent nature. Furthermore, this effect seems to act preferentially on medium-large Z impurities since no change in the electron density profiles is observed. To the knowledge of the author, this feature is shown in this work for the first time.

Zusammenfassung

Die dem Plasma ausgesetzten Wandkomponenten in einem zukünftigen Fusionskraftwerk, das Deuterium- und Tritium-Ionen magnetisch einschließt, werden höchstwahrscheinlich aus Wolfram sein. Diese Wahl ergibt sich aus der Notwendigkeit einer geringen Erosion des Wandmaterials (um eine lange Lebenszeit der Wandkomponenten zu gewährleisten) und der Vermeidung eines zu hohen Tritium-Rückhaltevermögens. Erfahrungen, die mit dem Tokamak ASDEX Upgrade (AUG) gesammelt wurden, haben gezeigt, dass ein zuverlässiger Betrieb mit einer vollkommen mit Wolfram beschichteten ersten Wand möglich ist. Die zentrale Anhäufung (Akkumulation) von Wolfram, welche zu übermässigen Strahlungsverlusten führen kann, wird durch den Einsatz zentraler Elektron-Zyklotron-Resonanz-Heizung (ECRH) vermindert. Obwohl diese Methode zur Verunreinigungskontrolle an AUG und mittlerweile an vielen anderen Tokamaks routinemässig zum Einsatz kommt, sind die ihr zu Grunde liegenden physikalischen Vorgänge immer noch nicht vollständig geklärt. Das Ziel dieser Dissertation ist es, weitere Erkenntnisse zum Effekt der ECRH auf den Verunreinigungstransport innerhalb des Zentralplasmas zu gewinnen. Dafür wurde der Transport von Argon in rein mittels ECR geheizten "L-mode" Entladungen(Entaldungen mit niedrigem Einschluss, "low confinement") eingehend untersucht. Darüber hinaus wurden auch Studien zum Verunreinigungstransport in "H-Mode" Entladungen ("high confinement") mit zentraler Deposition der ECRH und Strahlungskühlung durch Stickstoff (N) Einblasen durchgeführt. Für diese Untersuchungen wurde ein neues Röntgenkristallspektrometer (Johann Anordnung) zur Messung der Argonkonzentration und der Ionentemperatur an AUG aufgebaut. Zusätzlich wurden neue Methoden zur experimentellen Bestimmung der Argondichte durch den kombinierten Einsatz dieser Diagnostik und der Diodenarrays für weiche Röntgenstrahlung (SXR) entwickelt. Diese ermöglichen die Bestimmung vollständiger Profile der Transportkoeffizienten für Argon aus der linearen Abhängigkeit des Flussgradienten von der lokalen, normierten Argondichte. Im Vergleich zu klassischen χ^2-Minimierungsmethoden liefert der hier vorgeschlagene Lösungsweg Transportkoeffizienten, die intrinsisch unabhängig von der Modellierung periodischer Relaxationsmechanismen, wie z.B. der Sägezahn Instabilität, sind. Des Weiteren erlaubt die gute räumliche Auflösung der Messungen die Beobachtung lokaler Strukturen in den Profilen der Transportkoeffizienten, die bisher nicht detektierbar waren. Die Methode wurde auch mit der χ^2-Methode zur Bestimmung der Transportkoeffizienten verglichen. Im Rahmen der Fehlerabschätzungen stimmen beide Methoden miteinander überein. Die Resultate bei ECR-geheizten "L-Mode" Entladungen bestätigen teilweise die Erhöung der Diffusivität und das Auftreten einer nach außen gerichteten Konvektion, die bereits in früheren Untersuchungen beobachtet wurden. Andererseits zeigen die neuen Ergebnisse, dass der Effekt der ECRH viel stärker um den Depositionsradius lokalisiert ist als bisher angenommen. Darüber hinaus weisen die vorgestellten Resultate eine vielversprechende qualitative Übereinstimmung mit Turbulenzsimulationen auf. Der Verunreinigungstransport in "H-Mode" Entladungen mit N-Strahlungskühlung, zeigt ein zyklisches, mit dem Auftreten von magneto-hydro-dynamischen (MHD) Instabilitäten korreliertes Verhalten. In Gegenwart einer starken m/n=1/1 MHD-Modenaktivität tritt eine starke, nach außen gerichteten Konvektion auf, die Verunreinigungen aus dem Plasmazentrum entfernt. Der Effekt ist wesentlich größer als bei ECR-geheizten L-Mode Entladungen. Da die hintergrund Plasmaparameter keine großen Variationen aufweisen, ist es sehr wahrscheinlich, dass diese auswärts gerichtete Konvektion nicht turbulenter Natur ist. Darüber hinaus scheint dieser Effekt bevorzugt auf mittel- bis hoch-Z Verunreinigungen zu wirken, da sich die Elektronendichteprofile nur geringfügig verändern. Soweit dem Verfasser bekannt, wurde dieser Effekt erstmalig im Rahmen dieser Arbeit beobachtet.

Contents

Chapter 1

Introduction

The sustainability of our economical system is a studied problem since mid XX century, but is seldomly (if ever) applied as the theoretical and practical basis of our economies. Our market-based economies mainly still rely on the assumption of infinite growth which *"naturally"* implies the access to infinite resources. In his thinkpiece commissioned by the UK Sustainable Development Commission in 2008 [1], Herman Daly argues that:

..the quantitative expansion of the economic subsystems increases environmental and social costs faster than production benefits..

Daly states that the current economic system only worked at a time when, for example, the amount of fish catched was determined by the number of fishing boats. Today the limiting factor is the number of fish in the sea.

The term "Natural Capital" clearly exemplifies the reduction of the ecosystem to a passive player in our markets. When *capitalized*, the environment is simply seen as a source for material inputs and as a sink for wastes. From this point of view, the ecosystem is thus a subset of the economy, instead of being the economy an integral part of an ecosystem which is finite, non-growing, and materially closed (i.e., no matter enters or leaves it). Growth (quantitative enlargement) should be substituted by development (qualitative improvement), and by a "steady-state economy", sustainable long-term (though not forever), where population is roughly constant and the flow of matter and energy taken from the environment and transformed into wastes is minimized.

It is therefore undoubtful that the energy problem must be solved not only on a scientific level, but also on a complex and profound remodelling of the society's political and economic system, so to re-integrate society with the surrounding ecosystem. In this framework, fusion may play an important role for electricity production in the near future. Before giving an overview of the basics of fusion power, a few important general implications are given here.

Resource Aviability
As will be explained shortly, near-future fusion power plants will most likely rely on the "burning" of deuterium (D) and tritium (T). The natural isotopic abundance of deuterium is roughly 0.015%, and it is expected to be extracted from sea water. At the present electricity production, its abundance is therefore almost *infinite*. Tritium has to be generated through lithium (Li). Assuming the installation of a total 1000 GWe fusion power plants

starting in 2050 and installed in a period of 100 years, the Li available in the earth's crust could be depleated in roughly 250 years [2]. If its extraction from seawater (mean content 0.17 *ppm* [2]) were proven feasible, the resources could be considered "without limitation" as for the deuterium.

Waste Production

All fossil fuels have implications from a global warming point of view through CO_2 production and non-negligible health implications. Nuclear fission has an almost zero carbon impact, but the long lived (up to millions of years) radioactive waste produced should be stored in deep, *final* geological or dedicated repositories which imply major short and long term health risks. Large fission-electricity producers such as Germany have decided (already almost a decade ago) to use this technology as *Brückentechnologie* (bridge-technology) up to the moment when a full substitution of the fission electricity production with renewable energy sources were possible (hopefully before 2020). Fusion would have approximately zero carbon-impact and the fusion reaction does not produce any radioactive wastes. Tritium is radioactive (with a half life of 12 years) but only a limited initial amount will be necessary for the start-up of the power plant while the rest will be produced directly on-site. The reactor materials will on the other hand be activated by the 14 MeV fusion neutrons but the use of low activation ferritic-martensitic steels at the moment under study should be able to guarantee a $\sim$100-150 year hands-on limit: a few generations maximum.

Geopolitical Stability

The reservs of all major energy sources (oil, coal, and gas) are located in specific regions around the world. More than 60% of the oil reserves are located in the middle east, 14% in North America, 11% in Eurasia (Europe and the region of the ex USSR), 10% in South and Central America, the rest in Africa, Pacific Asia and Oceania. More than 70% of the total gas reserves are concentrated in Eurasia and the Middle East, while coal is one of the most distributed, since about 30% of the total is equally found in North America, Eurasia and Pacific Asia & Oceania together. The same can be said for uranium, 50% of known resources of which are located in three countries (Australia, Kazakhstana and Russia). So localised resources have obvious geopolitical implications, having a major influence on foreign policies. Since the fuels for fusion should be extracted from seawater (at least deuterium, in case Li extraction was not proven feasible), this major aspect of geopolitical instability would be strongly relieved. Moreover, because of the scientific nature of the project, most of the technical and scientific knowledge of fusion power is international by definition, distributed in all the major regions around the world (refer to the ITER site [3] for more informations). Ultimately, because of its technical and physical complexity, the past decades have given the possibility to study all aspects of a fusion power plant far from profit-related points of view and, when fusion will reach "maturity", the international community will have gained enough experience to deliver a fully developed technology to the energy industry.

1.1 Magnetically Confined Fusion

The exploitation of nuclear reactions for energy production has its basis on the difference in nuclear binding energy for the various elements. As shown in figure 1.1, the binding energy per nucleon (measure of the difference in mass between the element and the sum of the masses of its nucleons), decreases on both sides of iron ($^{56}_{26}Fe$), for both heavier and lighter nuclei. This leads to the fact that the fission of nuclei heavier than Fe will yield nuclei with a total mass which is smaller than that of the original element, while fusion of nuclei lighter that Fe will yield an atom whose mass is smaller than the sum of the two original elements. In both cases, the excess in mass/energy is released as kinetic energy of the final products. In present fission power plants and in future fusion devices, this kinetic energy is converted to electricity through a triple conversion: the kinetic energy of the fission/fusion neutrons is transferred as heat to the liquid coolant (usually water) and the steam produced is re-converted to kinetic energy through which turbines finally produce electricity.
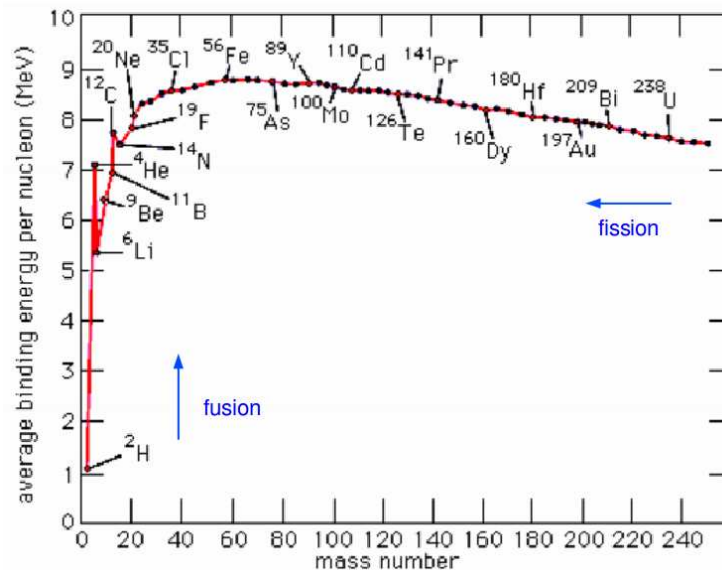
Figure 1.1: *Average binding energy per nucleon of various elements versus their mass number.*

These steps are common to any thermo-electric power plant, whether coal, oil, gas, uranium or hydrogen isotopes are used. What changes drastically is the aviability of the fuel, the efficiency of the reaction (and of the technological tools necessary to generate it) as well as the by-products/wastes produced. Limiting the comparison to fission and fusion, as can already be seen from figure 1.1, a fissile uranium atom producing two atoms of average atomic mass ~ 120 will release $< 200\ MeV$, approximately $< 1\ MeV$ per nucleon. A deuterium-tritium fusion reaction will instead release $\sim 17.6\ MeV$ shared between an helium ion and an neutron:

$$^{2}D +^{3}T \ \rightarrow \ ^{4}_{2}He\left(3.5\ MeV\right) + n\left(14.1\ MeV\right) \tag{1.1}$$
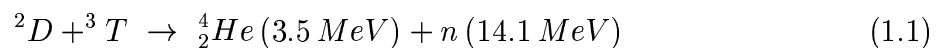
Dividing this energy by the total number of nucleons participating in the reaction (and thus

obtaining a measure of energy per unit mass) yields 3.52 $MeV/nucleon$, approximately a factor 3.5 larger than its fission counterpart. In comparison to oil, coal or gas, both fission and fusion provide more than a factor 10^6 in energy equivalent. This is due to the much weaker Electro-Magnetic interaction which is involved in the chemical reactions

Of the various fusion reactions between light nuclei, the D-T reaction has been chosen because of its high reaction parameter at feasible plasma temperatures which results from a resonance in the ^5_2He compound nucleus. Figure 1.2 shows the reaction parameter for different possible fusion reactions versus ion temperature. Present tokamak plasmas reach temperatures of a few $10 \ keV$, approximately identical to those at which a fusion power plant is predicted to work. At these temperatures, the D-T reaction has its peak efficiency, which is more than an order of magnitude larger than those of the other reactions.
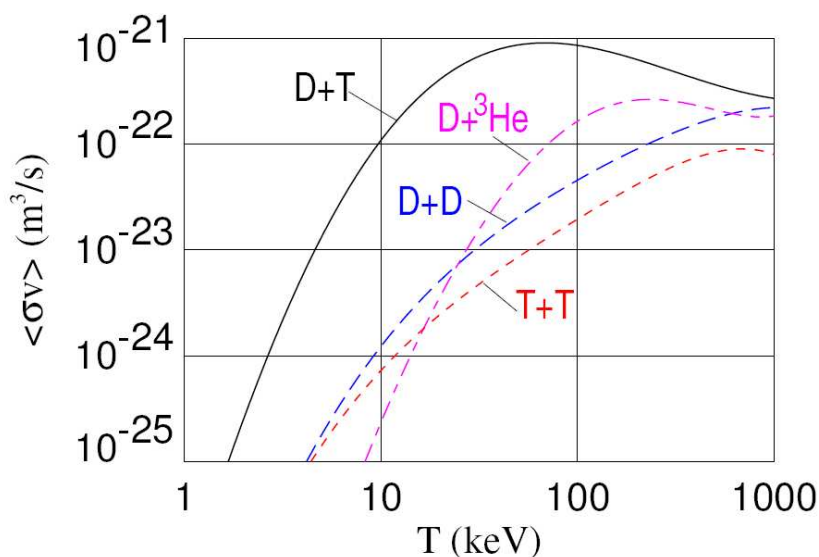

Figure 1.2: *Reaction parameter $< \sigma v >$ of the various fusion reactions involving deuterium (D), tritium (T) and helium-3 (^3He) versus ion temperature.*

As already introduced in the previous section, tritium will be mainly produced in a self-sufficient manner at the fusion power plant through $n + Li$ reactions [2]. For magnetic confinement fusion, it is foreseen that this will be done in the first wall of the fusion power plant which will serve as tritium-breeder as well as heat exchanger.

Magnetic confinement fusion aims on performing fusion reactions by confining a hot ($\sim 10 \ keV$) D-T plasma of moderate density ($10^{20} \ m^{-3}$) in toroidal systems through the use of helical magnetic fields of a few teslas. The strength of the magnetic field required to confine a plasma is determined by the desired kinetic pressure. The helicity of the field lines is instead necessary to reduce as much as possible particle drifts due to inhomogenity of the toroidal magnetic geometry. Of the various possible configurations, the most performing is at the moment the "Tokamak" whose schematic view is shown in figure 1.3. The toroidal field component is imposed externally through a set of coils shown in blue in figure 1.3, while the helicity of the field lines is imposed by generating a poloidal field component through a current (green arrow) induced in the plasma via the transformer effect (central green coils in figure).
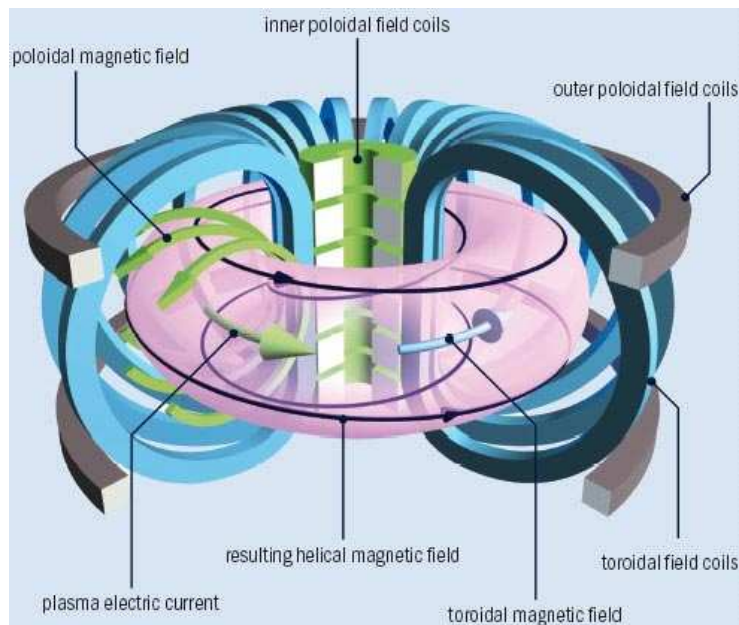
Figure 1.3: *Schematic view of a tokamak device.*

The efficiency of a fusion power plant will depend mainly the external power P_{ext} necessary to sustain the fusion reaction (mainly heating) and on the released fusion power P_{fus}. This is usually expressed in the form of a "gain factor":

$$Q = \frac{P_{fus}}{P_{ext}} \tag{1.2}$$

If the fusion power is equal to the injected heating power, then $Q = 1$ (so-called *Breakeven*). Although most present-day tokamaks still mainly work with hydrogen or deuterium, a few experiments with D-T have been performed and $Q = 0.6$ has been reached at the JET tokamak [4]. In a fusion reactor, a large part of the heating will be instead directly supplied by the energetic alpha particles produced in the D-T fusion reaction (equation 1.1) delivering a heating power P_α which will be defined in the next section. If the energy transfered to the main plasma ions through collisions balances the power losses by heat transport and by radiation losses, then no external heating will be needed and $Q \to \infty$. This condition is called *Ignition* or *Burn Condition*.

1.2   Burn condition and impurities

The ignition condition can be recovered from a simple power balance:

$$P_\alpha = P_{transp} + P_{rad} \tag{1.3}$$

where P_{transp} represents the losses by heat transport and P_{rad} those by radiation. As could already be seen in equation 1.1, the α-particle energy is a fifth of the fusion power and can be written as a function of the deuterium and tritium densities, and their reaction parameter:

$$P_\alpha = P_{fus}/5 = n_{Fuel}^2 \langle \sigma v \rangle E_\alpha = f_{Fuel}^2 n_e^2 \langle \sigma v \rangle E_\alpha \tag{1.4}$$

where $n_{Fuel} = n_D = n_T$ and $f_{Fuel} = n_{Fuel}/n_e$ is the concentration of fuel ions with respect to the electron density.

The radiation losses have to take into consideration contributions from Bremsstrahlung, recombination radiation and line radiation from all the elements present in the plasma (fuel ions, helium ions and all other elements commonly referred to as *impurities*). This can be expressed as a function of a radiative loss parameter L equal to the total power density radiated per unit electron and ion densities:

$$P_{rad} = n_e^2(f_{Fuel}L_{Fuel} + f_{He}L_{He} + f_I L_I) \tag{1.5}$$

where f_{He} and f_I are the density fractions from helium and impurity ions respectively.

Finally, the heat transport losses can be described empirically through the ratio between the plasma's stored energy W_{plasma} and an energy confinement time τ_E:

$$P_{transp} = \frac{W_{plasma}}{\tau_E} = \frac{3 f_{tot} n_e k_B T}{2\tau_E} \tag{1.6}$$

where $f_{tot} = 2 - f_{He} - (<Z> -1)f_I$ is the total particle fraction which includes electrons, fuel ions, helium ions and all the impurity ions present in the plasma resulting in a mean atomic number $<Z>$ and total density fraction f_I.

Substituting equations 1.4, 1.5 and 1.6 in the power balance equation 1.3 and reordering the terms, the ignition condition is met for:

$$n_e T \tau_E \geq \frac{3}{2} \frac{f_{tot} k_B T^2}{f_{Fuel}^2 <\sigma v> E_\alpha - (f_{Fuel}L_{Fuel} + f_{He}L_{He} + f_I L_I)} \tag{1.7}$$

This formulation is not complete because it does not take into account the dilution of fuel ions due to the helium residence within the burning plasma. This will depend on the particle transport inside the plasma, but also on the efficiency with which it is pumped out once it has reached the plasma edge. Both processes can be described using an empirical confinement time $\tau_\alpha^* = \rho \tau_E$. Since at steady state the total He production rate will be equal to the exhaust rate, the total He content inside the plasma can be expressed as:

$$\frac{f_{Fuel}^2 n_e^2}{4} <\sigma v> = \frac{f_{He} n_e}{\tau_\alpha^*} = \frac{f_{He} n_e}{\rho \tau_E} \tag{1.8}$$

Taking into consideration the pumping efficiency and the recycling of He at the plasma edge, the proportionality factor ρ is usually assumed ~ 5.

Using equations 1.7 and 1.8, the ignition conditions for different He confinement times and different impurity concentrations can be evaluated. The black curve in figure 1.4 marks the boundary for ignition versus ion temperature for the ideal case in which no impurities are present and the alpha particles deliver their full energy to the plasma but remain an infinitely small time inside the plasma, thus not diluting it nor radiating any power. The
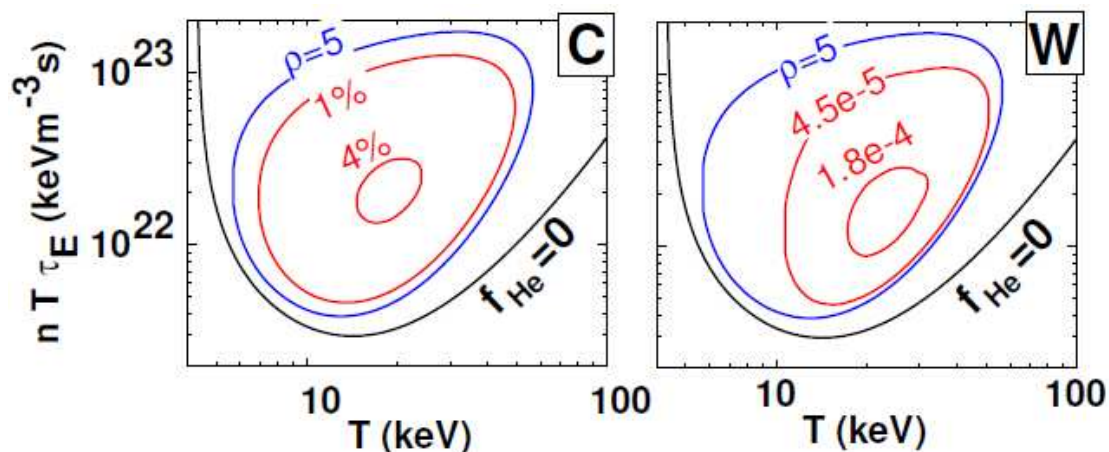
Figure 1.4: *Burn condition for different C (left) and W (right) impurity concentrations plotted as triple product versus ion temperature. The black line indicates the ignition limit without impurities nor helium contamination; the blue line ($\rho = 5$) considering helium with confinement time $\tau_\alpha^* = 5\,\tau_E$; red lines consider He and additional impurities (C and W) (figure from [5]).*

blue curves represent the case of no impurities, but $\tau_\alpha^* = 5\tau_E$, while the red curves show the operational space for different carbon (left) and tungsten (right) concentrations. As can be easily seen in these graphs, the acceptable concentration of carbon and tungsten impurities is very low. The situation for tungsten is much worse than for carbon since the W ions in the core of a burning plasma will not be fully ionized, thus still emitting strong line radiation even in the very centre. This is partially balanced by the lower sputtering yield of W at low temperatures which guarantees a lower tungsten influx in comparison to carbon [6]. In both cases, by incrementing the impurity concentrations the operational space is largely reduced because of both fuel dilution and of radiative losses.

1.3   Thesis motivation and outline

For the reasons explained in the previous section, it is of major importance to study the possibility of controlling the impurity concentrations inside the plasma. This strongly depends on the impurity sources and on their transport inside the plasma. The effect of the transport on the core-to-edge concentration ratio can be seen in figure 1.5 where impurity transport simulations of an ITER plasma have been performed with the electron, fuel and helium densities shown in the two top plots [5]. In the two cases (left and right), different anomalous/turbulent diffusivities (central plots, black curves labelled "an") have been assumed and the central peaking of various impurities computed. In case of large central D_{an}, all external impurities would exhibit a flat concentration profile (plot bottom left). Only helium reveals a small peaking due to its central source. In case the anomalous transport is particultly low (right), the heavier impurities tend to accumulate in the plasma centre due to the neoclassical inward convection. Since the neoclassical diffusion and convection (evaluated from the theory of particle collisions) may be seen as a lower limit in transport, it is of major importance to understand how to act on the turbulent transport of impurities so to enhance it where needed thus avoiding central impurity accumulation.

Results from different experiments have proven that one of the possible solutions to this problem is the use of high power electron wave heating which increases the impurity diffusivity and may even give rise to an outward impurity convection [7–10]. A possible explanation for this is given by recent turbulence theories which predict that positive convection could be driven by density fluctuations caused by parallel compression [11]. The instability should only appear in regions of the plasma with low safety factor q, low shear s, $T_e \gg T_i$ and $R/L_{Te} > 2 \cdot R/L_{Ti}$, where $L_T = -T/\nabla T$. Since the last condition is not often encountered in H-mode plasmas, it is of major interest to investigate the operational space in which an outward convection may occur.

This thesis concentrates on the experimental determination of the transport coefficients of argon in purely electron-heated L-mode plasmas and in nitrogen seeded H-modes at ASDEX Upgrade (AUG). The major goal is to investigate the effect of Electron Cyclotron Resonance Heating (ECRH) on impurity transport for different plasma conditions. The work performed can be roughly divided in three sections. The first part has been dedicated to the optimization, calibration and installation of the Compact

Figure 1.5: *Simulations of impurity peaking in ITER. Electron, D/T and He density profiles are shown in the top plots; central plots show the impurity diffusivity (set anomalous values in black and calculated neoclassical in colour); resulting core peaking (bottom) of the impurity concentration for the different impurities (figure from [5]).*

Soft X-Ray (CSXR) spectrometer on AUG and to the development of the analysis procedures for its spectral features. The second part is centred on the development of new methodologies for the application of the Gradient-Flux method to the evaluation of the impurity transport coefficients. As will be better understood in the next chapters, both parts are equally important for the impurity transport analysis and the test of the new turbulent theories introduced above which represent the third and last part of this work.

The analysis methods developed for the CSXR spectrometer have given the possibility of delivering a spatially localized argon temperature measurement even in absence of neutral beam injection (NBI). Since the conditions required by the turbulence theories explained in [11] ($T_e \gg T_i$ and $R/L_{Te} > 2 \cdot R/L_{Ti}$) are not commonly accessible with NBI heating but the theoretical calculations require the knowledge of T_i, the new methods have given the possibility evaluating the core ion temperature even in purely ECR heated discharges (which was not possible before). As far as the determination of the transport coefficients is concerned, the impurity transport analysis presented in this work delivers profiles with higher spatial resolution than those typically given by χ^2-minimization methods. Differ-
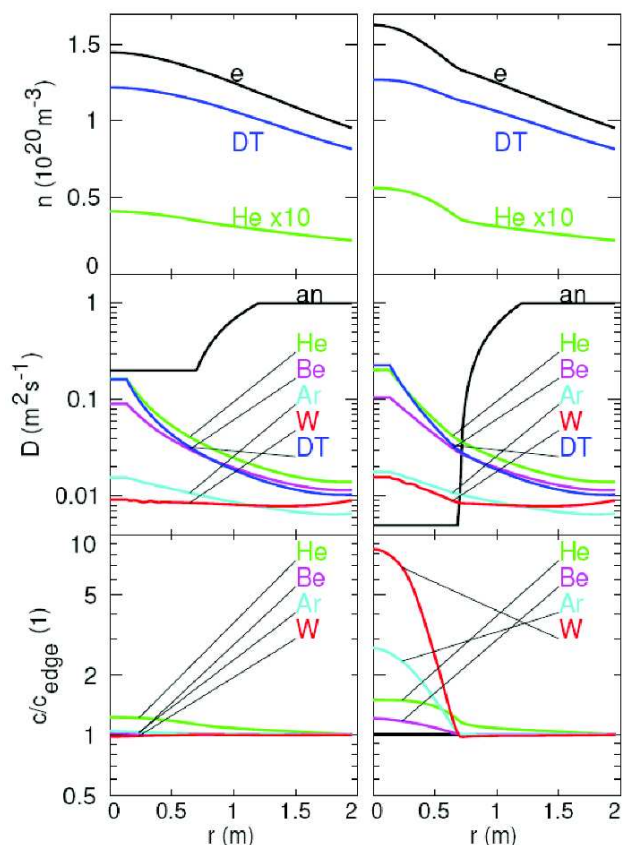
ently from previous findings, results indicate that the diffusivity enhancement and rise of outward convection is very localized around the ECRH deposition radius.

The thesis is organised as follows. Chapter 2 gives an introduction to the theoretical background of impurity transport in tokamak plasmas concentrating on the radial particle fluxes. The derivation of the *classical* transport coefficients is explained in section 2.1, their extension to toroidal systems (and thus to *neoclassical* theory) is exemplified in section 2.2. The main concepts of anomalous/turbulent transport are illustrated in section 2.3. Chapter 3 delivers an in-depth explanation of the Compact Soft X-Ray (CSXR) spectrometer, its optimization, calibration and installation on AUG. The analysis procedures developed for the spectral signatures are explained in chapter 4. The method used for the evaluation of the Ar transport coefficients (called Gradient-Flux method) and the new methodology for its application are explained in chapter 5. In particular, section 5.3 gives a full explanation of how the total argon density profile evolution can be evaluated through the combined use of the SXR and CSXR diagnostics and section 5.4 is dedicated to the treatment of the SXR raw data of non-sawtoothing and sawtoothing plasmas. Chapter 6 illustrates the results of the Ar transport analysis for purely ECR heated L-mode discharges and for nitrogen seeded H-mode discharges in ASDEX Upgrade.

An outline of the ASDEX Upgrade tokamak and its heating systems is given in Appendix A. Appendix B explaines the main concepts behind the diagnostics for ion and electron temperature profile measurements, density profile determination and a description of the Soft X-Ray (SXR) diagnostic (one of the main tools used for the determination of the Ar transport coefficients).

Chapter 2

Theoretical Background

A charged particle moving in a magnetized plasma is subject to fluctuating forces due to the motion of other charged particles which then give rise to fluctuating electric and magnetic fields. These fluctuations are usually ordered depending on their scale lengths. If they are below or equal to the Debye length λ_D they are spoken of as Coulomb collisions which give rise to collisional transport. If their scale lengths are much larger than λ_D their fluctuations give rise to turbulence and anomalous transport.

As summarized by Fussmann [12] in his review on impurity transport and neoclassical predictions (1991), in the '50s Langmuir and Rosenbluth came to a conclusion that Coulomb collisions between like-particles (electron-electron or ion-ion) do not play a role in the radial transport. All collisional transport would be due to the highly inefficient collision between unlike particles. In a pure hydrogenic plasma, because of the small momentum exchange of electron-proton collisions, a very high confinement should be expected. A decade later, the impurity ions present in the plasma were found to accumulate in the plasma centre. This accumulation could be theoretically explained in the '70s and '80s taking toroidal effects into account. This formulation was named *neoclassical*. Investigating different collisionality regimes, it was concluded that (in most cases) impurities should accumulate in the centre. This is not the case in most tokamak plasmas: transport close to neoclassical predictions has in fact been observed [13, 14], but in most cases the transport level is far higher than expected. Historically, this enhancement in transport of unknown origin was named anomalous. It is now an established explanation that this is caused by turbulence.

This chapter gives a brief overview of the theory of impurity transport concentrating on the radial fluxes. Sections 2.1 and 2.2 introduce classical and neoclassical theories, deriving the classical radial fluxes and explaining qualitatively their extension to toroidal systems. Section 2.3 describes the main concepts of turbulent transport theory.

2.1   Classical Transport

Considering a two-species magnetized plasma (a and b particles), for any force $\overrightarrow{F}_a$ and $\overrightarrow{F}_b$ acting on the two particles, the drifts perpendicular to the magnetic field associated to them will be given by:

$$\overrightarrow{u}_a = \frac{\overrightarrow{F}_a \times \overrightarrow{B}}{n_a e_a B^2} \qquad\qquad \overrightarrow{u}_b = \frac{\overrightarrow{F}_b \times \overrightarrow{B}}{n_b e_b B^2} \qquad\qquad (2.1)$$

where $\vec{u}_a$ is the centre of mass velocity of particle a, e_a its charge, n_a its density and $\vec{B}$ the total magnetic field vector. If these forces are internal forces, their action will be reciprocal $\vec{F}_a = -\vec{F}_b$ (Newton's law). Combining this condition with eq. 2.1, the ambipolarity of fluxes is readily demonstrated:

$$e_a n_a \vec{u}_a + e_b n_b \vec{u}_b = 0 \tag{2.2}$$

Already from this simple formula, the condition posed by Langmuir and Rosenbluth can be seen: identical particles (a=b) will just exchange position, but no net transport will be generated since they cannot be distinguished. On the other hand, unlike particles of the same polarity (protons/deuterons and impurity ions) will drift in opposite directions while unlike particles of opposite polarity (electrons and ions) will drift in the same direction. The last collisional process is therefore the only one giving rise to unidirectional fluxes.

In a generalized formulation, the kinetic equation can be expressed as a function of the velocity distribution $f_a(\vec{x}, \vec{v}, t)$ of the particle a. The total variation in time of f can be subdivided into its spatial, velocity and time components and rewritten as:

$$\frac{df_a}{dt} = \frac{\partial f_a}{\partial t} + \vec{v}\frac{\partial f_a}{\partial \vec{x}} + \frac{e_a}{m_a}\left(\vec{E} + \vec{v}\times\vec{B}\right)\frac{\partial f_a}{\partial \vec{v}} = \sum_b C_{ab}(f_a, f_b) \tag{2.3}$$

where $\vec{E}$ is the electric field and C_{ab} the so-called collisional operator [15]. Equation 2.3 stems from the Boltzmann equation having substituted the force term with the Lorentz force $(\propto \vec{E} + \vec{u}_a \times \vec{B})$. It is a generalized version to the Vlasov equation, which assumes the total time derivative of the distribution function equal to zero by excluding all collisions. Including these effects, the term on the right hand side will be a source/sink term for particles which, due to the collisions, may move in a non continuous manner in the phase space $(\vec{x}, \vec{v}, t)$.

Multiplying equation 2.3 by powers of the velocity v^k (where k is an integer) and integrating it over the velocity space, the conservation laws (commonly referred to as moments of the Fokker-Planck equation) to which the particle a is subject to can be evaluated. The zeroth moment delivers the law of particle conservation:

$$\frac{\partial n_a}{\partial t} + \nabla(n_a \vec{u}_a) = 0 \qquad\qquad \int C_{ab} dv^3 = 0 \tag{2.4}$$

where the equation on the right expresses the fact that the sum of all collisions have to balance so not to change the total number of particles present in the system.

The first order moment delivers the equation for the momentum conservation:

$$m_a n_a \left[\frac{\partial \vec{u}_a}{\partial t} + (\vec{u}_a \cdot \nabla)\,\vec{u}_a\right] = e_a n_a \left(\vec{E} + \vec{u}_a \times \vec{B}\right) - \nabla p_a - \nabla \cdot \pi_a + \sum_{b \neq a} \vec{F}_{ab} \tag{2.5}$$

This equation takes into account the variation of the momentum of particle a due to the Lorentz force, the pressure forces (∇p_a and the stress tensor $\nabla \cdot \pi_a$) and the viscosity driven fluxes due to the interaction with all other species present in the plasma

$(\sum_{b \neq a} \overrightarrow{F}_{ab} = \int m_a \overrightarrow{v} C_{ab} d^3 v)$. Since the total momentum must be conserved, $\overrightarrow{F}_{ab}$ is equal and opposite to $\overrightarrow{F}_{ba}$ (contribution to the fluxes of b). By assuming the stress tensor divergence-free ($\nabla \cdot \pi_a = 0$), the evaluation of these first two moments are sufficient to calculate the classical radial particle fluxes.

If the magnetic field is very strong, the frequency at which collisions occur ν_a (defined later on in this section) will be much smaller then the gyrofrequency $\omega_{ca} = e_a B / m_a$. Moreover, if we assume that the plasma is close to thermal equilibrium, the Larmor (gyration) radius $\rho_{La} = v_a / \omega_a$ will be smaller than the perpendicular gradient lengths of the density $L_n = -n / \nabla n$ and temperature $L_T = -T / \nabla T$. These conditions can be expressed in terms of a small numbers $\delta_{1,2}$:

$$\delta_1 = \frac{\nu_a}{\omega_{ca}} = \frac{\nu_a m_a}{e_a B} << 1 \qquad \qquad \delta_2 = \frac{\rho_a}{L_{n,T}} = \frac{v_a}{\omega_{ca} L_{n,T}} << 1 \qquad (2.6)$$

In temporal equilibrium $\partial \overrightarrow{u_a} / \partial t = 0$, expanding eq. 2.5 in terms of δ, the first two orders will be:

$$e_a n_a (\overrightarrow{E} + \overrightarrow{u}_a^{(0)} \times \overrightarrow{B}) = \nabla p_a \qquad (2.7)$$

$$e_a n_a \overrightarrow{u}_a^{(1)} \times \overrightarrow{B} = \sum_{b \neq a} \overrightarrow{F}_{ab} \qquad (2.8)$$

By vector multiplication with the magnetic field, the 0th and 1st order velocities can be then extracted:

$$\overrightarrow{u}_a^{(0)} = \frac{\overrightarrow{E} \times \overrightarrow{B}}{B^2} - \frac{\nabla p_a \times \overrightarrow{B}}{e_a n_a B^2} \qquad (2.9)$$

$$\overrightarrow{u}_a^{(1)} = \frac{\sum_{b \neq a} \overrightarrow{F}_{ab} \times \overrightarrow{B}}{e_a n_a B^2} \qquad (2.10)$$

At zeroth order approximation (equation 2.9), two terms contribute to the flows. The first one, named $E \times B - drift$, is in the same direction for all particles since it does not depend on charge. The second, perpendicular to both the magnetic field and the pressure profile, is commonly called *diamagnetic velocity* and has opposite sign for particles of opposite charge. Both components of $\overrightarrow{u}^{(0)}$ are flows in the poloidal direction so these two terms will not participate directly to the radial particle flux.

The flows at first order, which depend on the viscosity vectors $\overrightarrow{F}_{ab}$, can be evaluated with a few more assumptions on the velocity distribution function. Since we have assumed local thermodynamic equilibrium, f can be approximated with a perturbed Maxwellian. Concentrating on the radial particle flux, let the perturbation be in the direction x of the temperature and density gradients. Expanding the un-perturbed Maxwellian f_0 around the position of the guiding centre of the particle (the centre of mass when averaging over many gyration periods around the magnetic field) yields:

$$f = f_0 + f_1 = f_0 + \left.\frac{\partial f_0}{\partial x}\right|_{x=0} x_{gc} = f_0 + \left.\frac{\partial f_0}{\partial x}\right|_{x=0} \frac{v_z}{\omega_c} \tag{2.11}$$

where x_{gc} is the position of the guiding centre and v_z the particle velocity along the direction perpendicular to the gradients and to the magnetic field (assumed along y). The unperturbed distribution can be written as:

$$f_0 = \frac{n}{\pi^{3/2} v_T^3} \ e^{-v^2/v_T^2} \tag{2.12}$$

where $v_T = \sqrt{2k_B T/m}$ is the thermal velocity. Calculating the derivative in equation 2.11, the perturbation component f_1 will be:

$$f_1 = f_0 \left(\frac{\nabla n}{n} - \frac{3}{2}\frac{\nabla T}{T} + \frac{v^2}{v_T^2}\frac{\nabla T}{T}\right)\frac{v_z}{\omega_c} \tag{2.13}$$

With these assumptions, the viscosity term $\overrightarrow{F}_{ab}$ can be directly calculated [15]:

$$\overrightarrow{F}_{ab} = -m_a n_a \nu_{ab} \left[\frac{\nabla p_b}{e_b n_b} - \frac{\nabla p_a}{e_a n_a} - \frac{3}{2}k_B \nabla T \left(\frac{m_{ab}}{e_b m_b} - \frac{m_{ab}}{e_a m_a}\right)\right] \times \frac{\overrightarrow{B}}{B^2} \tag{2.14}$$

where m_{ab} is the reduced mass and the collisional frequency ν_{ab} is defined as:

$$\nu_{ab} = \frac{16\sqrt{\pi}}{3(4\pi\epsilon_0)^2} \frac{1}{m_a} \left(\frac{1}{m_a} + \frac{1}{m_b}\right) \frac{e_a^2 e_b^2 \, ln\Lambda_{ab}}{(v_{T,a}^2 + v_{T,b}^2)^{3/2}} n_b \tag{2.15}$$

The factor $ln\,\Lambda_{ab}$ in equation 2.15 is commonly called Coulomb logarithm and can be defined in a general manner as the natural logarithm of the ratio between the largest and smallest impact parameters of the Coulomb scattering process considered $ln\Lambda = ln(b_{max}/b_{min})$ [16–18]. In a classical formulation, the maximum and minimum impact parameters can be respectively identified with the Debye shielding length λ_D and with the distance at which a 90° deflection takes place:

$$ln\,\Lambda = \frac{\lambda_D}{r_0} \tag{2.16}$$

where:

$$\lambda_D = \sqrt{\frac{\epsilon_0 T}{n_e e^2}} \qquad r_0 = \frac{e_a e_b}{12\pi\epsilon_0 T} \tag{2.17}$$

The latter has been evaluated assuming thermal particles at temperature T. Because of the logarithm function, the clear dependence of $ln\,\Lambda$ on temperature and density is relatively weak and $ln\,\Lambda$ can be roughly considered a constant.

Introducing 2.14 into 2.10, an analytic approximation of the first order flows can be obtained:

$$u_{\perp a}^{(1)} = \frac{m_a}{e_a B^2} \sum_{b \neq a} \nu_{ab} \left[\frac{\nabla p_b}{e_b n_b} - \frac{\nabla p_a}{e_a n_a} - \frac{3}{2}k_B \nabla T \left(\frac{m_{ab}}{e_b m_b} - \frac{m_{ab}}{e_a m_a}\right)\right] \tag{2.18}$$

These flows are parallel to the pressure gradients, therefore radial. Reordering the terms, assuming $T_a = T_b = T$, substituting $p_{a,b} = n_{a,b}k_B T$, and multiplying by n_a to evaluate the particle fluxes, the full equation for the classical particle fluxes will be:

$$
\begin{aligned}
\Gamma_{\perp a} &= n_a u_{\perp a}^{(1)} \\
&= -\nabla n_a \frac{m_a k_B T}{e_a^2 B^2} \sum_{b \neq a} \nu_{ab} + \\
&\quad + n_a \frac{m_a k_B T}{e_a^2 B^2} \sum_{b \neq a} \nu_{ab} \frac{e_a}{e_b} \left\{ \frac{\nabla n_b}{n_b} - \frac{\nabla T}{T} \left[\frac{3}{2} \frac{m_{ab}}{m_b} - 1 - \frac{e_b}{e_a} \left(\frac{3 m_{ab}}{2 m_a} - 1 \right) \right] \right\}
\end{aligned} \tag{2.19}
$$

Expressing the flux density through a diffusive and convective ansatz (the terms proportional to the density gradient ∇n_a named diffusive terms, convective those proportional to the density n_a):

$$
\overrightarrow{\Gamma} = n \overrightarrow{u} = D \nabla n + \overrightarrow{v}\, n \tag{2.20}
$$

it is then easy to spot in 2.19 the classical diffusion coefficient:

$$
\begin{aligned}
D_{CL}^a &= \frac{m_a k_B T}{e_a^2 B^2} \sum_{b \neq a} \nu_{ab} = \frac{k_B T / m_a}{e_a^2 B^2 / m_a^2} \sum_{b \neq a} \nu_{ab} \\
&= \frac{v_{Ta}^2}{2 \omega_{ca}^2} \sum_{b \neq a} \nu_{ab} = \frac{\rho_a^2}{2} \sum_{b \neq a} \nu_{ab}
\end{aligned} \tag{2.21}
$$

which is identical to the diffusion coefficient of a random walk with characteristic radial step length equal to the Larmor radius ρ_{La} and collision frequency $\nu_a = \sum \nu_{ab}$ as stepping frequency. The remaining terms, proportional to the density n_a are the convection terms. In order to be able to comment these terms better, the particular case of equation 2.19 for an impurity ion in ionization stage q in a hydrogenic plasma is given below:

$$
\overrightarrow{\Gamma}_q = \frac{\rho_q \nu_{qH}}{2} \left[-\nabla n_q + q\, n_q \left(\frac{\nabla n_H}{n_H} - \frac{1}{2} \frac{\nabla T}{T} \right) \right] \tag{2.22}
$$

The diffusive fluxes (first term in equation 2.22) are obviously in the direction opposite to the impurity density gradient and tend to flatten the impurity density profile. The other terms give instead rise to convective fluxes which depend on the hydrogen density and temperature gradients respectively. For typical peaked H density and temperature profiles, the first (proportional to $\nabla n_H / n_H$) is directed towards the centre of the plasma, giving rise to a peaking of the impurity density profile, while the second, called *temperature screening*, is directed radially outwards and tends to moderate the impurity peaking due to the first convective term. The ordering of these terms can be seen when the fluxes go to zero and an equilibrium is reached. By integrating over the radius between the plasma centre $r_0 = 0$ and a generic radial position r, the ratio of the impurity density at the centre and at r will be:

$$\frac{n_q}{n_{q0}} = \left(\frac{n_H}{n_{H0}}\right)^q \left(\frac{T}{T_0}\right)^{-q/2}$$ (2.23)

The opposite action of the density and temperature terms can be easily seen in this equation. A strong dependence on the charge state of the impurity can also be noted, leading to a stronger convection for higher charged impurities. It is moreover important to recall that equation 2.22 is a limit case when only one impurity is present in the plasma. This is obviously unrealistic, so when classical (and neoclassical as will be seen shortly) fluxes are evaluated, all impurities present in the plasma have to be taken into consideration.

2.2   Neoclassical Transport

The equations that give rise to the classical radial particle flux 2.19 assume cylindrical geometry, so no information on the anisotropy of the toroidal magnetic field geometry is contained in the classical diffusion and convection coefficients. Bending a straight cylinder into a torus, the radial variation of the magnetic field will roughly follow its major component (the toroidal one, B_T), which varies along the major radius R of the tokamak approximately with $1/R$. Travelling along the magnetic field lines, a particle will therefore pass through regions of different magnetic field and will be subject to forces proportional to its gradient and to the curvature of the field lines. Qualitatively speaking, the first consequence of this is that no net separation between parallel and perpendicular motion can be done anymore. Consequently, a local treatment of the particle motion is not suitable, and an average of its motion over the magnetic flux surface will be necessary. This can be done under the assumption of constant density and temperature on a flux surface and a gyro-averaged treatment of the particle motion.
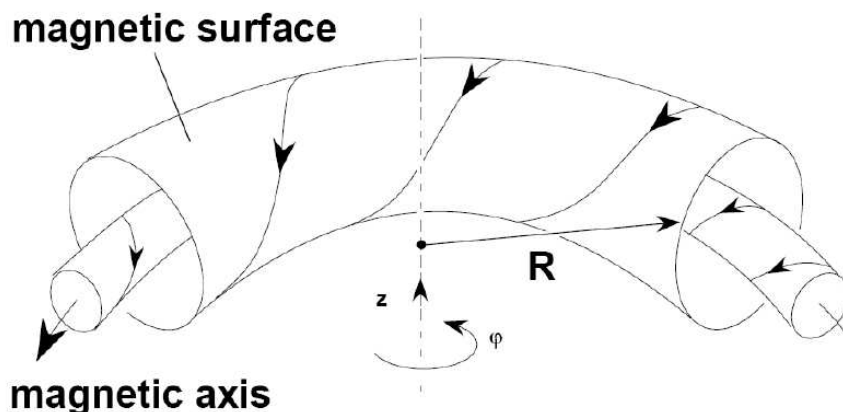

Figure 2.1: *Section of a tokamak plasma showing the nested magnetic flux surfaces and the helical field lines. The pitch angle of the magnetic field lines is exagerated to better exemplify their winding aroung the flux surface.*

The flux surface average of an arbitrary scalar quantity F can be defined as:

$$< F > \; = \; \left(\frac{\partial V}{\partial \Psi} \right)^{-1} \oint F \frac{dS}{|\nabla \Psi|} \tag{2.24}$$

$$\int F \, dV \; = \; \int_0^\Psi d\Psi \, \frac{\partial V}{\partial \Psi} < F > \tag{2.25}$$

where V and S are the volume and surface of the flux surface, Ψ the poloidal flux ($|\nabla \Psi| = RB_p$, B_p being the poloidal magnetic field). Flux surface averaged quantities are usually expressed in normalized flux coordinates ρ, constant on the flux surface, perpendicular to it and increasing from centre to edge. Since different flux surface labels are commonly used, we define here a few for completeness:

$$\rho_{pol} = \sqrt{\frac{\Psi - \Psi_o}{\Psi_s - \Psi_o}} \qquad \rho_{tor} = \sqrt{\frac{\Phi - \Phi_o}{\Phi_s - \Phi_o}} \qquad \rho_{vol} = \sqrt{\frac{V - V_o}{V_s - V_o}} \tag{2.26}$$

called *rho poloidal*, *rho toroidal* and *rho volume* respectively, the labels 'o' and 's' referring to the magnetic axis and the separatrix respectively. Φ is the toroidal magnetic flux, V the volume within the flux surface. The only flux surface label used in throughout this thesis is ρ_{pol}. For semplicity, the subscript *pol* will be omitted from now on.

As explained in [12] and [5], taking the toroidal component of the momentum equation 2.5 and averaging over the flux surface, one is left with the radial flux for toroidal symmetry:

$$\langle \Gamma_a^r \rangle = \frac{dr}{d\Psi} \left(n_a \langle RE_t \rangle + \frac{1}{e_a} \langle RF_{a,t} \rangle \right) \tag{2.27}$$

where circular flux surface geometry has been assumed, r begin the radius of the flux surfaces. The first term is related to the toroidal electric field, the second to the toroidal friction force. By dividing these in components perpendicular and parallel to the magnetic field, the perpendicular one will simply deliver the classical fluxes (same as the results obtained in section 2.1, but averaged over the flux surface), while the parallel ones will give the contributions due to parallel friction forces, the neoclassical fluxes:

$$\langle \Gamma_a^r \rangle_\parallel = \frac{dr}{d\Psi} \frac{1}{e_a} \left\langle \frac{RB_t F_{\parallel a}}{B} \right\rangle \tag{2.28}$$

Three contributions to this flux are usually distinguished according to the collisional regime of the plasma. This is usually defined in terms of *collisionality*, which is equal to the ratio between collisional frequency $\nu_a = \sum_b \nu_{ab}$ and the bounce frequency ν_B of a trapped particle (defined later on in this chapter):

$$\nu_a^* = \frac{\nu_a}{\nu_B} \tag{2.29}$$

For the case of high collisionality the regime is referred to as *Pfirsch-Schlüter* (PS), in the case of low collisionality as *Banana*. An intermediate term, know as *Plateau* (roughly

independent of collisional frequency), is usually incorporated in the latter which is then referred to as *Banana-Plateau* (BP) regime. As already anticipated in the introductory paragraphs to this chapter, only a qualitative explanation of these contributions is given here. For a detailed derivation refer to [15].

2.2.1 Pfirsch-Schlüter

For the case of a highly collisional plasma the stress anisotropy will be kept small by collisional randomization but, since the mean free path is small, variations of the pressure within a magnetic flux surface are anyway possible [15]. To cancel this pressure anisotropy parallel flows, called Pfirsch-Schlüter flows, build up. Following [5], in order to evaluate the parallel friction force $\overrightarrow{F}_{\parallel a}$, the parallel fluid velocity $\overrightarrow{u}_{\parallel a}$ has to be known. In first order with respect to the small parameter δ, this can be done noting that the magnetic field anisotropy on a magnetic flux surface leads to a non divergence free first order perpendicular fluid velocity $\overrightarrow{u}_{\perp a}^{(0)}$. Decomposing the perpendicular diamagnetic velocity (equation 2.9) along the toroidal ($\overrightarrow{e}_t$) and parallel ($\overrightarrow{e}_{\parallel}$) directions:

$$\overrightarrow{u}_{\perp a}^{(0)} = \frac{1}{e_a n_a} \frac{\partial p_a}{\partial \Psi} \left(R \overrightarrow{e}_t - \frac{RB_t}{B} \overrightarrow{e}_{\parallel} \right) \tag{2.30}$$

since the toroidal part has zero divergence and RB_t is constant on the flux surface, the cause for the non-vanishing divergence can be found in the $1/B$ term:

$$\nabla \cdot \overrightarrow{u}_{\perp a}^{(0)} = -2 \, \overrightarrow{u}_{\perp a}^{(0)} \cdot \frac{\nabla B}{B} \tag{2.31}$$

The magnetic field gradient thus leads to a charge separation, pushing ions in the direction $\overrightarrow{B} \times \nabla B$, and electrons in the opposite direction. In order to guarantee total non-divergent flows $\nabla \cdot \overrightarrow{u}_a^{(0)} = 0$ and cancel this separation, parallel flows will build up:

$$\overrightarrow{u}_{\parallel a}^{(0)} = \frac{RB_t}{e_a n_a} \frac{\partial p_a}{\partial \Psi} \left(\frac{1}{B} - \frac{B}{\langle B^2 \rangle} \right) \overrightarrow{e}_{\parallel} + C_a \overrightarrow{B} \tag{2.32}$$

The last term proportional to the magnetic field has to be added for completeness noting that the result is in any case divergent free. Neglecting this term for the time being and skipping the remaining calculations, the PS diamagnetic drift is found to be directed radially outward. The resulting flux surface averaged diffusion coefficient will finally be:

$$D_{PS}^a \approx \left(\frac{dr}{d\Psi} \right)^2 RB_t^2 \left\langle \frac{1}{B^2} - \frac{1}{\langle B^2 \rangle} \right\rangle \frac{m_a k_B T}{e_a^2} \sum_{b \neq a} \nu_{ab} \tag{2.33}$$

Assuming the tokamak has small inverse aspect ratio $\epsilon = r/R$ so that $dr/d\Psi = R_{axis}B_p = R_0 B_p$, the radial derivative of the poloidal flux Ψ and the flux surface averaged terms in 2.33 can be approximated with:

$$\left(\frac{dr}{d\Psi} \right)^2 RB_t^2 \approx q/\epsilon \qquad \frac{1}{\langle B^2 \rangle} \approx \frac{1 - \epsilon^2/2}{B_0^2} \qquad \left\langle \frac{1}{B^2} \right\rangle \approx \frac{1 + 3\epsilon^2/2}{B_0^2} \tag{2.34}$$

where q is the so-called "safety factor":

$$q \approx \frac{r}{R}\frac{B_t}{B_p} \tag{2.35}$$

In first order, the PS diffusion can be therefore expressed as an enhancement of the classical diffusion by a factor $2q^2$:

$$D_{PS}^a \approx 2q^2 \; D_{CL}^a \tag{2.36}$$

Going one step backward and expanding the flux surface averaged term in equation 2.32 of the parallel flow velocity in first order with respect to the vacuum magnetic field:

$$\frac{1}{B} - \frac{B}{\langle B^2 \rangle} \approx \frac{1}{B} - \frac{B}{B_0^2}$$

it can noticed that this term will change sign when radially crossing the plasma axis where $B = B_0$. The parallel flow is thus positive on the low field side ($B < B_0$, external part of the torus $R > R_0$) and negative on the high field side ($B > B_0$, inner part of the torus). As can be seen in figure 2.2, the radial component of the resulting fluxes will therefore be always directed outward.
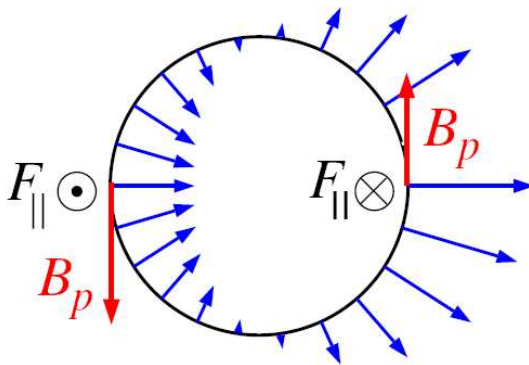

Figure 2.2: *Pattern of PS fluxes (blue) for a cylindrical flux surface due to the poloidal variation of the parallel flow velocity and thus of the parallel friction forces $F_\parallel$ (figure from [5]). The direction of the poloidal magnetic field component is also shown in red.*

2.2.2 Banana-Plateau

For the case of a low collisional frequency ν_a, the particles will move freely along the magnetic field lines trying constantly to maintain the pressure isotropic on the magnetic flux surfaces and the free particles streaming along the magnetic field lines will feel the ∇B

before any collisions take place. The pressure anisotropy is kept small by the free parallel motion, but the stress anisotropy is enhanced by particle trapping.

The trapping of particles due to the anisotropy of the magnetic field is the basic principle of magnetic mirror confinement systems. These machines are linear devices (so-called magnetic bottles) where the *necks* of the system exhibit a higher magnetic field with respect to the rest of the machine. Particles moving along the field lines will be reflected at these positions if their velocity parallel to the magnetic field is such that:

$$|v_{\parallel}| \leq |v_{\perp}| \sqrt{\frac{\Delta B}{B}} \tag{2.37}$$

The main reason behind this is the conservation of the particle's energy and of its magnetic moment:

$$E = \frac{1}{2}mv_{\parallel}^2 + \mu B + e\phi \qquad\qquad \mu = \frac{mv_{\perp}^2}{2B} \tag{2.38}$$

where ϕ is the electric potential. If $\phi = 0$ and since the magnetic moment is a constant, passing from regions of low magnetic field to regions of high B, the parallel velocity will decrease in order to keep the total energy constant. In the specific case of a tokamak, the minimum magnetic field is encountered on the outboard side (therefore named Low Field Side LFS) $B_{min} = B_{LFS}$. The maximum magnetic field is encountered on the inboard side (named High Field Side HFS) $B_{max} = B_{HFS}$. As can be seen from equation 2.38, the particle will have its maximum parallel velocity on the LFS, its minimum on the HFS. A reflection will occur only if $v_{\parallel} = 0$ before passing the high field region of the plasma. Setting $v_{\parallel,HFS} = 0$ and imposing the conservation of energy at both LFS and HFS:

$$E_{LFS} = \frac{1}{2}mv_{\parallel,LFS}^2 + \mu B_{LFS} = \mu B_{HFS}$$

Substituting the expression for the magnetic moment, condition 2.37 is easily recovered for our specific case. For large aspect ratio tokamaks $\epsilon = r/R << 1$, high and low field side magnetic fields can be approximated as $B_{HFS} \sim B_0/(1-\epsilon)$ and $B_{LFS} \sim B_0/(1+\epsilon)$ and the bounce condition written as:

$$\left|\frac{v_{\parallel}}{v_{\perp}}\right|_{LFS} \leq \sqrt{\frac{B_{HFS} - B_{LFS}}{B_{LFS}}} \sim \sqrt{\frac{1+\epsilon}{1-\epsilon} - 1} = \sqrt{\frac{2\epsilon}{1-\epsilon}} \sim \sqrt{2\epsilon} \tag{2.39}$$

The blue and red lines in figure 2.3 show the projection on the poloidal plane of two full trapped particle orbit. Because of their shape, they are commonly referred to as "banana orbits".

The radial transport in this regime originates mathemetically from the last term in equation 2.32 proportional to the magnetic field and can be evaluated from the parallel momentum balance. The derivation given here is instead from a more general random walk point of view (refer to [5, 15] for a more complete treatment).

If particles on such orbits collide, the transport they give rise to is much higher than the classical contribution. This can be understood taking into account that the characteristic
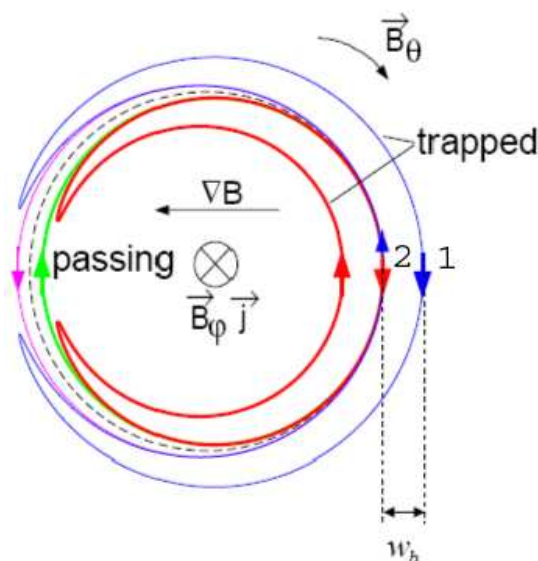
Figure 2.3: *Circular poloidal cross section of a tokamak plasma showing two trapped particle orbits (blue, red) and two passing orbits (green, magenta). The machine axis is on the left had side of the figure. Direction of the plasma current, toroidal and poloidal magnetic fields and the magnetic field gradient are also labeled (figure from [19]).*

length of these orbits is the full excursion of the banana orbit, much larger than the Larmor radius ρ_L, used as step size for the evaluation of the classical diffusion coefficient in random walk formulation (equation 2.21). The step size of these collisions can be evaluated from the equation of the conservation of canonical toroidal angular momentum:

$$p_\varphi = m_a R v_\varphi + e_a \Psi = const. \tag{2.40}$$

where v_φ is the velocity of the particle in the toroidal direction φ and Ψ is the poloidal magnetic flux. Since this quantity will be constant along the whole particle trajectory, imposing $p_\varphi(1) = p_\varphi(2)$ for the two positions on the midplane along the blue orbit in figure 2.3:

$$m_a R v_\varphi^{(1)} + e_a \Psi^{(1)} = m_a R v_\varphi^{(2)} + e_a \Psi^{(2)}$$

and expanding the poloidal flux variation in the radial direction $\delta\Psi \sim d\Psi/dr\ \delta r \sim R B_p w_b$ where w_b is the radial extension of the trajectory (the *banana width*), equation 2.40 can be re-written as:

$$
\begin{aligned}
2 m_a R \left| \delta v_\varphi \right| &= e_a \left| \delta \Psi \right| \\
&= e_a R B_p w_b
\end{aligned}
$$

Since $\delta v_\varphi \sim v_T \sqrt{\epsilon}$, an approximation of the width of the trapped particle orbit can be finally obtained:

$$w_b \approx \sqrt{\epsilon} \frac{m_a v_T}{e_a B_p} = \sqrt{\epsilon} \rho_p \tag{2.41}$$

where ρ_p is the poloidal gyro radius. The quantity w_b is the maximum width of the banana orbit and the step size of the random walk.

In order to evaluate the diffusion coefficient in the BP regime, the collision frequency has also to be known. Going back to figure 2.3, it can be noticed that both red and blue trapped orbits pass through point 2. If these two orbits collide so to reverse the parallel velocities of the guiding centre, the orbit centres will jump of a factor w_b. Since the difference between co and counter parallel velocity in a banana orbit is $\delta v_\parallel \sim \sqrt{\epsilon}$, the minimum change in $v_\parallel$ (and thus in pitch angle of the orbit) necessary for the inversion to occur is $\sim \sqrt{\epsilon}$. Since, as explained in section 2.1 the classical collision frequency ν_a refers to a change in pitch angle due to Coulomb scattering of roughly $\Delta \alpha \sim 90°$, the collision frequency for a change of $\sqrt{\epsilon}$ will be [15]:

$$\nu_{a,eff} = \frac{\nu_a}{\Delta \alpha^2} \approx \frac{\nu_a}{\epsilon} \tag{2.42}$$

Estimating the fraction of trapped particles in large aspect ratio approximation as $n_t/n \approx \sqrt{\epsilon}$, and expressing the poloidal Larmor radius in terms of the safety factor and of the toroidal Larmor radius :

$$\rho_p = \frac{m_a v_T}{e_a B_p} = \frac{m_a v_T}{e_a B_t} \frac{B_t}{B_p} = \frac{\rho}{\epsilon} q$$

the random walk estimate of the diffusion coefficient for collisions between trapped particles will be:

$$
\begin{aligned}
D_{BP} \quad &\approx \quad \frac{n_t}{n} \frac{\nu_a}{\epsilon} w_b^2 \\
&= \quad \sqrt{\epsilon} \frac{\nu_a}{\epsilon} \left(\sqrt{\epsilon} \rho_p \right)^2 = \sqrt{\epsilon} \frac{\nu_a}{\epsilon} \left(\frac{q}{\sqrt{\epsilon}} \rho \right)^2 \\
&\approx \quad \frac{q^2}{\epsilon^{3/2}} D_{CL} \tag{2.43}
\end{aligned}
$$

roughly a factor $q^2/\epsilon^{3/2}$ with respect to the classical one.

At this point, the collisionality parameter introduced at the beginning of section 2.2 can be better understood. The time necessary for a trapped particle to perform one bounce (named *bounce time* τ_B) is equal to the distance from LFS to HFS along the magnetic field lines divided by the parallel velocity of the particle. The bounce frequency ν_B introduced in section 2.2 will be its inverse. Approximating the LFS-HFS distance as $L \approx qR$, since the parallel velocity of a trapped particle is $v_\parallel \sim v_T \sqrt{\epsilon}$:

$$\nu_B = \frac{v_\parallel}{L} \approx \frac{v_T \sqrt{\epsilon}}{qR} \tag{2.44}$$

For high collisionality $\nu_a >> \nu_B$, collisions will occurr with a very high probability before a trapped particle is able to complete one bounce. In this case the fraction of trapped particles will be very small and the neoclassical fluxes dominated by the Pfirsch-Sclüter regime. For low collisionalities, since the probability of a collision before having completed one at least one bounce will be very low, the fraction of trapped particles will instead be very high and the transport dominated by the Banana regime.

2.2.3   Ware Pinch

When considering also the toroidal electric field imposed to generate the plasma current, the trapped particles will be accelerated when travelling in the direction of the electric field and decelerated when, after having bounced back, travelling against it. The effect can be mathematically dealt with starting from the conservation of canonical angular momentum 2.40 recalled here:

$$p_\varphi = mRv_\varphi + e_a\Psi = const. \tag{2.45}$$

By differentiating with respect to time along the particle trajectory [15] one obtains:

$$\frac{d\Psi}{dt} = \frac{\partial\Psi}{\partial t} + \overrightarrow{v}_\varphi \cdot \nabla\Psi = -RE_t + v_\varphi RB_p = -\frac{m}{e_a}\frac{d(Rv_\varphi)}{dt} \tag{2.46}$$

where E_t is the toroidal induced electric field which sustains the plasma current and v_φ the particle toroidal velocity. Integrating between two time points at which the toroidal velocity vanishes:
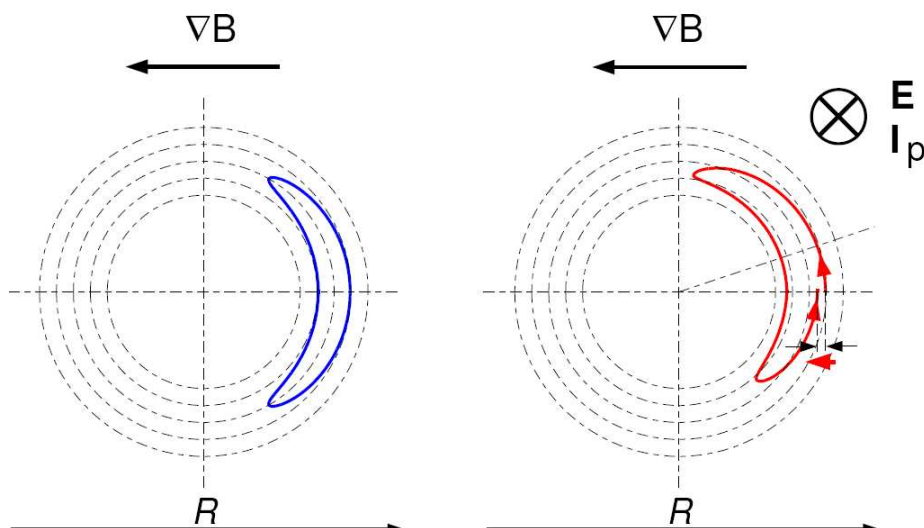

Figure 2.4: *Trapped particle guiding-centre orbits when neglecting the toroidal electric field (left) and when considering its effect (right) (figure from [20]).*

$$\overrightarrow{v}_\varphi \cdot \nabla\Psi = -RE_t = \overrightarrow{u}_{\perp a} \cdot \nabla\Psi \qquad (2.47)$$

it can be noticed that the trapped orbit will remain on average tied to the flux surface and, as the surface moves inward in response to the toroidal electric field, the particle moves with it. The orbit will thus move inwards as shown on the right side of figure 2.4.

The final convection velocity can be written as:

$$v_{ware}^a = -k_{ware}(\nu)\frac{E_t}{B_p} \qquad (2.48)$$

which is commonly referred to as *Ware pinch* since it was first formulated by Ware [21]. The factor $k_{ware}(\nu)$ is collisionality dependent and goes to zero for high collisionalities, i.e. when the trapped orbits can only travel a portion of the banana orbit before colliding.

2.3 Turbulent Transport

As already introduced at the beginning of this chapter, the transport routinely observed in a tokamak is up to orders of magnitude higher than the neoclassical predictions. It is thought that this enhancement is caused by micro-instabilities in the density and in the temperature which, generating local fluctuating electrostatic potential, lead to local fluctuating $E \times B$ drifts called *drift waves*. Since the $E \times B$ flows are independent of particle mass and charge, the associated radial transport is equal for all species. The main turbulent instabilities which give rise to radial particle transport are named after their precursor: Ion Temperature Gradient mode (ITG), the Trapped Electron Mode (TEM) and the Electron Temperature Gradient mode (ETG). The scale lengths of the fluctuations are of the order of the ion Larmor radius for ITG and TEM, of the electron Larmor radius for ETG. Since ETG instability is analogous to ITG but at smaller scales, a brief explanation of the causes of only the ITG and TEM modes is given below.

ITG
These modes are essentially interchange instabilities. Above a certain critical ion temperature gradient, a temperature perturbation will generate a density perturbation which then translates into an oscillation of the electrostatic potential. As can be seen on the right hand side of figure 2.5, the resulting local charge separation will lead to $E \times B$ flows. On the low field side (right) these flows will "feed" the perturbation by enhancing the high temperature regions (central green arrow) and cooling even further the low temperature ones (top and bottom green arrows). On the high field side (left in figure), the perturbation will instead be damped since the $E \times B$ flows are always in the same direction, contrary to the temperature gradient which reverses. An ITG is thus stable on the HFS but unstable on the LFS.

These modes become unstable for large wavelengths such that $k_\perp \rho_i < 1$, where $k_\perp$ is the wave number of the fluctuation in the direction perpendicular to the magnetic field and ρ_i the ion Larmor radius. On the other hand, their instability depends strongly on the ion temperature gradient which has to raise above a certain level in order to trigger the instability. Depending on the profile of the safety factor, on the value of the electron density gradient and on the ratio between electron and ion temperatures T_e/T_i, the mode
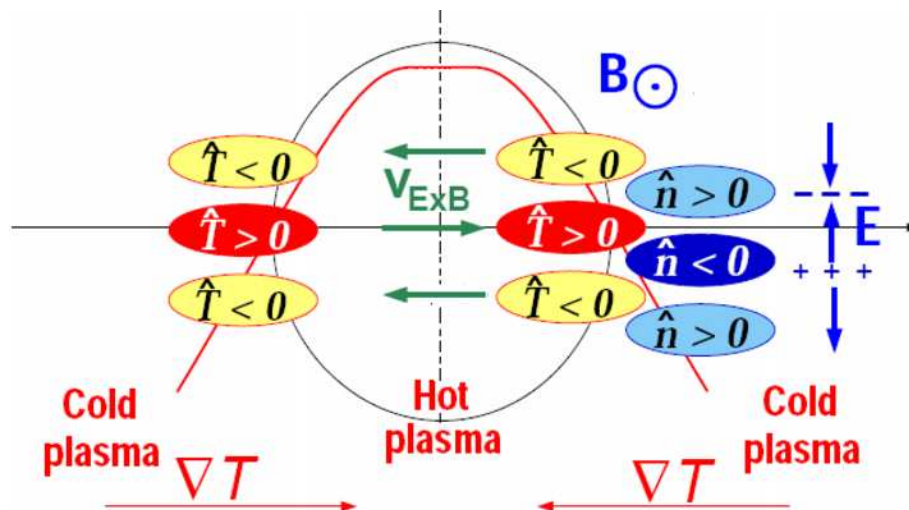
Figure 2.5: *Scheme of an ITG instability on a poloidal cross section [5]. The starting temperature oscillation $\tilde{T}$ and the subsequent density $\tilde{n}$ and electric field oscillations (in blue) which then give rise to fluctuation $E \times B$ drifts (green) are shown. The machine axis is on the left hand side.*

will be an ITG, a TEM or a mixture between these. The stability diagram for the case of $T_e = T_i$ is shown in figure 2.6. The threshold is usually expressed in terms of the normalized logarithmic gradients (also called normalized gradient lengths), already introduced in section 2.1, but recalled here for completeness:

$$\frac{R}{L_n} = -R\frac{d}{dr}log\left(n\right) = -R\frac{\nabla n}{n} \qquad\qquad \frac{R}{L_T} = -R\frac{d}{dr}log\left(T\right) = -R\frac{\nabla T}{T} \qquad (2.49)$$

where R is the tokamak major radius. The ITG threshold $R/L_{T_i,crit}$ is not a universal number, but depends strongly on plasma parameters. In particular, it increases with increasing T_i/T_e and with increasing R/L_{n_e}.

TEM
As already said in the previous section, TEM and ITG instabilities are strictly related. TEMs are still on the ion Larmor radius scale, but where the slow average motion along the field lines is caused by trapping rather than by inertia.

   As shown in the section dedicated to neoclassical transport, the average parallel motion of trapped electrons is slow in comparison to those on passing orbits. This motion is therefore not fast enough to re-equilibrate the parallel gradients. The drive for this instability is mainly a resonant interaction between the modes and the trapped electrons at the precession frequency. Analogously to ITG but on the electron side, the threshold for trapped electron modes is a critical electron temperature gradient $R/L_{T_e,crit}$ (which is a function of the electron density gradient) and depends strongly on the fraction of trapped electrons. As can be seen in the stability diagram in figure 2.6, TEMs are the dominant instabilities for large R/L_{n_e}. Moreover, for $T_e/T_i > 1$ (e.g. plasmas with strong electron heating) the ITG threshold may not be met and TEMs will be again dominant.
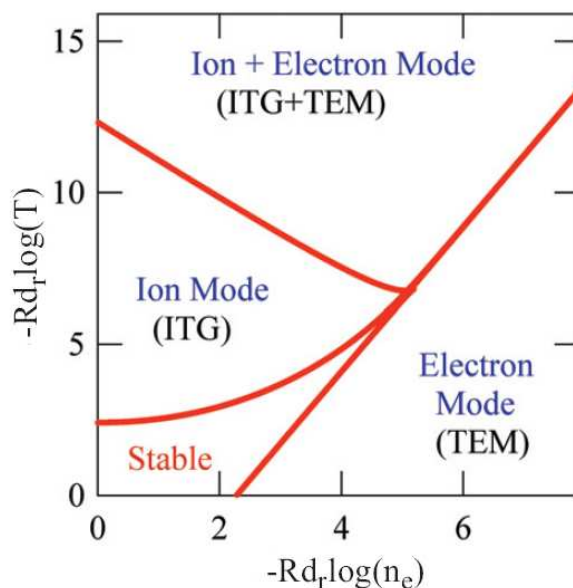
Figure 2.6: *Stability diagram of ITG, TEM modes (figure from [22]).*

2.3.1 Radial Fluxes

Transport induced by electrostatic turbulence is usually referred to as "electrostatic" or "$E \times B$" transport. What is relevant for the radial particle fluxes is the phase relation between the fluctuation potential $\tilde{\phi}$ and the density fluctuations $\tilde{n}_a$. The response of the density perturbation $\tilde{n}_a$ can be expressed as a linear combination of the logarithmic gradients [23]:

$$\tilde{n}_a = \left(A_a \frac{R}{L_{n_a}} + B_a \frac{R}{L_{T_a}} + C_j \right) \phi \tag{2.50}$$

where A, B and C are complex coefficients. The quasi-linear particle flux can be then evaluated through:

$$\Gamma_a = \langle \tilde{n}_a \tilde{v}_{E \times B} \rangle \propto \left\langle \tilde{n}_a \tilde{\phi} \right\rangle \tag{2.51}$$

which can be written in the familiar diffusive and convective form:

$$\begin{aligned}
\frac{R\Gamma_a}{n_a} &= \left(D \frac{R}{L_{n_a}} + D_T \frac{R}{L_{T_a}} + RV_P \right) \phi \\
&= D \left(\frac{R}{L_{n_a}} + C_T \frac{R}{L_{T_a}} + C_P \right) \phi
\end{aligned} \tag{2.52}$$

where $C_T = D_T/D$ and $C_P = RV_P/D$, the coefficients D, D_T and V_P respectively named diffusion coefficient, thermo-diffusion and convection velocity. In general, these coefficients depend themselves on the logarithmic density and temperature gradients, so a linear dependence as in equation 2.52 is not generally met. This approximation can only be done

in the case in which the impurity may be considered a "trace" whose charge concentration in the plasma is small enough not to modify the quasi-neutrality condition so not to influence the turbulence by main ion dilution or by excitation of impurity modes. In this case, any modification of the logarithmic gradients of the impurity species will not modify the transport coefficients and equation 2.52 will be valid for any R/L_{T_a} and/or R/L_{n_a} [11].

The evaluation of the particle fluxes and thus of the transport coefficients requires non-linear models which couple the effect of the fluctuating potential $\tilde{\phi}$ on the perturbed velocity distribution function which depends on $\tilde{\phi}$. Numerical codes such as GS2 [24, 25] are therefore needed to solve the gyrokinetic equation.

2.4 Total Radial Particle Flux

For the evaluation of the total radial particle flux, all contributions from collisions and turbulence have to be added up. A general formulation for the collisional part, leads to a total contribution to the radial particle flux of particle a caused by collisions with all other particles b:

$$
\begin{aligned}
\Gamma_a^r &= \sum_{x=CL,PS,BP} \sum_{b\neq a} (-D_x^{ab} \nabla n_a + v_x^{ab} n_a) \\
&= \sum_{x=CL,PS,BP} \sum_{b\neq a} D_x^{ab} \left[-\nabla n_a + \frac{e_a}{e_b} \left(\frac{\nabla n_b}{n_b} + H_x^{ab} \frac{\nabla T}{T} \right) n_a \right]
\end{aligned} \tag{2.53}
$$

where H_x^{ab} are the temperature gradient factors (as in equation 2.22 for the classical case, $H_{CL}^{q,H} = -1/2$) which depend strongly on collisionality. CL, PS and BP stand for Classical, Pfirsch-Schlüter and Banana-Plateau regimes. The full set of collisional transport coefficients can be evaluated by numerical codes such as NCLASS [26] or NEOART [27]. The contributions from the anomalous transport ($\Gamma_{an}^a = -D_{an}\nabla n_a + v_{an}n_a$) can then to be added to the collisional part to evaluate the total theoretical radial particle fluxes:

$$
\Gamma_a^r = \Gamma^{an} + \Gamma^{coll} \tag{2.54}
$$

Chapter 3

The Compact Soft X-ray Spectrometer at AUG

Since the discovery of x-rays by Röntgen in 1895, the observation of their diffraction in crystals by von Laue in 1912 and the wavelength dependence of the diffracting angle demonstrated by Bragg in 1913, crystal spectroscopy is still a very powerful tool in analysis of the X-ray spectral regime. Compared to solid state or other detector technologies it yields the highest spectral resolution and through various geometries, from flat to curved crystals, symmetric or asymmetric cuts, crystal spectrometers can be adapted to different experimental conditions with ease.

The Bragg law relates the dispersed radiation of wavelength lambda to the crystal lattice spacing (d) and to the angle of incidence of the x-rays on the crystal lattice (θ_B), the Bragg angle:

$$n\lambda = 2d \; sin\theta_B \qquad (3.1)$$

where n is the order of dispersion.

Many different geometries have been applied in Bragg spectrometers. Flat crystals have resolving power that can exceed $\lambda/\delta\lambda = 10\,000$ [28]. This enables wavelength identification, doppler broadening and shift, and intensity measurements of the spectral lines, but because of no intrinsic focusing power the luminosity is low. By bending the crystal, a mirror focusing action can be combined with the natural diffraction properties of the crystal and the use of other optical elements that would lead to a reduction in intensity can be avoided. Moreover, with the use of an asymmetrically cut crystal (diffraction planes not parallel to the crystal surface), the intrinsic aberrations of a bent crystal can be reduced. The X-ray spectrometer installed on ASDEX Upgrade (AUG) makes use of all these principles using an asymmetrically cut spherically bent quartz crystal in the Johann geometry. Basics of the Johann spectrometer geometry with asymmetrically cut crystals are given in section 3.1, section 3.2 deals with the specifics of the experimental setup on AUG, section 3.3 and 3.4 on the calibration of the spectrometer.

3.1   Spectrometer Basics

A flat crystal bent to a radius of curvature R determines a focusing Rowland circle of radius R/2. X-ray photons of wavelength λ incident on the crystal at an angle $\theta_B = arcsin(n\lambda/2d)$
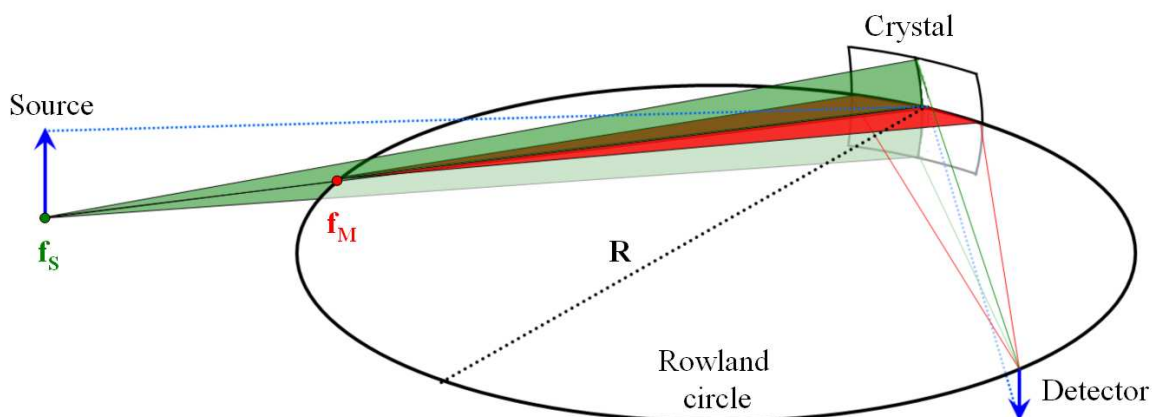
Figure 3.1: *Symmetric Johann configuration: red rays are on the diffracting meridional plane; green rays on the sagittal plane.*

relative to the diffracting planes are focused on one point of this circle. A cylindrically bent crystal focuses only in one direction but leaves divergent rays along the cylinder's axis. By bending the crystal two-dimensionally both sagittal and meridional rays will be focused, thus increasing the luminosity of the spectrometer. This focusing action is different for the two planes. As can be seen in figure 3.1, spherical crystals are naturally astigmatic. The meridional (also called horizontal or diffraction) plane and sagittal (vertical) plane have different focal spots. Rays on the sagittal plane that satisfy the Bragg condition will be reflected as by a spherical mirror, while rays on the meridional plane will be focalized on the Rowland circle. Best spectral resolution will be obtained positioning the detector at a distance f_M from the crystal:

$$f_M = R \, sin\theta_B \tag{3.2}$$

where θ_B is the Bragg angle of the ray incident on the center of the crystal.

The sagittal focal length f_S (position of the source in order to obtain maximum spatial resolution) can be evaluated from the mirror equation, keeping in mind that the incident rays lie on a plane tilted of an angle $\varphi = \pi/2 - \theta_B$ with respect to the normal of the crystal (along the dotted black line R in figure 3.1).

$$\frac{1}{f_s} + \frac{1}{f_M} = \frac{2 \, sin\theta_B}{R}$$

Substituting the value of f_M from equation 3.2, the sagittal focal can be evaluated:

$$f_S = \frac{f_M}{sin^2\theta_B - 1} = \frac{f_M}{-cos \, 2\theta_B} \tag{3.3}$$

The focusing properties can be further enhanced by using a crystal with the atomic planes of the crystal not parallel to the crystal surface but tilted by an angle α, called asymmetry angle (so-called asymmetrical cut). If the asymmetry angle is chosen well, the incident rays can be near to perpendicular to the crystal surface. This leads to a decrease in range of angles incident on the crystal surface which in turn decreases the astigmatism of the system and consequently increases its resolving power.
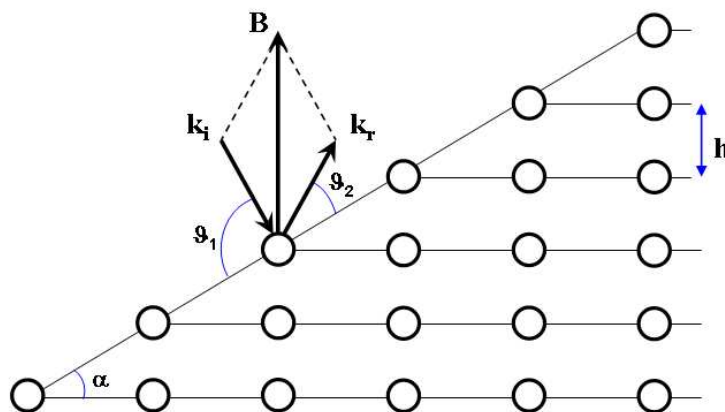
Figure 3.2: *Scheme of Bragg diffraction on asymmetrically cut crystals (figure from [29]).*

From a mathematical point of view, the focalization properties of these crystals is due to a modification of the ray divergences. Differently from the symmetric case, there is no specular reflection on an asymmetrically cut crystal. Defining k_i and k_r as the incident and diffracted wave vectors and B as the reciprocal lattice vector, by projecting the Laue equation

$$\overrightarrow{k_r} = \overrightarrow{k_i} + \overrightarrow{B} \tag{3.4}$$

parallel and perpendicular to the crystal surface and taking into consideration the elastic scattering condition:

$$|\overrightarrow{k_r}| = |\overrightarrow{k_i}| = 2\pi/\lambda \tag{3.5}$$

the Bragg law and the classical grating equation for asymmetric diffraction is obtained:

$$\begin{cases} sin \, \vartheta_2 - sin \, \vartheta_1 = (\lambda/d) \; cos \, \alpha \\ cos \, \vartheta_2 - cos \, \vartheta_1 = (\lambda/d) \; sin \, \alpha \end{cases} \tag{3.6}$$

The angles $\vartheta_1 = \theta_B + \alpha$ and $\vartheta_2 = \theta_B - \alpha$ are the incident and diffracted glancing angles with respect to the Bragg and asymmetry angles.

In the limit of symmetrical diffraction ($\alpha = 0$) the first equation in 3.6 is simply the Bragg law while the second gives the expression for specular reflection ($\vartheta_2 = \vartheta_1 = \theta_B$). For asymmetry angles different from zero, there will be no specular reflection and the input and output divergences will differ. Achieving the derivative of the grating equation the exit divergence will differ from the input divergence by an "asymmetry factor" b:

$$\Delta\vartheta_2 = \frac{sin \, \vartheta_1}{sin \, \vartheta_2} \; \Delta\vartheta_1 = b \; \Delta\vartheta_1 \tag{3.7}$$

This factor b is one of the reasons for the enhanced focusing properties of these crystals. Figure 3.3 shows the difference between the two schemes. The figure on the right is the particular case of the spectrometer installed on AUG where the incident rays are near to
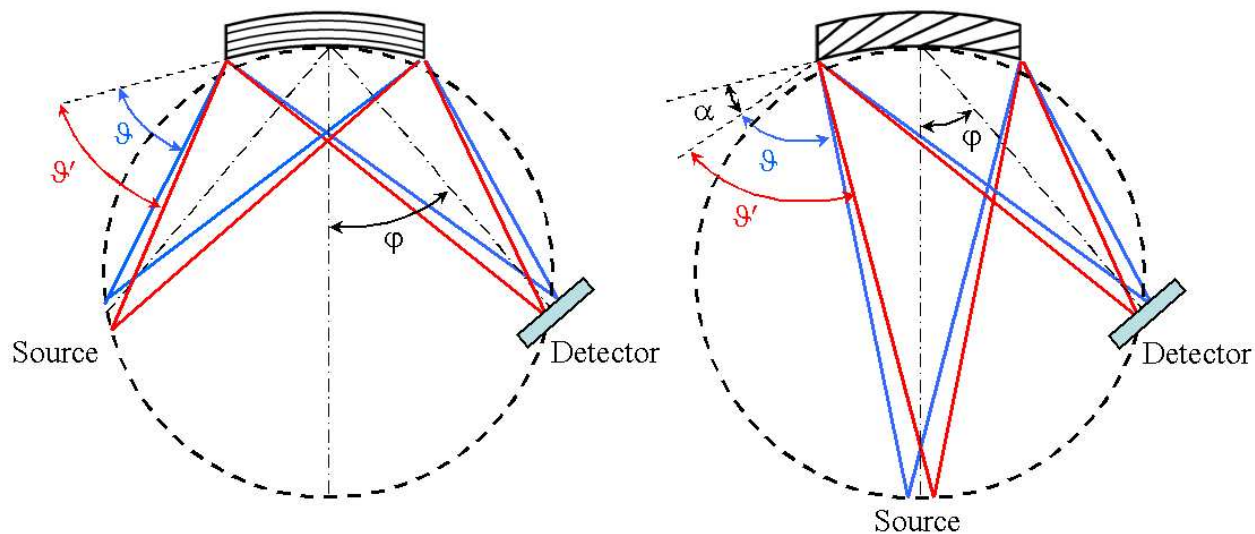
Figure 3.3: *Scheme of symmetric (left) and asymmetric (right) Bragg diffraction schemes.*

normal to the crystal surface but have an angle $\vartheta_1 = \theta_B + \alpha$ with the diffraction planes. With this setup, if a point source is positioned in the center of the sphere representing the crystal (defined by the label "source" in figure 3.3), all the rays would have the same incident angle on the crystal surface, so the diffracted rays would be perfectly monochromatic. Consequently, by keeping the source small, the range of angles incident on the crystal will anyway be very small, thus keeping high the spectral resolution.

The resolving power of such a spectrometer depends on crystal angular width ω, dimension (width l and height h) and radius of curvature, Bragg angle and detector resolution Δx_D. The various contributions are exemplified in table 3.1 [30]. The resulting instrument resolution will be the gaussian propagation of all these factors. Curvature defects, refractive index and penetration depth corrections are not taken into account (see [28] for more in-depth analysis).

Crystal width	$\frac{\delta\lambda_l}{\lambda} = \left(\frac{l}{4R}\right)^2 \frac{1}{2\,tan^2\,\theta_B}$
Crystal height	$\frac{\delta\lambda_h}{\lambda} = \left(\frac{h}{4R}\right)^2 \frac{1}{2\,sin^2\,\theta_B}$
Detector resolution	$\frac{\delta\lambda_D}{\lambda} = \frac{\Delta x_D}{2R} \frac{cot\,\theta_B}{sin\,\theta_B}$
Crystal angular width	$\frac{\delta\lambda_\omega}{\lambda} = \frac{\omega}{tan^2\,\theta_B}$

Table 3.1: Contributing factors to the resolving power of a Johann spectrometer

As can be seen in table 3.1, all contributions decrease with increasing Bragg angle, crystal curvature radius and detector resolution, and with decreasing crystal dimensions. In general, classic Johann spectrometers have large curvature radius, Bragg angle as close as possible to 90° (depending on the lattice constant d and required visible spectral range) and a limited crystal size thus reaching up to $\lambda/\Delta\lambda \sim 10000$. Side effects of these spectrometers

are the upper limit in luminosity due to crystal size limitations and large space occupancy
due to big curvature radius.

3.2   The CSXR on AUG

The Compact Soft X-Ray (CSXR) installed
at AUG employs a large 20x35 mm^2 quartz
crystal ($10\bar{1}0$) asymmetrically cut by 21.9°
and spherically bent to a radius of 500 mm
[31].   The crystal is made of high purity
quartz which makes it resistive to high neu-
tron fluxes in thermonuclear devices and
is mounted on a fused quartz substrate
by means of "optical contact" technique to
avoid the presence of glue layer of undefined
thickness.

The unusual strong bending of the crys-
tal guarantees a very light and compact de-
vice (25 cm Rowland radius, about 10 kg
weight). For symmetrically cut crystal this
would lead to a loss of resolving power due
to an increase of astigmatism of the crystal.
In this specific case, the asymmetrical cut
guarantees a ∼ 90° incidence with respect
to the crystal surface and a 68.1° Bragg an-
gle as shown in the right part of figure 3.3.
A bellow installed on the detector arm al-
lows small adjustments to the final detector
position.

The spectrometer is connected directly
to the upper middle port (E-port) in sec-
tor 2 of AUG (figure 3.4). The line of sight
from this port goes approximately through
the center of the poloidal cross-section. The
minimum visible normalized radius for typ-
ical AUG discharges is r/a∼0.18.

The detector used is a back illumi-
nated CCD camera (DO420-BR-DD, AN-
DOR Technology. Ltd.) which applies a
deeply depleted chip for improved radiation

Figure 3.4: *Schematic view of spectrometer
mount at AUG with the LOS in red.*

hardness. The camera has its maximum quantum efficiency between 1 and 10 keV and pixel
area of 26 μm^2, 1024x256 pixels. For this application the CCD has been initially used in
Full Vertical Binning (FVB) acquisition mode (8 ms time resolution) but, because of the
high luminosity of the diagnostic, the system has been upgraded to achieve 50 sub-row
binning acquisitions thus increasing the time resolution to 4 ms.

The CCD camera is controlled by a PC via a PCI controller card. Due to maximum
length of the controller cable of 15 m the PC had to be placed inside the torus hall and
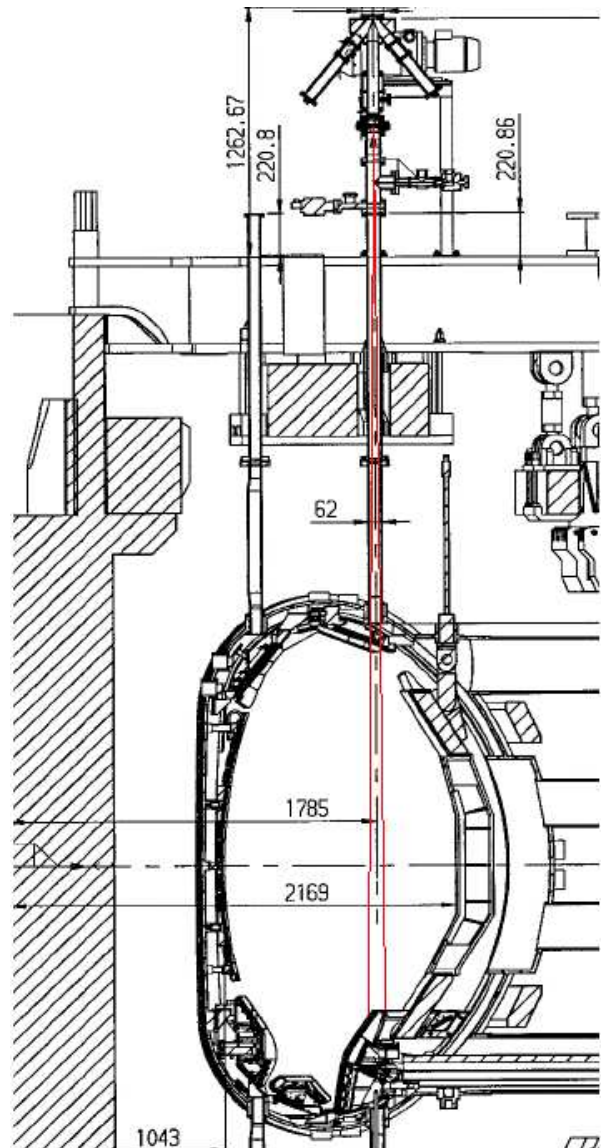
connected to the outer network via an optic fiber connection. The PC has therefore been shielded with paraffin blocks for protection from neutron irradiation.

The pumping system (Pfeiffer TSH 071 E) guarantees an active pumping down to $\sim 1.5 \cdot 10^{-6}$ mbar. Since the pump station is positioned beside the spectrometer on the top of the AUG torus, the turbo molecular pump has been shielded against magnetic field with a 3 cm thick iron case. The CCD camera has been shielded against neutron irradiation with a 2 cm thick cylinder of borated flexi-panel (Shieldwerx SWX-227A) which surrounds the CCD camera entirely. A few side holes and a back fan guarantee sufficient air circulation for cooling purposes.

3.2.1   Main Spectrometer Characteristics

A geometrical ray tracing code has been developed to give precise indication of the crystal illumination characteristics. Using equation 3.3 with $\theta_B = 68.1°$ and $f_M = 50.$ cm, the sagittal focal length results to be $f_s = 148.7$ cm from the crystal surface, around halfway between the crystal and the vacuum vessel.
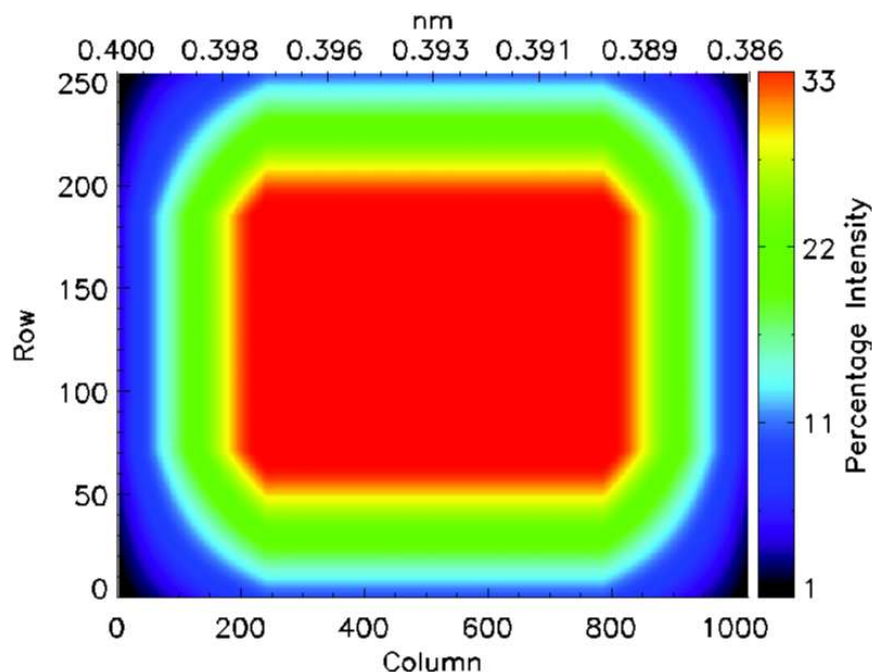

Figure 3.5: *Ray tracing results for CCD illumination. Top abscissa axis is the wavelength range, bottom one in pixels of the CCD.*

The E-port has a circular section of 6.2 cm in diameter, but a rectangular blend positioned in front of the port aperture restricts the opening to 4.8 cm in the toroidal direction. Due to these limitations and to those imposed by the crystal dimensions, the maximum crystal wetted area is only ~ 33 % of the its surface, decreasing for edge wavelengths and sagittal focal spots. This can be seen in figure 3.5, a surface plot of the crystal wetted area projected on the CCD detector, vs. the wavelength range (top) and the CCD pixel
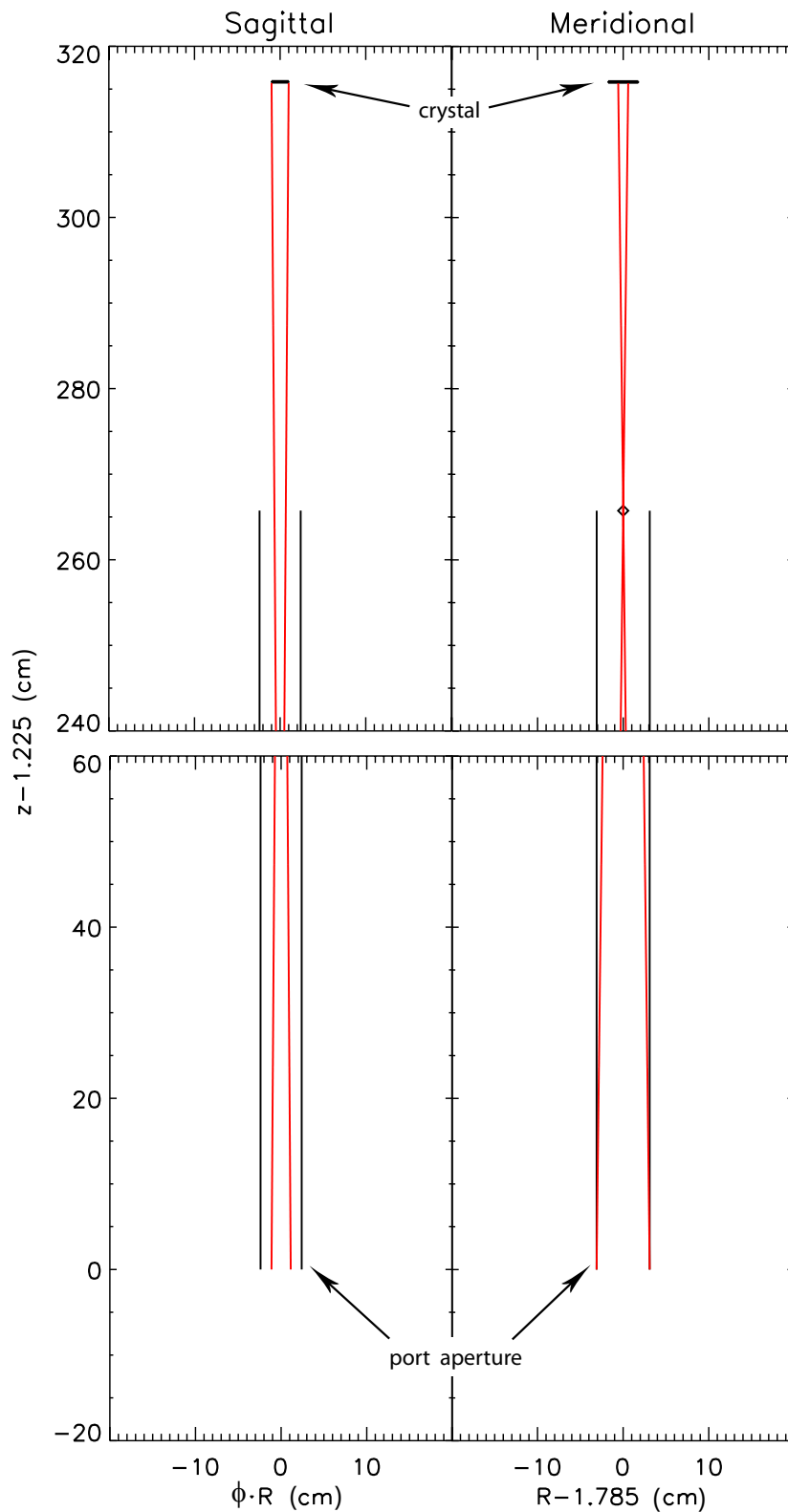
Figure 3.6: *Crystal illumination (top) and port width limitations (bottom) in the sagittal (left) and meridional (right) planes with respect to the toroidal and radial directions respectively. Apart from crystal thickness, all other quantities are in scale. The crystal is totally illuminated in the sagittal plane for most central wavelengths, while port limitations determine a 33% maximum illumination in the meridional plane for all wavelengths.*

columns (bottom). This maximum illumination holds only for 53 % of the CCD chip meridionally, 45 % sagittally (red region in surface plot 3.5), the rest is decreasingly less illuminated down to few percent because of further vignetting. When switching to 50 sub-row binning acquisition mode, the detector has been re-aligned so to view the 50 most central rows in figure 3.5.

Crystal illumination for the most central focal spot in the sagittal and meridional directions can be also seen in figure 3.6. The orientation of the spectrometer has been chosen to have the highest possible luminosity within the geometrical restrictions. Rotating the spectrometer of 90° so to have the crystal meridional plane in the toroidal direction would decrease the crystal wetted area of a further 25%.

The port shading has been precisely determined and translated into a geometric factor which has to be taken into consideration for intensity measurements. Since the crystal is optimized for the w-line of He-like Ar at 0.39492 nm which falls near to the center of the visible spectral range (as can be seen in figure 3.7), this is not a problem for argon concentration, temperature or poloidal rotation measurements. Its correction adds further errors only to the analysis of spectra at the edge of the wavelength range. As can be seen in figure 3.7, of the four resonance lines of He-like argon, only the z line falls in this non-uniformly lit region. Its intensity can be corrected by convoluting the spectra with the vignetting curve.

Finally, since the resolving power has an inverse dependence on the crystal size, the low active crystal surface turns out to be a positive factor for the resolving power. The final resolving power for He-like argon measurements is ~ 4000, which translates in an instrument function corresponding to a minimum detectable argon temperature of $\sim$430 eV.
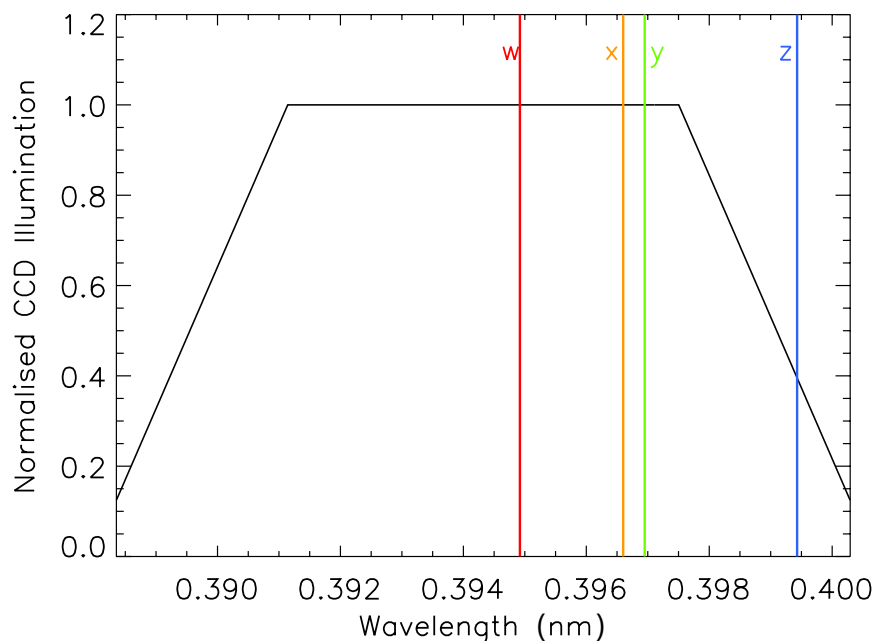

Figure 3.7: *Normalized intensity distribution on the CCD chip.*

3.3 Intensity Calibration

One of the main goals for the construction of this spectrometer is to test a new concept of soft X-ray spectrometer for impurity concentration monitoring in ITER (EFDA Task Reference: TW5-TPDS-DIARFA). To this purpose, an absolute intensity calibration of the instrument is mandatory prior to the installation on the tokamak. This has been achieved with the use of a custom X-ray tube that simulates the plasma extended source. The X-ray source has been characterized in energy, current behaviour and checked for non-linearities, its photon flux calibrated through the use of an independent Si(Li) detector. The experimental setups for both source characterization and spectrometer calibration can be seen in appendix D.

3.3.1 Source Characterization

Before calibrating the spectrometer in intensity, the source itself must be characterized both in energy and in intensity. This has been done using silver (Ag), tin (Sn) and copper (Cu) anodes. The composition of all anodes has been analyzed, revealing a >99% purity for Copper and Tin anodes. The silver anode has been manufactured in situ by depositing a few μm silver on a copper anode, its thickness determined knowing the penetration of electrons of energies <10 keV in solids (see appendix C). Their main K and L shell lines are listed in table 3.2, energies of the transitions are given in keV and in nm in brackets. Highlighted in bold are those used for the energy calibration of the tube. Because of the poor energy resolution of the Si(Li)detector, the Ag and Sn L lines result blended together (as shown in figure 3.8 for the Ag lines), thus the sum of the components had to be used as fit function. Relative intensities of the spectral lines have been extracted from [32].

	$K\alpha_1$	$K\alpha_2$	$K\beta_1$	$L\alpha_1$	$L\alpha_2$	$L\beta_1$	$L\beta_2$	$L\gamma_1$
29 Cu	**8.0478**	**8.0278**	**8.9053**	0.9297	0.9297	0.9498		
	(0.1541)	*(0.1544)*	*(0.1392)*	*(1.334)*	*(1.334)*	*(1.305)*		
47 Ag	22.1629	21.9903	24.9424	**2.9843**	**2.9782**	**3.1509**	**3.3478**	**3.5195**
	(0.056)	*(0.0564)*	*(0.0497)*	*(0.4155)*	*(0.4163)*	*(0.3935)*	*(0.3703)*	*(0.3523)*
50 Sn	25.2713	25.0440	28.4860	**3.4440**	**3.4354**	**3.6628**	**3.9049**	**4.1311**
	(0.0491)	*(0.0495)*	*(0.0435)*	*(0.36)*	*(0.3609)*	*(0.3385)*	*(0.3175)*	*(0.3)*

Table 3.2: K and L shell emission lines of Cu, Ag and Sn in keV and in nm in within brackets [32].

For a precise intensity calibration of both the X-ray tube and the spectrometer, all the contributions to the signal must be taken into account. The detection efficiency has been calculated through ADAS (Atomic Data and Analysis Structure, set of computer codes and data collections for modelling the radiating properties of ions and atoms in plasmas [33]) with the filter and detector characteristics described below.

- background: bremsstrahlung has been approximated linearly for the range of interest.

- filters: the system is equipped with a visible light filter. This is an 0.2 μm Aluminium - 2 μm Mylar (Polyethylene Terephthalate) and 2 μm Beryllium.

- detector efficiency: the Si-Li detector has an active layer of ∼4000 μm and a dead layer of ∼ 0.1 μm. Both have to be taken into account in the transmission evaluation.
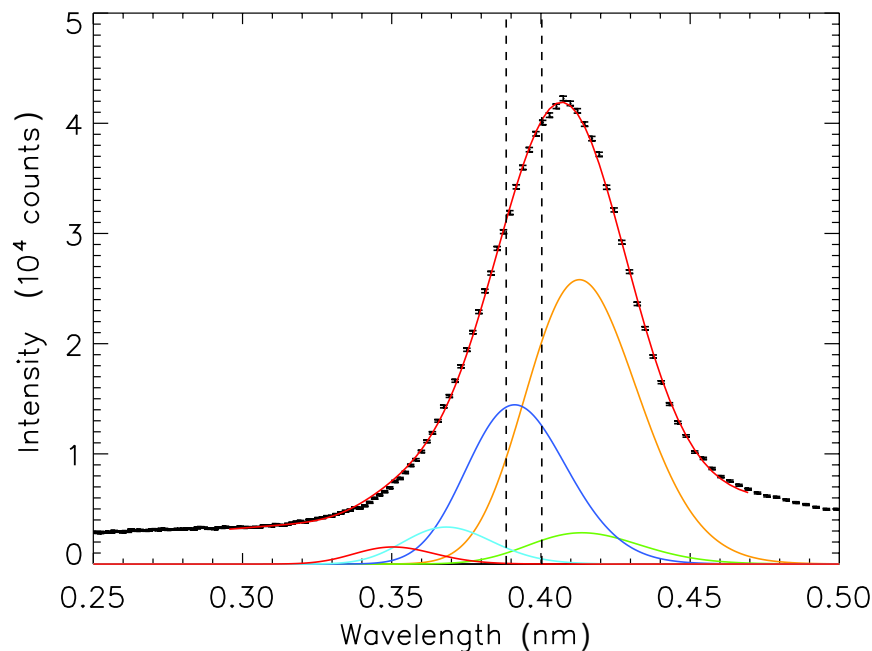
Figure 3.8: *Fitting of the blended silver lines through the Si(Li) detector. Vertical dotted lines represent the spectral range of the spectrometer.*

The intensity calibration must be achieved with the Ag Lβ_1 spectral line since it is the only one available which fits into the range of the spectrometer. Fitting the blended spectral components of the Ag L-shell as shown in the plot in figure 3.8 (where the two vertical dotted lines indicate the spectrometer spectral range) the total number of photons emitted in the Lβ_1 transition per unit time per unit area and per unit steradian can be calculated:

$$I_\gamma^{tube} = \frac{0.301075}{t_{exp} \cdot Et} \cdot \int \frac{I_{tot}(x)}{T} dx \qquad (3.8)$$

where: t_{exp} = acquisition time in seconds (real, taking into account the detector dead time)
Et = Etendue of the system,
$I_{tot}(x)$ = total number of counts of the blended spectrum for channel x,
T = transmission of the filter at the energy of the lines.
0.301075 = the percentage contribution of Lβ_1 to the total blended intensity [34].

3.3.2   Spectrometer Intensity Calibration

After its calibration, the X-ray tube has been installed on the spectrometer. The geometry of the system has changed drastically (figure D.2 in appendix D), but since the calibration of the tube has been achieved with precise evaluation of the geometry of the system, these contributions can be easily evaluated. Figure 3.9 shows the gaussian fit of the Lβ_1 as seen by the spectrometer CCD camera.

The fraction of input photons detected by the Johann spectrometer detector will depend on different factors:

- detection efficiency,

- crystal reflection efficiency and defects,

- Beryllium filter absorption,

- vignetting and geometrical restrictions,

If all these quantities were to be evaluated, the errors would levitate terribly. Since the source has been calibrated and the crystal is completely illuminated in this setup, all these contributions can be summed up in what could be called an *Efficiency Factor* (ϵ) which relates the detected counts to the emitted photons. This factor is equal to the ratio between the emitted photon flux from equation 3.8 and the total number of line counts per second detected by the spectrometer CCD camera. This efficiency factor is a direct link from the number of counts detected per unit time to the number of photons emitted by the source per unit time, solid angle and area.

$$\epsilon = \frac{I_\gamma^{tube}}{I_{counts}^{johann}} \quad \left(\frac{photons}{sterad \cdot m^2 \cdot count} \right) \tag{3.9}$$

In order to evaluate the correct intensity of any spectral line when passing to the AUG geometry (or to any other geometry), what still has to be considered is the crystal wetted area. In the case of the experimental setup used for the spectrometer intensity calibration (figure D.2 of appendix D), the crystal was totally illuminated. On the other hand, as stated in section 3.2.1, geometrical limitations of the top E port of AUG result in a vignetting of the system and in an incomplete illumination of the crystal surface. A geometric correction factor G equal to the percentage of crystal wetted area has to be thus considered. The photon intensity of any spectral line can be therefore expressed as:
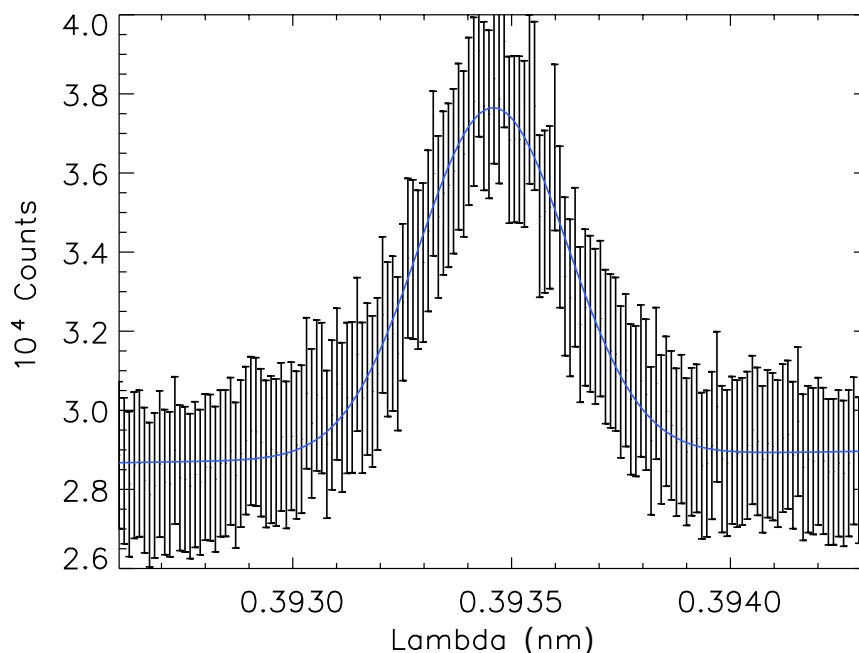

Figure 3.9: *Gaussian fit of the $L\beta_1$ line as seen by the spectrometer CCD camera.*

$$I_\lambda = \frac{I_{counts}}{t_{exp}} \cdot \epsilon \cdot G \cdot 4\pi \quad [\frac{photons}{s \cdot sterad \cdot m^2}] \tag{3.10}$$

where I_{counts} is the total number of counts of the fitted spectral line detected for an exposure time t_{exp}.

3.4   Spectrometer Instrument Function

The instrument function which could be extracted from the calibration through the silver $L\beta_1$ line shown in figure 3.9 results in a $\lambda/\Delta\lambda \sim 900$. This value is underestimating by far the theoretical value of ~ 5000 evaluated by Radivojevic and Stepanenko [31] and the later experimentally determined widths of the spectral lines. For this reason the instrument function has been re-evaluated on AUG plasma discharges through a tungsten line present in the spectra.

The width of a spectral line is determined by the gaussian propagation of its doppler broadening $\Delta\lambda_T$ and of the instrument function of the spectrometer $\Delta\lambda_{instr}$

$$\Delta\lambda = \sqrt{\Delta\lambda_T^2 + \Delta\lambda_{instr}^2} \tag{3.11}$$

The width due to doppler broadening is directly proportional to the square root of the ion temperature of the emitting species and inversely proportional to the square root of its mass:

$$\Delta\lambda_T = \frac{\lambda}{c} \left(\frac{2kT}{m_A}\right)^{1/2} \tag{3.12}$$
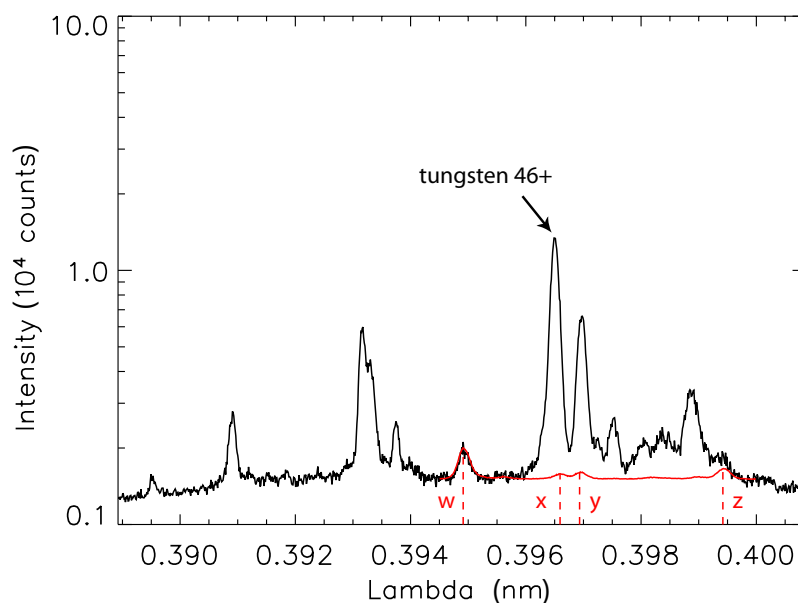

Figure 3.10: *Spectra (80 ms averaged) from discharge 23091. In red the contributions from He-like argon resonance lines.*

For this reason, for the same ion temperatures, the higher the mass of the emitting element, the lower will be the temperature contributions to the total width. Since AUG is covered with a full tungsten wall, the prime candidate for this evaluation is the emission from tungsten ions.

A few isolated tungsten lines have been found in the spectral range of the CSXR spectrometer. Most of the lines in the range are probably from ionization stages between 45+ and 47+. Discharge number 23091 has been chosen because of the low contributions from He-like argon resonances and strong emission from the core tungsten ions. An 80 ms averaged spectrum is shown in figure 3.10, in red the approximate contributions from the He-like argon resonance lines deduced from the intensity of the w-line in the centre of the spectrum. By evaluating the FWHM of this tungsten line and assuming its temperature equal to the electron temperature, $\Delta\lambda_T$ can be evaluated and the instrument function extracted through equation 3.11. $\Delta\lambda$ will be the experimental width of the fitted gaussian. Further proof of the reliability of this instrument function will be provided in section 4.2 through a comparison of the Ar ion temperatures with those of the $C6+$ ion evaluated by the Charge Exchange Recombination Spectroscopy (CXRS).

Chapter 4

Measurements With the CSXR Spectrometer

Since the CSXR spectrometer has only one line of sight, all the measurements achieved will not be radially resolved but integrated along the viewing path. As will be further explained in this chapter, approximate radial localization of the concentration, ion temperature and poloidal rotation measurements can anyway be achieved by modeling the emissivity characteristics of He-like argon in the specific plasma discharge.

While measurements of concentration and temperature are absolutely calibrated, only relative values for the rotation measurement are feasible at the moment. This is due to a non completely rigid mechanical structure which resulted in time variations to the detector position and thus to a loss of the original wavelength calibration. However, relative variations during a discharge can be evaluated precisely.

4.1 Argon Concentration

In coronal approximation the emissivity in a specific radiative transition between state i and state k can be written as:

$$\epsilon_{i,k} = n_1 n_e X_{1,i} \frac{A_{i,k}}{\sum_{m<i} A_{i,m}} = n_1 n_e X_{1,i} b_{i,k} \tag{4.1}$$

where n_1 is the density of the ground state, n_e the electron density, $X_{1,i}$ the electron impact excitation rate coefficient from the ground state to the excited state i, $A_{i,k}$ the transition probability between the excited state and k, $\sum_{m<i} A_{i,m}$ is the sum of all the possible transition probabilities from the upper state. The ratio between these last two constants is called branching ratio ($b_{i,k}$), and expresses the relative probability that the excited state i decays into state k.

The Coronal approximation is valid for low electron densities, $n_e \leq 10^{18} \ m^{-3}$, as in the solar corona. In this situation most of the atoms are in the ground state, collisions between electrons and atoms happen rarely and when they do, the excited state will have time to decay into the ground state before any other process can occur. In this approximation, $\epsilon_{i,k}$ will be approximately independent of electron density. At the other end, for densities $n_e \geq 10^{23} \ m^{-3}$, Local Thermal Equilibrium (LTE) approximation can be assumed, for which the electron and ion populations follow the thermal (Boltzmann) distribution, although

the photon radiation distribution may still be well below the blackbody level. Since the densities of tokamak plasma discharges range between 10^{18} and 10^{22} m^{-3}, neither of these assumptions may be applied for the full plasma radius and all the populating/de-populating processes of each excited level have to be taken into account solving full collisional-radiative models. The result of these models is commonly called Photon Emissivity Coefficient (PEC), equal to the emissivity normalized to the electron density n_e and to the density of the emitting ionization stage n_q:

$$PEC_\lambda(T_e, n_e) = \frac{\epsilon_\lambda(n_e, T_e)}{n_e \, n_q} \quad \left(\frac{photons \cdot m^3}{s}\right) \tag{4.2}$$

The intensity of the spectral line λ emitted by an ion A in ionization stage q along a Line Of Sight (LOS) through the plasma can therefore be expressed as:

$$
\begin{aligned}
I_{A,q}^\lambda &= \int_{LOS} n_e(r) \, n_A(r) \, f_{A,q}(r) \, PEC_\lambda(r) \, dr \\
&= \int_{LOS} n_e^2(r) \, c_A(r) \, f_{A,q}(r) \, PEC_\lambda(r) \, dr
\end{aligned}
\tag{4.3}
$$

where $n_A(r)$ the total ion density profile of the emitting species and $f_{A,q}(r)$ the fractional abundance of the emitting ionization stage q. In the second formulation, the n_A is expressed as a concentration level with respect to the electron density $c_A = n_A/n_e$.

The PEC coefficient depends only on electron density and temperature. The fractional abundance, on the other hand, doesn't depend only on n_e and T_e, but also on the transport characteristics of the plasma. In first approximation, the ionization equilibrium is evaluated from the ADAS database taking into consideration a full collisional radiative modeling, but neglecting transport. In the plasma centre, this assumption is in general a good enough approximation within the errors which arise from propagation of those of electron density and temperature profiles and of those of the photon emissivity coefficient, usually around $10 \div 20\%$ of the absolute value. More detailed treatment of impurity transport will be given in the next chapters. Finally the weighted average concentration of the ion A in the emission region can be recovered from equation 4.3:

$$< c_A >= \frac{I_{A,q}^\lambda}{\int n_e(r)^2 \, f_{A,q}(r) \, PEC_\lambda(r) \, dr} \tag{4.4}$$

where $I_{A,q}^\lambda$ is evaluated through equation 3.10.

For He-like argon, the emissivity profile of the resonance line w @ 0.39492 nm per unit argon ion can be seen in the bottom plot of figure 4.1. This has been evaluated for the T_e and n_e profiles shown in the top plot, fractional abundances and PEC for the specific transition in the central plot. As already stated in section 2.2, all quantities are plotted versus the poloidal flux surface label ρ. An example of the time trace of the argon concentration is shown in the top right plot of figure 4.6.
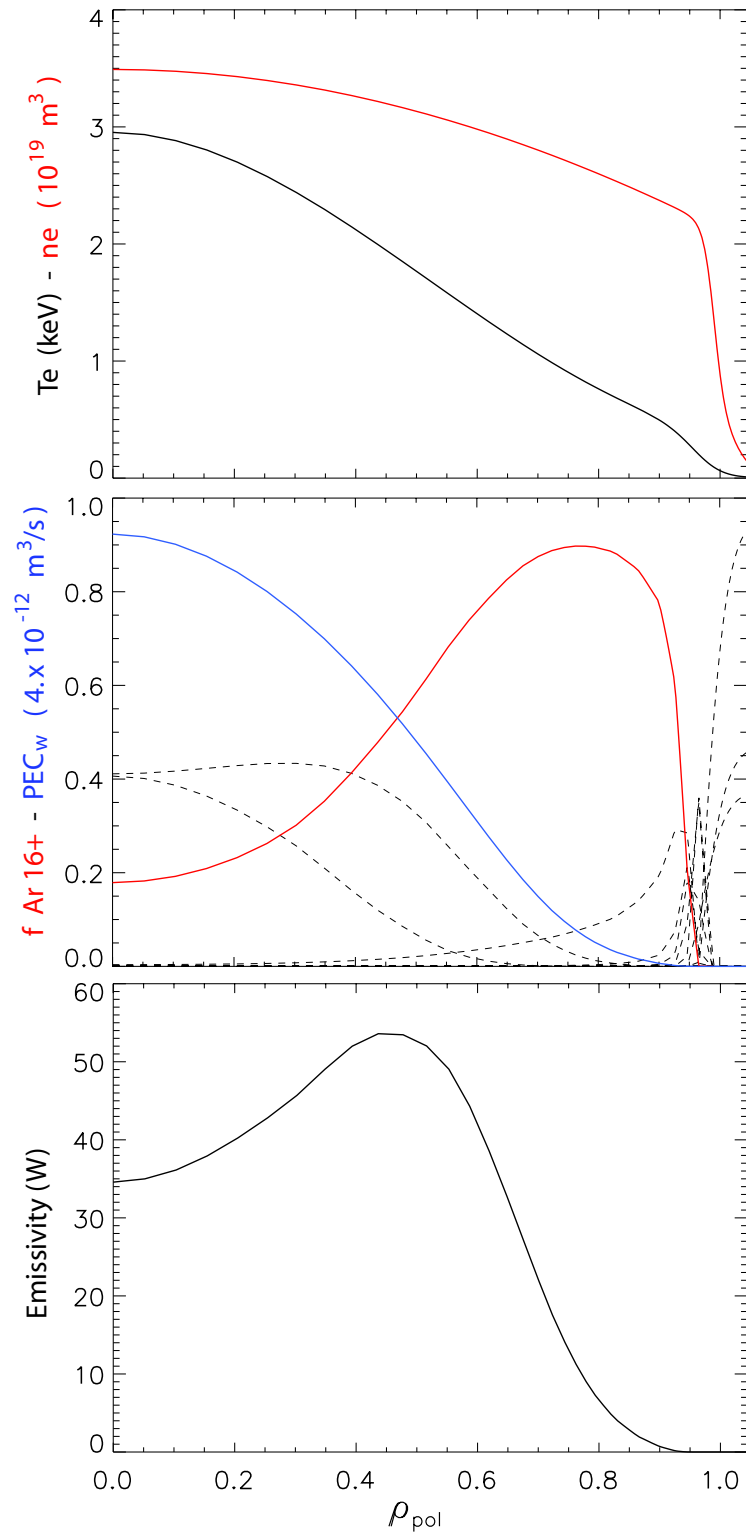
Figure 4.1: *Top plot: discharge 24146 electron temperature and density profile; middle: argon fractional abundances in corona equilibrium (red, other ionization stages represented with dashed lines), and PEC for the He-like w transition (blue); bottom: resulting He-like Ar w resonance line emissivity per unit Ar density.*

4.2 Ion Temperature

An example spectra of the fitting of the He-like argon w line is shown in figure 4.2. In black the raw data with error bars, restricted in range to more emphasize the width of the lines. The He-like resonance lines w, x and y are labeled, as well as the Li-like dielectronic satellites for $n \geq 3$. Since the w line is the most intense and has been found to be free from Tungsten spectral contamination, apart from those cases in which the detector saturates, this is the line used for argon ion temperature, poloidal rotation and concentration measurements. The red dashed line represents the instrument function.

In order to check the reliability of the ion temperature of argon evaluated by the CSXR, a comparison with the values from charge exchange recombination spectroscopy (CXRS) diagnostics has been performed. Ion temperatures given by CXRS are profile resolved while the CSXR is a line of sight integrated measurement. Therefore the comparison of the two diagnostics requires a comprehensive treatment of the He-like argon emission characteristics along the line of sight.

The emissivity profile of the He-like resonance line w @ 0.39492 nm can be calculated as explained in the previous section. The first moment of the distribution with respect to ρ will give an estimate of mean position of emissivity, the second moment the width of the distribution which can be interpreted as the error on the mean (equations on the left and right hand sides of 4.5 respectively).

$$\overline{\rho} = \frac{\int \rho\, \epsilon\, dl}{\int \epsilon\, dl} \qquad \sigma_\rho = \sqrt{\frac{\int (\rho - \overline{\rho})^2\, \epsilon\, dl}{\int \epsilon\, dl}} \qquad\qquad (4.5)$$
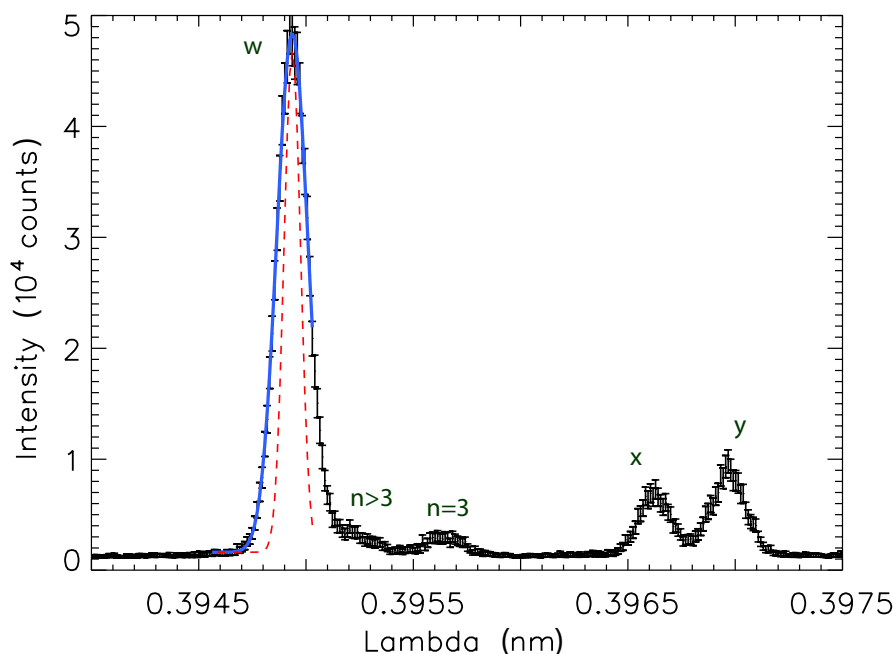

Figure 4.2: *Spectra from discharge 24146 (10 ms averaged at $\sim$ 1.5 seconds in the discharge). In blue the fit of the He-like argon resonance line w; the dashed red line is the instrument function evaluated as explained in 3.4.*

Since the emission profile is not symmetric, the second moment has been evaluated for two distinct regions centered on the mean value: $\rho < \overline{\rho}$ and $\rho > \overline{\rho}$.

The width of the emissivity profile distribution is not the only contribution to the uncertainty in the emissivity position. Another factor which has to be taken into account is the width of the line of sight along the radial plane. The aperture angle of the LOS along the meridional plane results to be 1.035°, corresponding to a maximum crystal illumination of 9.03 mm. This leads to a LOS diameter of $\sim$ 68.3 mm on the meridional plane, which reduces to $\sim$ 48 mm at the port entrance and goes up to $\sim$ 81.7 mm on the divertor. The value on the equatorial plane is the natural choice as average, and the LOS width is then evaluated centered on the mean rho poloidal previously evaluated.

The mapping of the LOS on ρ_p vs. the vertical distance from the E-port aperture at a specific time during the discharge is shown in figure 4.3. The black dot represents the evaluated mean position of emissivity, the red ones the width of the LOS at that position.

The final results can be seen in figure 4.4. The top plot shows the evolution in time of the central electron temperature. The corresponding evolution of the mean rho poloidal is shown on the bottom plot, black dots representing the mean value, red bands the error bars resulting from a gaussian propagation of the LOS width and the width of the emissivity distribution. The blue line is the minimum visible rho poloidal. Since the LOS coordinates in space are fixed, this value depends only on the plasma position and equilibrium reconstruction, and corresponds to the minimum value of the curve in figure 4.3.

The electron temperature dependence of $\overline{\rho}$ can be intuitively understood noting that, assuming a stiff electron temperature profile, with increasing temperatures in the
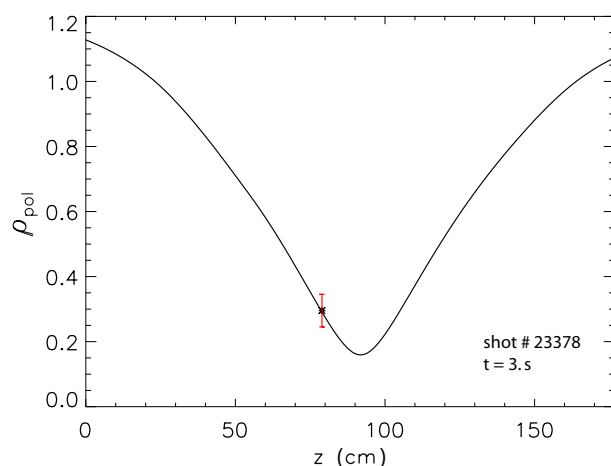

Figure 4.3: *Path of the CSXR line of sight mapped on ρ for discharge #23378 at 3 s. The black dot is the position of the evaluated mean rho poloidal, in red its error due to the physical width of the LOS.*
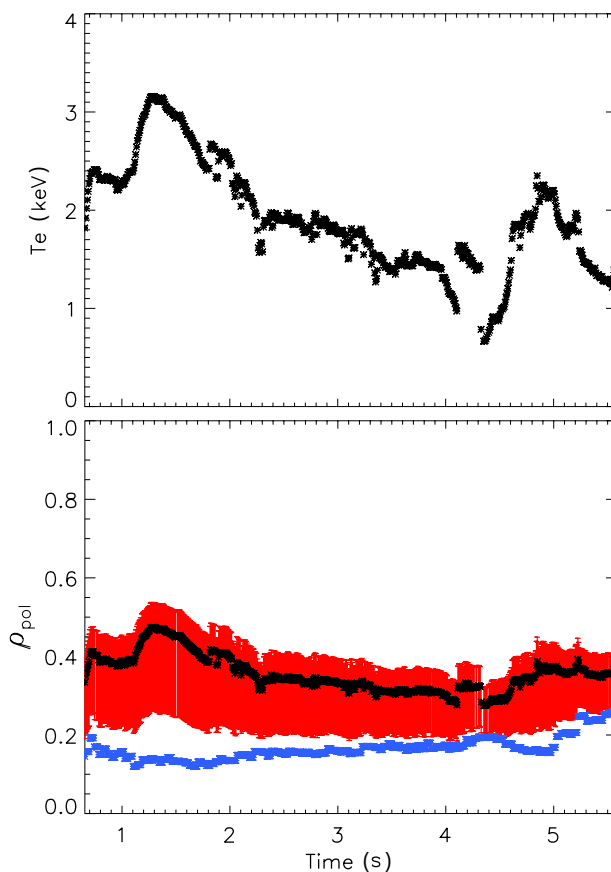

Figure 4.4: *Top: central Te time evolution; bottom: $\overline{\rho}$ of He-like argon w transition emission (black), distribution width (red) and minimum visible ρ (blue) for discharge #23378.*

core, the fractional abundance profiles in
figure 4.1 will move further outward, and so will the emissivity peak.

After having evaluated the position of emissivity, the CSXR He-like Ar temperature can be compared to the C^{6+} temperatures from the charge exchange diagnostic. The evolution of the CXRS T_i profile in time is shown in the surface plot in figure 4.5, color code of the scale on the right representing the ion temperature in eV. The black vertical lines show the radial measurement positions of the charge exchange, while the red "snake-like" line is the time evolution of $\overline{\rho}$ of He-like argon evaluated as explained. If a linear interpolation of the CXRS values on $\overline{\rho}$ is performed, the ion temperatures from the two diagnostics can be compared.
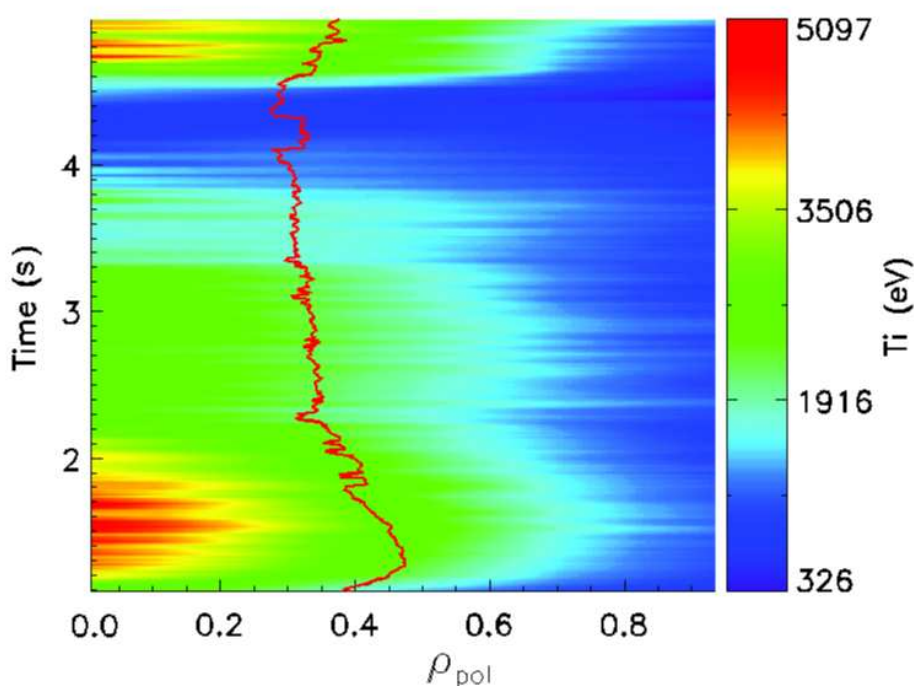
Figure 4.5: *Discharge 23378 C $^{6+}$ Charge Exchange ion temperature profile evolution in time. Red line represents the CSXR mean rho poloidal of emission used for interpolation, black vertical lines the CXRS measurement positions.*

The results are plotted in the top right graph in figure 4.6. The Ar^{16+} temperatures evaluated from the CSXR are plotted in red (with error bars) and the interpolated temperatures of C^{6+} from charge exchange in black. The agreement is very good for the full time range demonstrating that both the evaluation of the Ar temperature and the assumption for the position of emission are reliable.

Both these measurements are of major importance for the evaluation of the Ar transport coefficients in purely ECR-heated L-modes (presented in section 6.1). Due to the absence of NBI heating, the only available measurements of the ion temperature will be those from the CSXR spectrometer and from the NPA diagnostic (described in section B.5). The localization of these measurements is therefore of major importance for the evaluation of an ion termperature profile necessary for both neoclassical and turbulent transport simulations. Moreover, the localization of the measurements from the CSXR spectrometer allows the

rescaling of the total argon density measurement performed throught the SXR cameras (as will be explained in detail in section 5.3.3).
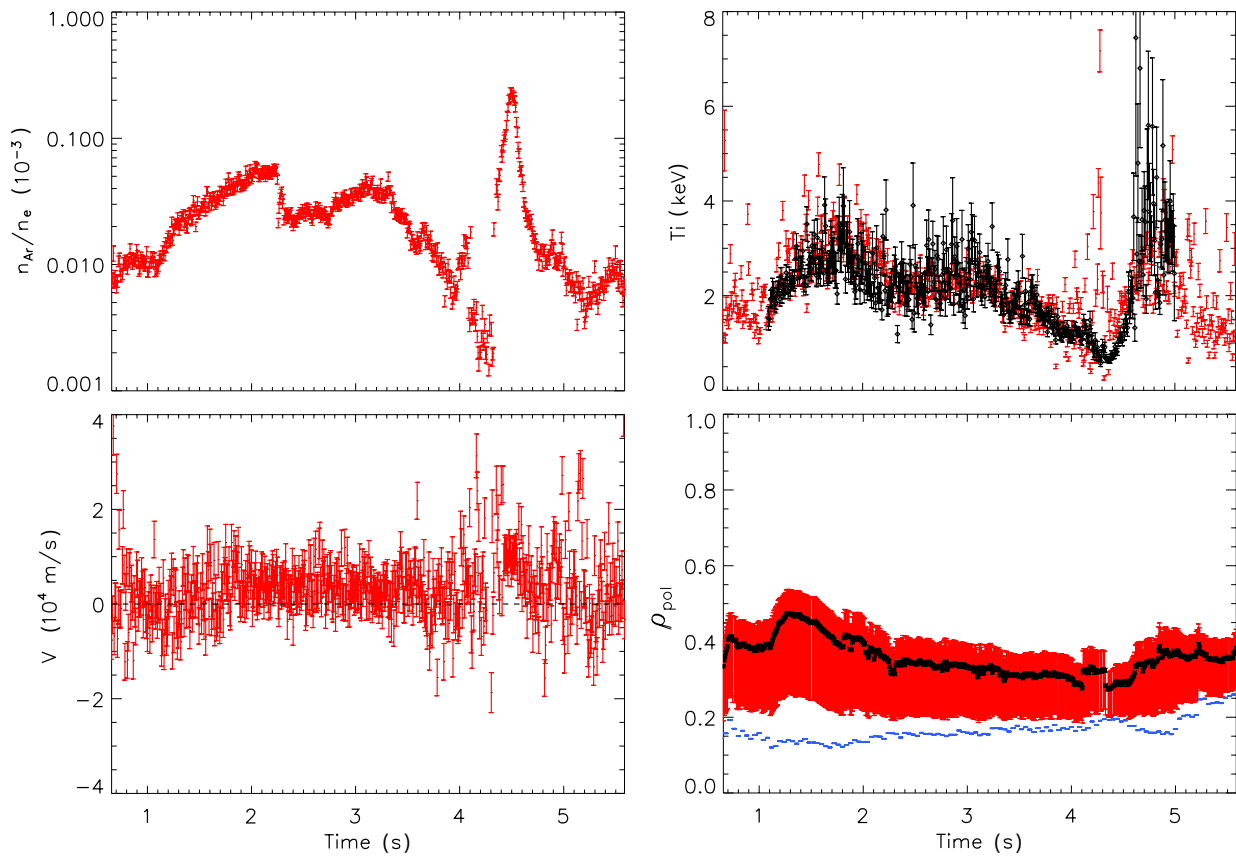

Figure 4.6: *Measurements from the CSXR spectrometer for discharge # 23378. From top left, clockwise: concentration, ion temperature, position of emissivity and poloidal rotation of He-like Ar.*

Chapter 5

Evaluation of Impurity Transport Coefficients

As already explained in chapter 2, a charged particle moving in a magnetized plasma is subject to fluctuating forces of various nature which give rise to a radial transport perpendicular to the magnetic field lines. For the description of the impurity fluxes arising from these processes, an ansatz of diffusive and convective flux density is commonly used. With this ansatz, the continuity equation can be transformed into a radial transport equation, and the temporal evolution of the radial impurity fluxes can then be calculated in terms of diffusion coefficient and drift velocity for given boundary conditions.

From an experimental point of view, most methods for the determination of impurity transport coefficients are based on spectroscopic diagnostics. Charge Exchange Recombination Spectroscopy (CXRS), Soft X-Ray radiation (SXR) measurements or passive spectroscopy are commonly used. For non-intrinsic impurities, single or sinusoidally modulated impurity puffs or laser-blow-off (LBO) provide the necessary impurity content in the plasma for their detection. The transport coefficients may be then evaluated through various techniques [5]. The technique used for this work is the commonly called Gradient-Flux method. This is a well known method but seldomly used. New solutions for its application are presented in this chapter.

Sections 5.1 and 5.2 explain the main principles of the technique, the main steps of the derivation of the impurity transport equation and the 1D transport code STRAHL. Being beyond the scope of this work to provide an in-depth explanation of the mathematical derivation of the radial impurity transport equation, for a more complete derivation refer to [5]. Section 5.3 will explain the integrated treatment of the experimental data of the Soft X-Ray (SXR) and CSXR spectrometer for the evaluation of the total argon density profile. Section 5.4 and 5.5 explicate the tratment of the SXR raw-data and give a few examples of the application of the Gradient-Flux method.

5.1   Radial Impurity Transport

The conservation of the particle density $n_{A,q}$ of the impurity ion A in the ionization stage q may be written as:

$$\frac{\partial n_{A,q}}{\partial t} = -\vec{\nabla} \cdot \vec{\Gamma}_{A,q} + Q_{A,q} \tag{5.1}$$

where $\Gamma_{A,q}$ is the flux density and $Q_{A,q}$ represents the sources and sinks due to ionization, recombination and charge exchange connecting the neighbouring charge states. Since the transport parallel to the magnetic field is far larger than that perpendicular to it, most density gradients on a magnetic flux surface even out. With this assumption, all quantities can be averaged over the flux surfaces (as explained in section 2.2) and the problem reduced to one dimension, the radial one perpendicular to the magnetic flux surfaces. This situation is met for light impurities [35] as in the present application of argon, while for heavier impurities, magnetic and geometrical asymmetries have a stronger effect leading to a poloidal variation of the particle flux.

Integrating equation 5.1 over the volume V inside the flux surface [15], for radii smaller than that of the Last Closed Flux Surface (LCFS) equation 5.1 can be written as:

$$\frac{\partial}{\partial t} \int n_{A,q}\, dV = -\oint \overrightarrow{\Gamma}_{A,q} \cdot \overrightarrow{dS} + \int Q_{A,q}\, dV \tag{5.2}$$

Recalling from equations 2.25 the difinition the flux surface average for an arbitrary scalar quantity F as:

$$< F > \;=\; \left(\frac{\partial V}{\partial \rho}\right)^{-1} \oint F \frac{dS}{|\nabla \rho|} \tag{5.3}$$

$$\tag{5.4}$$

$$\int F\, dV \;=\; \int_0^\rho d\rho \frac{\partial V}{\partial \rho} < F > \tag{5.5}$$

this time expressed in terms of the normalized poloidal flux coordinate ρ, the continuity equation becomes:

$$\frac{\partial}{\partial t} \int_0^\rho d\rho \frac{\partial V}{\partial \rho} n_{A,q} = -\frac{\partial V}{\partial \rho} < \Gamma_{A,q}^\rho > + \int_0^\rho d\rho \frac{\partial V}{\partial \rho} Q_{A,q} \tag{5.6}$$

Differentiating this equation with respect to ρ, for a time independent flux surface geometry we obtain:

$$\frac{\partial n_{A,q}}{\partial t} = -\left(\frac{\partial V}{\partial \rho}\right)^{-1} \frac{\partial}{\partial \rho}\left(\frac{\partial V}{\partial \rho} < \Gamma_{A,q}^\rho >\right) + Q_{A,q} \tag{5.7}$$

Choosing a flux surface label r calculated directly from the volume enclosed by the flux surface $V = \pi r^2 \cdot 2\pi R_{axis}$, where R_{axis} is the major radius of the plasma axis, the flux surface averaged continuity equation in cylindrical geometry can be written as:

$$\frac{\partial n_{A,q}}{\partial t} = -\frac{1}{r}\frac{\partial}{\partial r} r < \Gamma_{A,q}^r > + Q_{A,q} \tag{5.8}$$

If we now assume a diffusive and convective ansatz for the flux surface averaged radial impurity flux,

$$< \Gamma^r_{A,q} >= D(r) \frac{\partial n_{A,q}(r,t)}{\partial r} - v(r) \, n_{A,q}(r,t) \qquad (5.9)$$

where also D and v are flux surface averaged quantities, equation 5.8 can be finally transformed in the radial transport equation for the density of impurity A in ionization stage q:

$$\frac{\partial n_{A,q}(r,t)}{\partial t} = \frac{1}{r} \frac{\partial}{\partial r} \, r[D(r) \frac{\partial n_{A,q}(r,t)}{\partial r} - v(r) \, n_{A,q}(r,t)] + Q_{A,q}(r,t) \qquad (5.10)$$

5.1.1 STRAHL 1D Transport Code

Equations 5.10 for the different ionization stages of one impurity can only be solved numerically. For this scope, the 1D radial transport code STRAHL is used [5]. The radial transport equations can be re-written in matrix notation for the Z ionization stages of one impurity:

$$\frac{\partial \vec{n}}{\partial t} = \frac{1}{r} \frac{\partial}{\partial r} \, r[D(r) \frac{\partial \vec{n}}{\partial r} - v(r) \, \vec{n}] - S\vec{n} - R\vec{n} + \vec{d} \qquad (5.11)$$

where S and R are the matrices with the ionization and recombination rates, while $\vec{d}$ describes the source rate by ionization of the neutral impurity atoms. Ionization and recombination coefficients are taken from the ADAS database. Using a radial mesh of N points, STRAHL solves the $N \times Z$ coupled equations with the desired time resolution Δt for the confined plasma.

A decay length λ is commonly used as boundary condition at the outermost grid point

$$\frac{\partial \vec{n}}{\partial r} = -\frac{\vec{n}_N}{\lambda}$$

Wall recycling and transport of the impurities between the divertor, Scrape Off Layer (SOL) and pump duct are treated with a two chamber model. A block scheme of the model is shown in figure 5.1. The two directional fluxes between SOL and divertor, and the flux from the divertor and the pump duct are treated with an ansatz of decay times, $\tau_{SOL \to div}$, $\tau_{div \to SOL}$ and τ_{pump} respectively. Figure 5.1 also shows the wall recycling parameter R (which can be set to any value between 0 and 1) and the neutral impurity influx Γ_{in}.

Apart from solving the coupled radial transport equations and the wall recycling, the code gives also the possibility of evaluating the radiative emissivities of the impurity. Bremmsstrahlung, radiative recombination, line radiation and charge exchange contributions can be calculated by specifying rate coefficient files from the ADAS database. Moreover, very important for this application, the filtered emissivities in the SXR region can also be evaluated. By integrating them along the line of sights of the SXR diagnostic, direct comparison with the experimental measurements can be performed.

STRAHL gives also the possibility of invoking a simple model for sawtooth crashes. If the sawtooth inversion radius r_{inv} is known, at the crash times (defined by the user)
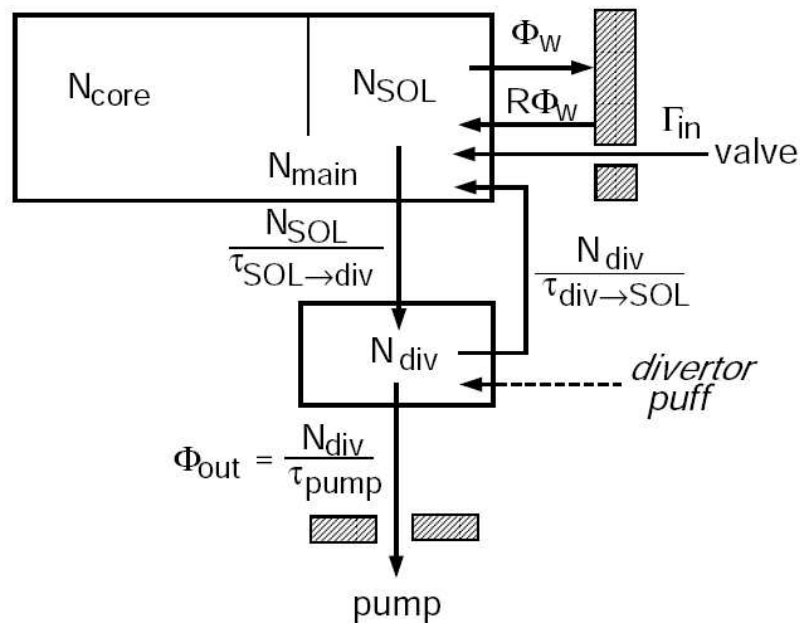
Figure 5.1: *Recycling two chamber model used by STRAHL.*

the code will redistribute the total impurity density inside a radius $r_{mix} = r_{inv} \cdot \sqrt{2}$ (called *mixing radius*) to completely flatten the density profile keeping the total number of particles constant.

5.2 The Gradient-Flux Method

By assuming that the flux surface averaged transport coefficients are the same for all ionization stages, equation 5.10 may be summed over all q (apart from the neutral), and the radial transport equation of the total impurity density written as:

$$\frac{\partial n(r,t)}{\partial t} = \frac{1}{r}\frac{\partial}{\partial r}\, r[D(r)\,\frac{\partial n(r,t)}{\partial r} \;-\; v(r)\,n(r,t)] + Q_{A,1}(r,t) \tag{5.12}$$

where the subscript A has been omitted. Almost all the source terms cancel out, leaving $Q_{A,1}$ with terms of ionization to the first ionization stage $S_{A,0}$, recombination $\alpha_{A,1}$ and charge exchange $\alpha_{A,1}^{cx}$ to the neutral atom:

$$Q_{A,1} = n_e\, S_{A,0}\, n_{A,0} - \left(n_e\, \alpha_{A,1} + n_H \alpha_{A,1}^{cx}\right) n_{A,1} \tag{5.13}$$

Since for most impurities these processes take place only outside or just inside the separatrix of a tokamak plasma, this term can be neglected for radii smaller than that of the LCFS. The radial flux at a certain radius r, at time t during the discharge can be therefore directly evaluated as the integral of the time derivative of the total impurity density within the radius r:

$$\Gamma(r,t) = -\frac{1}{r}\int_0^r \frac{\partial n(r',t)}{\partial t}\, r'\, dr' \tag{5.14}$$

Finally, reordering the terms of equation 5.12, the transport coefficients can be recovered from the slope and offset (D and v respectively) of the linear fit of the normalized flux vs. the normalized density gradient.

$$\frac{\Gamma(r,t)}{n(r,t)} = -\frac{D(r)}{n(r,t)}\frac{\partial n(r,t)}{\partial r} + v(r) \tag{5.15}$$

This method is commonly referred to as the Gradient-Flux method.

In order to evaluate the transport coefficients from equation 5.15, the knowledge of the total impurity density profile evolution is required. Since spectroscopic diagnostics measure the light emitted from one ionization stage (passive or charge exchange spectroscopy), or a sum of all the radiation emitted in a certain spectral range (e.g. Soft X-Ray diodes (SXR) or Bolometer detectors), the recovery of the total density profile is complicated. Moreover, most experimental impurity transport analysis are usually achieved with the use of a single diagnostic, since the comparison between different diagnostic techniques is often difficult due to the absence of absolute calibrations. Because of their complementary nature, the SXR detectors and the passive CSXR spectrometer described in the previous chapters can be used for the recovery of the absolute value of the total impurity density, as will be explained in the next sections.

5.3 Evaluation of the Total Argon Density

The total argon density time evolution after an impurity puff can be recovered with the aid of 2 diagnostics: the SXR diodes and the CSXR spectrometer. The high time and spatial resolution of the SXR cameras give the possibility of evaluating the argon SXR-emissivity profile evolution in time after an impurity puff. As explained in section B.7 these emissivities are not absolutely calibrated. The CSXR spectrometer can on the other hand give an absolute value of the argon density in the region of He-like Ar emissivity. The next sections will explain how the total argon density profile evolution can be evaluated through the use of the SXR diagnostic and then rescaled through the use of the argon concentration values given by the CSXR spectrometer.

5.3.1 Argon Density Profile

Let us first of all recall the equation for the emissivity in the SXR region explained in section B.7.

$$\epsilon_A^{sxr}(r,t) = n_e(r)\,n_A(r,t)\,L_A^{sxr}(r,t) = n_e(r)\,n_A(r,t)\sum_q f_{A,q}(r,t)\,k_{A,q}^{sxr}(r) \tag{5.16}$$

The transport dependence of this equation is completely contained in the impurity density n_A and in the fractional abundance $f_{A,q}$. The emissivity coefficients depend only on the electron temperature and density profiles which are taken directly from the experiment and are assumed constant in time during the time range of interest.
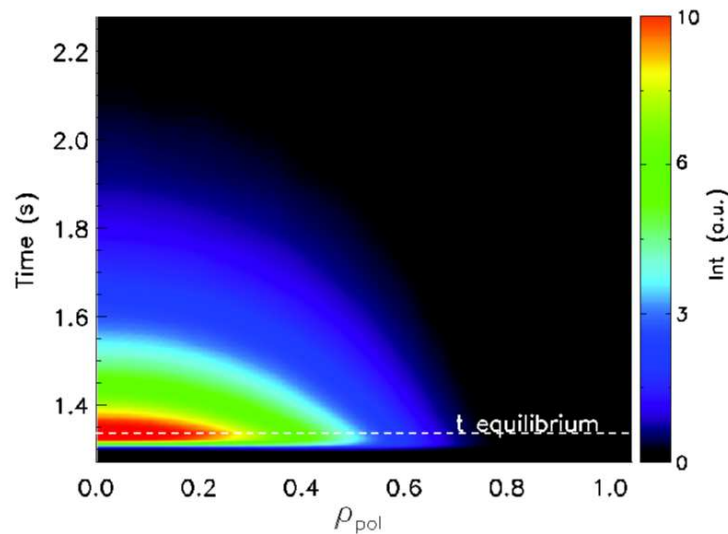
Figure 5.2: *STRAHL simulation: SXR background subtracted emissivity of an argon puff. White line represents the equilibrium time chosen for the evaluations*

As a starting point, the fractional abundances of the impurity ions is assumed not to depend on transport. Using the experimental equilibrium reconstruction, impurity puff rate, electron density and temperature profiles, the emissivity profile evolution due to the impurity puff can be simulated with STRAHL (figure 5.2). Within the assumptions made, whatever transport coefficients are chosen, the only parameter of the SXR emissivity profile evolution (eq. 5.16) which will be affected will be the total density profile $n_A(r,t)$. Therefore, if the simulated background subtracted SXR emissivity profile is divided by the total impurity density profile, the obtained function will be completely decoupled from transport. This normalized emissivity function $\epsilon'(r)$, contains all the information on the emissivity characteristics of the desired impurity with the experimental electron temperature and density, mapped on the equilibrium of the specific discharge.

$$\epsilon'(r) = \frac{\epsilon^{sxr}(r, t_{eq})}{n_A(r, t_{eq})} = n_e(r) \sum_q f_{A,q}(r, t_{eq}) \, k_{A,q}^{sxr}(r) \tag{5.17}$$

This process could in theory be done at any time point after the impurity puff where the impurity density is different from zero along the whole profile. For convenience, the time point is chosen at or just after the equilibrium of the impurity density profile is reached.

Taking now the experimental LOS-integrated signals from the SXR diodes, performing the one-dimensional Abel inversion (performed with routines from [36]) and subtracting the background contributions prior to the impurity puff, the experimental impurity emissivity profile evolution $I^{sxr}(r,t)$ can be recovered. Dividing it at each time point by the function $\epsilon'(r)$ it is possible to finally re-evaluate the total impurity density profile evolution in time.

$$n_A^{sxr}(r, t) = \frac{I^{sxr}(r, t)}{n_e(r) \, L_A^{sxr}(r, t)} = \frac{I^{sxr}(r, t)}{\epsilon'(r, t)} \tag{5.18}$$

5.3.2 Robustness of Method

In reality, the $\epsilon'(r)$ function is not completely decoupled from transport. The initial assumption of independence of the fractional abundances $f_{A,q}$ from transport is not entirely true, and its sensitivity to transport variations has to be studied.

Plasma parameters from a typical AUG L-mode discharge (#24146) have been used for this analysis. This discharge is the same one used in section 4.2 to explain the comparison of the argon temperature evaluated through the CSXR spectrometer and the carbon ion temperature from the charge exchange spectroscopy diagnostic. Main plasma parameters are $B_t = -2.4\ T$, $I_p = 0.8\ MA$, central electron density $\sim 3.5 \cdot 10^{19}\ m^{-3}$, ~ 0.65 MW central ECRH heating deposited at $\rho \sim 0.2$, standard LSN ASDEX Upgrade plasma configuration. Executing different STRAHL runs with a variation of the transport coefficients and evaluating the $\epsilon'(r)$ function, its sensitivity to transport can be estimated. The transport coefficients used are shown in the two left plots in figure 5.3.

A diffusion coefficient scan from $\sim$5-100 times the neoclassical values has been achieved (black to blue lines on plots). The convection velocity has been varied so to keep a constant concentration throughout the plasma radius. Neoclassical values are shown as dashed lines and have been evaluated using the NEOART code with argon as the only impurity species.
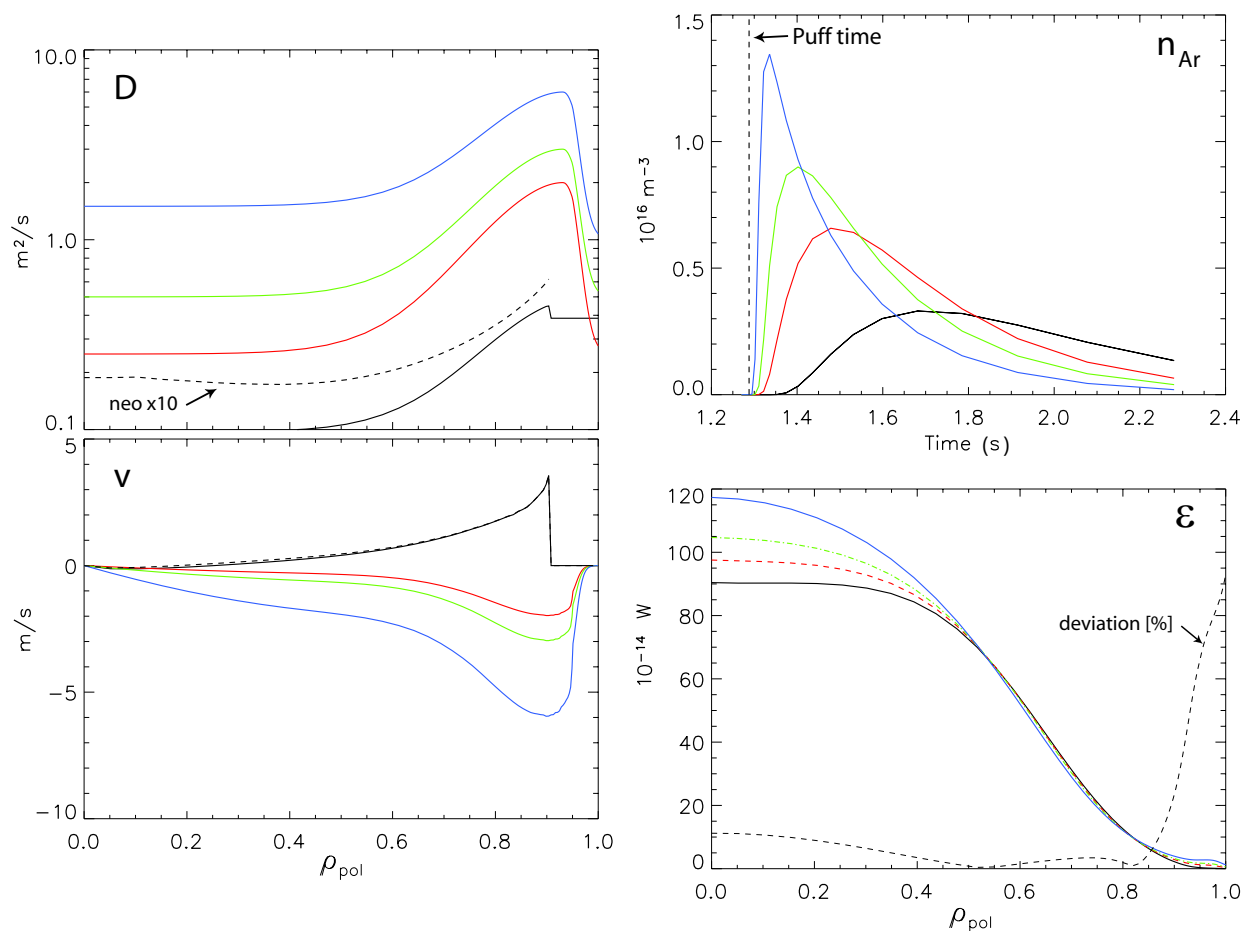

Figure 5.3: *24147 transport coefficient scan. Dashed lines refer to the neoclassical values evaluated considering argon as the only impurity specie (diffusion coefficient x 10).*

The same impurity puff has been simulated for each set of transport coefficients. After the influx phase of the impurity has ended and the equilibrium density profile is reached ($t = t_{eq}$), the SXR emissivity profile at t_{eq} is divided by the total impurity density profile at the same time point, yielding the normalized SXR emissivity profile $\epsilon'(r)$ (equation 5.17).

The effect of the transport variation on the argon density evolution in the plasma can be easily seen in the top right plot of figure 5.3, which shows the time evolution of the central argon density as simulated by STRAHL. The larger the transport coefficients, the faster the influx and the general time evolution of the density. The maximum central argon density also increases with increasing transport. The change in transport coefficients has on the other hand minor effects on $\epsilon'(r)$ for a major part of the plasma radius (bottom right plot in figure 5.3). By evaluating the mean value and standard deviation (black dashed line) of these curves, a maximum error of ~ 10 % is observed within $\rho_p < 0.8$. Outside of this region, the result is anyway meaningless because of the drop in sensitivity of the SXR cameras.

5.3.3   Rescaling of Argon Density

Because of the degradation in sensitivity of the SXR diodes, the known sensitivity function is not to be trusted in absolute values. On the other hand, assuming that all the diodes degrade similarly, the relative values between different channels are reliable. For the specific situation of argon, a rescaling parameter of the total density evaluated by the SXR can be given by the CSXR spectrometer. As explained in detail in the previous chapters, the spectrometer is calibrated in intensity and its LOS integrated measurements can be given a rough radial localization through the modeling of the He-like Ar emission characteristics. By taking the CSXR concentration measurement at the equilibrium time after the impurity puff, the impurity density at the radial location $\overline{\rho}$ can be evaluated by multiplying the concentration with the electron density at $\overline{\rho}$. The rescaling factor (f_{res}) will simply be the ratio between this value and the value of the SXR-evaluated impurity density at the same radial location and time point:

$$
\begin{aligned}
n_A(r, t) &= n_A^{sxr}(r, t) \cdot f_{res} \\[2ex]
&= n_A^{sxr}(r, t) \cdot \frac{c_A(t_{eq}) \cdot n_e(\overline{\rho})}{n_A^{sxr}(\overline{\rho}, t_{eq})}
\end{aligned}
\tag{5.19}
$$

Since $\overline{\rho}$ has been evaluated not taking transport into account, its stability to variations in transport has to be checked. This can be done by extending the sensitivity test used for ϵ'.

The results of the simulations can be seen in figure 5.4, where the emissivity profile of He-like Ar (per unit impurity atom) at equilibrium for the four different transport cases is plotted vs. ρ_p. The black dashed line shows how the emissivity profile would look like for the case of coronal equilibrium. Taking into consideration the central 3 cases (full black, red and green), the result of a simple mean and standard deviation of the $\overline{\rho}$ leads to a maximum error of ~ 0.03 in rho poloidal, corresponding to ~ 1 cm, inside precision of the deconvolution routine (ranging from a few centimeters at the edge to ~ 1 cm in the centre).

For the transport analysis, the first STRAHL simulation will be achieved with "typical" transport parameters (the red curves in figure 5.3), the subsequent one(s), for a fine tuning
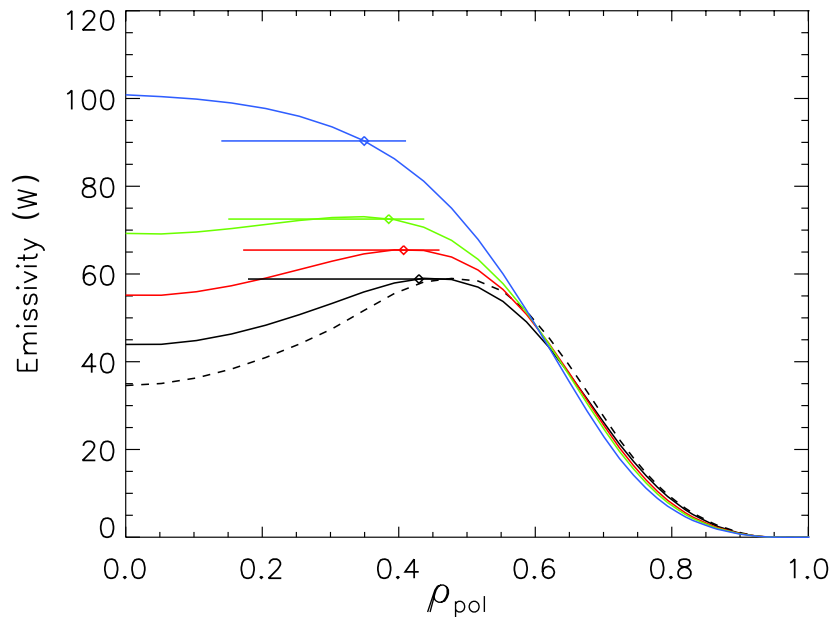
Figure 5.4: *He-like Ar emissivity profile at equilibrium for the different transport coefficients shown in figure 5.3.*

of the evaluated diffusion and convection coefficients, will be run with the coefficients obtained from the previous STRAHL run.

5.4   SXR Raw Data Treatment

As already stated in the introduction to this chapter, one of the reasons for a non extensive use of the Gradient-Flux method for impurity transport analysis is the absence of a direct measurement of the total local impurity density. Another reason is that the method is know to be very "noisy". In order to evaluate the fluxes and gradients with a certain statistics, the maximum possible number of time points should be analyzed. If the signals from the SXR are noisy or strong MHD activity is present, the normalized fluxes Γ/n and normalized gradients $(dn/dr)/n$ will be strongly influenced by these, thus adding systematic errors to the evaluation of the transport coefficients.. Usual deconvolution of the SXR lines of sight for impurity transport analysis employs a pre-deconvolution 1 kHz down sampling to suppress high frequency noise and fast MHD activity. This may filter successfully, but at the same time decreases the number of points available for the analysis and so introduces a statistical error. If strong low frequency MHD activity (e.g. sawteeth) is not present, a solution to this problem is fitting the raw data with a model function instead of down sampling it. By doing so, the time resolution of the raw data will be preserved, but the noise and fast MHD will be suppressed.

This can be performed through the use of the so-called "modified hyperbolic tangent" function (MTANH, equation $f(z)$ 5.4), commonly used for the fitting of electron temperature and density profiles in tokamak plasmas [37]. The fitting of the data inside and outside of the pedestal is achieved with polynomials up to 3rd order.

$$f(z) = a_0 - a_1 \cdot tanh(z) - a_1 \cdot a_4 \frac{z \cdot e^{-z}}{e^z + e^{-z}} \qquad (5.20)$$

where:

$$z = \frac{x - a_2}{a_3} \qquad tanh(z) = \frac{e^z - e^{-z}}{e^z + e^{-z}}$$

With slight remapping of the SXR raw data this function can be used for the fitting of the raw SXR signals without any changes. The fit parameters a will mainly lose their original physical meaning (pedestal width, height, etc., see [37] for full explanation), but a few
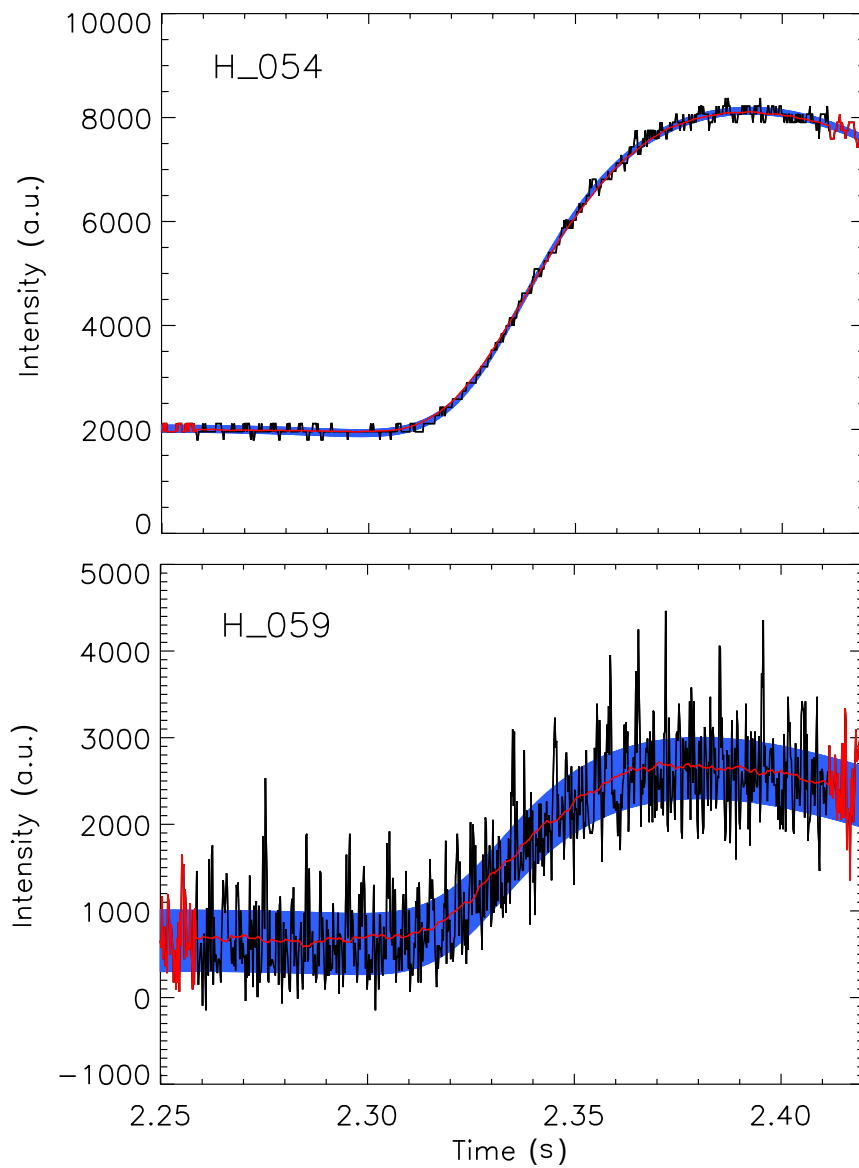

Figure 5.5: *Fitting of the SXR H camera channels 54 and 59 raw signals for discharge 24450.*

retain meaning also in this application:

- $2 \cdot a_3$ = rise time

- $a_0 - a_1$ = background value

- a_1/a_3 = maximum gradient

An example of its application to the present problem is shown in figure 5.5 for two channels of the H camera: in black the raw data; in blue the result of the fit (thickness of the band determined from the data-fit deviation) and in red a 15 ms smooth for comparison. The background evolution before the impurity puff is modeled through a 0th order polynomial, the first part of the decay after the equilibration time has been reached through a 3rd order one. The two channels have been chosen to exemplify the possibility of using this procedure also for low intensity signals. The top plot shows how a simple smoothing (red line) would cause a flattening of the gradients, while the fitting with the model function keeps the gradients intact. As for the low intensity signals such as that in the bottom plot, the fit function can still deliver the global evolution filtering out all noise. This case is particularly important in discharges where only a very low impurity density is accepted and where the SXR signals have low signal to noise ratio.

At this point, the fitting procedure is executed on all the SXR raw signals and the deconvolution routine is executed on the fitted signals. The resulting emissivity profile will have high time resolution, and at the same time be filtered from noise and fast-MHD. The final high quality deconvoluted SXR emissivity profile can be then evaluated, each time point divided by ϵ' and the first estimate of the evolution of the total argon density profile
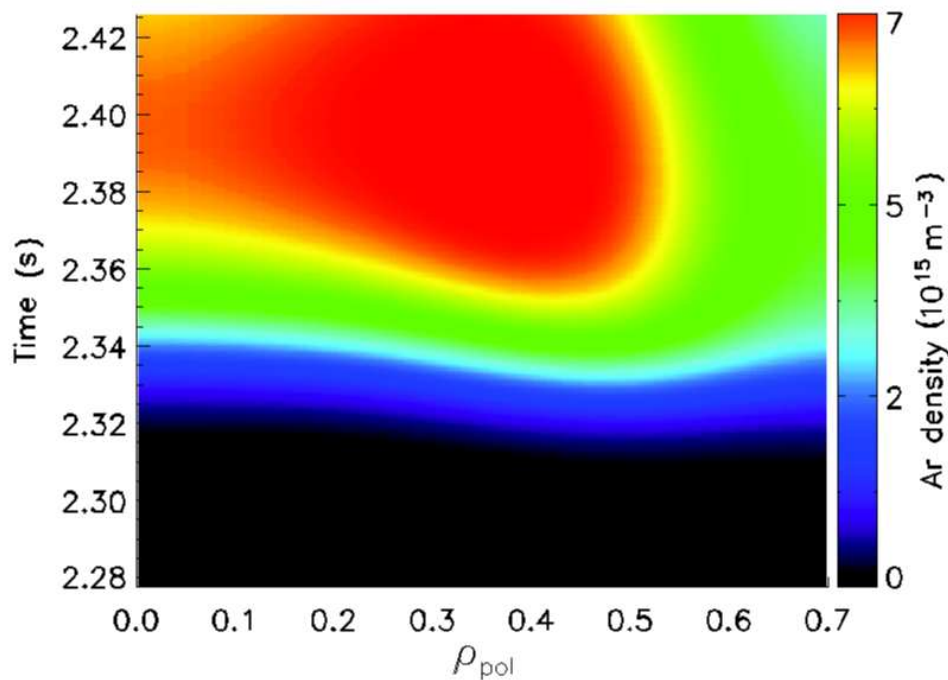

Figure 5.6: *Discharge 24450 total argon density profile evolution after an impurity puff at 2.3 seconds.*

recovered. The result for discharge number 24450 is shown in figure 5.6. The impurity puff has been executed at 2.3 seconds.

5.4.1   Sawtoothing Plasmas

In the case where strong low frequency sawtoothing MHD activity is present, the SXR raw data cannot be fitted with the procedure described in the previous section. Moreover, the full rise of the SXR emissivity profile cannot be analyzed and only the periods between sawtooth crashes will give indication of the non-sawtooth-induced impurity transport.

For almost constant sawtooth frequency, the background sawtooth cycle is also considered constant in time and subtracted from all other cycles so to leave only the con-
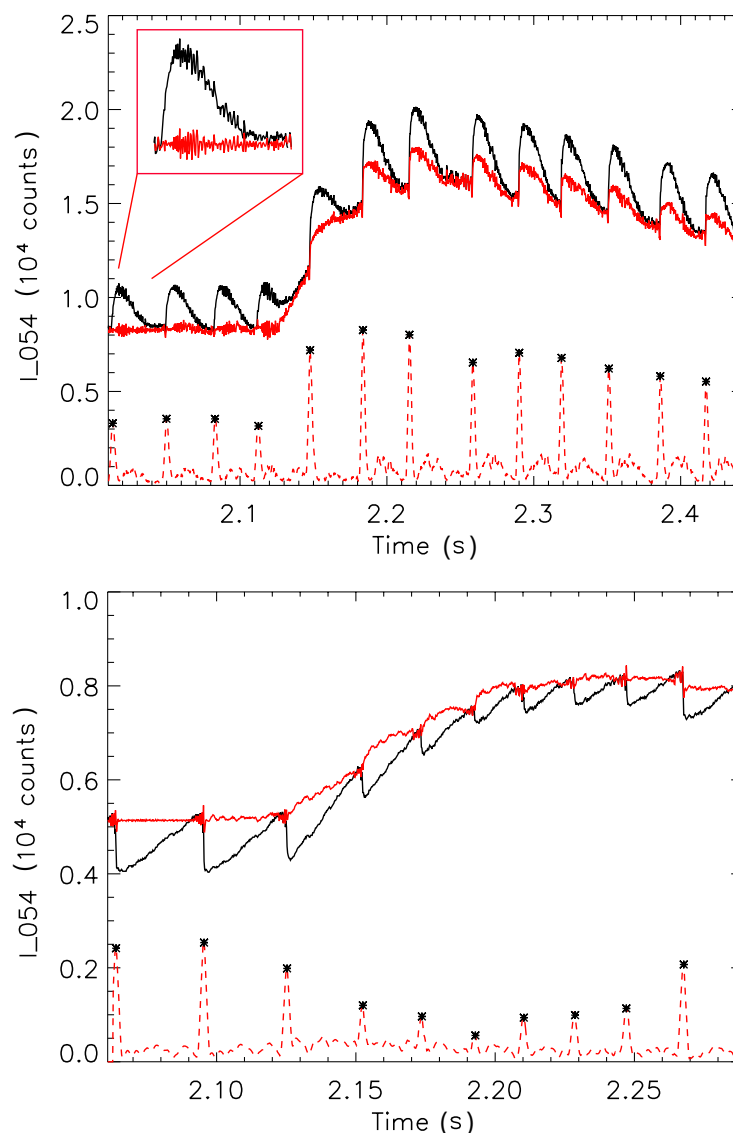
Figure 5.7: *Sawtooth subtraction of the LOS 54 of the SXR camera I for discharges 24709 and 24920. In black the raw signals, in red the result after the sawtooth subtraction. Dashed red line shows the derivative of the raw signal, the black dots the outcome of the routine for the sawtooth localization.*

tribution from the impurity. The resulting sawtooth-subtracted SXR signals will have a non-sawtoothing background prior to the impurity puff, while the sawtooth cycles after t_{puf} will contain only impurity-induced contributions. Examples of the sawtooth subtraction for the SXR line of sight 54 of camera I are shown in figure 5.7 for two different discharges. On the bottom plot the "typical" footprint, for discharge # 24920, on the top the "inverted" cycle for discharge 24709. Through the derivatives (dashed red lines) of the raw signal (black lines), the occurrence of sawteeth is automatically detected (black dots on the peaks of the dashed red line). The subtraction is then executed taking the signal level prior to the first S.T. crash as background, and subtracting the fisrt reference sawtooth cycle prior to the impurity puff (at ~ 2.1 seconds in figure) from each cycle. In the case in which the sawtooth period changes during the time interval of interest, the slope of the decay after the sawtooth crash is considered to remain constant. If the sawtooth period increases with respect to the reference S.T. cycle, the emissivity level before the next sawtooth crash is considered to remain constant at the background value (level prior to the sawtooth crash). This implies that an equilibrium is reached prior to the next S.T. crash, an assumption which is well met in the case shown (as example) in the red box in the top plot in figure 5.7. If the sawtooth period decreases, the crash size is scaled with it.

The routine for the sawtooth subtraction treats the two different sawteeth cycle types depending on the direction of the derivatives of the raw signal. This gives the possibility of achieving the sawtooth subtraction both inside and outside the inversion radius. Since the direction of the crash is detected automatically from the SXR raw data, no a priori information on the position of the inversion radius is needed.

After the sawtooth subtraction has been executed on each LOS of the selected SXR
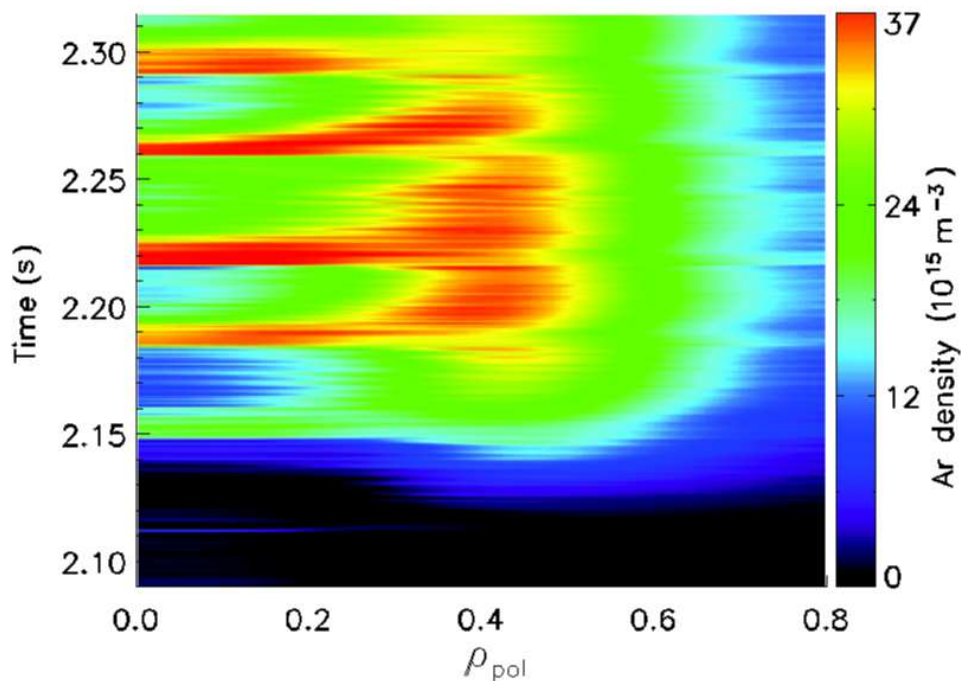

Figure 5.8: *Discharge 24709 total argon density profile evolution after an impurity puff at ~ 2.1 seconds.*

cameras, the deconvolution routine is executed. The resulting emissivity profile will contain only the contributions from the impurity emissions. As for the non-sawtoothing case, each time point of this profile is then divided by ϵ' and the first estimate of the evolution of the total argon density profile recovered. The result for discharge number 24709 is shown in figure 5.8. The impurity puff has been executed at ~2.1 seconds.

5.5 Application of the Gradient-Flux Method

Now that the total argon density evolution in time has been recovered and its systematic errors analyzed, the method can be fully applied for the evaluation of the impurity transport coefficients. From a computational point of view, derivatives and integrals in equation 5.15 are approximated with the symmetric three point formula and with the trapezoidal rule respectively [5]. The density flux and gradients at radial point k and time point j will be:

$$\frac{\partial n(r_k, t_j)}{\partial r} = \frac{n(r_{k+1}, t_j) - n(r_{k-1}, t_j)}{2\Delta r}$$

$$\Gamma(r_k, t_j) = -\frac{N(r_k, t_{j+1}) - N(r_k, t_{j-1})}{2\Delta t} \tag{5.21}$$

where Δr and Δt are the radial and time resolutions. $N(r_k, t_j)$ is the integral of the density within the radius r_k at time point j:

$$N(r_k, t_j) = \frac{1}{r_k} \int_0^{r_k} n(\tilde{r}, t_j)\tilde{r}d\tilde{r} = \frac{1}{r_k} \left[\Delta r \sum_{i=1}^{k-1} n(r_i, t_j)r_i + \frac{\Delta r}{2} n(r_k, t_j)r_k \right] \tag{5.22}$$

The chosen radial grid for the evaluation is equal or coarser than the one given by the deconvolution routine which depends directly on the number of lines of sights used. Usual deconvolutions are achieved with ~ 60 LOSs.

In order to give a comprehensive and reproducible path explaining how the transport coefficients are evaluated through this method, the list below gives an outline of the main steps which have to be executed.

1. Run STRAHL with a "standard" set of transport coefficients (red curve in figure 5.3) with electron temperature and density profiles from the experiment. Impurity puff rates and timing are also equal to the experimental values.

2. Extract the simulated total SXR emissivity profile at equilibrium, subtract the background contribution and divide the remaining profile by the total impurity density profile at the same time point. The result is the ϵ' function.

3. Read the previously deconvoluted (eventually fitted) experimental SXR emissivity profile evolution and subtract the background contribution. Divide the profile at each time point by ϵ' and obtain the total argon density profile evolution.
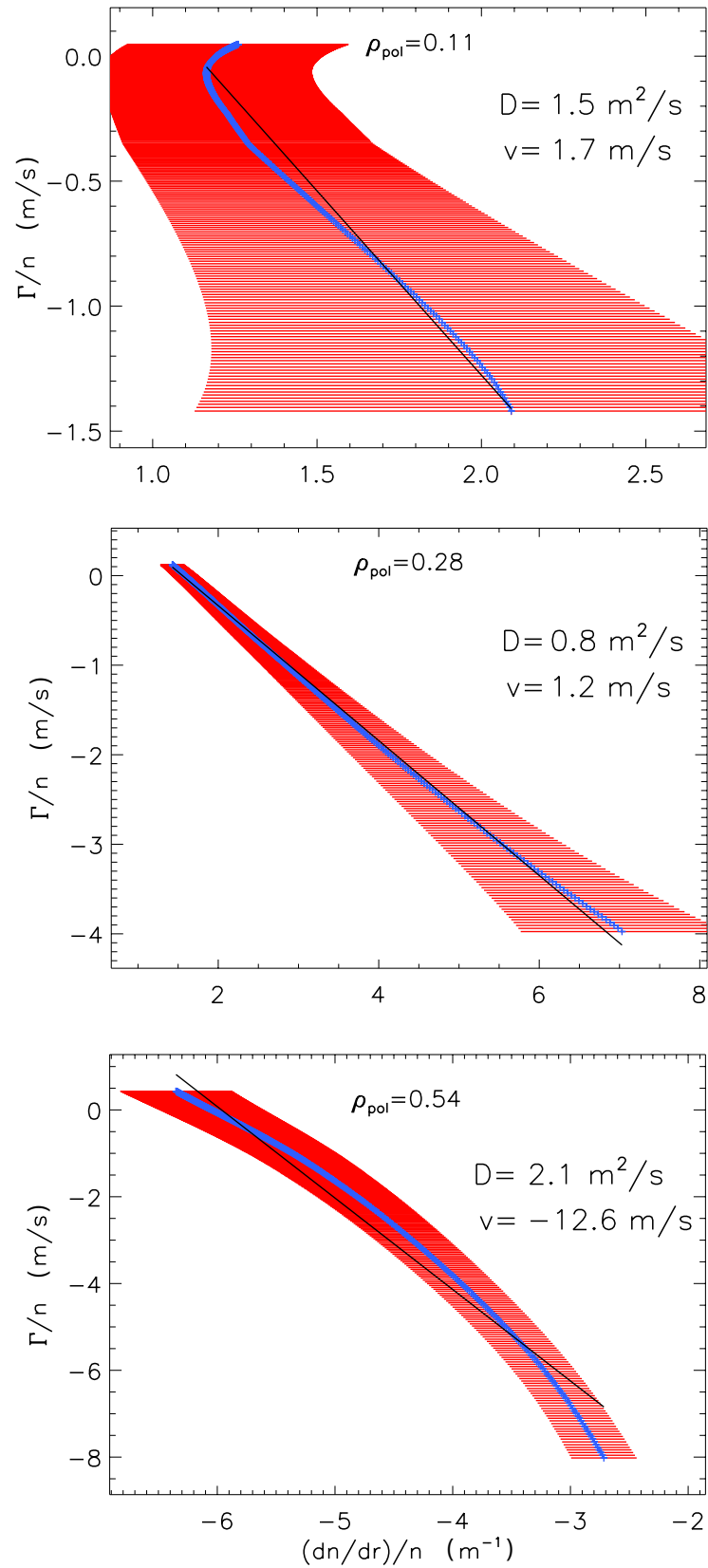
Figure 5.9: *Linear fit of the normalized flux vs. the normalized gradient for ρ_p equal to 0.11, 0.28 and 0.54 for discharge 24450. Blue dots the values, in red their error bars, black line is the result of the linear fit.*

4. For a chosen time range and number of radial points, calculate the normalized density gradient and the normalized flux, and execute the linear fit to extract the diffusion and convection coefficients.

The results from the linear fit for discharge number 24450 can be seen in figure 5.9 for three different ρ values. The sawtooth footprint in the SXR data could not be seen for this discharge because of their high frequency and low amplitude, so the sawtooth characterization could be done only through the ECE electron temperature measurement. The transport parameters evaluated for this discharge are therefore "sawtooth-averaged".

The best fit in the central plot is in the region of smallest error in the ϵ' but also at a position of maximum coverage with the SXR lines of sight (more precise deconvolution), but still inside the 1. keV electron temperature limit defined by the lower limit of the SXR filter. The top plot shows the fit for one of the most central points where the temperature is $>>$ 1.5 keV, but the number of lines of sight available for the deconvolution for these very central positions are limited.

5.5.1 Sawtoothing Plasmas

In the case of sawtoothing plasmas, two situations have to be distinguished. If the contribution of the puffed impurity to the sawtooth amplitude is marginal, the raw SXR data can be fitted after the background sawtooth subtraction has been performed and the analysis can proceed as for the non-sawtoothing case. In the case in which the impurity contributions to the sawtooth cannot be neglected, the Grad.-Flux method has to be applied only to the inter-sawtooth cycles. These cycles last few tens of milliseconds, so this type of analysis will suffer from low statistics and errors due to the high frequency noise and MHD activity which the fitting procedure could suppress. Analyzing each useful sawtooth cycle before the decay of the impurity density, the statistics can be improved. A mean value and standard deviation of the transport coefficients for each radial point can be then evaluated, returning the most probable value and an estimation of its error.

Chapter 6

Experimental Results

The study of impurity transport perpendicular to the magnetic field has to take into account all interactions and possible sources of transport, small and large scale instabilities, MHD, geometrical and asymmetry driven fluxes. The decoupling of all these players for a thorough and comprehensive analysis is many times impossible from an experimental point of view. As explained in chapter 2, classical and neoclassical contributions can be calculated if precise equilibrium reconstruction, background plasma parameters and impurity concentrations inside the confined plasma are known. Some effects due to macroscopic MHD activity can also be roughly quantified (e.g. sawtooth crashes as explained in section 5.1.1) Due to progress in computing technologies and to a great effort in the community, turbulence simulations have improved drastically in the last decades, and start to give quantitative predictions for core impurity transport [23].

The main scope of this thesis is to provide further knowledge on the effect of ECRH on the core impurity transport at ASDEX Upgrade. Previous experimental studies have shown that in NBI heated H-modes at AUG, central ECRH heating leads to an enhancement of the impurity diffusivity and to a drop in pinch velocities, thus to a sharp decrease of central impurity peaking [7]. In some cases, a positive convection velocity has also been observed, leading to a hollow impurity density profile in the centre. Outward convections have also been observed in ECRH heated L-mode discharges at TCV [9] as in Mode Conversion (MC) ICRF heated H-mode plasmas at JET [10]. In order to continue in this direction but emphasising even more the effect of ECRH, L-mode discharges with pure ECR heating have been executed (presented in section 6.1). The Gradient-Flux method (presented in section 5) has been used for the evaluation of the argon transport coefficients.

The last section of this chapter presents instead the results for impurity investigations in nitrogen seeded H-mode discharges. Recent experiments at ASDEX Upgrade (*Kallenbach et al.*, to be published) have shown that divertor temperature feedback control with nitrogen seeding leads to a global improvement in confinement. Section 6.2 analyses the influence of this improvement and of the seeding itself seeding on impurity transport.

6.1 ECR Heated L-modes

The choice of L-modes for the study of ECRH driven transport is manyfold. The high performing H-modes, characterized by steep gradients at the edge (as shown in figure 6.1), are subject to cyclic relaxation of the pressure profiles which expel particles and energy

from the pedestal (labelled "H-mode edge barrier" in figure) called Edge Localized Modes (ELMs). Since H-modes are also more prone to strong MHD activity and their high performance is not of major interest for this specific study, it is more conveninet to perform low power discharges which ensure the stability of the profiles for long time periods and give the possibility of concentrating on the turbulent argon transport.

Moreover, the L-modes have been performed with pure ECR heating whose effects can be more easily spotted in the absence of neutral beams. The reason for this is the different nature of the heating mechanism explained in sections A.1 and A.2 in the appendix: neutral beams at AUG heat predominantly ions ($\geq$ 50 %) with a broad radial profile, while ECRH is a spatially localized pure electron heating. The shallow

Figure 6.1: *Temperature profiles of L-mode (blue) and H-mode (black) regimes.*

deposition leads to strong local gradients in the electron temperature profile, while the species-selective property of ECRH leads to an increase in electron temperature while leaving the ions cold. Since no other auxiliary heating system is used in these discharges, the power partitioning between the two species will depend solely on Coulomb interactions, and therefore the temperature difference $T_e > T_i$ will decrease proportionally to the plasma collisionality [38]. The access to regimes with $T_e \gg T_i$ and strong electron temperature gradients gives the possibility of testing recent turbulence theories which predict the rise of a positive (outward) convection in plasma regions of low shear parameter s and low safety factor q (typical values for the plasma centre) for strong difference between the normalized logarithmic temperature gradients $R/L_{T_e} > 2 \cdot R/L_{T_i}$ [11].

In order to study the variations in turbulent transport due to ECRH, the suppression of all macroscopic MHD-driven transport would be preferable. This is unluckily not the case in all discharges presented in this section. Suppression of sawteeth is possible through different methods which make use of electron cyclotron heating/current drive systems [39, 40] which require the deposition of counter-current (ctr-ECCD) in a narrow region just inside the inversion radius or co-current (co-ECCD) just outside. For the experiments proposed here, the use of these methods would require the constant deposition of power close to the inversion radius (usually at $\rho_p \sim 0.3 \div 0.4$) for all discharges from on- to off-axis cases. This would reduce drastically the differences in electron temperature profiles between the on- and off-axis cases and thus reduce the possibility of observing differences between the two.

Another possibility to avoid sawteeth relies on decreasing the plasma current. This leads to a rise in the value of the safety factor at the edge (q_{95}) increasing q over the full profile and driving the central value (q_0) above 1. The decrease of plasma current results on the other hand in a global decrease of confinement ($\tau_E \propto I_p$ [9, 41]) which in turn leads to a decrease in impurity confinement and thus to a lower sensitivity to the effects of ECRH.

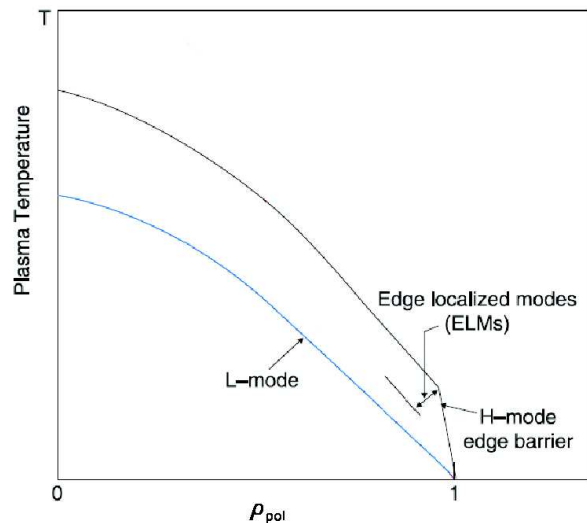For the reasons explained above, all L-mode discharges presented here have been exe-

cuted at an intermediate current (800 kA) using only ECR heating (no current drive). In the cases of sawtoothing plasmas, the inter-sawtooth cycles have been analysed as described in section 5.4.1, while the crashes were modelled through STRAHL as explained in section 5.1.1. Two discharges (#24709 and #24916) are very similar in main plasma parameters and are taken as examples for on- and off-axis ECRH deposition characterization. Because of the complexity of the on-axis case, another example (#24648) is given with lower ECRH power within the sawtooth inversion radius. In order to keep the total injected power equal to the previous discharges, one Gyrotron was set off-axis. This also stabilized the discharge thus creating better conditions for the observation of the effects of the ECRH around the central ECRH deposition radius. As shown in table 6.1, all discharges have been executed with toroidal magnetic field in the range $2.37 < B_t < 2.42$. As explained in section A.2, the choice of the magnetic field in this range is compulsory in order to guarantee that the resonance layer for ECRH (in X2-mode at 140 GHz) is located almost at the plasma axis.

Discharge #	$\overline{n}_e$ (m^{-3})	B_t (T)	P_{ECRH} (MW)	ρ_{ECRH} , $(power\,fraction)$	ρ_{inv}	τ_{ST} (ms)	q_{95}
24709	3.12	-2.37	1.2	0.22	0.4	33	4.75
24916	3.2	-2.42	1.2	0.6	0.3	22	4.66
24648	3.8	-2.32	1.2	0.35 (2/3) / 0.8 (1/3)	0.42	21	4.55

Table 6.1: Central line averaged electron density $\overline{n}_e$, toroidal magnetic field B_t, ECRH power P_{ECRH}, deposition position ρ_{ECRH} and power fraction when the power is deposited at different radii (in brackets), inversion radius ρ_{inv}, sawtooth period τ_{ST} and q_{95} for the different L-mode discharges presented in this chapter.

As a reference for the typical sawtooth averaged transport parameters observed in ASDEX Upgrade, figure 6.2 shows the transport coefficients for H-, CDH- (Completely Detached H-mode) and L-mode plasmas with $1.9 < B_t\,(T) < 2.7$, $P_{tot}\,(MW) < 9.1$, $4.5 < \overline{n}_e\,(10^{19}m^{-3}) < 12$, main ion effective mass $1.2 < m_{eff}\,(amu) < 1.9$ and $I_p = 1\,(MA)$ [5]. The abscissa is the poloidal flux surface label $\rho = \rho_p$.
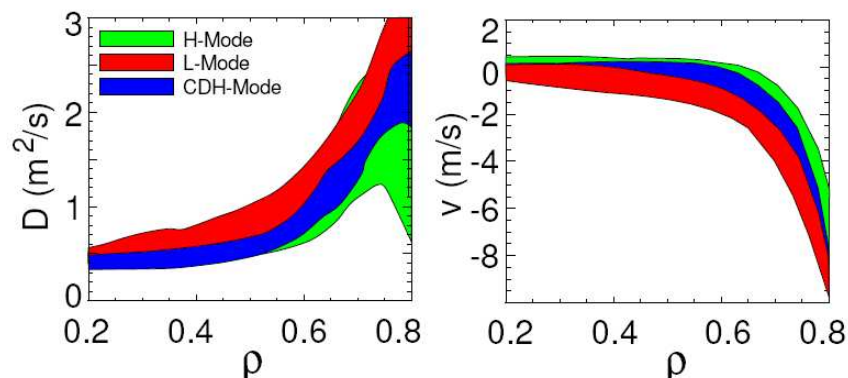

Figure 6.2: *Sawtooth averaged transport coefficients for Ne and He in ASDEX Upgrade for H-, CDH- and L-mode discharges [5]. The thickness of the coloured bands define the range of measured coefficients for different confinement regimes.*

6.1.1 On-axis ECR heating

All discharges executed with central ECR heating within the inversion radius behave very similarly. The example chosen to describe their characteristics is discharge # 24709, where $\sim 1.2\ MW$ ECRH power was deposited at $\rho_{ECRH} \sim 0.22$. Argon was injected at 2.1 s with a puff rate of $\sim 1.3 \cdot 10^{21}\ el/s$ for a duration of 20 ms.

The evolution of the main parameters are shown in figure 6.3. As can be judged from the H_α signals and from the divertor thermocurrents I_p, where no signs of the ELMs is visible, this is a stable L-mode discharge. The decrease of the I_{div} shortly after 2.1 seconds is due to the cooling effect of the radiating argon, whose approximate total radiated power can be estimated from the bolometer measurement (P_{rad}, central left plot in red) to be around $\sim 80\ kW$. Nevertheless, since the main plasma parameters are stable (electron temperature and density on the top left plot, blue and black respectively) and the density does not exhibit peaking (orange trace, ratio $H1/H5$ of the centre and edge channels of the interferometer), the argon introduced may be considered a trace.

The discharge is strongly, but relatively regularly sawtoothing (bottom-right plot in figure 6.3). The inversion radius $\rho_{inv} \sim 0.4$ has been estimated with the aid of both ECE and SXR diagnostics by tracking the direction of the crash and pinpointing the position at which an inversion is observed in the signals of both ECE and SXR . A closer look at the
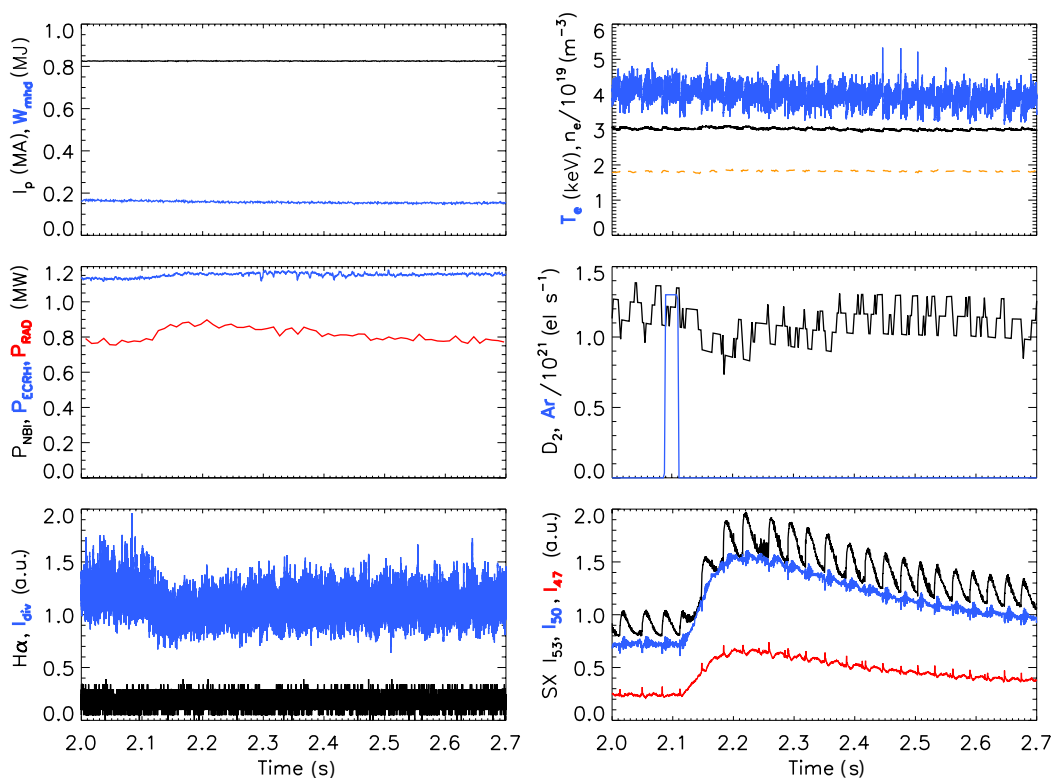

Figure 6.3: *Plasma parameters of discharge #24709. Clockwise from top left: plasma current (black) and stored magnetic energy (blue); central line averaged electron density (black), central electron temperature (blue) and density peaking factor H1/H5 (dashed orange); deuterium (black) and argon puffing rate (blue); evolution of three SXR channels (tangential $\rho \sim 0.1, 0.4, 0.6$ in black, blue and red respectively); divertor H_α (blue) and thermo-currents (black); ECRH power (blue) and total radiated power (red).*

electron temperature and soft X-ray signals in a smaller time range (figure 6.4) provides more indications on the nature of these sawteeth. The electron temperature detected by the ECE diagnostic exhibits strong oscillations of the order of magnitude of the sawtooth crash itself (top left plot) which are reflected in SXR line of sight integrated signals (bottom left). The plots on the right hand side show instead the evolution of the R/L_{Te} and R/L_{ne} evaluated from the IDA fits in the same time range (blue to red from the start to the end of the time window, reflected in the vertical bands in the plots on the right). The increase of R/L_{Te} usually observed at the ECRH deposition radius ($\rho_{ECRH} \sim 0.22$) is barely visible while the high gradient values within $\rho \sim 0.15$ may be an artefact since, the minimum visible radius of the ECE diagnostic for this discharge is $\rho \sim 0.12$.

The oscillations in T_e and n_e are caused by a strong $m/n = 1/1$ mode located around $\rho \sim 0.5 \div 0.55$ (position of minimum variation of the R/L_{Te}) coupled to smaller 2/1 and 3/1 modes, as found from analysis of magnetic coils and SXR spectra [42,43]. This behaviour is observed in all L-mode discharges executed for this work at low/medium density, with $> 1 \; MW$ ECRH deposited inside the inversion radius. Similar mode activity has been previously observed and theoretically modelled at TCV [44]. In this work, sawteeth of this kind have been named "saturated" since, before the crash, the SXR signals reach a saturated value during which an increasing intensity of mode activity is observed. The saturation phase terminates with the sawtooth crash after a rapid growth of the $m/n = 1/1$
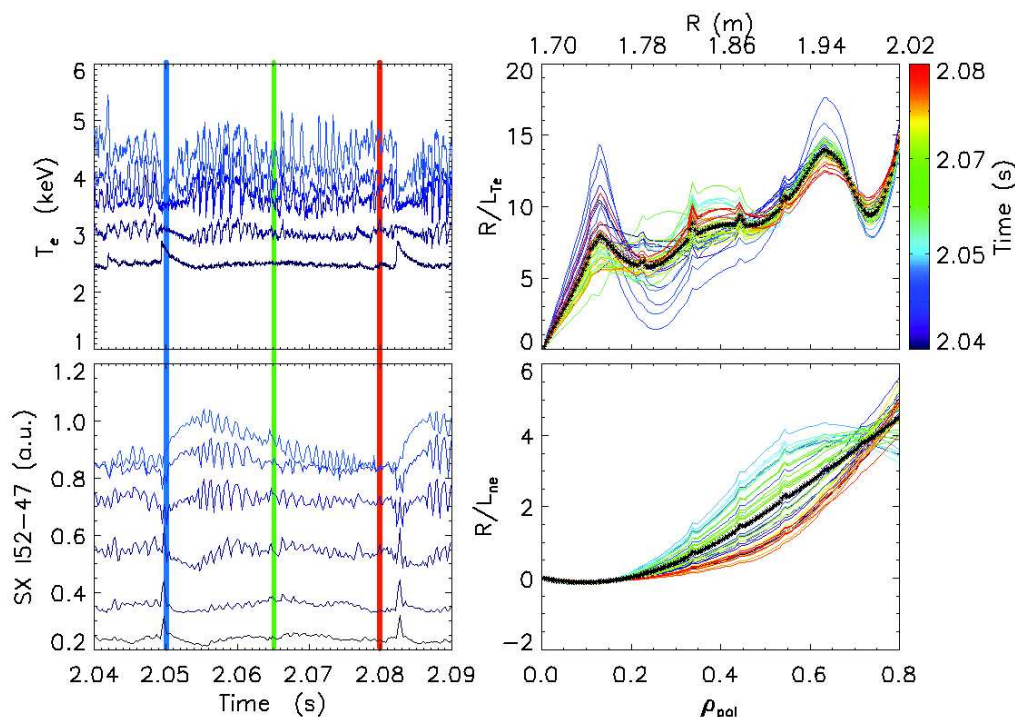

Figure 6.4: *Left: ECE and SXR temporal evolution of different channels during sawtooth cycles of discharge #24709 (increasing intensity corresponds to more inboard channels, colour bands defined on the right). Right: normalized gradient lengths of T_e and n_e obtained from IDA fits for the same time range (colour code corresponds to time, black dots are the mean values).*

mode. The same situation is observed at ASDEX Upgrade for the electron temperature but, differently from [44], the SXR signals in-between sawtooth crashes are "inverted", such that the SXR emissivity decreases instead of increasing. This could indicate that the relaxation during the crash transports the impurities inwards, while the transport in-between crashes is radially outwards, leading to the hypothesis of a suppression of impurity pinch within $\rho \sim 0.3 \div 0.4$.

v/D profiles from equilibrium density

The argon transport coefficients for this discharge have been evaluated with the n_e and T_e profiles averaged over the range of interest $2.1 < t < 2.4$ s, shown in figure 6.5. Simulations with varying profiles have also been achieved, but no appreciable change in the results has been obtained. Ion temperature profiles have been estimated from the two measurements available for this discharge (in red in figure 6.5), the central value from the NPA and the other from CSXR spectrometer. The fit has been performed assuming that T_i will approach T_e before reaching the separatrix, at $\rho \sim 0.8 \div 0.9$. which could be the case for high enough electron density [45]. On the other hand, only the core profiles are of interest for the scope of this analysis, so slight differences at of T_i and T_e at the edge will not play an important role.

Following the steps explained in section 5.5, the time evolution of the total argon density profile has been evaluated by dividing the deconvoluted, background subtracted SXR emissivity profile of argon (from pinhole cameras H and I) by the normalized soft X-ray emissivity function ϵ'_{Ar} (evaluated through STRAHL assuming a standard set of transport coefficients). The full profile has been rescaled through the value of the Ar concentration given by the CSXR spectrometer (explained in section 5.3.3. Taking the total argon density profile just before a sawtooth crash after equilibrium has been reached (such that $\Gamma(r, t) = 0$ in equation 5.15), the v/D profile can be directly evaluated from the normalized total argon density gradient:
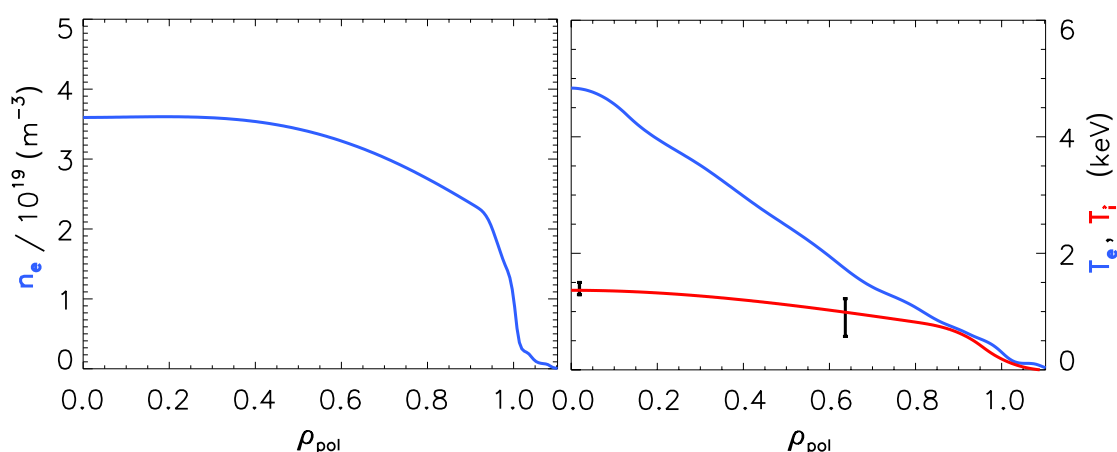

Figure 6.5: *Electron density n_e (left), electron T_e and ion temperature T_i (right, blue and red respectively) profiles for discharge # 24709. The black points with error bars show the available ion temperature measurements for this discharge.*

$$\frac{v(r)}{D(r)} = \frac{1}{n(r, t_{eq})} \frac{\partial n(r, t_{eq})}{\partial r} \tag{6.1}$$

Figure 6.6 shows the steps and the result of this evaluation at $t_{eq} = 2.3\ s$ in the discharge. Top left is the ϵ' function, bottom left the background subtracted local SXR emissivity profile, top right the total argon density profile and bottom right the estimated v/D profile. The blue lines represent the error bars evaluated assuming 5% error on the raw SXR signals. Errors on the electron temperature and density profiles have not been taken into account. Despite the large error bars, the region $\rho \leq 0.3$ provides further indication of a suppression of the central impurity pinch.
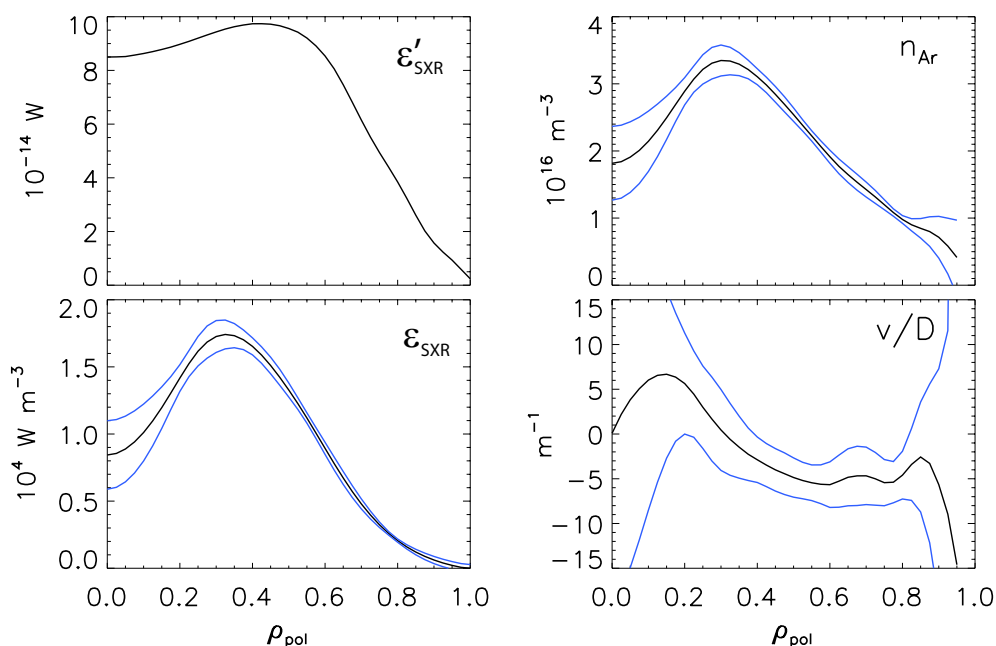
Figure 6.6: *Evaluation of the v/D profile for discharge 24709. From bottom left clockwise: SXR emissivity profile at equilibrium, ϵ' function, total argon density profile at equilibrium and resulting v/D profile. The blue lines denote the error bars.*

v and D profiles from the Gradient-Flux method

When evaluating the full profile of both the diffusion D and the convection v coefficients (figure 6.7) this central positive convection region is confirmed. Because of the sensitivity limits imposed by the SXR sensitivity curve of the present setup (explained in section B.7 and 5.3.2), the evaluation of the transport coefficients is possible only up to $\rho \sim 0.55$ where the electron temperature drops below the $\sim 1.5\ keV$ limit. Outside of this radius, the diffusion coefficient has been adapted to fit the argon influx phase as best as possible while the convection velocity has been set to zero. These assumptions may give realistic mean transport through the region $\rho > 0.55$, but the "real" profiles outside of this radius cannot be evaluated. Due to the sensitivity limit and to the low SNR at the edge of the detection range, the convection velocity in this region evaluated through the G-F method exhibits strong oscillations. After the first evaluation with the "typical" transport coefficients, the

values of $v(\rho > 0.45)$ are adapted so to approximately match the equilibrium $\sim v(t_{eq})/D(t_{eq})$ evaluated previously. Moreover, since the modified tanh function fitting procedure for the SXR raw signals explained in section 5.4 could not be applied, the full profile from the centre up to $\rho \sim 0.55$ has been smoothed over two adjacent points.

In order to test the method and the results obtained, a scan in transport coefficients has been performed. STRAHL simulations has been undertaken for each set of D and v profiles, the results of the simulations compared to the experimental data and the reduced χ^2 evaluated to define the quality of the fit. Since different SXR cameras may have slightly different sensitivity curves, only lines of sight from camera I (shown previously in figure B.7) have been used for the comparison. The choice has been further restricted to those LOSs whose minimum visible ρ is greater than the radial position at which the electron temperature falls below the sensitivity limit of the SXR diodes. This minimizes the effect of the systematic errors due to a change in the SXR sensitivity function.

The scan performed for discharge

Figure 6.7: *Profiles of the transport coefficients of discharge #24709 evaluated through the G-F method. The shaded area represents the region where the analysis cannot be performed.*

#24709 is shown in figure 6.8, black crosses representing the original values while the scanned profiles are plotted as dashed light blue lines. Because of the dense radial mesh used, the variation of single points in the profile would be physically meaningless. Since the profiles are time averaged, consistency and continuity of the values along the profile must be maintained, avoiding strong differences between neighbouring points. For these reason the scans have been performed varying three knots in the profile of the diffusion coefficient ($\rho = 0$, 0.35 and 0.62) and two in the convection velocity ($\rho = 0.15$ and 0.62). The neighbouring points (up to the neighbouring knots) have been consequently adapted so to maintain the profile continuous. All combinations in D and v have been scanned. The transport coefficients which have given the lowest χ^2 for all lines of sight are plotted in blue in figure 6.9, the black crosses are the original ones as in figure 6.8. Dashed lines represent the neoclassical transport evaluated taking concentrations of $1.5 \cdot 10^{-2}$ carbon, $5 \cdot 10^{-3}$ oxygen, $6 \cdot 10^{-5}$ tungsten and $7 \cdot 10^{-4}$ argon. Values for the Ar and W have been deducted from the CSXR and the grazing incidence spectrometer measurements while those of carbon and oxygen are typical concentration values observed in ASDEX Upgrade. To stress the importance of performing these calculations taking into account all the impurities present in the plasma, a second NEOART calculation has been performed with Ar as the only impurity. The neoclassical diffusion is in this case lower by a factor $\sim 4 \div 2.5$ when
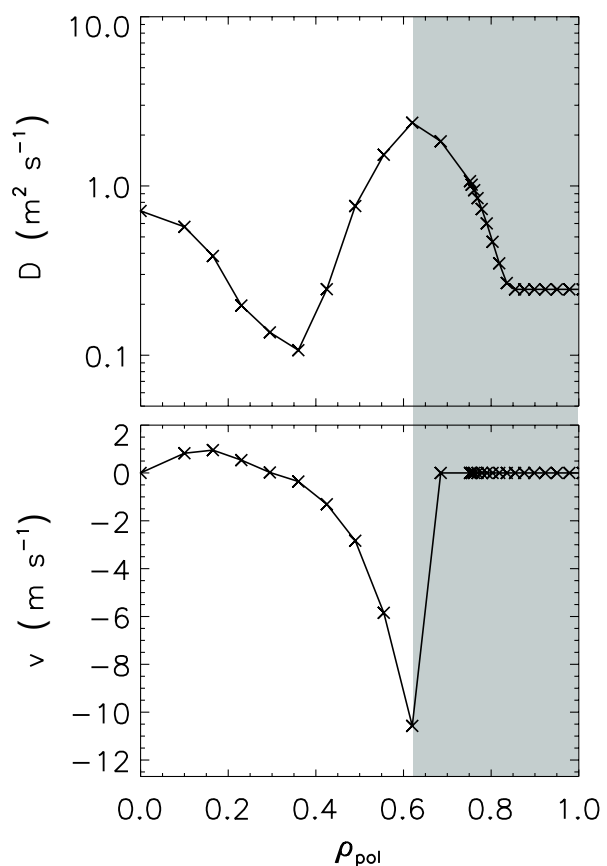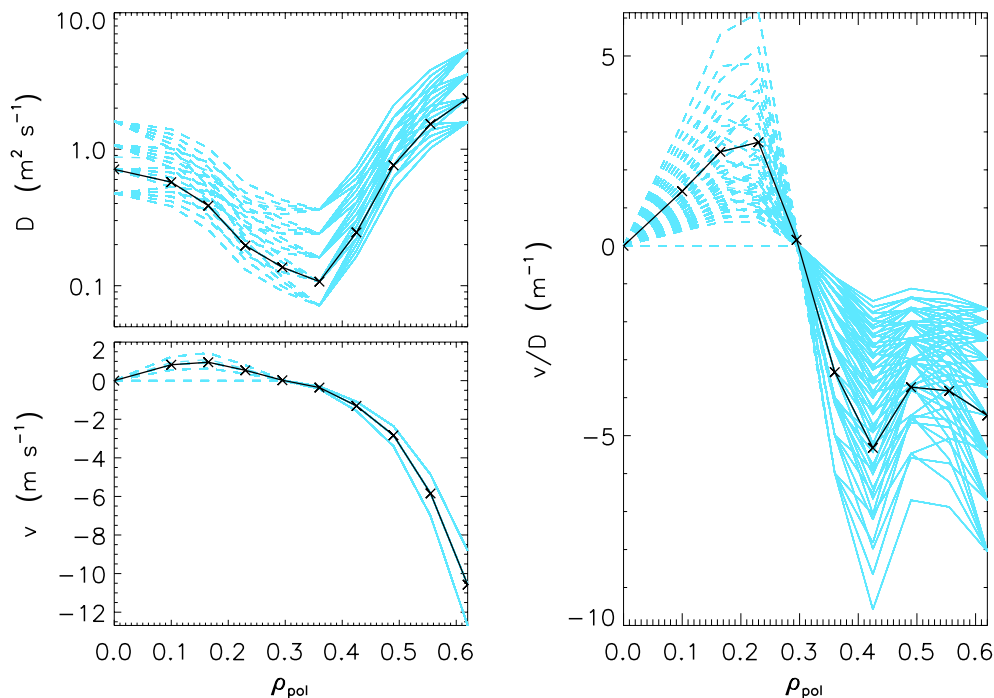
Figure 6.8: *Scan in transport coefficients for discharge 24709, convection and diffusion coefficients (top and bottom left) and corresponding v/D (right). Black crosses are the original profiles evaluated through the G-F method; light blue represent all the combinations of transport coefficients scanned. The radial range has been restricted to the sensitivity limit of the SXR diagnostic.*

considering the centre or moving around mid-radius.

The error bars on the optimum diffusion and convection profiles have been evaluated from the percentage variation in χ^2 with respect to the change in transport parameters. Naming a the scanned transport parameter, its error can be defined as [46]:

$$\sigma_a^2 = \frac{2}{\partial^2 \chi^2 / \partial a^2} \tag{6.2}$$

As for the previous scan in D and v, the variation in transport coefficients has been performed scanning 3 knots and adapting the neighbouring points so to keep the profile consistent. It must be stated that these error bars will only give an indication of the statistical errors due to the 5% precision imposed to the SXR signals. Since the (large) errors of the electron density and temperature profiles have not been taken into account, these values should be considered as lower estimates of the precision with which the transport coefficients can be evaluated.

The discrepancy between the values obtained from the G-F method and those minimizing the χ^2 are negligible within the error bars for the convection velocity, while substantial difference is observed for the diffusivity, reaching a maximum of a factor ~ 3 at $\rho \sim 0.35$. This is probably due to a time change in the transport parameters during the different phases of the sawtooth cycles, a qualitative explanation of which will be given shortly.

Comparison of the time evolution of the simulated (red) and experimental data (green) on which a 5% error (black) is assumed, is shown in figure 6.10. The background sawtooth
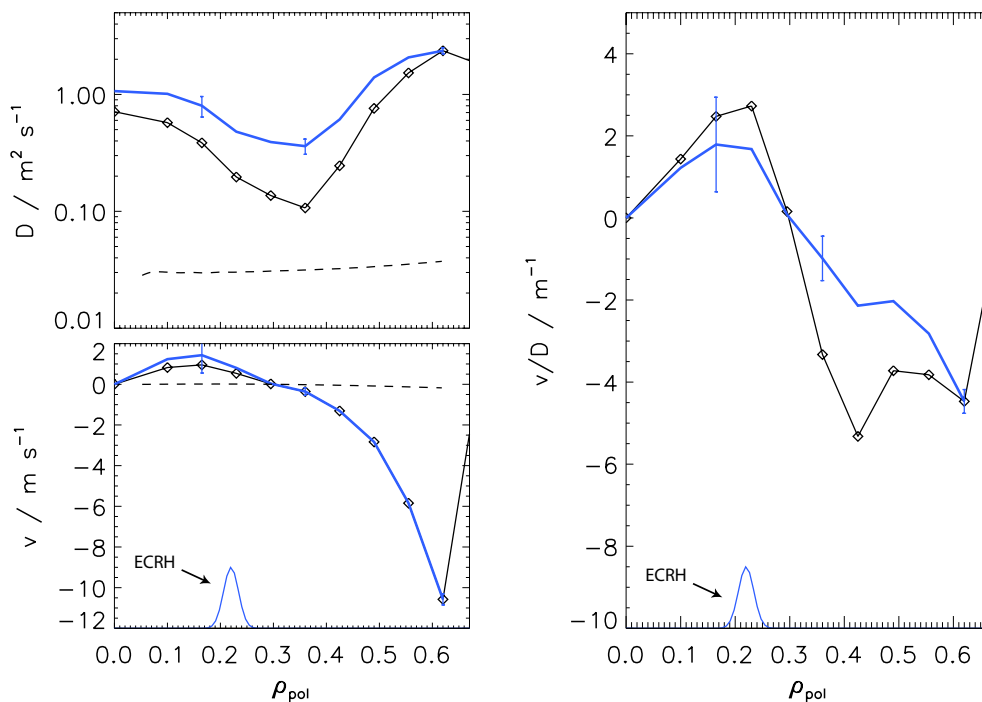
Figure 6.9: *Discharge 24709 transport coefficients (left) and corresponding v/D within the sensitivity limit of the SXR diagnostic. Black squares are the original profiles evaluated through the G-F method; blue lines those for which the χ^2 is minimum; dashed lines represent the neoclassical contributions evaluated through NEOART. The ECRH deposition position is also shown.*

cycles, subtracted prior to the analysis, have been added to the results of the STRAHL simulation. The agreement with the experimental data is quite good, reproducing accurately the full rise of the various SXR signals, apart from the short rise phase after the sawtooth crash for the most central channels ($\rho < 0.21$) and an over-estimation of the full rise ($2.13 < t < 2.2$)of the two most edge channels. The values at equilibrium are well simulated, indicating that the v/D profile is trustworthy. The complexity of the analysis for this discharge is also visible in the sawtooth shape whose atypical behaviour cannot be modelled with this simple method. The reasons for this are manifold. First of all, the transport parameters given in figure 6.9 are mean values over the different phases in-between the sawtooth crashes. The same is valid for the electron temperature and density profiles used for the simulation. The use of time dependent T_e and n_e profiles does not give substantial change in the results because of two independent reasons. First of all, due to the absence of ECE data within $\rho < 0.12$, and to the fact that neither the interferometer channels nor the lines of sight of the core thomson scattering system pass through the plasma axis, the electron temperature and density profiles in the centre exhibit large error bars and cannot provide sufficiently precise measurement for such a modelling. Secondly, the change in electron profiles is coupled to a change in transport which is also not modelled here. This change during the first phases after the sawtooth crash can be expected because of both the change in MHD (suppressed during the rise phase of the electron temperature as can be seen in figure 6.4), and a change in background plasma parameters. Moreover, the neoclassical transport coefficients plotted in figure 6.9 are also evaluated with mean T_e and
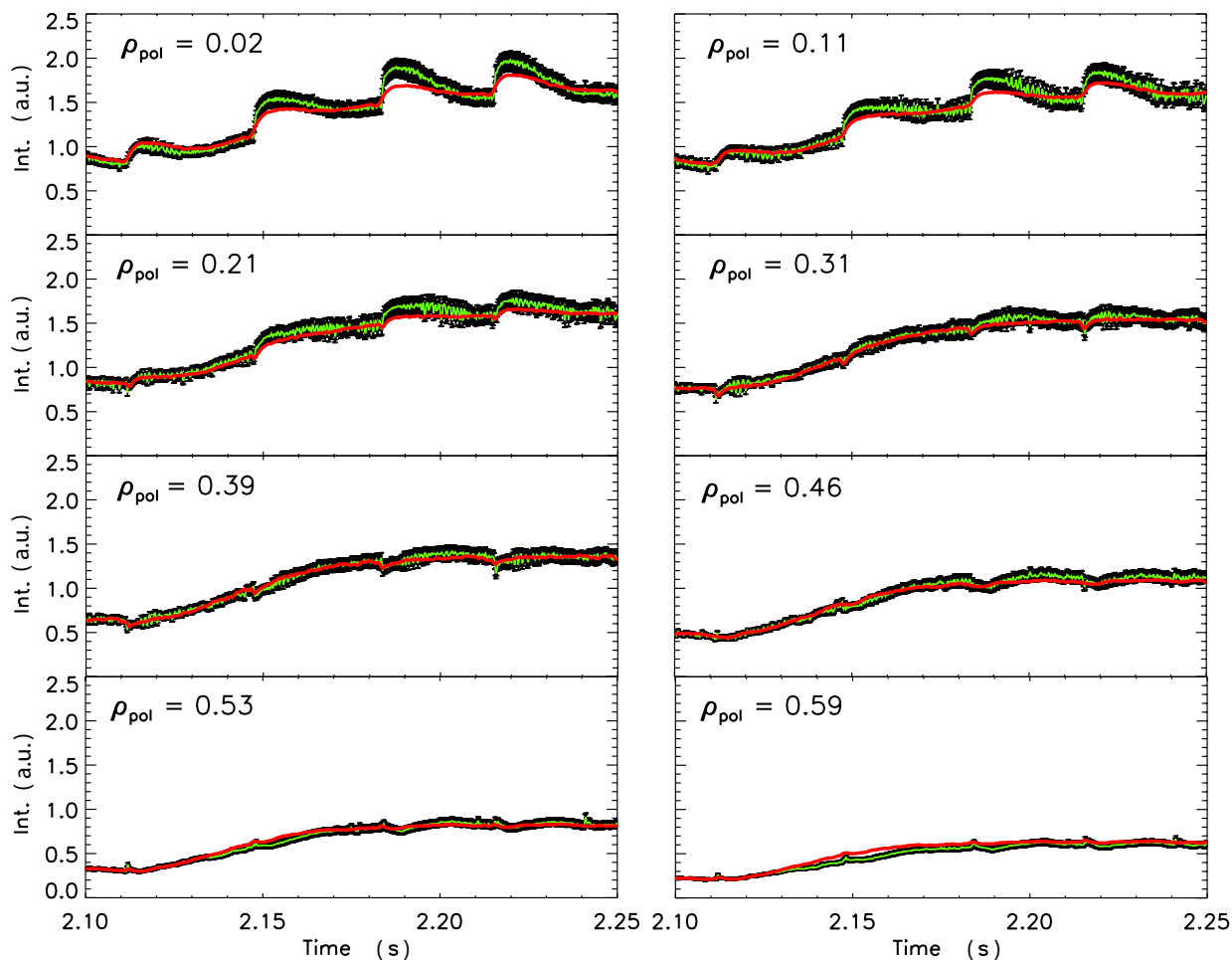
Figure 6.10: *Comparison of the experimental data (green, black error bars = 5% of the signal) with the simulated results from STRAHL (red) for discharge #24709 with the best-fit transport parameters in figure 6.9. For better comparison, the contribution from the background sawteeth cycles has been added to the simulated data.*

n_e profiles as well as with an ion temperature profile which is constructed on two experimental points and on an apriori assumption for the edge. Since neoclassical transport has a strong dependence on the ion temperature profiles, these values could be under-estimated. Ultimately, NEOART calculations assume nested flux surface geometry which, because of the strong mode activity, is itself not guaranteed for the full plasma radius. These aspects are also crucial for turbulent simulations: the imprecise knowledge of the electron profiles, poses large errors on the type of turbulent drive in action, since this depends on the normalised gradients R/L_{Te}, R/L_{ne} and R/L_{Ti} while the non-nested flux surface geometry leads to a disturbance in the parallel motion which gives rise to the parallel friction responsible for many turbulent modes. For all of these reason, GS2 simulations within the inversion radius have not been executed. Outside ρ_{inv} the electron profiles are more stable and the turbulent simulations have been performed at $\rho \sim 0.61$, at the lower limit of the sensitivity range of the SXR diagnostic for this discharge. Results obtained from the GS2 simulations will be reported later on in this section.

6.1.2   Off-axis ECR heating

The discharge chosen to investigate the transport of Ar with off-axis ECRH is #24916. This discharge is not a completely stable L-mode, since the I_{div} traces exhibit strong variations in time, but it is neither an H-mode since no ELM signature is visible in the H_α (shown at the bottom left plot in figure 6.11). A probable explanation for this behaviour is a fluttering of the edge plasma parameters oscillating between L-mode and a marginal H-mode. Including the contributions from Ohmic and ECRH heating, the total heating power delivered for this discharge is $\sim 1.5\ MW$ ($\sim 1.1\ MW$ from the ECRH and $\sim 0.4\ MW$ from
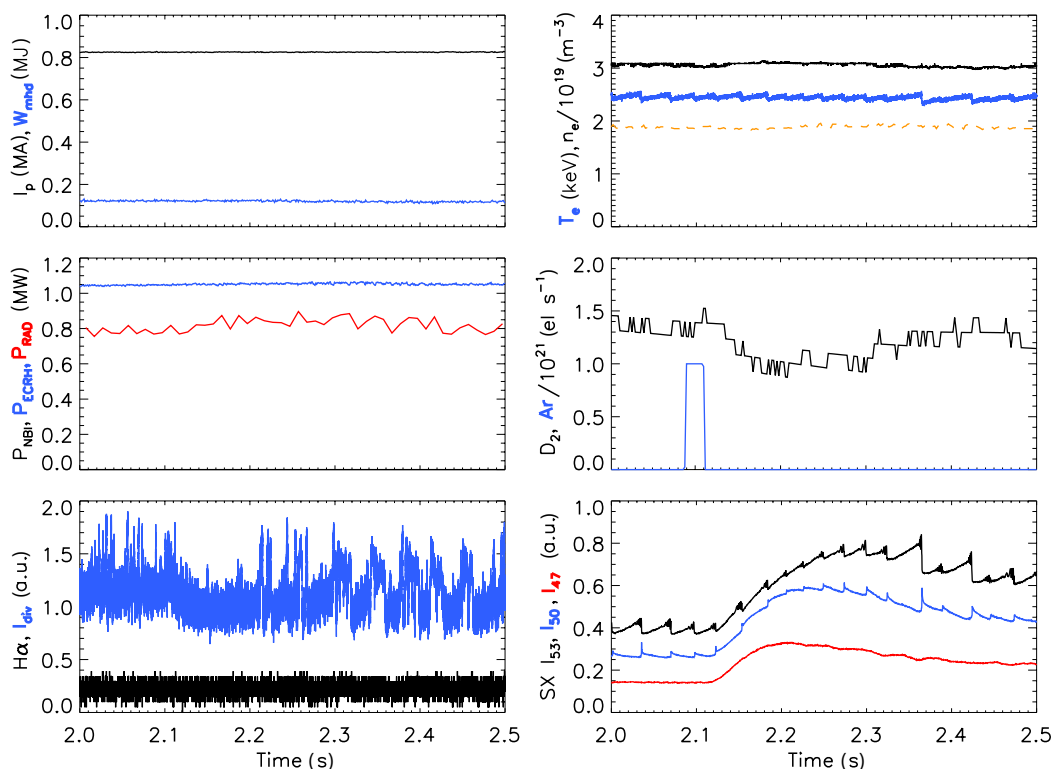
Figure 6.11: *Plasma parameters of discharge # 24916 (refer to figure 6.11 for the definition of the signals).*
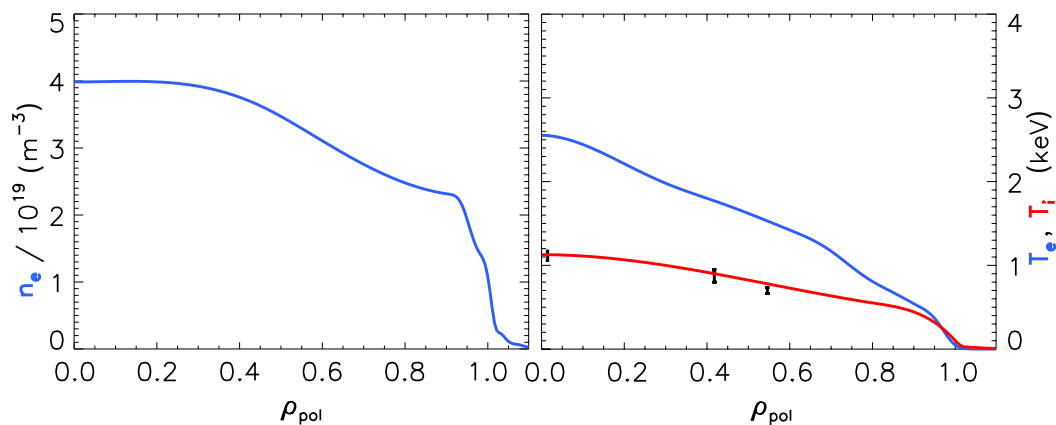

Figure 6.12: *Electron density (left), electron and ion temperature (right in blue and red respectively) profiles for discharge # 24916.*

the Ohmic heating), at the limit of the H-mode threshold $P_{L-H} \sim 1.5 \div 1.7 \ MW$. Because of the naturally unstable nature of this discharge, the Ar puff at 2.1 s (central right plot, blue) has been lowered by more than 20% with respect to the previous example. This is also reflected in the minor enhancement of the total P_{rad} just after the argon injection (central left plot, red). Also the sawtooth cycles (bottom right) evolve in time, changing both in period and in amplitude. Fortunately, during the rise phase of the argon puff ($2.1 < t < 2.25 \ s$) used for the evaluation of the transport coefficients, all these players are relatively constant: the sawtooth period and amplitude maintain roughly the same value and the central electron temperature and density, as well as the electron density peaking, are stable (top right). Restricting the time range and observing the sawtooth cycles, the electron temperature and density gradients evolution shortly before the argon puff (figure 6.13) it can be noted that also the profiles are relatively stable, not exhibiting strong variations within a few sawtooth cycles. The full profiles can be seen in figure 6.12. The electron density profile is more peaked with respect to the one in discharge #24709, while the electron temperature exhibits central values lower by almost 50%. Both these factors may be ascribed to the ECRH off-axis deposition. On the other hand, since the total delivered ECRH power is approximately the same as for the previous example, the $T_e \sim 1.5 \ keV$ limit is still approximately at $\rho \sim 0.65$. The ion temperature profile is instead very similar to the previous case.

As shown in figure 6.13 the sawtooth activity of this discharge is "classical", since both electron temperature and SXR emissivity drop sharply at the crash and rise constantly in-between crashes. The only strong macroscopic MHD activity present is the $(1, 1)$ sawtooth
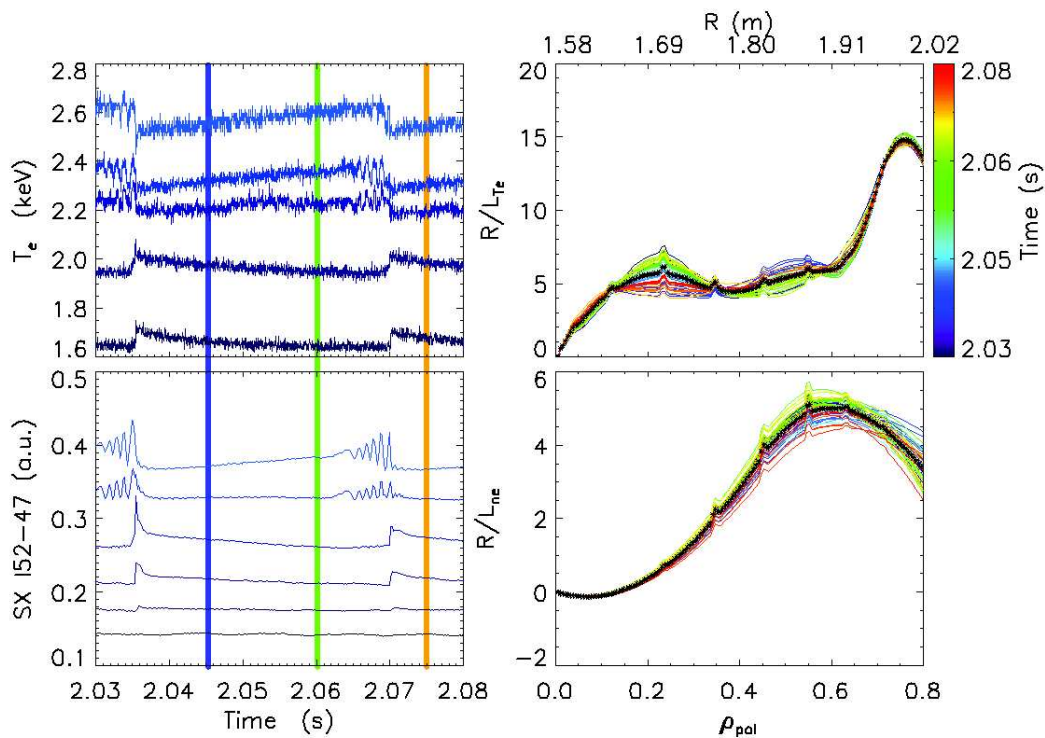

Figure 6.13: *Left: ECE (top) and SXR (bottom) evolution during sawtooth cycles of discharge # 24916. Right: normalized gradient lengths of T_e and n_e for the same time window.*
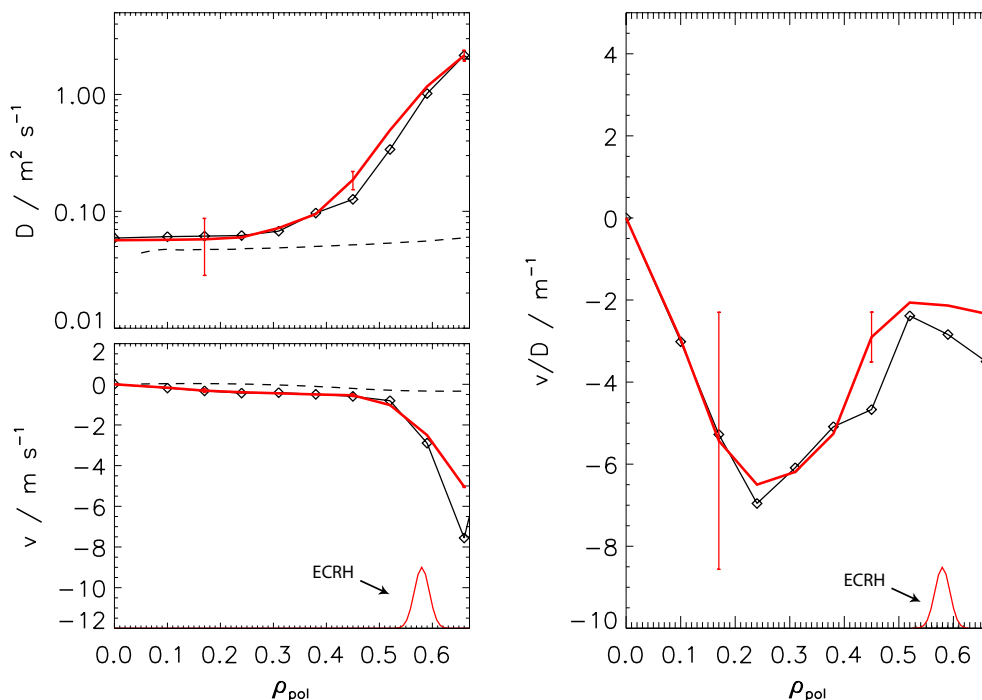
Figure 6.14: *Full profiles of the transport coefficients of discharge # 24916: black squares are the original coefficients evaluated through the gradient-flux method, in red those delivering the minimum χ^2 and dashed line represents the neoclassical values.*

precursor. The normalised temperature and density gradients evaluated from the IDA fits (on the right in figure 6.13) are relatively stable. The temperature profile variations inside mixing radius (the inversion radius is at $\rho_{inv} \sim 0.3$, $\rho_{mix} \sim 0.42$) can be clearly seen. The ECRH deposition radius is in the range $0.56 < \rho_{ECRH} < 0.62$.

The absence of strong MHD activity permits a clearer analysis in this case than for the previous discharge. This is reflected in the precision of the transport coefficient evaluated through G-F method. Skipping the full explanation given in the previous section to thoroughly explain the method for the evaluation of the transport coefficients, the final results can be seen in figure 6.14. As for the previous case, the original transport parameters are plotted as black crosses, those giving a minimum χ^2 in red while the dashed lines represent the neoclassical values evaluated with $1.5 \cdot 10^{-2}$ carbon, $5 \cdot 10^{-3}$ oxygen, $3 \cdot 10^{-5}$ tungsten and $1.5 \cdot 10^{-4}$ argon. As for the previous case, a second NEOART calculation has been performed with Ar as the only impurity, resulting in a neoclassical diffusion again lower of a factor ~ 3 up to mid-radius.

The difference between the values calculated through the G-F method and those minimizing the χ^2 are negligible, demonstrating the precision of the method. The central diffusivity of argon is in the range of the calculated neoclassical value. The convection velocity is instead negative throughout the whole analysed radial range, decreasing strongly for $\rho > 0.5$, while the neoclassical values are slightly positive for $\rho < 0.25$, marginally negative for the rest of the range. The comparison of the simulated and experimental data is plotted in figure 6.15. The agreement of the simulation with the experimental data is particularly good up to channels at $\rho \sim 0.64$, further demonstrating the quality of the evaluated transport coefficients.
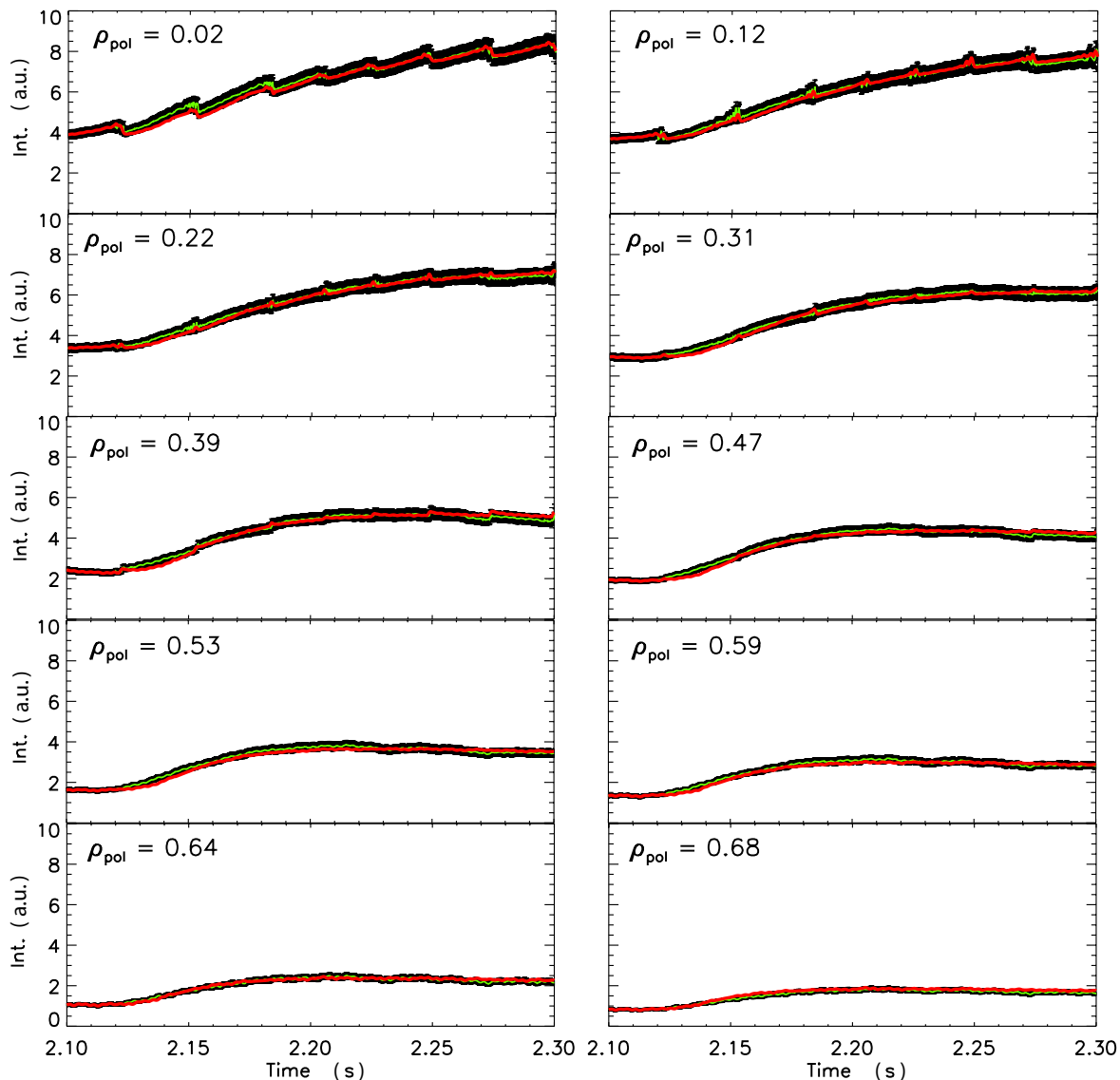
Figure 6.15: *Comparison of the experimental data (green with black error bars) with the simulated results from STRAHL for discharge #24916 with transport parameters in figure 6.14. The contribution from the background sawteeth cycles have been added to the simulated data so to better compare them.*

On the plot on the right hand side of figure 6.14, the drift parameter v/D exhibits a convex region located around $\rho \sim 0.4 \div 0.6$, the ECRH deposition located at ~ 0.6. This could be an error intrinsic to the method used for the evaluation the transport coefficients, but as will be further explained briefly and in the next section, the experimental data suggests that this decrease in negative drift parameter is due to the the electron cyclotron heating. This effect of ECRH can be also noticed when comparing the transport coefficients with those from the previous case with on-axis heating. The two profiles are overplotted in figure 6.16, transport coefficients of the on-axis case in blue, off-axis in red.

The diffusion coefficient of the off-axis case (top left) decreases continuously edge-to-centre reaching a minimum only at the centre of the plasma. The on-axis case (in blue) is a factor ~ 5 higher for $\rho > 0.35$, radius at which it rises again to mid-radius values. Also the
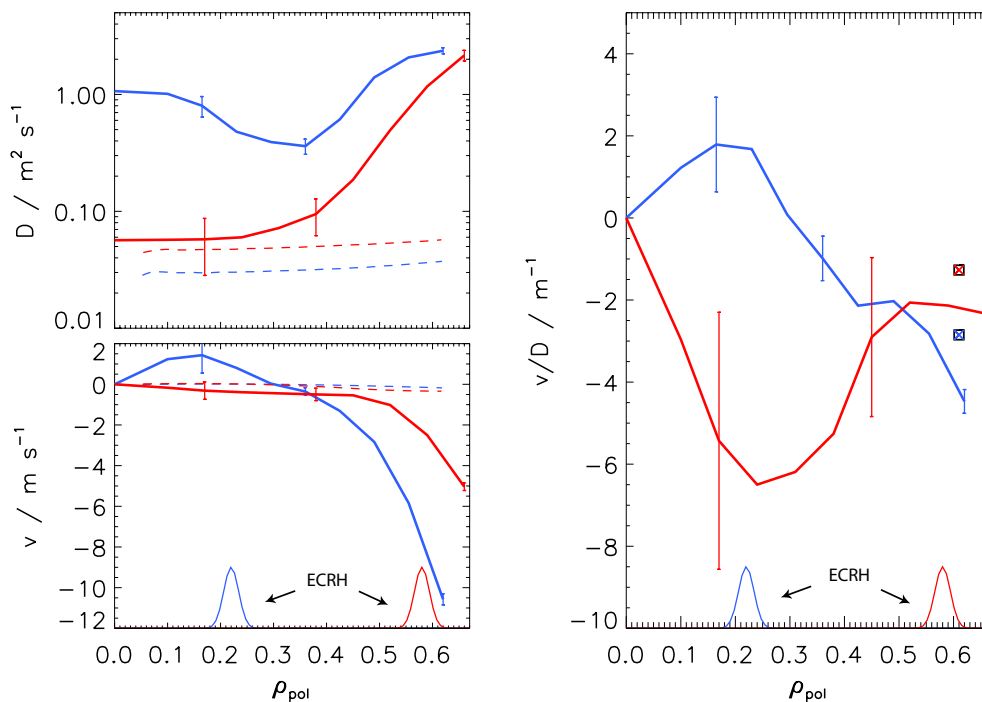
Figure 6.16: *Comparison of the argon transport coefficients for on-axis (discharge #24709, in blue) and off-axis (#24916, in red) ECRH deposition. Dashed lines are the neoclassical values evaluated through NEOART, blue/red dots are the GS2 calculations.*

convection velocities (bottom left plot) exhibit strong differences. The positive region in the centre of the plasma observed for on-axis heating around the ECRH deposition radius $\rho_{ECRH} \sim 0.22$ is not visible when the ECRH is moved off-axis. Moving further outward, e.g. at $\rho \sim 0.55$, a stronger pinch can instead be observed for the on-axis heated discharge, the blue trace being lower by more than a factor 2 with respect to the red trace. Around the deposition radius of the ECRH, the two discharges behave very similarly, indicating that the effect of ECRH is quite localized and leads to a suppression/reduction of impurity pinch.

Turbulent simulations with the linear code GS2 have been performed [47] for both discharges at $\rho \sim 0.61$ (blue and red dots respectively in figure 6.16). Since linear simulations require an a-priori assumption on the mode growth saturation level and on its growth time, only v/D values can be delivered. For the on-axis case, a mean of all the contributions to the full $k_y - spectrum$ of the turbulent modes returns a $v/D \sim -2.85\ m^{-1}$ while for the off-axis case $v/D \sim -1.27\ m^{-1}$. As can be seen in figure 6.16 these values are slightly higher (in absolute value) than the experimental values, but a decrease in drift parameter is observed by when the ECRH is not deposited in this region (blue curve). The GS2 simulations would therefore confirm the hypothesis delivered above of a reduction of impurity pinch in the region of deposition, even if the deposition is located around mid-radius such as in the case of discharge #24916.

Since the on-axis case is particularly complicated because of the strong MHD whose effects cannot be decoupled in any way from the other contributions, confirmation of these results require other examples with deposition in-between the two radii scanned up to now. The heating scheme has to stabilize the strong MHD observed in discharge #24709 and at

the same time deposit ECR power centrally enough to be well inside the sensitivity limit of the SXR diagnostic and to provide a peaked electron temperature profile for the excitation of turbulent modes of interest.

6.1.3   Combination of On- and Off-axis ECRH

The stabilization of the MHD modes observed in discharge #24709 is obtained in discharge #24648. The total ECRH power is still $\sim 1.2\ MW$, but $\sim 0.8\ MW$ is deposited within
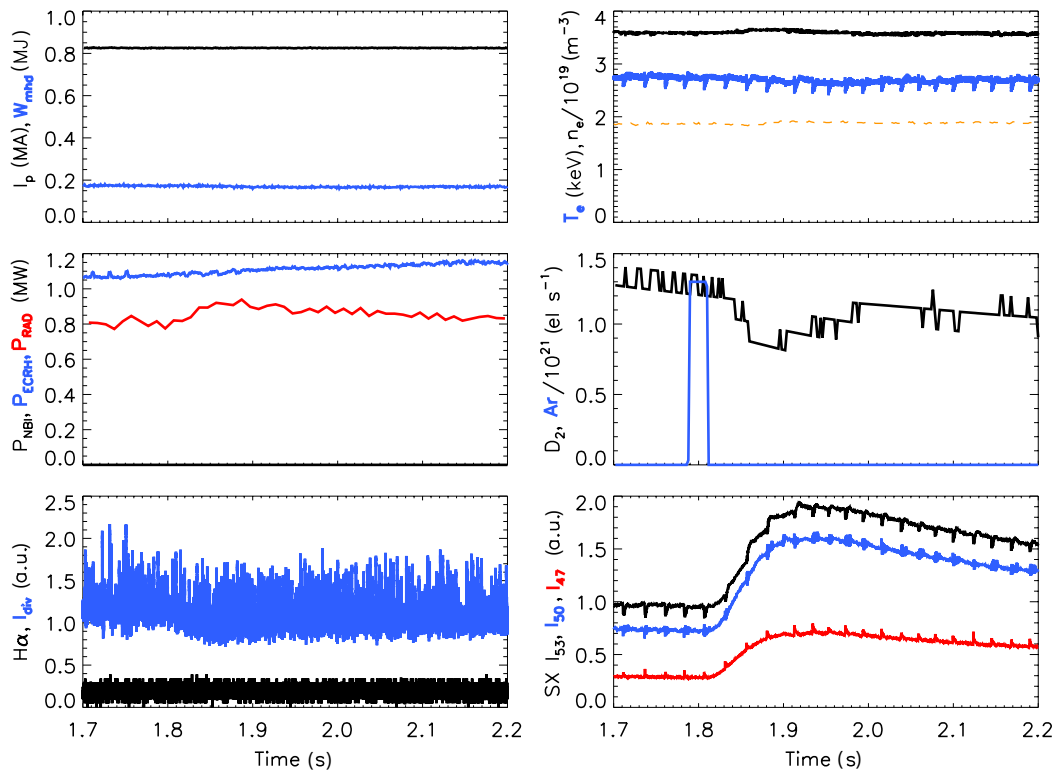

Figure 6.17: *Plasma parameters of discharge # 24648 (refer to figure 6.11 for the definition of the signals).*
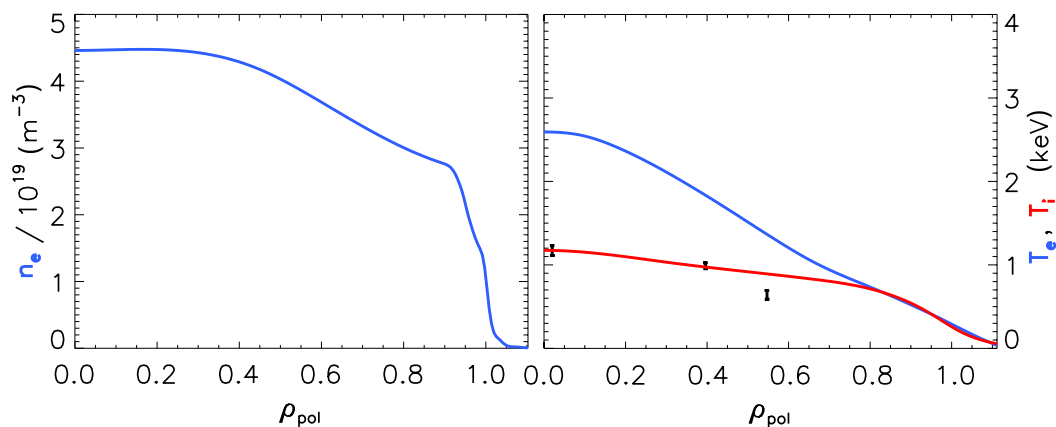

Figure 6.18: *Electron density (left), electron and ion temperature (right in blue and red respectively) profiles for discharge # 24648.*

the inversion radius at $\rho \sim 0.36$ while ~ 0.4 MW outside at $\rho \sim 0.8$. Apart from a slightly higher central electron density ($\overline{n}_e \sim 3.8 \cdot 10^{19}$ m^{-3} instead of $3 \cdot 10^{19}$), the main plasma parameters (shown in figure 6.17) are very similar to those observed with off-axis ECRH. The increased stability of this discharge is due to both the higher density and the decreased central electron heating. This guarantees a sufficient distance from the H-mode threshold, as reflected by the I_{div} traces in the bottom left plot in figure 6.17 which do not show the transient behaviour of the previous discharge. The argon puff rate is of the same value of discharge #24709, leading to an increase of the P_{rad} of a maximum of ~ 100 kW.

The electron and ion temperature profiles shown in figure 6.18 are very similar to those of the off-axis case. This is due to the fact that, despite the higher density, since two-thirds of the ECRH power are deposited more centrally than in #24916. The shape of the profiles are different, but the central and edge temperature values are the almost identical in the two cases. As for the electron density, the shape of the profile is also very similar to that of discharge #24916, exhibiting approximately the same peaking $H1/H5$ (top right plot in figure 6.17). Because of the absence of large portions of the ECE data in the range $0.26 < \rho < 0.49$, the electron temperature profiles from integrated data analysis could not be used. The T_e profile shown in figure 6.17 has been obtained through a spline fit while the n_e has been evaluated through IDA.

The unavailability of this large portion of the ECE data and the malfunctioning of more than one SXR pinhole camera are problematic also for the evaluation of the sawtooth inversion radius. With the use of SXR camera I only, it can be restricted to the range $0.4 < \rho_{inv} < 0.45$. As shown in the top left plot of figure 6.19 , the sawteeth can be considered of the saturated type, with period comparable to the other discharges. The SXR emissivity rises for a fraction of the sawtooth period ($\tau_{ST}/4$) and remains stable at the
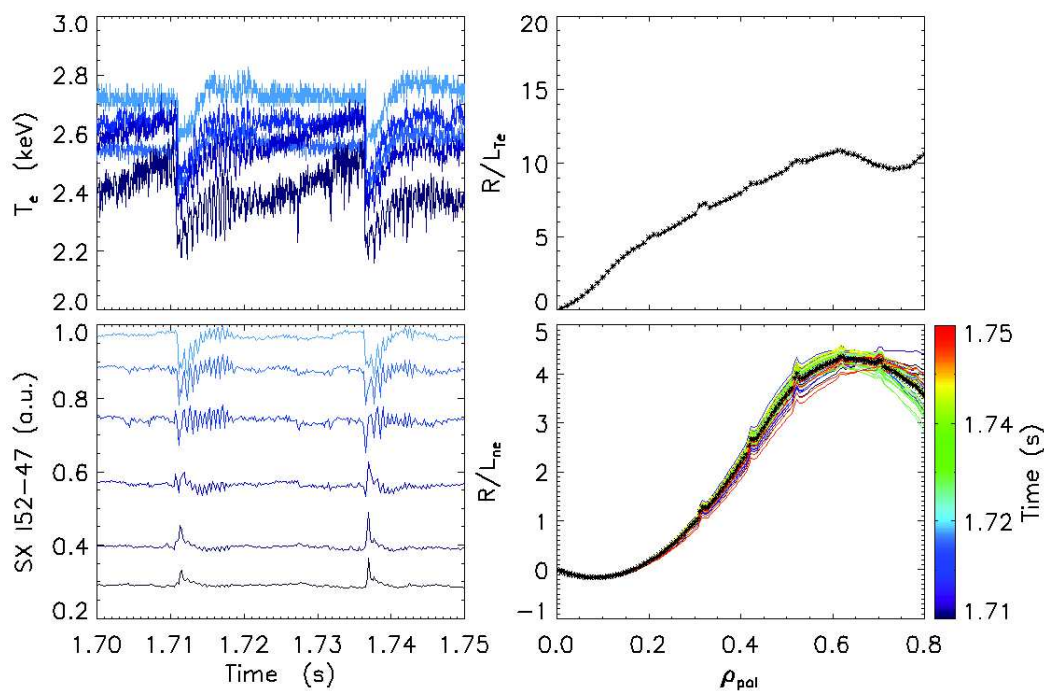

Figure 6.19: *Left: ECE (top) and SXR (bottom) evolution during sawtooth cycles of discharge # 24648. Right: normalized gradient lengths of T_e and n_e for the same time window..*

saturated value until the next crash occurs (bottom left plot). The electron temperature has approximately the same behaviour apart from a slight increase shortly before the sawtooth crash. Unluckily, because of the large gap in ECE data just around the most central ECRH deposition radius, a complete characterization of the T_e can not be done. Apart from the 1/1 sawtooth precursor, analysis on the magnetic and SXR signals have pointed out the existence of a 2/1 mode $\sim 6\ kHz$ located around $\rho \sim 0.5 \div 0.6$ [42, 43].

The plot on the top right of figure 6.19 shows the R/L_{Te} for the mean T_e of figure 6.18, while the full evolution of the density gradients from IDA is visible in the bottom right plot.

The results of the evaluation of the transport coefficients through the gradient-flux method are illustrated in figure 6.20. As for the previous case, the values given by the G-F (black dots) are quite close to those which minimize the χ^2 in the scanned range. Large differences are only observed in the region $\rho < 0.35$ and are probably due to a non complete sawtooth subtraction in the preparation of the SXR raw data. The region of major interest, around the deposition radius, is on the other hand well characterized. The neoclassical transport coefficients, calculated taking $1.5 \cdot 10^{-2}$ carbon, $5 \cdot 10^{-3}$ oxygen, $1 \cdot 10^{-4}$ tungsten and $4. \cdot 10^{-4}$ argon concentrations, are consistent with the experimental data within $\rho < 0.15$. Performing the same calculation with Ar as the only impurity, the neoclassical diffusion is found to be lower by a factor $\sim 3 \div 2$ up to mid-radius.

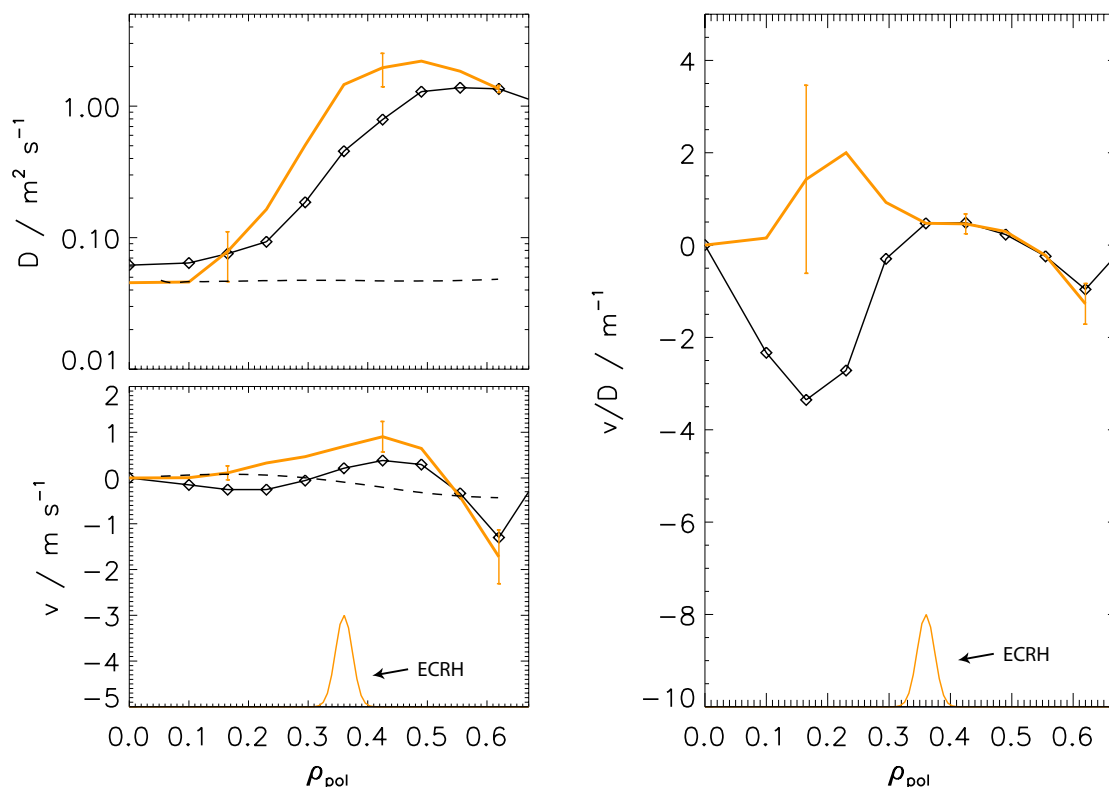Remembering the the most central ECRH deposition radius is located at $\rho \sim 0.36$, a

Figure 6.20: *Full profiles of the transport coefficients of discharge # 24648: black crosses are the original coefficients evaluated through the gradient-flux method, in red those delivering the minimum χ^2 and dashed line represents the neoclassical values. ECRH deposition position is also shown.*
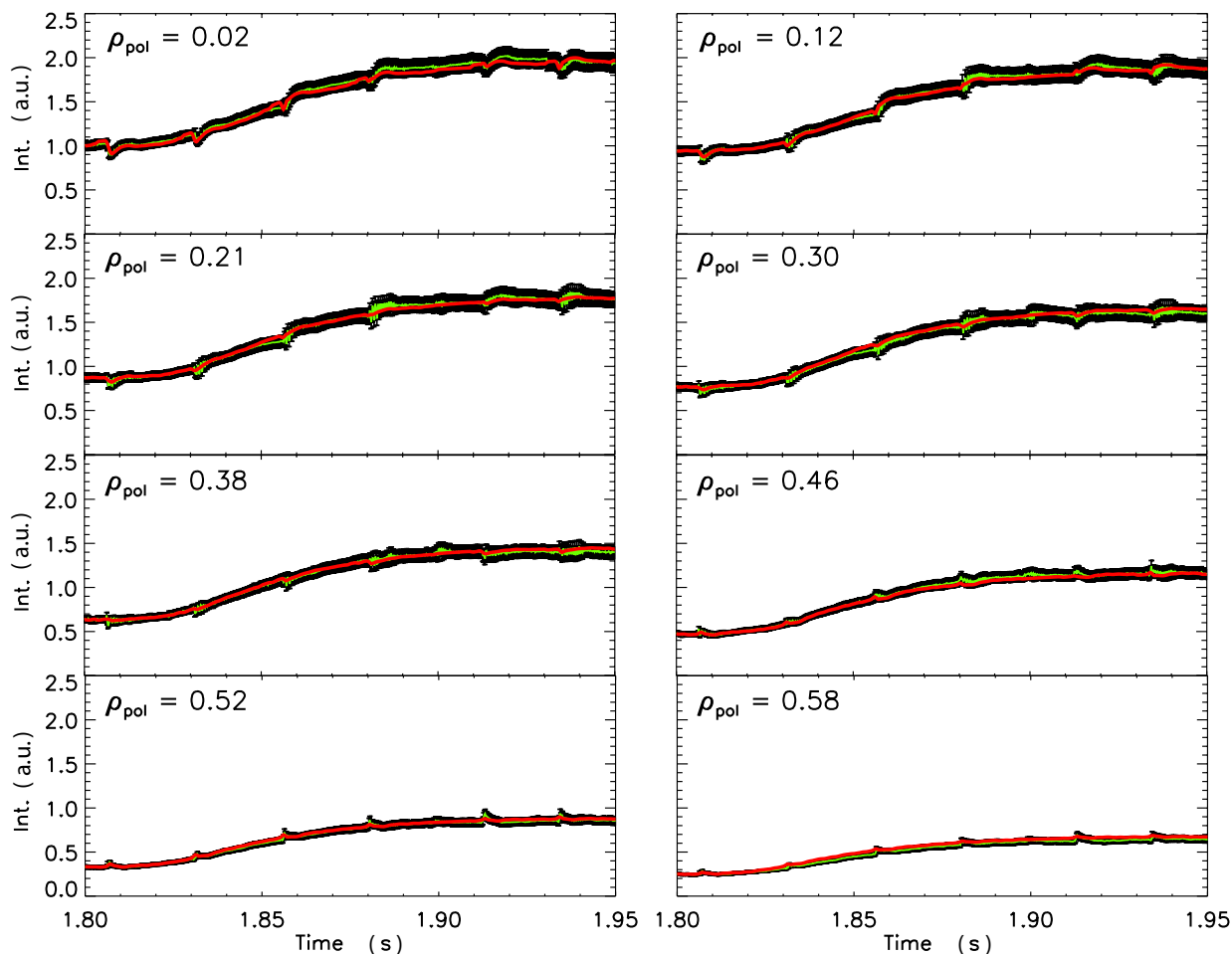
Figure 6.21: *Comparison of the experimental data (green with black error bars) with the simulated results from STRAHL for discharge #24648 with transport parameters in figure 6.20. The contribution from the background sawteeth cycles have been added to the simulated data so to better compare them.*

sharp increase in argon diffusion around the deposition radius is also observed in this case as for the on-axis heated discharge #24709. This transition in diffusivity is also coupled to a transition in the convection velocity from roughly zero (within $\rho < 0.25$) to positive with a maximum approximately at $\rho \sim 0.4$, while becoming negative again at $\rho \sim 0.5$. The good quality of these transport coefficients is demonstrated by the good agreement between the STRAHL simulation performed with these transport coefficients and the experimental data for different lines of sight of the I camera (figure 6.21). As for the previous examples, the previously subtracted background sawtooth cycles have been added to the simulated LOS integrated signals.

6.1.4   L-mode Summary

So to better compare the results presented in the previous subsections, the transport coefficients of all three discharges are shown in figure 6.22: the on-axis case #24709 is plotted in
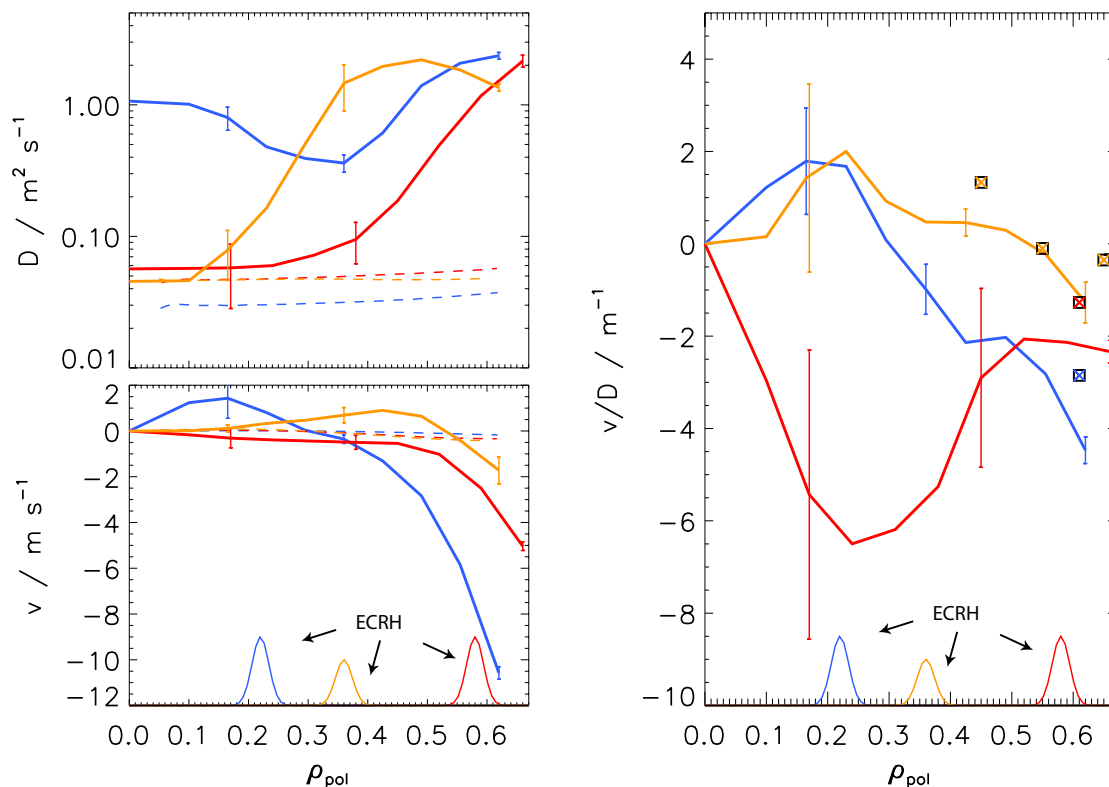
Figure 6.22: *Comparison of the argon transport coefficients for on-axis (discharge #24709, in blue) and off-axis (#24916, in red) and mixed scheme (#24648 in orange) ECRH deposition. Dashed lines are the neoclassical values evaluated through NEOART.*

blue, the off-axis case #24916 in red and #24648, discharge with the mixed heating scheme, in orange. Despite the difference in deposition radius ($\rho \sim 0.22$ and ~ 0.36 respectively) and in ECRH power deposited within the inversion radius (~ 1.1 *MW* and ~ 0.8 *MW*), both #24709 and #24648 (blue and orange) exhibit a strong increase in diffusion around the ECRH deposition radius . When the ECRH is deposited further outward ($\rho \sim 0.58$, red trace), no increase in diffusivity is observed. In the very centre ($\rho < 0.2$), the values for off-axis heating (red) and for mixed-heating scheme (orange) are consistent with the neoclassical calculations.

As far as the convection velocity is concerned, positive values are found for both cases with central ECRH within the inversion radius (blue and orange), while for off-axis ECRH, a decrease in inward convection is also observed around the deposition radius, but the values remain negative. From the data available, the ECRH would seem to be responsible for a positive convection independently of where the deposition is performed. The strong natural inward convection which is typically observed off-axis would then mask the effect of ECRH. This would on the other hand not happen in the very centre of the plasma where, since the impurity pinch is naturally lower in absolute value, a global outward convection can then be observed.

Results from GS2 turbulent simulations [47] are in partial agreement with the experimental findings. These have been performed at radii greater than the inversion radius ($\rho_{inv} \sim 0.4$, 0.3 and 0.42 for discharges #24709, #24916 and #24648 respectively) to guar-

antee the presence of nested flux surface geometry and steady main plasma parameters. Three radial locations have been considered ($\rho = 0.45$, 0.55 and 0.66) for discharge #24648 to better analyse the positive-to-negative trend of the experimental drift parameter, while because of the strong MHD activity of #24709, the calculations for this discharge and for #24916 have been performed only at $\rho = 0.61$. The results for all discharges are plotted as squares in the plot on the right hand side of figure 6.22.

As already stated in section 6.1.1, the two available points for the on- and off-axis heated discharges are slightly higher in absolute value, but reproduce the decrease of impurity peaking in this region when ECRH is deposited here. The three radial points evaluated for discharge #24648 reproduce the experimentally determined decreasing trend and invert approximately in the same region. As already stated, the non complete sawtooth subtraction performed for this discharge probably damps the outward convection within the inversion radius. If this were true, a further increase in v/D would be expected within the inversion radius, and would thus approach the simulation value.

From a theoretical point of view, it is predicted that turbulent contributions to the outward convection may come from both TEM or ITG turbulence, but through two different mechanisms. For TEMs, this can be caused by parallel velocity fluctuations which give rise to density fluctuations by parallel compression [11]. This parallel compression can only take place in regions of the plasma which exhibit low values of the safety factor q and low shear, and will therefore vanish when moving towards the edge of the plasma. For ITG type turbulence, outward convection contributions come from the thermodiffusive component which goes to zero with increasing mass of the impurity. For the experimental results presented here with a very flat ion temperature gradient, it is the parallel compression TEM turbulence which should gives rise to the outward convection in the very centre of the plasma. For the off-axis ECRH case, the conditions for $v > 0$ are not met neither in the TEM nor in the ITG case, confirmed by the fully negative v/D experimental profile. On the other hand, a decrease of impurity pinch is also observed for the purely off-axis heated discharge. There could therefore be other processes, independent from the two shortly explained above, which would lead to a damping in pinch around the ECRH deposition radius.

Discussion on the Method

The Gradient-Flux method applied as explained in chapters 5 and 6 has proved to provide reliable results. When varying these transport coefficients in the search for a best fit on the raw SXR line of sight integrals, the final profiles minimizing the χ^2 are completely consistent with the results obtained through the G-F method only in the case of the off-axis ECR heated discharge (#24916). A slight difference is visible only at the edge of the visibility range ($\rho > 0.6$) where the G-F method slightly overestimates the convection velocity. This could be due to the change in SXR sensitivity function at the lower end of the visibility range of this diagnostic, as already discussed in sections B.7 and 5.3.2. Since the transport coefficients evaluated through the G-F method are roughly independent of the sawtooth induced transport, this result also confirms that the simple sawtooth crash model (briefly explained in section 5.1.1) is good enough to explain standard sawteeth.

Discharge #24709 exhibits complex sawtooth cycles and main plasma parameter evolution during the time range of interest. The main problem in analysing this case is the evolution in background plasma and magnetic topology which determines a variation in turbulence and MHD driven transport during the full time range of interest. Since the χ^2 minimization routine does not take this into account, it adapts the transport coefficients so to (erroneously) compensate for this variation and fit initial increase in emissivity after the sawtooth crash (figure 6.10). Since the G-F method delivers reliable (roughly) sawtooth-independent transport coefficients, it may well be that the G-F transport coefficients represent the mean inter-sawtooth transport better than those minimizing the χ^2.

Discharge #24648 is instead characterized by "saturated" sawteeth which, as explained in [44], exhibit a crash amplitude which is less pronounced than that of standard sawteeth. For radii greater than the inversion radius ($\rho_{inv} \sim 0.42$), the G-F method delivers transport coefficients which are consistent with those from the χ^2-minimization within its error bars. Similarly to the case of discharge #24709, the simple tool available in STRAHL for the simulation of the sawtooth crash may not characterize the "saturated" type completely as it does with the "standard" sawteeth.

For these reasons, it is not at the moment possible to completely define which transport coefficients (G-F or χ^2-minimization) better describe the experimental findings. It is therefore very important to discuss the transport coefficients evaluated through the G-F
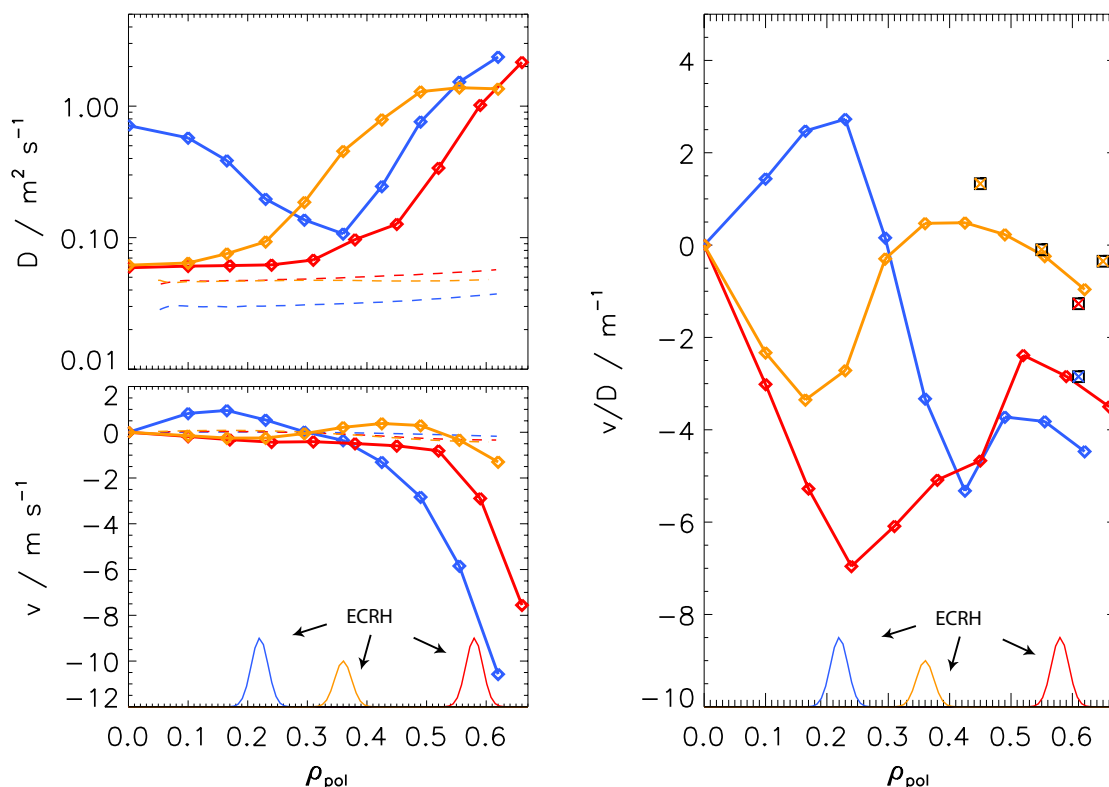

Figure 6.23: *Comparison of the argon transport coefficients evaluated through the G-F method for on-axis (discharge #24709, in blue), off-axis (#24916, in red) and mixed scheme (#24648 in orange) ECRH deposition. Dashed lines are the neoclassical values evaluated through NEOART, boxes are the GS2 calculations.*

method and compare them with the GS2 calculations.

As can be seen in figure 6.23, the main characteristics of the transport coefficients of the different discharges are very similar to those minimizing the χ^2. Also the approximate neoclassical behaviour in the centre of the plasma for off-axis and mixed heating discharges (red and orange) is well reproduced. The characteristics of the convection velocities change slightly in the very centre of the plasma for discharge #24648, easily visible in the drift parameter plot on the right of figure 6.23. Differently from the χ^2-minimization profiles (shown in figure 6.22), the v/D profile of #24648 (orange) is negative and approximately equal to that of #24916 (red). The negative-positive transition is slightly within the ECRH deposition radius and the further decreasing trend for $\rho > 0.45$ is confirmed by the GS2 calculations.

An interesting feature which is visible here, but was not as clear in the χ^2-minimization coefficients, is an almost constant decrease in drift parameter around the ECRH deposition radius for any deposition radius. The v/D values for on-axis heating reach a maximum of < 3 (at $\rho \sim 0.2$), for mixed heating (only 2/3 of the previous ECRH power deposited within the inversion radius) < 1 (at $\rho \sim 0.4$) while for pure off-axis heating $v/D < -2$ (at $\rho \sim 0.6$). The hypothesis of an almost constant damping of the drift parameter around the ECRH deposition radius imposed to a common negative background v/D would then seem more realistic.

6.2   Nitrogen seeded H-modes

Since ASDEX Upgrade has been equipped with a full tungsten coated first wall, the absence of the beneficial intrinsic edge carbon radiation has led to intolerable power loads on the divertor tiles at heating power above 7.5 MW. Especially in case of medium-high power H-mode discharges performed during boronized operation, this can led to the destruction of the divertor tungsten coatings due to too high local power fluxes. The access to such regimes has therefore required the substitution of the carbon radiation fraction by that of a seed impurity. In order to avoid excessive core radiation, the choice has fallen on nitrogen which, exhibiting a radiation peak at lower electron temperatures with respect to Ne and Ar, radiates predominantly in the Scrape Off Layer (SOL) and in the divertor [48].

The use of nitrogen as a seed impurity has led not only to a reduction in the divertor power load, but also to a global improvement in energy confinement and to a decrease in ELM size [48]. It is of major interest to understand how this is reflected in the impurity transport and confinement inside the plasma and what effects the seeding has on the transport of other, heavier impurities. To this purpose, a set of medium heating H-
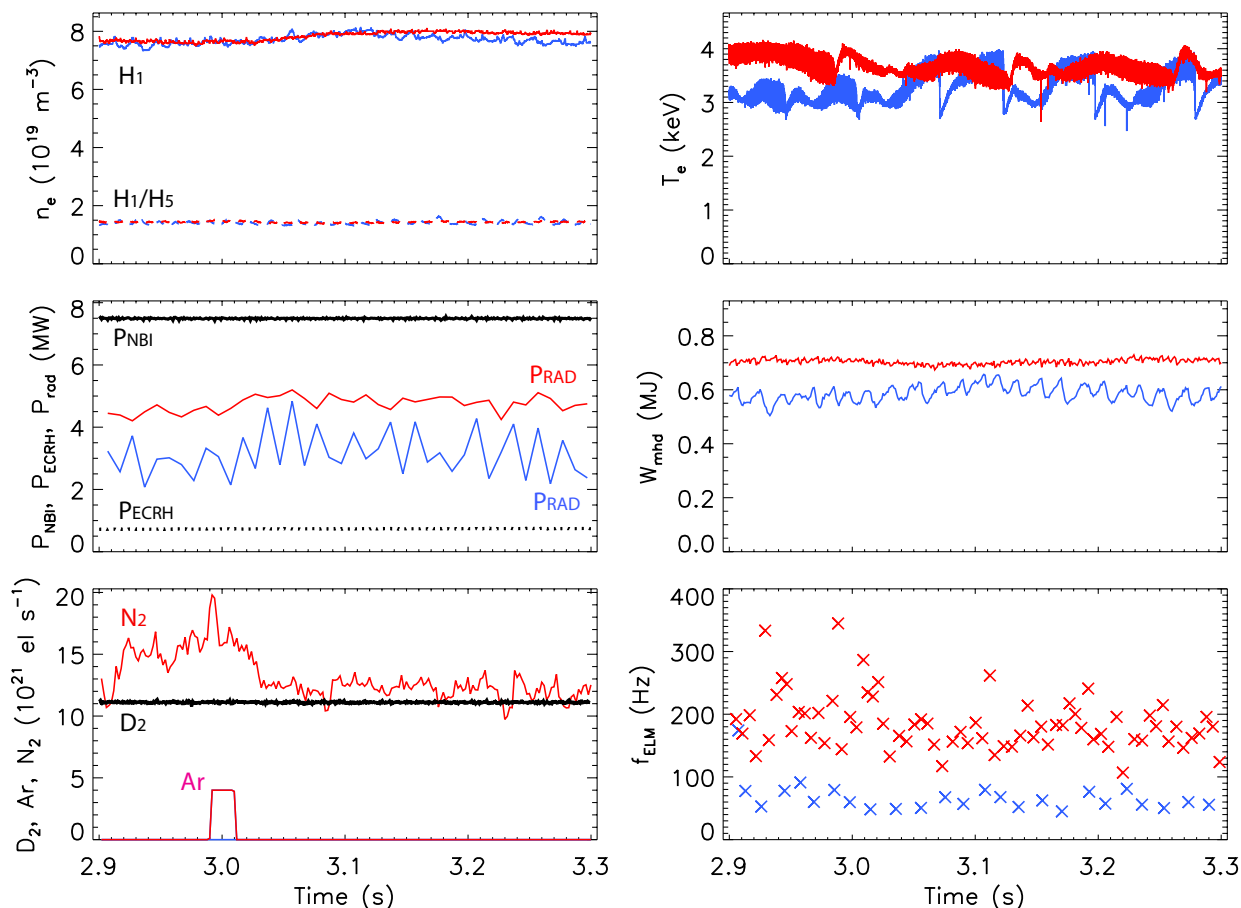

Figure 6.24: *Main plasma parameters of discharges #25446 (blue) and #25447 (red). From top left clockwise: central $\overline{n}_e$ (H1) and density peaking factor $H1/H5$ (dashed lines); central T_e; plasma energy W_{mhd}; ELM frequency; gas fuelling (D_2 and Ar rates are equal for both discharges, N_2 is solely for #25447); NBI and ECRH heating power (black full and dashed lines) and total radiated power from bolometry.*

mode discharges with nitrogen seeding have been performed and argon was puffed during their flat-top to evaluate the transport coefficients. The impurity transport analysis has been performed for one of these discharges (#25447). The non-seeded reference discharge (#25446) is also qualitatively analysed.

The main parameters of both discharges are shown in figure 6.24, the reference #25446 in blue, the seeded discharge #25447 in red. Both discharges have been performed at $1\ MA$ plasma current, approximately identical central electron density $\overline{n}_e \sim 7.7 \cdot 10^{19}\ m^{-3}$ and density peaking (top left plot, thick and dashed lines respectively), heating power ($P_{NBI} \sim 7.5$ and $P_{ECRH} \sim 0.8$), toroidal magnetic field ($B_t \sim 2.44\ T$), safety factor at the edge $q_{95} \sim 4.58$ and deuterium puffing rate $\sim 12 \cdot 10^{21}\ el./s$ (bottom left plot in black). The Ar puff for the transport analysis was performed at ~ 3 seconds at $4 \cdot 10^{21}\ el./s$ rate for a duration of $\sim 20\ ms$ (in magenta in the bottom left plot). The feedback control on the divertor thermo-current measurements for discharge #25447 has been performed setting $T_{div} = 8$ (refer to [48] for a detailed explanation of the feedback scheme). The $q = 1$ surface is located at $\rho \sim 0.35 \div 0.4$ for the seeded discharge, $\rho \sim 0.3 \div 0.35$ for the non-seeded reference case (evaluated through ECE and SXR data), main mode activity characterized by the $m/n = 1/1$ mode in both cases [42].

Despite the same heating power, the central electron temperature of the seeded discharge (top right in red) is approximately 1 keV higher than that of reference (blue). Only shortly after the argon puff ($t > 3\ s$) and for short periods when strong sawtooth activity builds up, the central T_e of discharge #25446 approaches that of #25447. The total radiated power (central left plot) is approximately 60% higher in the seeded discharge and the plasma energy (W_{mhd} centre right) increases of $\sim 15\%$. The bottom right plot shows the ELM frequency for both discharges: the seeded discharges (red) exhibits a mean frequency $\overline{f}_{ELM} \sim 190$, more than double that of the non-seeded discharge $\overline{f}_{ELM} \sim 70$.

The electron temperature, ion temperature and electron density profiles in the time range of figure 6.24 are shown in figure 6.25. The electron temperature and density profiles have been evaluated as mean values of the IDA fits, the error bars representing the standard deviation. The ion temperature profile (central plot) has instead been evaluated as a modified TANH function fit of the data from the

Figure 6.25: *Time averaged electron temperature, ion temperature and electron density profiles for discharges #25446 (blue) and #25447 (red). Dashed black lines represent the ratios between the profiles.*

charge exchange and CSXR diagnostics. Since no data was available for $\rho > 0.8$, the error bars (fit errors) are shown only within this radius. While the electron density profiles re-
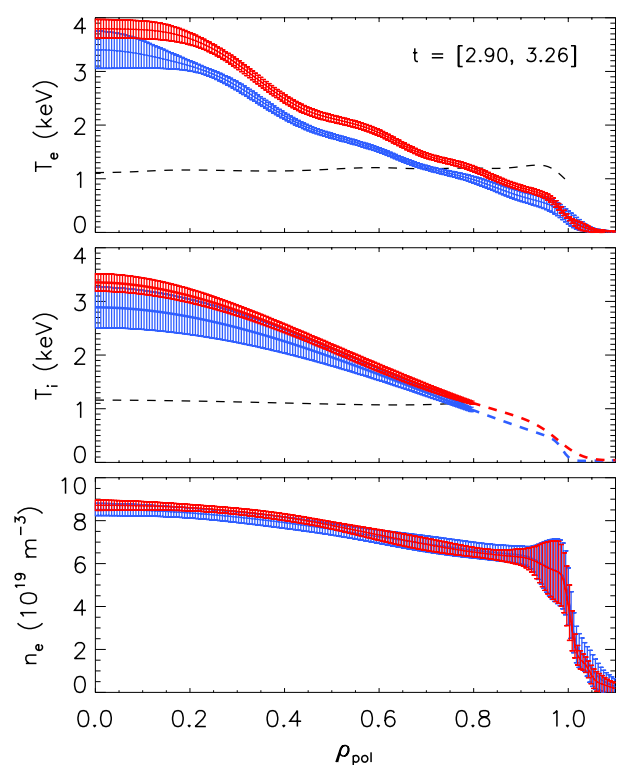
main approximately unchanged with or without the nitrogen seeding, the ion and electron temperature profiles exhibit a $\sim 15 \div 20\%$ enhancement. As exemplified by the temperature ratios of the two discharges (dashed lines in the two top plots in figure 6.25), this enhancement is approximately constant throughout the full plasma cross-section.

The global confinement can be also characterized by the so-called H-factor, ratio between the experimental confinement time τ_E and a scaling confinement time calculated from a large set of H-mode discharges from independent devices (named ITER $98P(y, th, 2)$):

$$H_{98} = \frac{\tau_E^{exp}}{\tau_E^{scal}} \tag{6.3}$$

When evaluating it for both discharges, an increase from ~ 0.8 to ~ 1 is observed when the nitrogen seeding is performed. Since all the parameters in the scaling remain constant, this is undoubtfully and increase in confinement.

6.2.1 General discharge behaviour

Before discussing the results for the argon transport in the seeded discharge, a first qualitative characterization of both discharges can be performed when having a closer look at the time evolution of the SXR, ECE and magnetic signals. The top plot in figure 6.26 shows the evolution of five central SXR signals of camera H (with minimum ρ greater than the minimum visible radius of the ECE diagnostic so to better compare their evolution) for discharge #25447. The tangential radii of the lines of sight are labelled on the right of the plot. The ECE electron temperature measurement evolution at approximately the same radii (also labelled) are plotted in the second graph. The third plot shows the total magnetic perturbations of MHD modes with odd toroidal numbers ($n = 1, 3, ..$) evaluated as the difference between two magnetic coils 180° apart toroidally but at the same poloidal position while the last plot is the complete magnetic spectrogram from one magnetic coil. As can be seen in the last plot, the major MHD activity is the 1/1 mode at $10 \div 15$ kHz [42].

The full rise of the SXR signals after the argon puff at ~ 3.0 seconds is easily visible in-between the first two sawtooth crashes (at ~ 2.985 s and ~ 3.13 s). Concentrating on the second sawtooth crash at the centre of the time range in-between the red and black vertical lines, a few important qualitative characteristics of this discharge can be gathered. First of all, the crash footprint in the SXR channels is inverted with respect to what was previously defined as "standard": at the crash, the most central SXR channels (top two traces in the top plot in figure 6.26) exhibit an increase in emissivity while a decrease is visible for radii $\rho \geq 0.31$ (bottom two traces). Moreover, in the time range $3.08 < t < 3.12$ s (centred on the red vertical line in the plots) the SXR emissivity levels of the three most central channels are approximately equal. This effect is also visible in the next sawtooth cycle ($3.12 < t < 3.26$ s) where, after a first stationary phase, the emissivity of the most central lines of sight approach a common value. For stable electron temperature and density profiles, in case of a flat or slightly peaked electron density profile, this could be possible only for hollow impurity density profiles.

These changes in the SXR emissivity are correlated with the changes in the central electron temperature (second plot from the top). The most central ECE channels (around the ECRH deposition radius $\rho \sim 0.2$) exhibit a fast ~ 10 ms rise just after the sawtooth crash and then decay slightly for almost half of the considered sawtooth period (until $t \sim 3.075$ s). At this time, the 1/1 mode starts growing (visible in both bottom plots). For
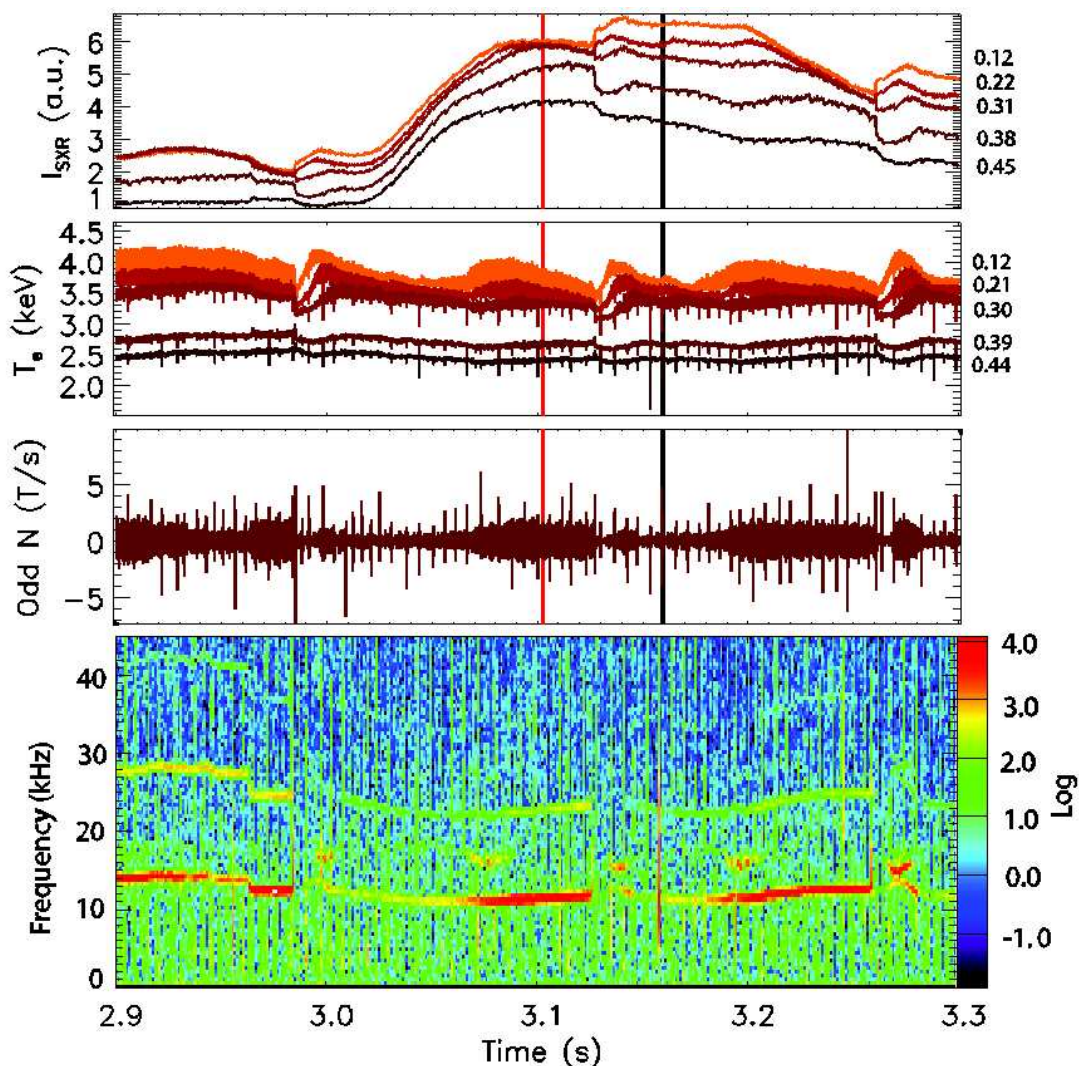
Figure 6.26: *Discharge #25447: evolution of the central SXR signals (top), the ECE T_e measurements (centre): the minimum visible ρ of the SXR lines of sight and the ρ of emission of the ECE channel are labelled on the left side of the two plots. Last two plots show the total MHD activity with odd toroidal mode numbers and the full magnetic spectrum in the same time range. The argon puff was performed at ~ 3 s.*

the remaining ~ 60 ms before the next sawtooth crash, the ECE shows strongly oscillating and slightly increasing central T_e. Both the SXR and the ECE evolution are in phase with the evolution of the 1/1 mode.

An even clearer idea of what is happening can be obtained when looking at the electron density and temperature profiles as well as the SXR LOS-integrated emission profiles shown in figure 6.27. The available profiles in a 5 ms window centred on the vertical lines in figure 6.26 have been overplotted to provide an idea of the stability of the profiles. For SXR camera H (bottom), negative values of ρ corresponds to lines of sight passing below the plasma axis. Since the electron temperature and density fits are obtained through Integrated Data Analysis and assume flux-averaged quantities, the profile on the negative side of ρ is simply a mirrored replica of the one on the positive side. The same can be said for the ECE measurements, since for this discharge they are all located on the LFS. The

asymmetry visible in the SXR profiles is partially due to geometric effects of LOS lengths and in part to LFS-HFS asymmetries in the emitting background tungsten. As can be seen in the bottom plot, the SXR emissivity characteristics change drastically before (red) and after (black) the sawtooth crash, passing from approximately flat to slightly hollow. Because of the relatively flat n_e profile and temporally constant T_e profiles, the hollowness of the pre-crash SXR LOS-integrated emissivity profile can be caused solely by a hollow impurity density profile, confirming the previous hypothesis.

It seems therefore clear that the sawtooth period is characterized by at least two distinct phases in which a change in impurity transport is observed:

1- shortly after the sawtooth crash, during the phase of low 1/1 MHD activity (time range $2.985 < t < 3.075$), characterized by an approximately flat SXR LOS-integrated emissivity profile;

2- in coincidence with the rise of the 1/1 mode ($t > 3.075$) and for the remaining time range until the sawtooth crash, for approximately constant electron temperature and density profiles a hollow SXR profile is formed from the previously flat profile

At the sawtooth crash, the hollow impurity density profiles collapses and the impurities fill up the central region again.
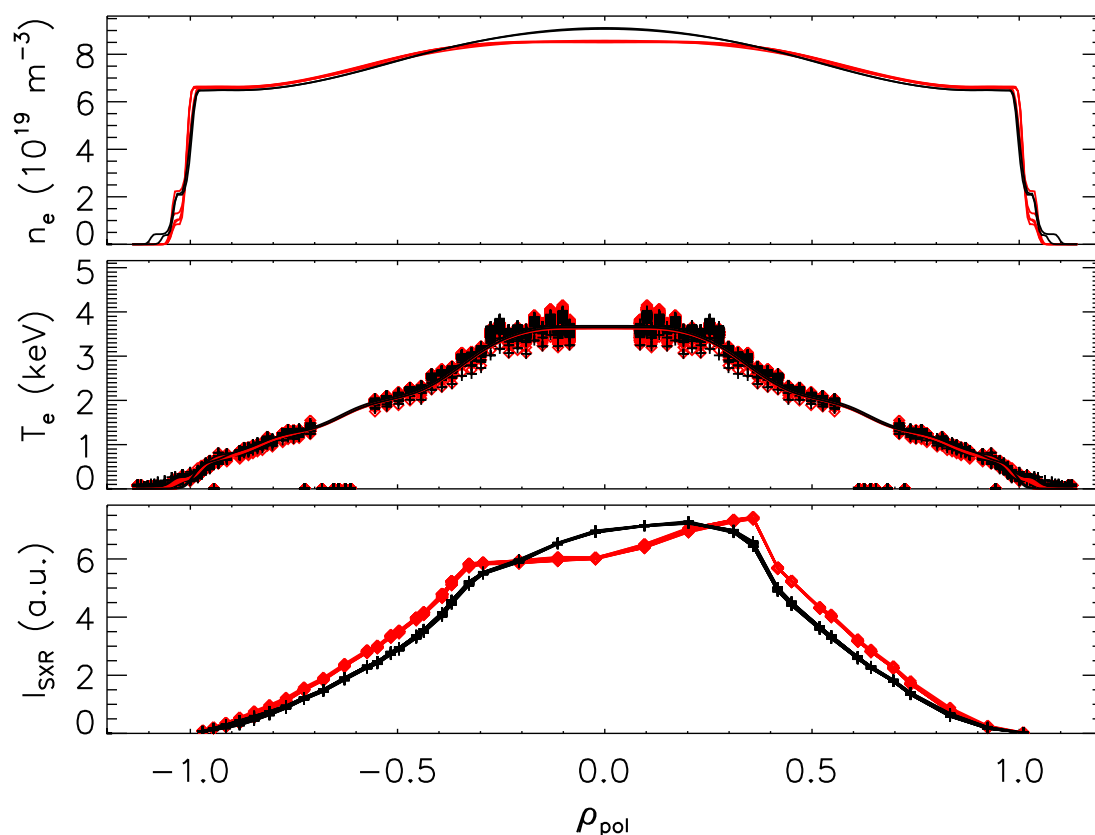

Figure 6.27: *Discharge #25447 electron density IDA fits (top), electron temperature IDA fits and ECE data (central plot, lines and crosses respectively), SXR LOS integrated emissivity profiles (bottom) for the two time points indicated by the vertical lines of identical colours in figure 6.26.*

The characteristics of these phases are completely independent of the puffed Ar. Proof of this is given in figures 6.28 and 6.29 which show the same parameters of the previous figures but for a time interval $\sim 800\ ms$ after the Ar puff, when the argon contribution is negligible. As for the previous case, the electron temperature and density profiles are approximately constant shortly before and after the sawtooth crash. The time evolution of central electron temperature (central plot in figure 6.28) is very similar to that encountered in the previous time interval and so is the MHD activity. Likewise, the three most central lines of sight of the SXR diagnostic approach a common value during the last fractions of the sawtooth cycle and the crash is also inverted. Consequently, the profile of the SXR LOS-integrated emissivity (bottom plot in figure 6.29) is slightly hollow just before the sawtooth crash. It is important to remind that, since these profiles are not Abel-inverted, a slight hollowness in the LOS-integrated profile will translate in a much stronger one in the local emissivity profile and a flat line integrated profile will lead to a slightly hollow local one. Moreover, since the electron density profiles are approximately stable, in order to maintain quasineutrality the outward convection must act mainly on the medium-high Z (or A) impurities which participate in the SXR emissivity. If the outward convection would influence all ions independently of the ionization stage or mass, then a hollow ion density profile would lead to a hollow electron density profile as well.

As a reference, the same plots are given for the non-seeded discharge #25446 in figures 6.30 and 6.31. The Ar transport parameters for this discharge cannot be evaluated because the Ar puff does not behave as a trace. This can be easily noticed in the electron temperature time evolution (central plot in figure 6.30), where the sawtooth cycles change completely characteristics when the argon is puffed (as for the previous discharge, at $\sim 3\ s$). While exhibiting a shape similar to that of discharge #25447 for $t < 3\ s$, for later time points the most central ECE channels peak strongly when the 1/1 mode starts to grow. This can be seen even more clearly in the central plot in figure 6.31 where the T_e profile before the crash (red) is much more peaked than that after the sawtooth crash (black). Although the argon concentration is approximately equal to that of discharge #25447 (maximum $\sim 3.0 \cdot 10^{-4}$), this behaviour may be related to the Ar itself, considering that it slowly vanishes with decreasing argon concentration. Since, as for the seeded case, the electron density is approximately constant in time, the electron temperature increase in the centre implies an increase in confinement in this most central region. The SXR LOS-integrated profiles instead do not exhibit any hollowness. The sawtooth crash direction (visible in both the top plot in figure 6.30 and in bottom plot in figure 6.31) is "standard", flattening after the crash has occurred.
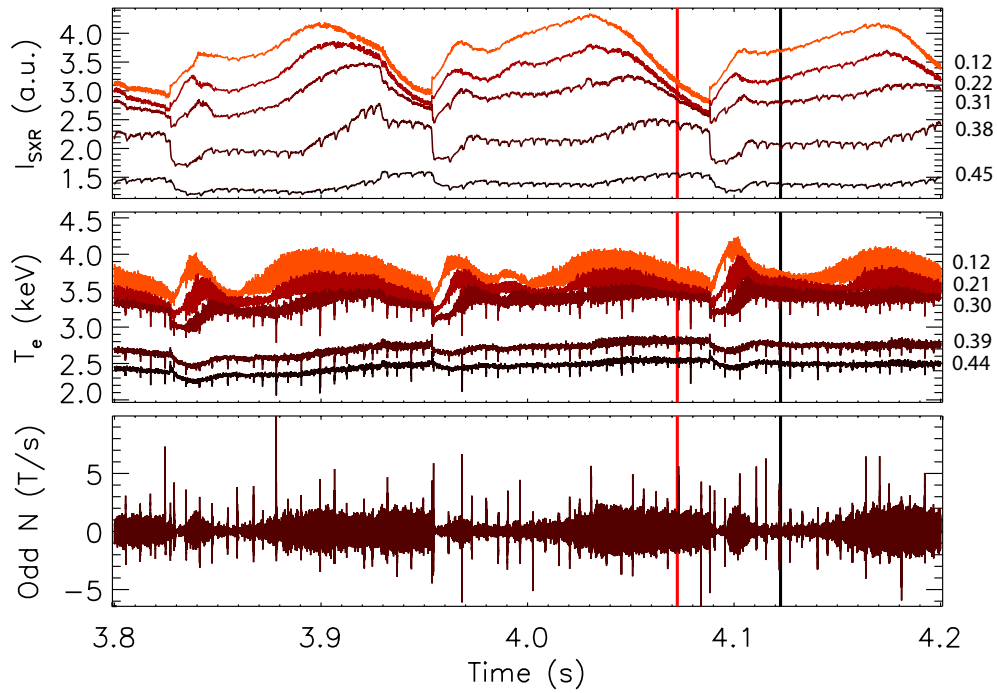
Figure 6.28: *Discharge #25447 evolution of the central SXR signals (top), ECE T_e measurements (centre), total MHD activity with odd toroidal mode numbers (bottom) $\sim$ 800 ms after the argon puff.*
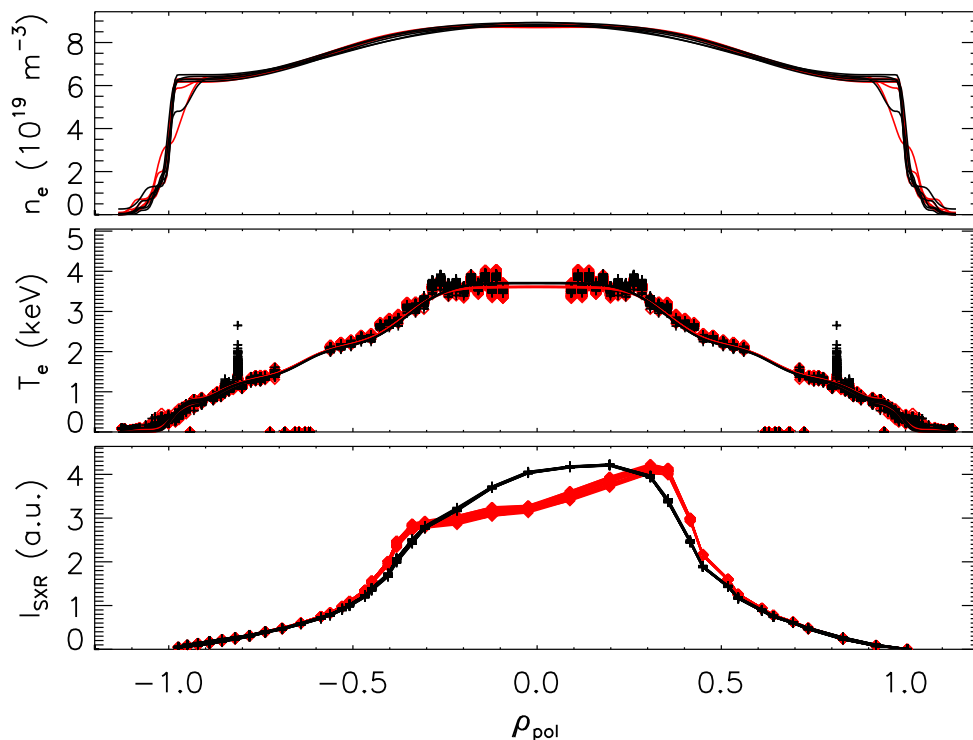

Figure 6.29: *Discharge #25447 electron density IDA fits (top), electron temperature IDA fits and ECE data (central plot, lines and crosses respectively), SXR LOS integrated emissivity profiles (bottom) for the two time points indicated by the vertical lines of identical colours in figure 6.28.*

Figure 6.30: *Discharge #25446 evolution of the central SXR signals (top), ECE T_e measurements (centre), total MHD activity with odd toroidal mode numbers (bottom). The argon puff was performed at ~ 3 s.*

Figure 6.31: *Discharge #25446 electron density IDA fits (top), electron temperature IDA fits and ECE data (central plot, lines and crosses respectively), SXR LOS integrated emissivity profiles (bottom) for the two time points indicated by the vertical lines of identical colours in figure 6.30.*
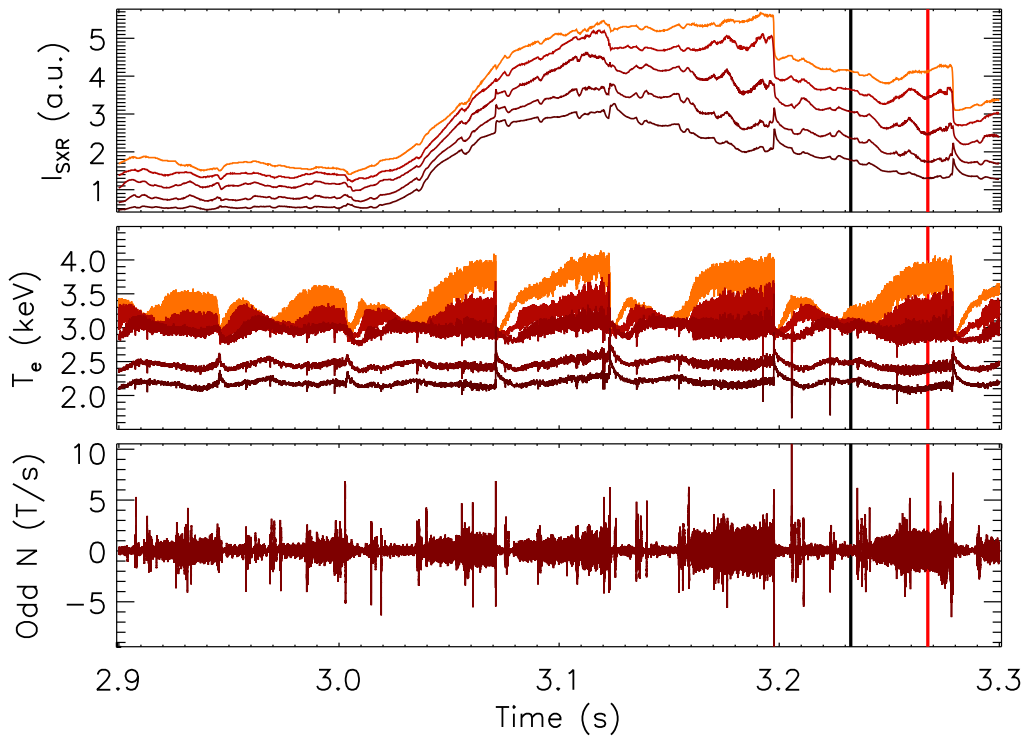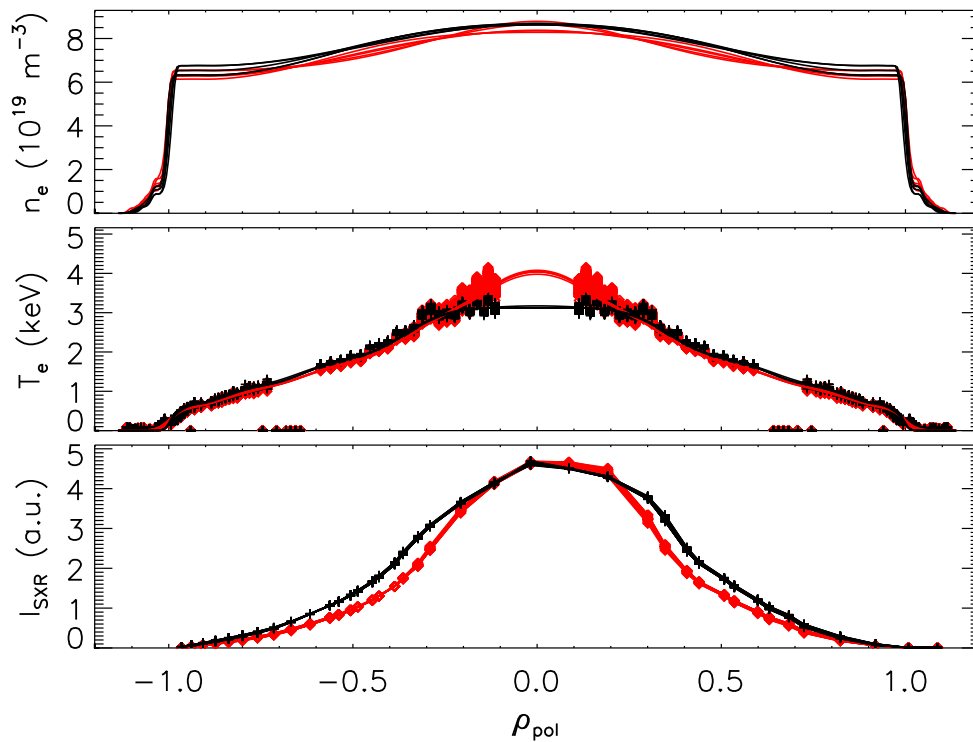
6.2.2 Evaluation of the transport coefficients

As a consequence of this first qualitative analysis, the rise in SXR emissivity after the sawtooth crash in discharge #25447 cannot be modelled with only one set of transport coefficients (as will be shown in the next paragraphs). In order to keep the analysis as simple as possible, it has been chosen to use two sets: the first one for the phase of low 1/1 mode activity (shortly after the sawtooth crash, $3.015 < t < 3.075$ s); the second one for the remaining time interval up to the next crash ($3.075 < t < 3.11$ s). The same method used for the L-modes has been applied here to the first time window. The resulting transport coefficients are plotted in figure 6.32: the squares are the original values evaluated through the G-F method while thick lines represent those minimizing the χ^2.

As for the analysis in the previous sections, the error bars on the profiles which minimize the χ^2 have been evaluated from the variation in χ^2 through formula 6.2 so do not give precise error estimates on the transport coefficients. The neoclassical diffusion and convection coefficients (dashed lines) have been evaluated taking $5 \cdot 10^{-3}$ carbon, $5 \cdot 10^{-3}$ oxygen, $3 \cdot 10^{-5}$ tungsten, $1.5 \cdot 10^{-2}$ nitrogen and $3.5 \cdot 10^{-4}$ argon concentrations. The nitrogen concentration has been deduced from a similar discharge (same heating, electron density and D_2 gas puff rate) while tungsten and argon concentrations have been evaluated through the spectroscopic measurements described in the previous sections.

The large difference between the values evaluated through the G-F method and those minimizing the χ^2 is probably due to two factors connected with the the short time range analysed (60 ms). First of all only a very small amount of Ar has probably reached the centre in this phase (as will be seen shortly); second, the short time range leads to a low data statistics which enhances the errors on the G-F linear fit. This is indicated by the size

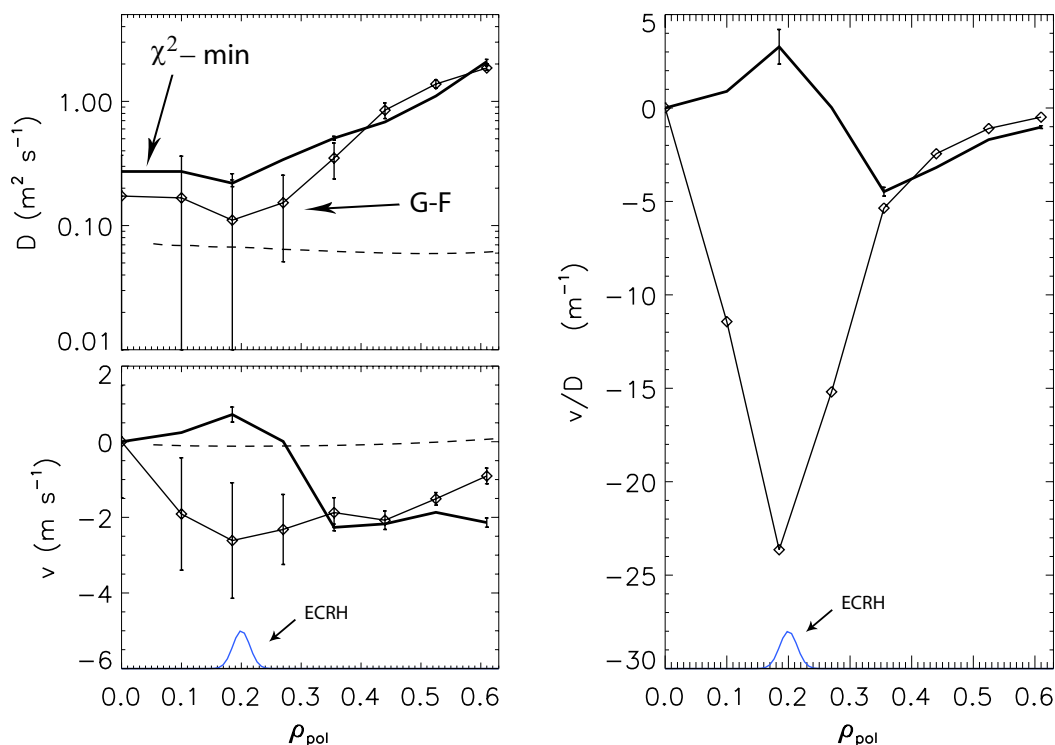Figure 6.32: *Transport parameters for the first phase ($t < 3.075$ s) of discharge #25447.*
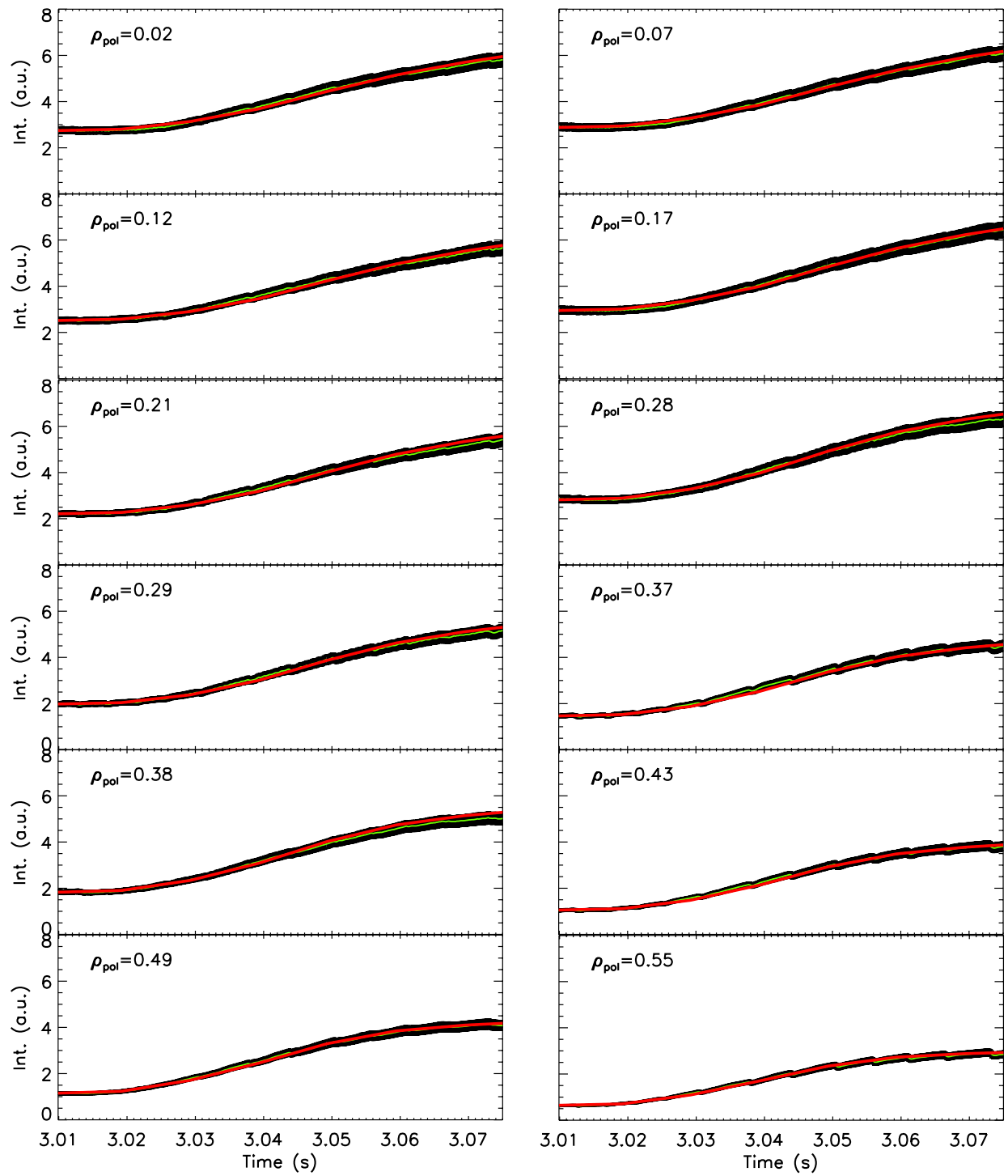
Figure 6.33: *Comparison of the experimental data with the simulated results from STRAHL for discharge #25447 with the best-fit transport parameters in figure 6.32.*
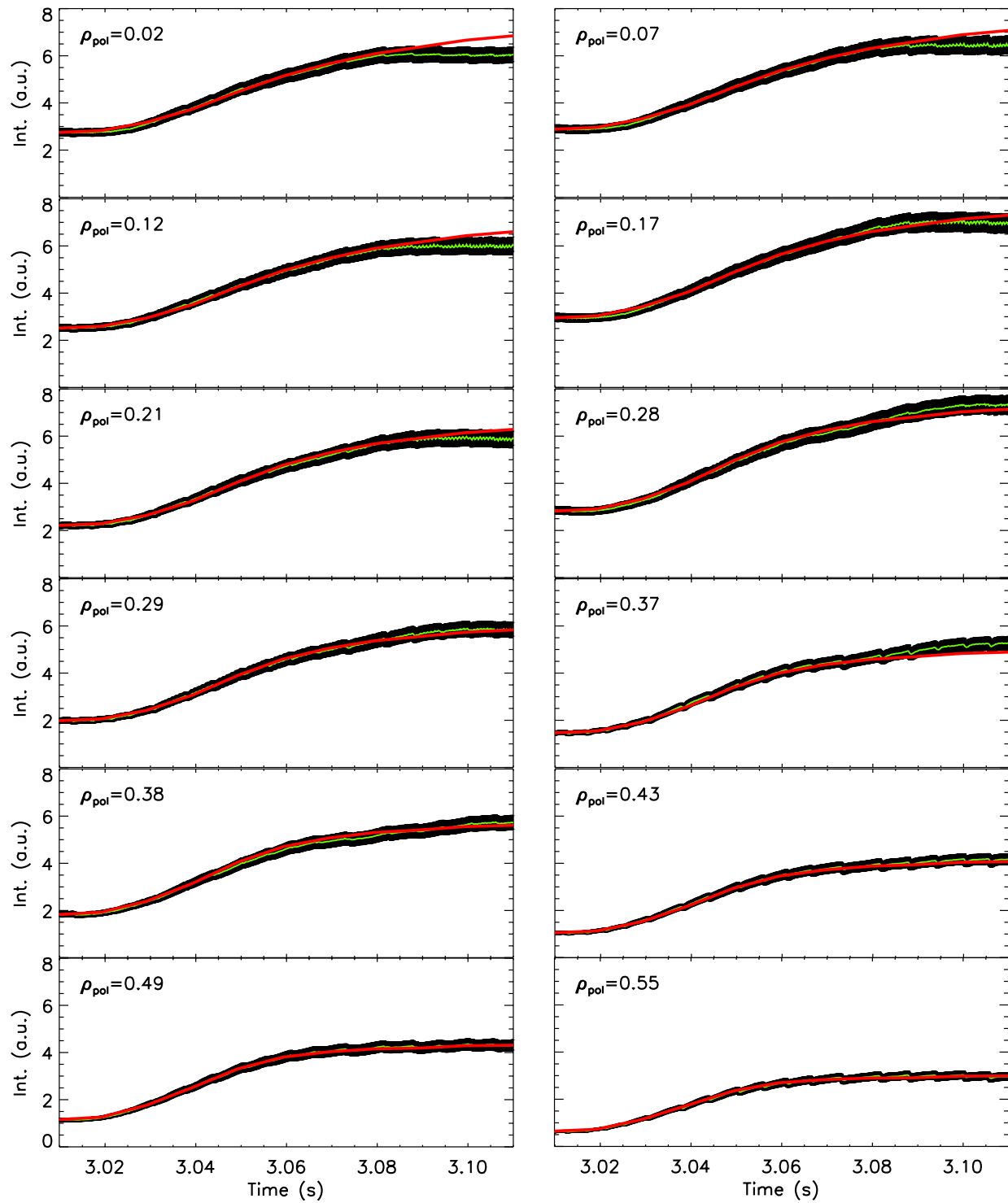
Figure 6.34: *Comparison of the experimental data with the simulated results from STRAHL for discharge #25447 for the full time range of interest with the transport parameters in figure 6.32.*

of the error bars of the G-F transport parameters, evaluated from the errors of the linear fit of the normalized flux versus the normalized density gradient. As expected, the consistency of the two methods is thus limited to regions where the statistics is high enough ($\rho > 0.3$). For this reason the transport coefficients used from now on are those minimizing the χ^2 which, in this case, provide a more previse and complete characterization of the dynamics involved.

Although this discharge is very different from the L-modes analysed in the previous sections, a positive convection region is also found here around the ECRH deposition radius for the transport coefficients minimizing the χ^2. Differently from the L-modes, the central diffusivity does not exhibit a local increase around ρ_{ECRH}, although the minimum D is anyway not neoclassical, but about a factor ~ 3 higher. An enhancement in diffusivity is therefore still observed, although not as local as for the L-modes.

When comparing the STRAHL simulation with these transport coefficients with the experimental LOS-integrated SXR emissivities (figure 6.33) the agreement is very good for the full time range of interest and for all lines of sight of the H camera. If the same transport coefficients are instead used to simulate up to $t = 3.11$ s (figure 6.34), the lines of sight with $\rho_{min} < 0.21$ exhibit a much stronger peaking than found experimentally, while those with $0.21 < \rho_{min} < 0.37$ are slightly less peaked than the experimental values. This confirms the hypothesis of (at least) one change in transport within this time range. Since the lines of sight with $\rho_{min} > 0.4$ are well characterized up to $t = 3.11$ s, it may be expected that the change in transport occurs only within this radius.

The transport parameters for the second part of the time range ($3.075 < t < 3.11$ s)
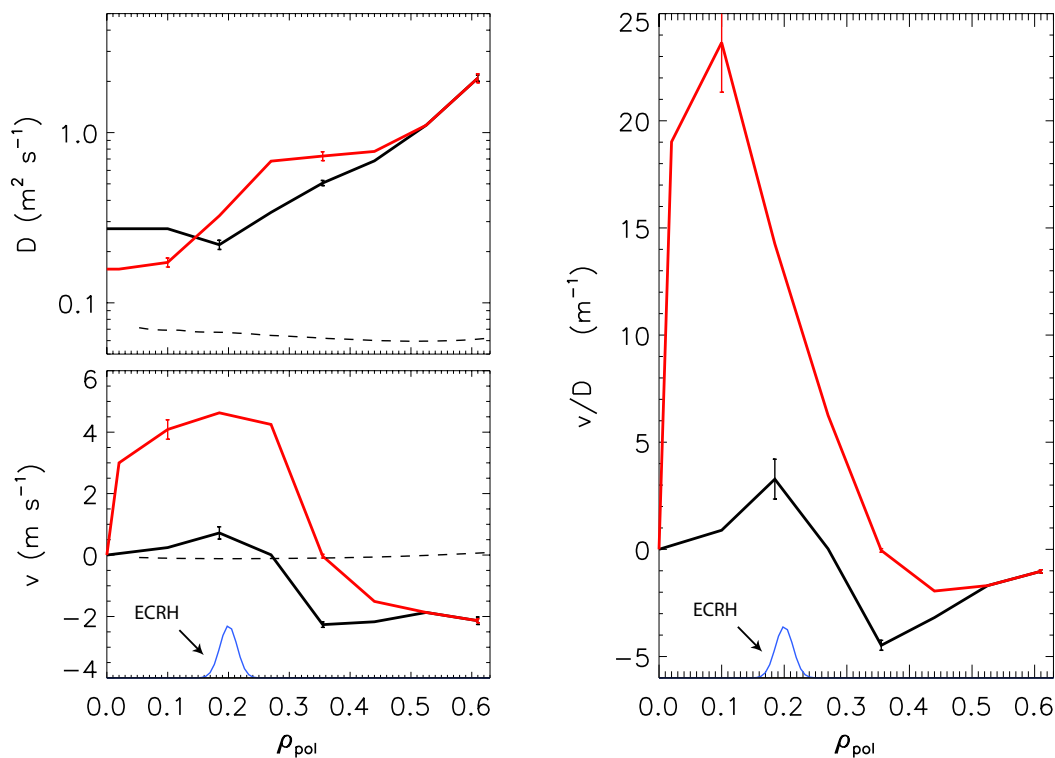
Figure 6.35: *Transport parameters for the first ($t < 3.075$ s in black) and second ($3.075 < t < 3.11$ s in red) inter-sawtooth phase of discharge #25447.*

Figure 6.36: *Comparison of the experimental data with the simulated results from STRAHL for discharge #25447 with the black transport parameters in figure 6.35 up to 3.07 seconds and with the red transport parameters in figure for the remaining time range.*

have been evaluated using the first set up to $t = 3.075\ s$ and searching for a second set to minimize the χ^2 for the remaining time range. The first set of coefficients has been used as starting point 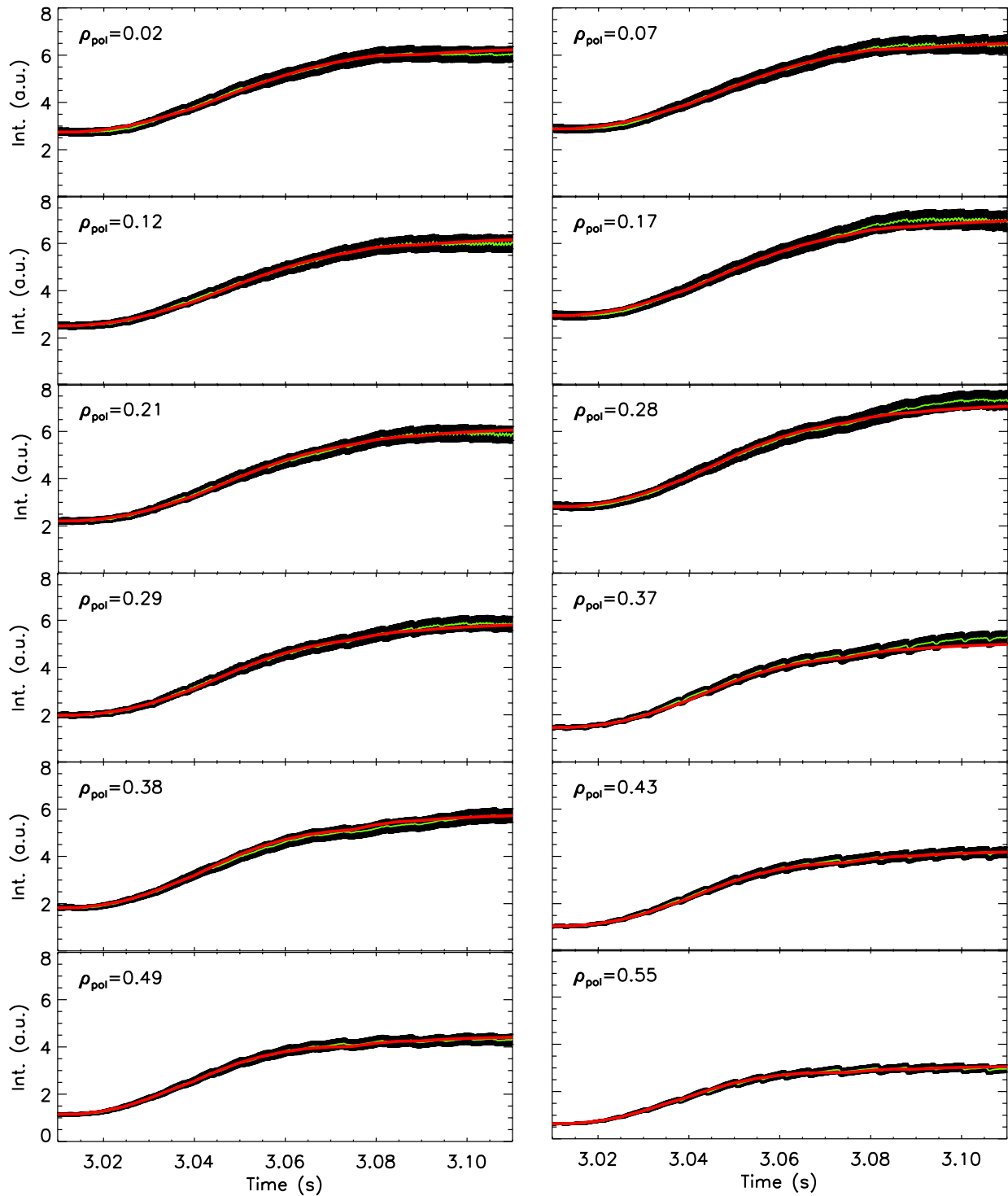for the second time interval. The results of this operation can be seen in figure 6.35, where both sets of transport coefficients are over-plotted on the same graph (1st set in black, 2nd in red). When comparing the final STRAHL simulation with the experimental data, the agreement is satisfactory for all lines of sight, even though the most central ones still exhibit a slight over-peaking. Since some of the LOS shown in figure 6.36 cross the plasma above the axis and some below (e.g. $\rho = 0.0$ and 0.02; $\rho = 0.29$ and 0.28; $\rho = 0.38$ and 0.39 respectively) the difference in emissivity which can be noticed between such neighbouring channels is probably due to inboard-outboard poloidal asymmetries. Differently from camera I, camera H views the plasma from a non-zero poloidal angle (refer to figure B.7) so it can detect such such asymmetries. As for the previous L-mode discharges, the transport coefficients given in 6.35 do not take these asymmetries into account since they are flux surface averaged quantities.

The transport coefficients in red in figure 6.35 exhibit a very strong positive convection velocity within the inversion radius (located at $\rho \sim 0.35 \div 0.4$). Since the diffusion coefficient remains very low in the centre, the drift parameter (on the right) reaches extremely high values within ρ_{inv} indicating an "impurity hole" in the centre of the plasma. This seems to be confirmed by both the n_{Ar} profile evolution calculated through the methods developed for this thesis (and described in section 5.3) and by the final STRAHL result with the transport coefficients plotted in figure 6.35. The two surface plots are shown in figure 6.37, the STRAHL result on the left, the other on the right. The colour code represents the total argon density evaluated through the methods described in section 5.3. The general trend of both results is very similar showing a slow influx up to the centre for $t < 3.08$ and a further outflux of Ar from the region $\rho < 0.2$ for the remaining time period. The peak in argon density is in both cases located at $\rho \sim 0.35 \div 0.4$, approximately at the $q = 1$ surface.

The results obtained in this section have to be anyway interpreted with caution. The reason for this is that the evolution of the background (distinctly visible in figure 6.28) has
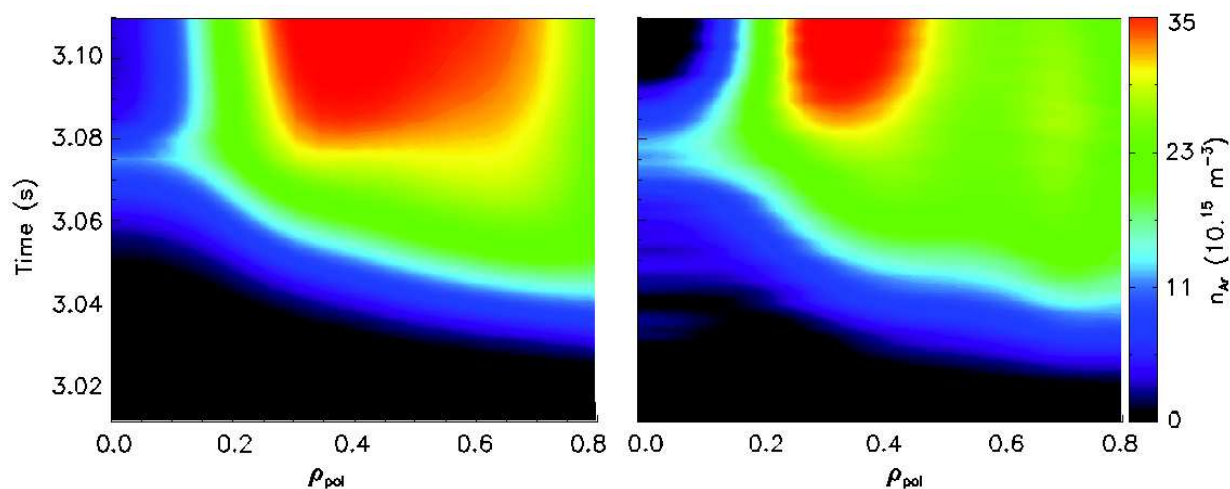

Figure 6.37: *Argon density time evolution for discharge #25447 evaluated through STRAHL (left) with transport parameters in figure 6.35 and through the method described in section 5.3.*

not been taken into account. A subtraction of the background contributions has not been attempted because the development of the various phases of the SXR signals are not always constant in time, varying depending on the cycle taken into consideration. The excursion of the background LOS-integrated SXR signals (top plot in figure 6.28) has been estimated to be approximately $10 \div 20\%$ of the maximum value of emissivity during the argon puff which would lead to an even higher underestimation of the central argon density.

A more precise estimation of the equilibrium argon density profiles (and consequently of the v/D profile) has been performed evaluating the equilibrium density profile for the background contributions shortly before the sawtooth crash prior to the argon injection (at $t = 2.96\ s$, see figure 6.26). The method used is the one described in section 5.3 and already applied in section 6.1.1 to produce figure 6.6 for the first analysed L-mode discharge. The results for discharge #25447 can be seen in figure 6.38. The top plot shows the equilibrium argon density at $t = 3.11\ s$ as evaluated through the STRAHL simulation with the transport coefficients in figure 6.36 (red) and as evaluated through the alternative method (blue). The corresponding v/D profiles are shown at the bottom. Due to the strongly varying electron temperature gradients in the IDA fits (shown in red in the top plot of figure 6.25) the blue curve exhibits slightly oscillatory edge values, but is in general of the same order of the results obtained through the χ^2 minimization. Within $\rho < 0.3$ the background correction has instead a stronger effect, leading to a factor ~ 5 lower in v/D. Even with this rough background correction, the argon density profile remains extremely hollow, confirming again the presence of a large outward convection region in the very centre.
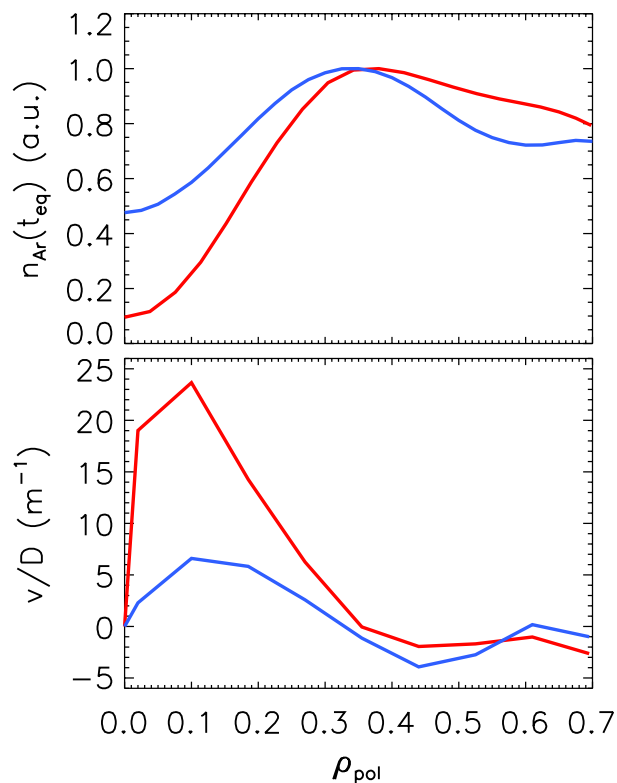

Figure 6.38: *Normalised equilibrium argon density profiles (top) and drift parameter (bottom) for the second set of transport parameters evaluated through the χ^2 minimization routine (red) and from the method described in section 5.3 (blue) taking the background values just before the sawtooth crash prior to the Ar injection.*

It is anyway clear that a cyclical change in impurity transport occurs during the sawtooth cycle, in phase with the onset of the $m/n = 1/1$ mode. Since neither the electron temperature profiles nor the electron density profiles vary strongly before or after the sawtooth crash, it is probable that the strong outward convection observed before the sawtooth crash is not of turbulent nature, but in some way related to the observed MHD activity. This effect seems to act preferentially on medium-large Z (or A) impurities since no change in the electron density profile is observed.

Chapter 7

Conclusions and Outlook

This work has concentrated on the characterization of the effects of Electron Cyclotron Resonance Heating (ECRH) and of nitrogen seeding on impurity transport in ASDEX Upgrade (AUG). A new spectroscopic diagnostic (the Compact Soft X-Ray spectrometer) for He-like argon measurements has been optimised, calibrated and installed on AUG. New methods for the evaluation of the total argon density profile evolution through the integrated use of this diagnostic and of the Soft X-Ray (SXR) diodes arrays have been developed. This has enabled the evaluation of the transport coefficients employing the linear relation between the normalized density gradient and the normalized flux (commonly referred to as the "Gradient-Flux" method) instead of using classical χ^2-minimization methods.

The Compact Soft X-Ray (CSXR) spectrometer, a crystal X-ray spectrometer of the Johann type, now routinely performs line-of-sight (LOS) integrated measurements of argon concentration, ion temperature and flow velocity at a $250\ Hz$ acquisition rate. Only a small amount of Ar ($c_{Ar} > 10^{-5}$) is necessary to provide good enough Signal to Noise Ratio (SNR) for precise measurements. This is outstanding for such a compact ($R = 500\ mm$) Johann spectrometer and is due mainly to two factors. The quartz crystal employed is asymmetrically cut by $21.9°$ and spherically bent to a radius of $500\ mm$. The spherical bending of the crystal guarantees a focusing of the incident rays in both the sagittal and meridional planes, leading to a very high luminosity which enables the acquisition of spectra up to $4\ ms$ time resolution. The asymmetrical cut guarantees quasi-normal incidence of the rays on the crystal surface, thus minimizing the common spherical aberration of Johann spectrometers. These features also lead to a decrease of the incident ray divergences thus increasing the instrument resolution to $\delta\lambda/\lambda \sim 4000$. Argon temperatures above $> 430\ eV$ can be therefore measured.

Although the measurements are LOS-integrated, an approximate radial localization is performed through the modelling of the emissivity characteristics of the He-like Ar ion. Apart from the Neutral Particle Analyser (NPA) no other diagnostic can deliver approximate spatially localized bulk ion temperature measurements for discharges without Neutral Beam Injection (NBI). This feature of the CSXR spectrometer has therefore given the possibility of performing purely ECR heated discharges without giving up the ion temperature information completely. The spatial localization has been found reliable when tested against the measurements of the charge exchange diagnostic in NBI heated discharges.

New methodologies have been developed for the experimental determination of the total

argon density profile evolution through the integrated use of the CSXR and the SXR diagnostics. Used in combination with the 1D impurity transport code STRAHL, the SXR diagnostic delivers the profile evolution of the argon density after a non-disturbing argon puff. Since the SXR diagnostic does not provide an absolute measurement, the resulting high time resolution profile is re-scaled through the use of the concentration measurement from the CSXR spectrometer. The evaluation of the full profiles of the argon transport coefficients is then performed using the Gradient-Flux method. In comparison to classical χ^2-minimization methods, the approach proposed here delivers transport coefficients intrinsically independent of the modelling of periodic relaxation mechanisms such as sawtooth crashes. This is usually performed by assuming that the crash leads to a complete flattening of the total impurity density profile within a mixing radius $\rho_{mix} = \sqrt{2}\,\rho_{q=1}$. For standard sawtooth activity, the results of this method have been found in very good agreement with results from χ^2-minimization. For more complicated sawtooth footprints (humpback or saturated sawteeth), the two methods deliver slightly different solutions. This could be due to a errors intrinsic in the G-F method or to the inexact modelling of the sawtooth crash. This last explanation is in fact confirmed by other experimental findings [44] which conclude that non-standard sawtooth crashes may exhibit incomplete reconnection and mixing. The higher spatial resolution of the G-F method also enables the detection of previously undetectable local structures in the profile of the transport coefficients.

These experimental methods have been first of all applied to the study of argon transport in purely ECR heated low confinement (L-mode) discharges in AUG. Results from different experiments have proven that one of the possible solutions to impurity accumulation in tokamak plasmas is the use of central high power electron heating. This increases the impurity diffusivity and sometimes gives rise to an outward impurity convection [7–10] thus flushing medium-high Z impurities out of the plasma centre. Although this method is routinely used at AUG for central impurity control, a comprehensive explanation of the physics underlying these phenomena is still not known.
Recent turbulence theories predict that positive convection could be driven by density fluctuations caused by parallel compression [11]. The instability should only appear in regions of the plasma with low safety factor q, low shear s, $T_e >> T_i$ and $R/L_{Te} > 2 \cdot R/L_{Ti}$. Since the last conditions are not often encountered in NBI heated H-mode plasmas, purely ECR heated L-modes have been performed to access the parameter range predicted by theory and scan the the operational space in which an outward convection may occur. The ECRH deposition position has been scanned within and outside of the $q = 1$, clearly indicating that the rise of a positive convection is limited to deposition radii within the $q = 1$ surface. Differently from previous findings, the enhancement in diffusivity and positive convection are found to be very localized around the ECRH deposition radius. This local effect can be more easily detected through this analysis method because of its intrinsic high spatial resolution. The experimental results are found in promising qualitative agreement with a set of quasi-linear gyrokinetic turbulent simulations with the code GS2 [47]. These results of these experiments also confirm and provide a quantitative estimates of previous studies with ECRH deposition scans performed with the new ECRH system at ASDEX Upgrade [49].

Experimental results on the argon transport in nitrogen seeded H-modes with central ECRH ($\sim 10\%$ of the total heating power) show a cyclic behaviour of impurity transport connected

to the occurrence of Magneto-Hydro-Dynamic (MHD) $m/n = 1/1$ instabilities. During the quiescent (or low amplitude) phases of the 1/1 mode, a small outward convection has been detected around the ECRH deposition radius, confirming an impurity flushing effect by ECRH even in H-mode discharges. Differently from the L-mode cases, no local increase of the argon diffusivity was found. The diffusion coefficient is nonetheless approximately a factor 3 larger than neoclassical levels. In the presence of intense 1/1 mode activity, the rise of a very strong outward impurity convection is observed. This effect acts on timescales much slower than typical MHD timescales (e.g. the 1/1 rotation period $> 10\ kHz$ or the sawtooth crash) and is sensibly larger than what observed in the quiescent phase. Since the main plasma parameters do not exhibit large variations, it is very probable that this outward convection is not of turbulent nature. Furthermore, this effect seems to act preferentially on medium-large Z impurities since no change in the electron density profiles is observed. Such a behaviour is not seen in the non-seeded discharge taken into consideration as reference. It is nonetheless not clear whether this effect is caused by the nitrogen or by the 1/1 mode and if the rise of this specific mode is related to the nitrogen seeding. To the knowledge of the author, this feature is shown in this work for the first time.

The experimental methods for the determination of impurity transport coefficients developed for this work have been proven reliable and exhibit positive features in comparison to classical χ^2-minimization methods. Nonetheless, it is of major importance to further benchmark them with other codes available in different experimental facilities around the world. Analysis of the same discharges with different methods could provide indications on improvements which could be implemented in both methods. Moreover, since χ^2-minimization methods often provide more comprehensive solutions in plasma discharges exhibiting complex features, the two methods could also be coupled: the Gradient-Flux method delivering first estimates of the transport coefficients which can then be fine-tuned through the use of χ^2-minimization routines. Both methods rely anyway on an extremely good knowledge of the electron temperature and density profiles so it would be of major importance to improve these measurements.

As a further outlook, since AUG will be soon equipped with higher ECRH power, it would be of major interest to carry on with experiments on the effects of ECRH on impurity transport by performing discharges with higher ECRH power. This would guarantee the flexibility of delivering power at different radii without falling below the sensitivity curve of the SXR diagnostic. Further scans in the R/L_{Te} and R/L_{Ti} parameter space could thus be performed and the recent theories proven or "falsified".

It would be moreover of great interest to analyse the impurity transport during a sawtooth crash. The methods proposed here could give an idea of how the impurity density profile changes during a sawtooth crash thus giving indications on the accuracy of the usual modelling.

Although interesting features in impurity transport in nitrogen seeded H-modes have been found in this work, the confinement improvement is still unexplained. Since the increase in both electron and ion temperatures is observed for the full profile up to the pedestal region, it is very probable that a change in impurity transport could be detectable at the plasma edge. This will be possible when an extension to the full plasma radius will be implemented in the experimental method proposed here. Since a central confinement improvement has also been observed in the presence of argon, it would be of major interest to study the

variation in impurity transport in discharges with different seeding gasses (e.g. Ar, N_2 as already indicated in [50]).

Appendix A

ASDEX Upgrade and its Heating Systems

The tokamak fusion experiment ASDEX Upgrade (Axial Symmetric Divertor EXperiment Upgrade, in brief AUG) is the largest fusion experiment in Germany and one of the leading experiments worldwide. Since its first plasma in 1991, it has undergone many diagnostic upgrades, a complete change of first wall from carbon to tungsten-coated plasma facing components (PFCs) and has been equipped with about 30 MW of additional heating. The reactor-relevant plasma shape and high heating power gives it the capability to tackle many of the physical issues arising during the design and construction of the International Thermonuclear Experimental Reactor (ITER). Geometrically, AUG is a scaled-down version of
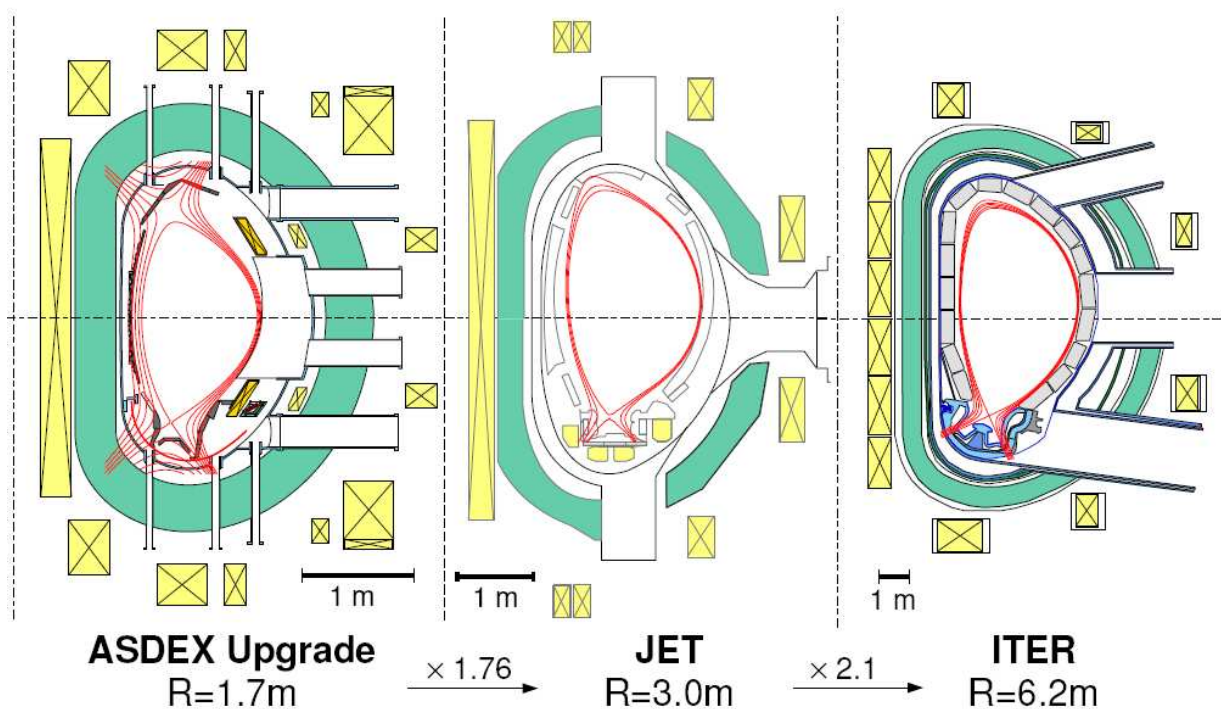

Figure A.1: *Scaled poloidal cross-sections of ASDEX Upgrade, JET and ITER. Major radii of the machines are also shown for comparison on the bottom of each cross-section.*

the ITER configuration by a factor 4 and by less than a factor 2 with respect to JET, the largest operating fusion experiment in Europe (figure A.1). Its installed external heating power assures that the energy fluxes through the plasma boundary are very close to those in ITER. This similarity can be expressed as the ratio between the heating power and major radius [51] which in ASDEX Upgrade is $P/R \approx 18~MW/m$ vs. $24~MW/m$ for ITER. Moreover, AUG is at present the only device of relevant size around the world with full tungsten Plasma Facing Components (PFCs). Since it has been concluded that carbon PFCs will not be suitable neither for ITER in DT phase nor for future commercial fusion reactors because of the unacceptable level of tritium retention in the carbon layers [52], this machine is a powerful tool for the demonstration of plasma scenarios with a reactor-relevant first wall.

From a heating capability point of view, of great importance for this thesis is the availability of high power Electron Cyclotron Resonance Heating (ECRH). In order to guarantee a high fusion power, only a low amount of impurities (non-fusing elements, i.e. any other element apart from deuterium and tritium) will be acceptable in the centre of a fusion plasma. Purely Neutral Beam Injection (NBI) heated H-mode plasmas have been found to be prone to accumulation of impurities in the plasma centre [8,53], leading to fuel dilution and to excessive radiation losses. On the other hand, it has been also noted that strong central wave heating (ECRH or Ion Cyclotron Resonance Heating, in brief ICRH) counterbalances this effect and flushes impurities from the centre part of the plasma [8,54–57]. The suggested explanation is that wave heating would lead to an enhancement of impurity diffusion and some have also shown the possibility that central ECRH may even lead to an outward convection [7,8,23] and thus to hollow impurity density profiles in the centre. A full explanation of these effects has nonetheless still not been found and further experimental and theoretical studies are necessary to understand the complex physics behind these

Major/Minor plasma radius	R_0/a	1.65 m/0.5 m = 3.3
Maximum height/width of plasma cross section	b/a	0.8 m/0.5 m = 1.6
Plasma Volume / surface	V_p/S_p	14 m^3/42 m^2
Maximum average triangularity	$<\delta>$	0.5
Maximum plasma current	I_p	1.4 MA
Maximum toroidal magnetic field	B_0	3.2 T
Maximum OH flux swing	Φ_{OH}	9 Vs
Discharge duration	t_{FT}	< 10 s
Maximum NBI power (box1/box2)	Deuterium	10 MW/10 MW
Full particle energy (box1/box2)	Deuterium	60 keV/93 keV
Maximum ECRH power/pulse length (ECRH1)	P_{ECRH1}	2 MW/2 s
Maximum ECRH power/pulse length (ECRH2)	P_{ECRH2}	1 MW/10 s
Maximum ICRH power/pulse length	P_{ICRH}	6 MW/10 s
Pumping speed of 14 TMP	Deuterium	14 m^3/s
Pumping speed of cryopump (CP)	Deuterium	100 m^3/s

Table A.1: Main parameters of the ASDEX Upgrade machine and heating system.

processes. The main parameters of the ASDEX Upgrade machine are give in table A.1. The remaining sections of this chapter focus on the main aspects of the heating capability of the machine which are of major importance for the scope of this work. A description of the concepts of NBI heating are given in section A.1, while section A.2 explains the basics of ECR heating.

As summarized in table A.1, ASDEX Upgrade is equipped with a maximum 30 MW external heating capability: 20 MW of NBI, 6 MW of ICRH and 3 MW of ECRH. The injection geometry of these heating systems is shown in figure A.2. The 20 MW of NBI power at AUG are delivered by two injectors with 4 sources each. The major difference between the injectors is the full particle energy and extracted current, 60 keV & 77 A for injector 1 (NBI1 in figure A.2) vs. 93 keV & 63 A for the NBI2. The different toroidal and poloidal angles of the 8 sources give the possibility to deliver heating and/or current drive with different power deposition profiles.

The ECRH system at AUG is made of two distinct systems. The first system (ECRH 1-4 in figure A.2) includes 4 gyrotrons capable of a total power of 2 MW for 2 second long pulses (or 2.8 MW for 1 second) at 140 GHz. Each gyrotron is equipped with its own transmission line and independent mirrors which can be adjusted in both the poloidal and toroidal planes providing flexibility of the power deposition position. The movement of the
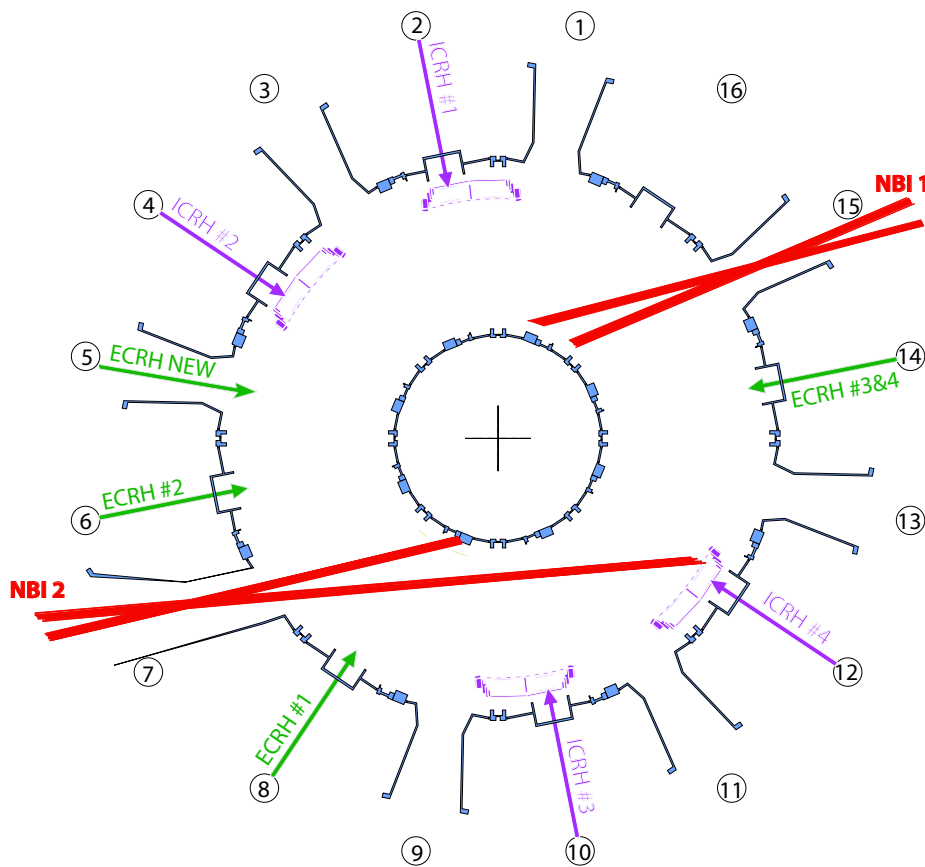

Figure A.2: *Overview of the heating systems at ASDEX Upgrade seen from the top of the machine. NBI systems are highlighted in red, ECRH in green and ICRH in purple.*

mirrors has to be done in-between discharges. The second system (ECRH NEW in figure A.2), consists up to now of 1 multi-frequency gyrotron (105 or 140 GHz) for a total power of 1 MW for the full 10 second maximum duration of an AUG discharge. Differently from the first system, the steering of the launching mirrors of these gyrotrons allow fast (10 ms/degree) poloidal movement during the discharge itself.

A.1 Neutral Beam Injection

The penetration depth of a neutral particle inside a plasma depends on its initial energy, on the main plasma ion and impurity density and on their temperature. From these parameters depend the cross-sections for the ionization of the neutral due to electron impact ionization ($D^0 + e^- \to D^+ + 2e^-$), ion impact ionization ($D^0 + A^q \to D^+ + A^q + e^-$) and to charge exchange ($D^0 + A^q \to D^+ + A^{q-1}$), where q is the ionization stage of the ion A. The probability for these reactions to occur is thus a function of the relative velocities (energies) of the beam neutrals with respect to that of the target particles. The effective cross section for ionization will be a weighed sum of the contributions from charge exchange, ion impact ionization and electron impact ionization. All ion species present in the plasma (main deuterium ions, but also all the impurities) have to be taken into account for this evaluation.

After the fast neutrals have been ionized, they will lose energy via Coulomb collisions with the plasma ions and electrons until they are slowed down to thermal energies (thermalization). Depending on their initial energy (beam energy) and on the energy of the electrons/ions in the plasma, these fast ions will transfer their energy predominantly to ions or to electrons. To explicate this, a critical energy can be defined [58], equal to the beam energy for which the rate of energy loss to ions is equal to that to electrons:

$$E_{cr} = 14.8 \cdot kT_e \cdot \left[\frac{A^{3/2}}{n_e} \cdot \sum_j \frac{n_j Z_j^2}{A_j} \right]^{2/3} \tag{A.1}$$

where A is the mass of the fast ions in a.m.u., A_j and Z_j the mass and atomic number of the plasma ions, the sum achieved over all ion species. For a pure deuterium plasma ($j = 1$, $n_j = n_D = n_e$, $A = A_j = 2$ and $Z_j = 1$), the value for this energy is $E_{cr} = 18.6 \cdot T_e$ keV. For beam AUG box 1 ($E_0 = 60$ keV), and $T_e > 2$ keV the fraction of ion heating from the full energy component will be 60 % of the total NBI power.

A.2 Electron Cyclotron Resonance

A particle of charge q moving in a magnetic field will rotate at a gyration frequency $\omega_c = qB/m$, where m is the mass of the particle and B the magnetic field. For the simplest case of injection perpendicular to the magnetic field, the basic principle of all wave heating mechanisms is that an electro-magnetic wave of frequency ω_0 equal (or sufficiently close) to one of the harmonics of the gyration frequency $n\,\omega_c$ will resonate with the particle and transfer its energy to it. With these assumptions, a first idea of the frequency range for electron heating can be provided by the simple formula:

$$f_0(GHz) = 28 \cdot B_0(T) \cdot n \tag{A.2}$$

For typical 2.5 T magnetic field at AUG, a second order resonance is found at 140 GHz. The resonance condition is however not the only one that has to be satisfied. In order to resonate with the particles, the wave must first of all reach the resonance position in the plasma.

The cut-off position defines the layer at which the wave is reflected. If this layer is between the launching and the resonance layers, the wave is reflected before it can reach the wave-particle resonance position and heat the plasma. This reflection position depends on the electron density, on wave frequency and polarization with respect to the tokamak magnetic field. This condition can be expressed as the limit for which the refractive index of the medium N for the specific wave of frequency ω goes to zero $N(\omega) \to 0$. For electron cyclotron waves with wave vector perpendicular to the static magnetic field $\overrightarrow{B_0}$ in ordinary mode (OM, electric field $\overrightarrow{E} \parallel \overrightarrow{B_0}$) and in extraordinary mode (XM $\overrightarrow{E} \perp \overrightarrow{B_0}$) the dispersion relations are respectively [18]:

$$N_\perp^2 = 1 - \frac{\omega_{pe}^2}{\omega^2} \tag{A.3}$$

$$N_\perp^2 = \frac{\left(1 - \frac{\omega_{pe}^2}{\omega^2} - \frac{|\omega_{ce}|}{\omega}\right)\left(1 - \frac{\omega_{pe}^2}{\omega^2} + \frac{|\omega_{ce}|}{\omega}\right)}{\left(1 - \frac{\omega_{pe}^2}{\omega^2} - \frac{\omega_{ce}^2}{\omega^2}\right)} \tag{A.4}$$

where $\omega_{pe} = (n_e e^2/\epsilon_0 m_e)^{1/2}$ is the so-called plasma frequency. Cut-off conditions are met for $\omega_{pe}^2/\omega^2 = 1$ and $\omega_{pe}^2/\omega^2 = 1 \pm |\omega_{ce}|/\omega$ respectively (shown in figure A.3). Since the plasma frequency is a function of electron density only, depending on the launched frequency ω, the cutoff conditions can be translated into density limits at which the wave is reflected. Table A.2 lists the cut-off condition for O-mode at the fundamental ($\omega = \omega_{ce}$) and the left-hand cut-off for X-mode at the fundamental and second harmonic ($\omega = 2\,\omega_{ce}$).

O1: $\omega = \omega_{ce}$	$\omega^2 = \omega_{pe}^2$	$n_{cutoff} \sim 9.72 \cdot 10^{18} B^2(T)\ m^{-3}$
X1: $\omega = \omega_{ce}$	$\omega^2 = \omega_{pe}^2/2$	
		$n_{cutoff} \sim 1.94 \cdot 10^{19} B^2(T)\ m^{-3}$
X2: $\omega = 2\omega_{ce}$	$\omega^2 = 2\omega_{pe}^2$	

Table A.2: Resonance, cut-off conditions and cut-off density for the fundamental O-mode and for fundamental and second harmonic X-mode.

For X1, an access problem is posed by the right-hand condition $\omega = \omega_R$. If the wave is launched from the low field side (LFS) of the tokamak, this will encounter the cut-off layer before reaching the resonance $\omega = \omega_{ce}$. For this reason, X1 heating can only be done through high field side (HFS) launchers. For the specific case of ASDEX Upgrade, O1 heating 70 GHz would be reflected at local density of $\sim 0.61 \cdot 10^{20}\ m^{-3}$, at the lower end of typical H-mode discharges. For this reason typical ECRH heating is executed in X2 mode at 140 GHz, where the cut-off condition is found at a local density of $\sim 1.2 \cdot 10^{20}\ m^{-3}$ and
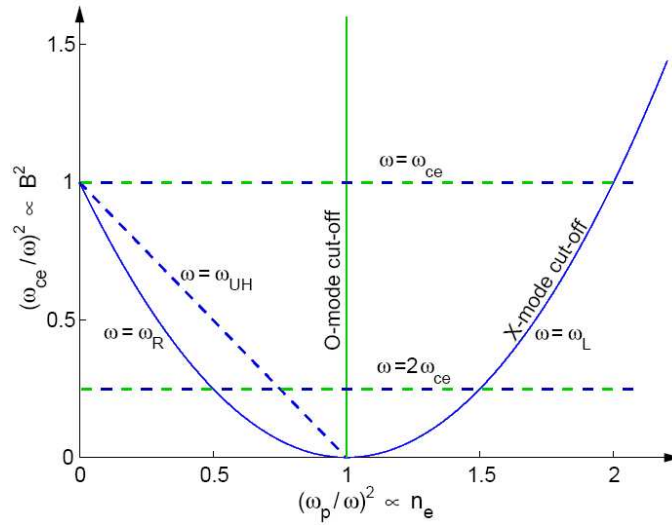
Figure A.3: *Wave cut-off and resonance conditions for O- and X-mode wave propagation in the plasma plotted as a function of $(\omega_{ce}/\omega)^2$ vs. $(\omega_{pe}/\omega)^2$, proportional to the magnetic field B^2 and to the electron density n_e respectively.*

the resonance is accessible from the LFS launchers.

There are different reasons for the attractiveness of this type of heating in a fusion device. First of all, electromagnetic waves at these frequencies propagate in air and in vacuum thus the power may be transmitted from the source to the plasma with large mirrors (quasi-optical) and/or with waveguides, but no antennae very close to the plasma are needed. Moreover, the absorption is very localized (typically a few centimeters) and very efficient (more than 99 % in X2).Finally, since ECRH heats only the electrons, a decoupling of electrons and ions can be achieved and, at low plasma collisionalities such that the heat partition between electrons and ions is low, high electron temperatures (and temperature gradients) can be accessed while keeping the ions "cold". As will be shown in chapter 6, for central densities $\sim 4 \cdot 10^{19}\ m^{-3}$ 1 MW of central ECR heating can easily yield temperature ratios $T_e/T_i > 2$.

Appendix B

Diagnostics at ASDEX Upgrade

At ASDEX Upgrade, the main diagnostics for these measurements are the Electron Cyclotron Emission (ECE) radiometer and the Thomson scattering for T_e, the DCN and CO2 Interferometers, the lithium beam (Li-beam) and the Thomson scattering for n_e. The main concepts of all are given in the following sections. An Integrated Data Analysis (IDA) of these different temperature and density diagnostics is achieved to provide the best fit to the experimental values. Refer to [59] for details on the method. Main deuterium ion temperatures can be measured through the Neutral Particle Analyzer (NPA) while impurity ion temperatures can be profile resolved through Charge eXchange Recombination Spectroscopy (CXRS) or can be given as Line Of Sight (LOS) integrated values from passive spectroscopic measurements as from the Compact Soft X-Ray spectrometer (CSXR) described in chapters 3 and 4.

B.1 Li-beam

The lithium beam impact excitation spectroscopy is based on the observation of Li I radiation (Li(2p)→Li(2s) at 670.8 nm) from neutral lithium atoms injected with an energy of 30-80 keV into the plasma [60]. A full collisional-radiative model is used to model the measured spatial line emission profiles. The occupation density of each excited state N_i of neutral lithium (eq. B.1) is modeled taking into consideration attenuation due to charge exchange ionization, excitation and de-excitation to any other bound state (described by coefficient a_{ij}). The coordinate x describes the position of entrance of the Li-beam in the plasma, $N_{Li} = 9$ the number of energy levels considered while b_{ij} are the Einstein coefficients of spontaneous emission. At $x = 0$ the lithium atoms are assumed to be in ground state where the boundary condition
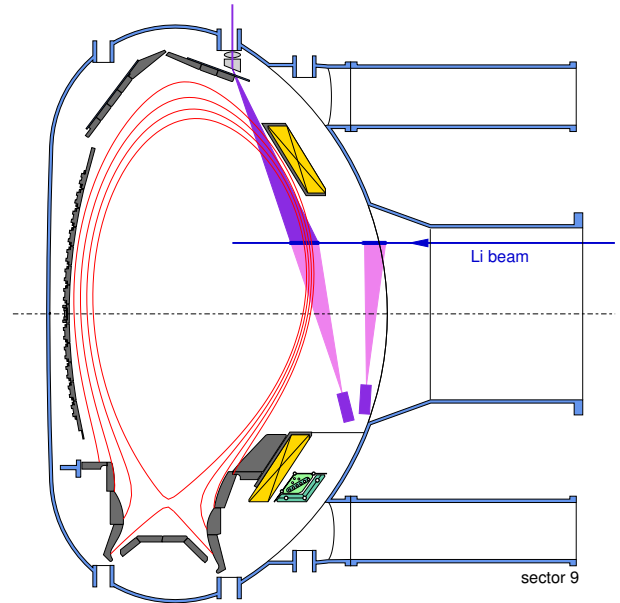

Figure B.1: *Lithium beam trajectory and diagnostic LOSs.*

117

has to be fulfilled (eq. B.2). By solving this system of differential equations, the electron density $n_e(x)$ along the path of the Li-beam can be finally recovered.

$$\frac{dN_i(x)}{dx} = \sum_{j=0}^{N_{Li}} [n_e(x)a_{ij}(T_e(x)) + b_{ij}N_j(x)] \tag{B.1}$$

$$N_i(x = 0) = \delta_{1i} \tag{B.2}$$

Apart from the electron density measurements described above, the Li-beam diagnostic can also deliver ion temperatures and densities through the analysis of the spectra from charge exchange of the lithium with the impurity ions [61].

The Li-beam diagnostic at ASDEX Upgrade provides profiles of electron density with a spatial resolution of $\sim 5\ mm$ and a maximum time resolution of $50\ \mu s$. Details about the modeling of the lithium beam and the used atomic data bases can be found in [62], [63], [64], [65] and [66].

B.2 Thomson Scattering

Electron temperature and density profiles can also be measured by the Thomson scattering diagnostic. The main advantage of this method is that a single measurement can deliver both temperature and density. This means that the profiles will be naturally aligned radially and can be used to re-align other profile diagnostics such as ECE or Li-beam whose relative radial positioning is less accurate.

The Thomson scattering diagnostic relies on the principle for which scattering of monochromatic light from free electrons will suffer from a doppler broadening depending on the velocity distribution of the ensemble of scattering electrons [60, 67]. The scattered power gives indication of the number of scattering particles (the electrons) and thus of their density, while the width of the scattered spectra will contain information on the electron temperature. Neglecting relativistic effects, for electrons with a Maxwellian velocity distribution the scattered power and the FWHM of the distribution can be written as [67]:
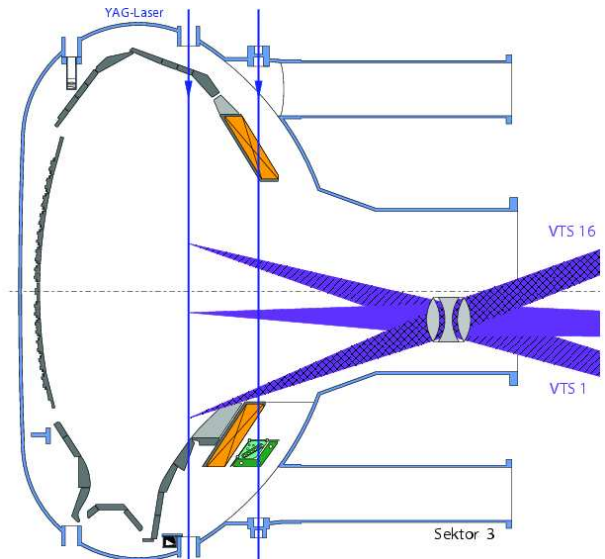

Figure B.2: *Vertical Thomson scattering geometries. Vertical lines depict the possible trajectories of the laser for central or edge measurements. The lines of sight of the first and last channels are also labeled (VTS 1 and VTS 16).*

$$\frac{d < P(\omega_s) >}{d\Omega} \quad = \quad \frac{< I_0 > n_e \sigma_0 sin^2\xi}{\sqrt{\pi}\, a\, k}\, exp\left[-\left(\frac{\omega_s - \omega_i}{a\, k}\right)^2\right] \qquad (B.3)$$

$$FWHM \quad = \quad \frac{a\,\lambda_i}{c}\sqrt{(1 - cos\vartheta)\, 2\, ln2} \qquad (B.4)$$

where I_0 is the incident intensity at frequency ω_i, ω_s the scattering frequency, σ_0 is the Thomson scattering cross-section, ξ the scattering angle, k the incident wave vector, the constant $a = \sqrt{2k_BT_e/m}$ and ϑ is the angle between the direction of acceleration of the particle and the direction of the outgoing radiation.

The Thomson scattering system at AUG (figure B.2) can be set for central or edge measurements and provides 16 spatial channels with 4 spectral channels each providing complete profiles with a time resolution of 8.3 ms. If operated in burst mode, 6 profiles every 100 ns with 50 ms dead time can be delivered [68, 69].

B.3 Interferometry

An electromagnetic wave of wavelength λ travelling along a path L in a medium of non uniform refractive index $N(x)$ will experience a phase change $\varphi = 2\pi/\lambda \int_L N(x)\, dx$ [60]. To precisely quantify this phase change, an interferometer compares it to that of a reference (vacuum) beam:

$$\phi \quad = \quad \frac{2\pi}{\lambda}\int_L N_V - N(x,t)\, dx$$

$$= \quad \frac{2\pi}{\lambda}\int_L 1 - N(x,t)\, dx \qquad (B.5)$$

The phase difference between these two beams is a line integrated measurement of the refractive index of the plasma. In a tokamak plasma, for short probing wavelengths ($\omega^2 >> \omega_{pe}^2$ and $\omega^2 >> \omega_{ce}^2$) this can be approximated as:

$$N \approx 1 - \frac{\omega_{pe}^2}{2\omega^2} \qquad (B.6)$$

Figure B.3: *Interferometer lines of sight at ASDEX Upgrade. In green the 5 horizontal channels of the DCN, in black the 3 vertical CO_2 channels.*

where ω the probing frequency. Since ω_{pe} depends solely on the electron density, a measurement of the refractive index is a direct measurement of this quantity. Substituting the equation of the plasma frequency in equation B.6 and B.5, the phase difference measured by the interferometer will be:
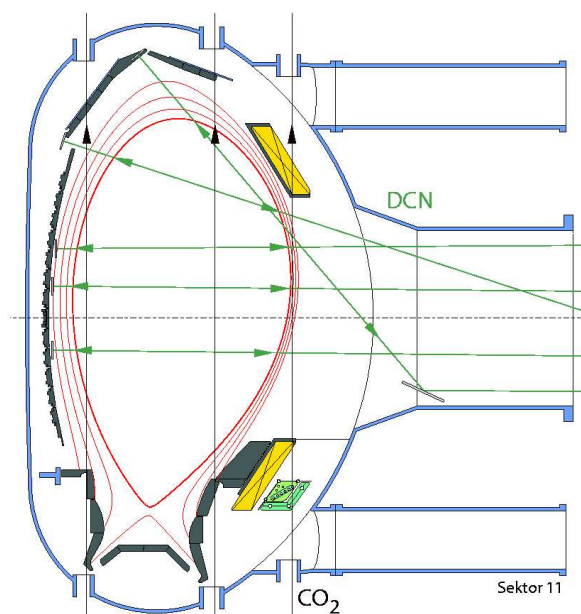
$$\phi = 2.28 \cdot 10^{-15} \lambda \int_L n_e(x, t) \, dx \tag{B.7}$$

As can be seen from this equation, the electron density sensitivity range will change depending on the probing wavelength ($\phi \propto \lambda$). The choice of the wavelength of the interferometer does not depend only on the density to be detected. In order to reduce the phase drifts caused by mirror vibrations, λ should be chosen as long as possible. On the other hand, short wavelengths are better to avoid absorption and refraction in the plasma.

The interferometer at ASDEX Upgrade is equipped with two different systems at different wavelengths (the CO2 laser at ~ 10.6 μm and a DCN laser at ~ 195 μm) for a total of 8 lines of sight, 5 horizontal (DCN) and 3 vertical (CO2) channels. A density resolution of $\sim 5 \cdot 10^{17}$ m^{-3} at a 10 kHz sampling rate can be delivered.

B.4 Electron Cyclotron Emission (ECE) radiometer

As already explained in section A.2, a charge q moving in a magnetic field will rotate at a gyration frequency $\omega_c = qB/m$. This motion leads to the emission of electromagnetic radiation at the cyclotron frequency ω_c. Since the major magnetic field component in a tokamak is the toroidal field generated by external coils whose radial dependence is approximately $B_t(R) \propto 1/R$, the detection at different frequencies will directly translate into spatially localized measurements. For electrons, second harmonic electron cyclotron frequency $2f = 2\omega_{ce}/2\pi$ are in the gigahertz range, i.e. $\approx 56\text{-}280$ GHz.

The intensity of this radiation depends only on the electron temperature. If the electron velocities perpendicular to the magnetic field (the or-

Figure B.4: *Electron Cyclotron Emission radiometer viewing geometry.*

bital velocities in the gyration) have a Maxwellian velocity distribution, the "apparent radiation temperature" can be identified with the temperature of the gyration $T = T_{e,\perp}$. Since in present fusion plasmas $h\nu << kT$ and the plasma is optcally thick, the emitted radiation is simply at black-body level and its intensity I_{BB} radiated power per unit area and unit solid angle is given by Planck's law in the Rayleigh-Jeans approximation [60]:
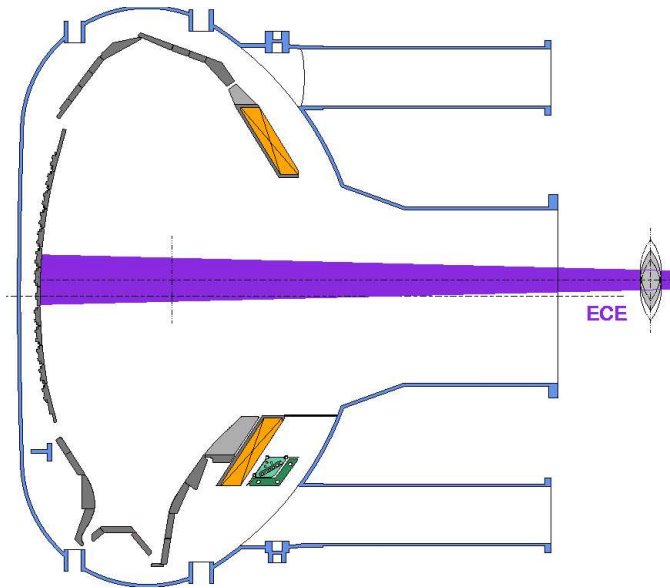
$$I_{BB} = \frac{\omega^2}{4\pi^2 c^3} kT_e \tag{B.8}$$

The 1D ECE radiometer at ASDEX Upgrade has 60 frequency channels along one line of sight which permit a full coverage of the plasma radius with a precision of ~ 1 cm at an acquisition rate of 1 MHz.

B.5   NP Analyzer

Deuterium ions which undergo charge exchange processes in any part of the plasma may be able to escape from the plasma core and reach the edge were they can then be detected. These neutral particles carry information on the region of the plasma where they have been neutralized so, by analyzing their energy spectrum, information about their original temperature can be extracted.

In order to be detected, the neutral particles must first of all escape from the confined plasma without undergoing charge exchange reactions, ion or electron impact ionization. If the mean number of collisions per unit path length is α, then the probability of an atom a (neutralized at a depth L in the confined plasma) to escape without being re-ionized will be [60]:

$$P_l = exp \left[- \int_L \alpha_a(l) dl \right] \tag{B.9}$$

The parameter α depends on the cross-sections and on the velocity of the atom and can be written as:

$$\alpha_a = \frac{1}{a} \left[\langle \sigma_e v_e \rangle_{v_a} n_e + \left(\langle \sigma_i v_i \rangle_{v_a} + \langle \sigma_{cx} v_i \rangle_{v_a} \right) n_i \right] \tag{B.10}$$

where suffix cx, e and i stand for charge exchange, electron and ion impact respectively. For 10 keV energy and 10^{20} m^{-3} main ion density, the attenuation length is ~ 0.1 m. In order to be able to detect neutral particles from the core of a plasma such as that at AUG, the line averaged density has to be of the order of $\int n_i dl \sim 10^{19}$ or a few times larger.

Once the neutral particles have been detected, the dependence of their energy spectrum on the temperature can be written as:

$$F(E, T) \sim e^{-E/kT} \tag{B.11}$$

where E is the energy of the neutral particle, T its temperature and k the Boltzmann constant.

The NPA at AUG has the possibility to set the lines of sight at different poloidal angles, thus providing the capability of central or edge ion temperature measurements.

B.6   CXR Spectroscopy

As already explained in section A.1, the fast neutrals from the NBI will be ionized from the plasma through electron and ion impact and through charge exchange (CX) with ionized background and impurity ions. It is on this last process that the CX diagnostic relies on.

The capture of an electron by an impurity ion A^q in ionization stage q occurs predominately at highly excited states due to the conservation of angular momentum [60]:

$$D^0 + A^q \rightarrow D^+ + (A^{q-1})^* \tag{B.12}$$

Because of this, when the excited impurity ion $(A^{q-1})^*$ decays, it will emit a photon which is typically in the visible range or near ultraviolet which is easy to measure with visible spectrometers. On the other hand, the analysis of the charge exchange spectra is quite complex because, excluding contaminating spectra from other impurities, it always contains two components: an active one due to CX reactions between the impurity and the fast neutral from the beam; a passive one due to CX with neutral deuterium already present in the plasma, (called thermal charge exchange). The active component is a local measurement since it is emitted at (or close to) the position of the CX reaction of the impurity with the beam neutrals. The thermal charge exchange is instead a LOS integrated measurement to which edge contributions are often dominant and can can therefore be considered a contaminating spectral feature for the active component.

The analysis of the active spectra delivers local measurements of impurity ion density (intensity of the spectral line), temperature (doppler broadening) and velocity along the line of sight (doppler shift). While temperature and flow measurements do not depend on absolute calibration in intensity, ion density measurements require also the knowledge of the beam density at the measured position. This is a complicated task since it requires the knowledge of the density of all species in the plasma. Nonetheless, this diagnostic is a powerful tool for impurity characterization in a tokamak plasma. The drawback of this diagnostic is the necessity of the neutral beams to execute the measurement. For the pure ECRH heated discharges presented in chapter 6, only the passive measurements

Figure B.5: *CXRS on beam 3 of injector 1.*

from the neutral particle analyzer and from passive spectroscopy (presented in section 4) and have been used.

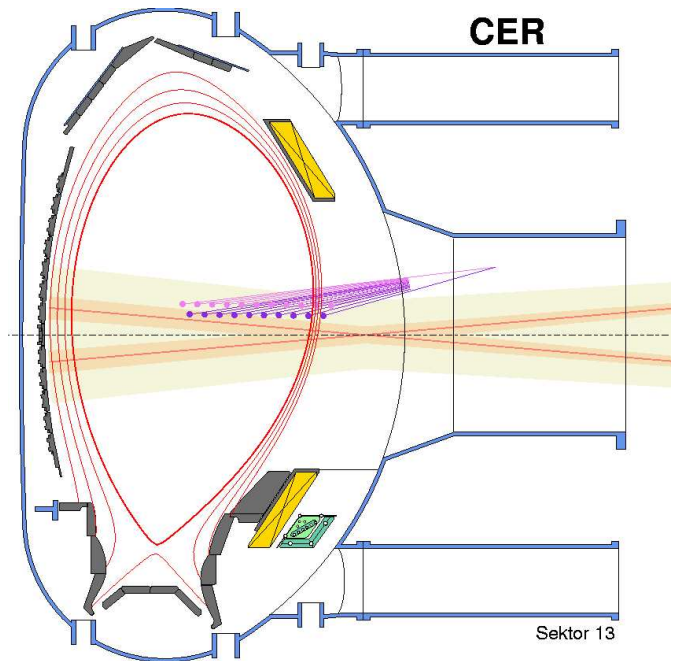ASDEX Upgrade is equipped with three charge exchange diagnostics: two core systems (CHR and CER) with 12 and 10 lines of sight respectively, maximum 10 ms repetition time; one edge system (CMR) with up to 15 channels and a 1.9 ms maximum repetition time. The lines of sight of the CER system can be seen in figure B.5.

B.7 Soft X-Ray Measurements

Sacrificing the spectral resolution of spectroscopic measurements and adding up all the light in a specific wavelength range, the spatial and temporal resolution of the measurements can be strongly enhanced with respect to classical spectrometers. Differently from bolometers, which integrate as much of the spectra as possible, measurements in the Soft X-Ray (SXR) region restrict this range to $\sim [1, 20]\ keV$. By doing so, information on the core of the plasma can be gathered neglecting all the contributions from the most outer, colder parts of the plasma. The lower end of the energy range is limited by the thickness of the Beryllium filters (usually 10-100 μm), while higher end depends on the depth of the depletion layer of the Silicon diode detectors (typically 100-300 μm). The sensitivity function for the present setup (75 μm beryllium filter and 300 μm diode depth) can be seen on the top plot in figure B.6. The Lyman-α and He-like resonance lines for various species are show in red and blue respectively. For these settings, contributions from O and Ne are outside of the sensitivity curve, while Si and Ar give strong contributions to the detected power.

Knowing the transmission of the Be filters as a function of photon energies [70] and the detection efficiency of the diodes, the current flowing in the diodes can be directly related to spectral power. Since an average energy of $E_{pair} = 3.62$ eV is
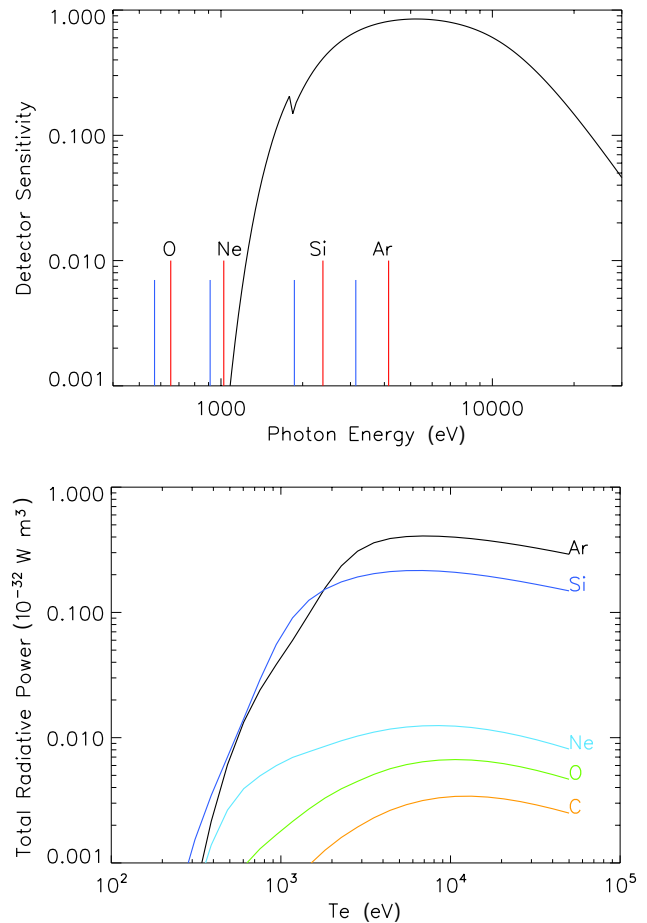

Figure B.6: *Top: SXR diagnostic spectral sensitivity function vs. photon energy for a 75 μm thick beryllium filter and a 300 μm deep Si diode active layer. Red and blue lines show the Lyman-α and He-like resonance lines for various species. Bottom: total power coefficients for these elements filtered with the sensitivity function of the above plot.*

needed for the excitation of one electron-hole pair, the mean detected charge per photon will be $Q = h\nu/E_{pair}$. For a total deposited power P from all photons passing the beryllium filter, the detected current will be $I = P/E_{pair} = P \cdot 0.276\ A/W$.

Unluckily, intense neutron irradiation creates defects in the diode lattice which lead to a global loss in detection efficiency. Assuming these defects are distributed isotropically in the depletion region, one would expect the sensitivity function shown in the top plot of figure B.6 to degrade in time. A sharper decay should also be expected at the high energy end of the sensitivity function due to the fact that this edge is directly determined by the diode characteristics and is not influenced by the Be filters. Simulating the SXR emissivity with the original sensitivity function (as will be shown in more detail in chapter 5) the light

detected will be less than what expected and will therefore lead to an underestimation of the total power. For this reason, only the relative values of the radiated power detected by different lines of sight can be trusted.

The soft X-ray emissivity at radius r, time t due to impurity species A can be written as:

$$\begin{aligned}
\epsilon_A^{sxr}(r,t) &= n_e(r)\, n_A(r,t)\, L_A^{sxr}(r,t) = n_e(r)\, n_A(r,t) \sum_q f_{A,q}(r,t)\, k_{A,q}^{sxr}(r) \\
&= n_e(r)\, n_A(r,t) \sum_q f_{A,q}(r,t)\, [k_{line}^{sxr}(r) + k_{brems}^{sxr}(r) + k_{rec}^{sxr}(r)]_{A,q} \quad \text{(B.13)}
\end{aligned}$$

where n_A is the total impurity density profile and L_A^{sxr} the impurity total radiative power coefficient in the SXR filtered region. This coefficient is the sum of all the radiative contributions from the emitting ionization stages due to line radiation (k_{line}^{sxr}), bremsstrahlung (k_{brems}^{sxr}) and radiative recombination (k_{rec}^{sxr}) which are filtered according to the detector spectral sensitivity and finally weighted on the fractional abundance of the emitting ionization stage $f_{A,q}$. The resulting total radiative power coefficient is shown for different elements in the bottom plot of figure B.6.

ASDEX Upgrade is equipped with 6 SXR pinhole cameras, for a total of ~ 180 lines of sight. The large number of LOS gives the possibility of calculating a tomographic reconstruction with good precision. This inversion procedure is considerably simplified when the emission can be considered constant on magnetic flux surfaces. In this situation, one dimensional Abel inversion can be done. Since it has been demonstrated [13] that argon has negligible inboard-outboard asymmetries in the AUG tokamak, for this work Abel inversion of the 60 LOS-integrated signals of camera H and the central channels of camera I (shown in figure B.7) has been achieved.
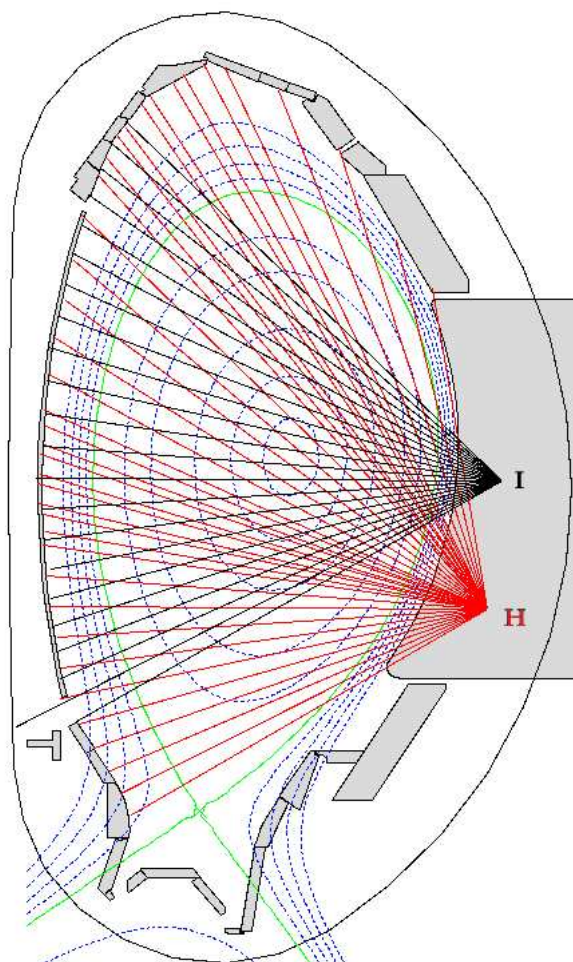

Figure B.7: *SXR cameras H and I setup on ASDEX Upgrade.*

Appendix C

Penetration and Energy Loss of Electrons in Solids

The maximum range of an electron of energy E_0 in a solid is:

$$R = \int_0^{E_0} \frac{dE}{dE/dx} = \frac{E_0^{5/3}}{\lambda_s \cdot 5 \cdot 2^{5/3} \cdot \pi \cdot a^{1/3} \cdot e^{10/3} \cdot N \cdot Z} \propto \frac{E_0^{5/3}}{N \cdot Z^{2/3}}$$

where: $a = 0.8853 \cdot a_H \cdot Z^{-1/3}$ [cm] is the effective screening radius

$e = 1.602 \cdot 10^{-19}$ [C] is the elementary charge

$N = N_a \cdot \rho/A$ is the number of atoms per unit volume in the target [71].

with $a_H = 5.292 \cdot 10^{-9}$ [cm] is the Bohr radius, $N_a = 6.022 \cdot 10^{23}$ [mol^{-1}] is Avogadro's number, ρ = density [g/cm^3] and A = atomic weight [g] of the irradiated specimen, and λ_s is an empirical constant.

The product *density · maximum range* will be:

$$\rho \cdot R \; [g \cdot cm^{-2}] = 5.025 \cdot 10^{-12} \frac{A \cdot E_0^{5/3}}{\lambda_s \cdot Z^{8/9}}$$

where A has to be inserted in a.u. and E_0 in eV.

For 10 keV electrons penetrating into a silver target (A = 107.8682, Z = 47, ρ = 10.5 [g/cm^3] and and $\lambda_s = 0.182$, the maximum range will be ∼0.43 μm.

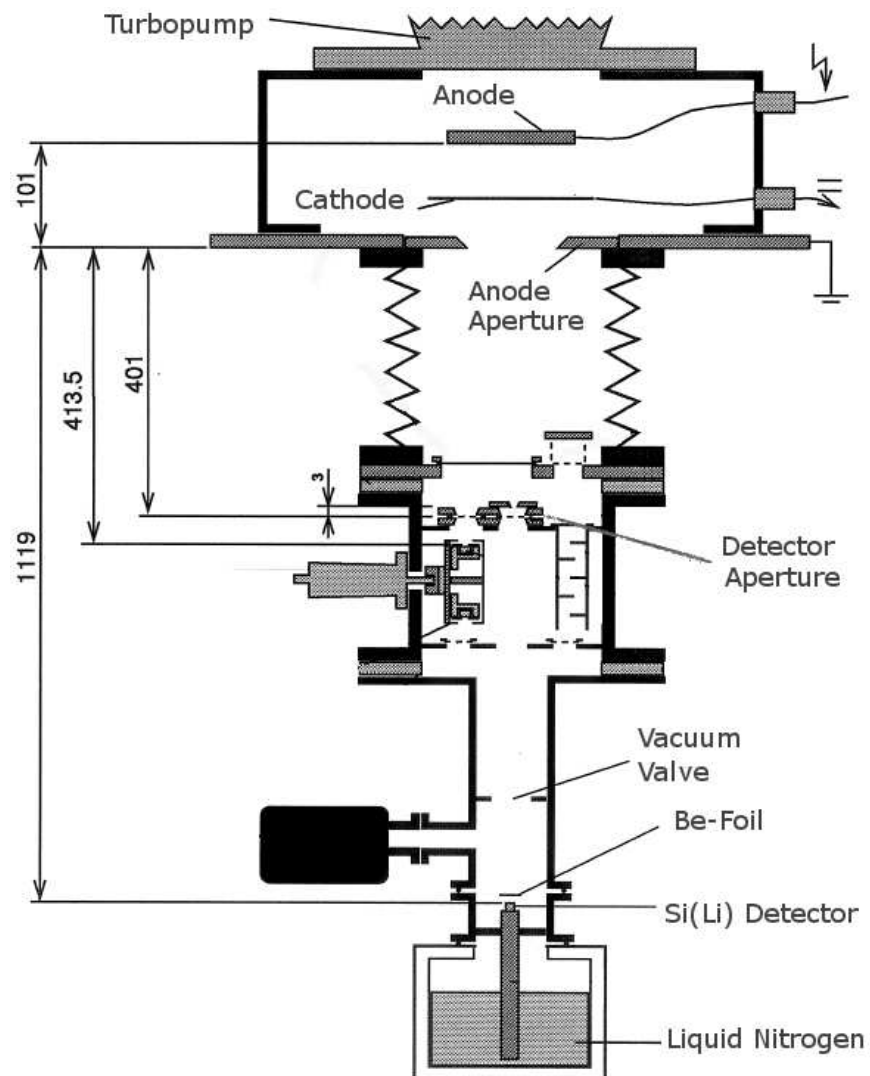# Appendix D

Geometries of Calibration Setup

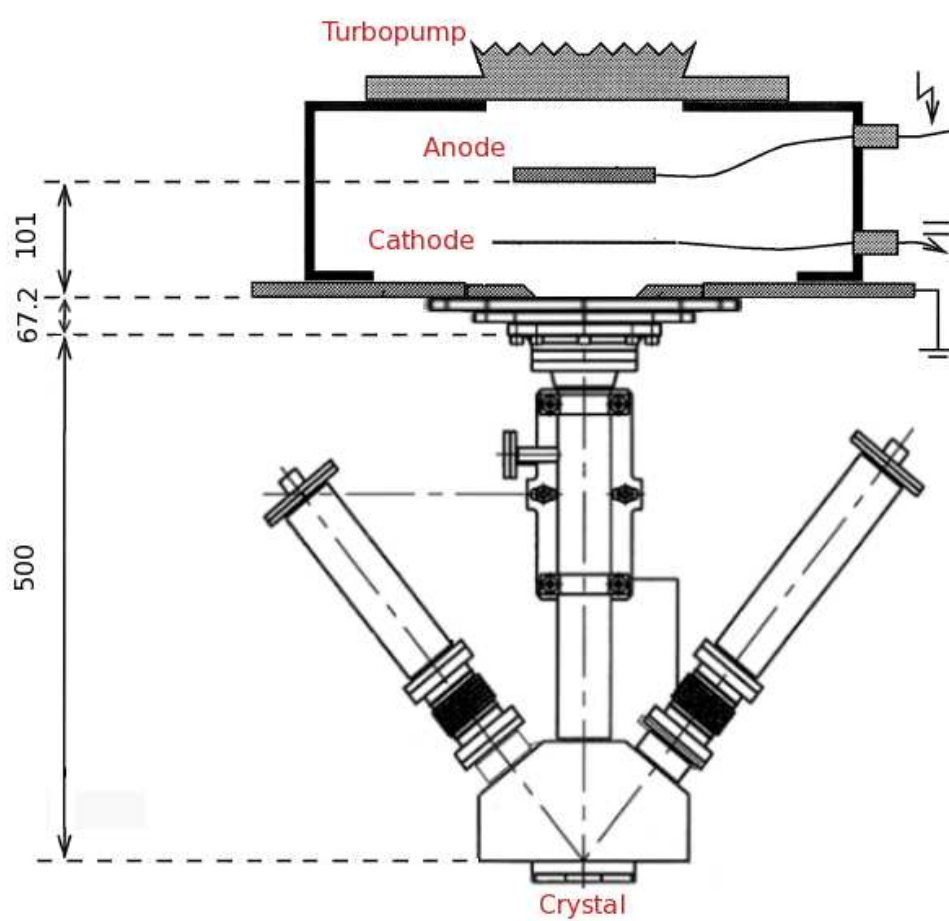Figure D.1: Tube geometry with Si(Li) detector

Figure D.2: Tube geometry with Johann spectrometer

Bibliography

[1] http://www.sd-commission.org.uk/publications/downloads/Herman_Daly_thinkpiece.pdf.

[2] D. Fasel and M. Tran, Fusion Eng. Design **75–79**, 1163 (2005).

[3] http://www.iter.org.

[4] http://www.jet.efda.org/.

[5] R. Dux, Impurity transport in tokamak plasmas, Technical Report 10/27, IPP, Garching, Germany, Dec. 2004.

[6] R. Neu, R. Dux, A. Kallenbach, T. Pütterich, M. Balden, et al., Nuclear Fusion **45**(3), 209–218 (2005).

[7] R. Dux, R. Neu, A. G. Peeters, G. Pereverzev, A. Mück, et al., Plasma Physics and Controlled Fusion **45**(9), 1815–1825 (2003).

[8] R. Neu, R. Dux, A. Geier, A. Kallenbach, R. Pugno, et al., Plasma Physics and Controlled Fusion **44**(6), 811–826 (2002).

[9] E. Scavino, J. S. Bakos, R. Dux, H. Weisen, and TCV Team, Plasma Physics and Controlled Fusion **45**(11), 1961–1974 (2003).

[10] M. E. Puiatti, M. Valisa, C. Angioni, L. Garzotti, P. Mantica, et al., Phys. Plasmas **13**(4), 042501 (2006).

[11] C. Angioni and A. G. Peeters, Physical Review Letters **96**(9), 095003–1 (2006).

[12] G. Fussmann, A. Field, A. Kallenbach, K. Krieger, and K.-H. Steuer, Plasma Phys. Controlled Fusion **33**(13) (1991).

[13] R. Dux, A. G. Peeters, A. Gude, A. Kallenbach, R. Neu, et al., Nuclear Fusion **39**(11), 1509–1522 (1999).

[14] R. Dux, C. Giroud, R. Neu, A. G. Peeters, J. Stober, et al., Journal of Nuclear Materials **313–316**, 1150–1155 (2003).

[15] F. Hinton and R. Hazeltine, Rev. Mod. Phys. **42**(2), 239 (1976).

[16] L. Spitzer, Astrophys. J. **116**, 299 (1952).

[17] S. Braginskii, Transport Processes in a Plasma, 1965.

[18] J. Wesson, Tokamaks, 1987.

[19] R. Dux, Neoclassical Transport, in European Joint Ph.D. Programme on Fusion Science and Engineering: First advanced course (Garching, Deutschland), Oct. 2008.

[20] J. Stober, Particle transport in magnetically confined fusion-plasmas at high density, Technical Report 10/27, IPP, Garching, Germany, May 2006.

[21] A. Ware, Phys. Rev. Lett. **25**, 916 (1970).

[22] X. Garbet, P. Mantica, C. Angioni, E. Asp, Y. Baranov, et al., Plasma Physics and Controlled Fusion **46**(12B), B557–B574 (2004).

[23] C. Angioni, R. Dux, E. Fable, A. G. Peeters, and ASDEX Upgrade Team, Plasma Physics and Controlled Fusion **49**(12), 2027–2043 (2007).

[24] M. Kotschenreuther, G. Rewoldt, and W. Tang, Computer Phys. Comm. **88**, 128 (1995).

[25] W. Dorland, F. Jenko, M. Kotschenreuther, and B. Rogers, Phys. Rev. Lett. **85**, 5579 (2000).

[26] W. Houlberg, K. Shaing, S. Hirshman, and M. Zarnstor, Plasma Phys. **4**, 3230 (1997).

[27] A. G. Peeters, Physics of Plasmas **7**(1), 268–275 (2000).

[28] C. Chantler and R. Deslattes, Rev. Sci. Instrum. **66**(11) (1995).

[29] M. S. del Rio., Rev. Sci. Instrum. **63**(1) (1992).

[30] F. Bombarda., MIT - RLE Report PTP 02/02, Cambridge, MA 02139 (2002).

[31] I. Radivojevic, M. M. Stepanenko, and ASDEX Upgrade Team, High Resolution Compact X-ray Spectrometer with Large Spherical Crystals for Ion Temperature Measurements, in Europhysics Conference Abstracts (CD-ROM, Proc. of the 33rd EPS Conference on Plasma Physics, Roma, 2006), edited by F. De Marco and G. Vlad, volume 30I, pages P–2.148, Geneva, 2006, EPS.

[32] http://xray.uu.se/hypertext/XREmission.html.

[33] http://www.adas.ac.uk/.

[34] http://xdb.lbl.gov/Section1/Table_1-3.pdf.

[35] R. Dux, A. G. Peeters, A. Kallenbach, R. Neu, and ASDEX Upgrade Team, Z-Dependence of Central Particle Transport in ASDEX Upgrade H-Mode Discharges, in Europhysics Conference Abstracts (CD-ROM), Proc. of the 26th EPS Conference on Controlled Fusion and Plasma Physics, Maastricht, 1999, edited by C. Bastian and C. Nieswand, volume 23J, pages 1409–1412, Geneva, 1999, EPS.

[36] Ralph Dux: Abel-inversion routines.

[37] A. Kallenbach, R. Dux, J. Gafert, G. Haas, L. D. Horton, et al., Nuclear Fusion **43**(7), 573–578 (2003).

[38] Y. P. Pereverzev G.V., ASTRA Automated System for TRansport Analysis, Technical Report 5/98, IPP, Garching, Germany, Feb. 2002.

[39] A. Mück, T. P. Goodman, M. Maraschek, G. Pereverzev, F. Ryter, et al., Plasma Physics and Controlled Fusion **47**(10), 1633–1655 (2005).

[40] A. Manini, F. Ryter, F. Leuterer, E. Poli, W. Suttrop, et al., Optimisation of Sawtooth Control using ECCD in ASDEX Upgrade, in Europhysics Conference Abstracts (CD-ROM, Proc. of the 32nd EPS Conference on Plasma Physics, Tarragona, 2005), edited by C. Hidalgo and B. P. van Milligen, volume 29C, pages P–4.073, Geneva, 2005, EPS.

[41] M. Shimada, D. J. Campbell, V. Mukhovatov, M. Fujiwara, N. Kirneva, et al., Nuclear Fusion **47**(6), S1–S17 (2007).

[42] M. Maraschek, private communication.

[43] V. G. Igochine, private communication.

[44] I. Furno, C. Angioni, F. Porcelli, H. Weisen, R. Behn, et al., Nucl. Fusion **41**(4), 403 (2001).

[45] M. Reich, A new diagnostic for edge ion temperatures at ASDEX Upgrade with lithium-beam charge exchange recombination spectroscopy, PhD thesis, Ludwig-Maximilians-Universität München, 2004.

[46] P. Bevington, Data Reduction and Error Analysis for the Physical Sciences, McGraw-Hill Book Company, New York, 1969.

[47] C. Angioni, private communication.

[48] A. Kallenbach, R. Dux, M. Mayer, R. Neu, T. Pütterich, et al., Nuclear Fusion **49**(4), 045007 (2009).

[49] J. Stober, A. Gude, F. Leuterer, A. Manini, R. Neu, et al., First Experiments with the Extended ECRH System on ASDEX Upgrade, in Europhysics Conference Abstracts (CD-ROM, Proc. of the 34th EPS Conference on Plasma Physics, Warsaw, 2007), edited by P. Gasior and J. Wolowski, volume 31F, pages P–5.138, Geneva, 2007, EPS.

[50] R. Neu, J. Fuchs, A. Kallenbach, J. Rapp, R. Dux, et al., Submitted to the 23rd IAEA Fusion Energy Conference.

[51] K. Lackner, Fusion Science and Technology **54**(4), 989–993 (2008).

[52] H. Bolt, V. Barabash, G. Federici, J. Linke, A. Loarte, et al., J. Nucl. Mater. **307-311**, 43 (2002).

[53] R. Dux, K. K. Kirov, R. Neu, G. Pereverzev, A. G. Peeters, et al., Dependence of Impurity Transport on the Heating Profile in ASDEX Upgrade, in Europhysics Conference Abstracts (CD-ROM, Proc. of the 30th EPS Conference on Controlled Fusion and Plasma Physics, St. Petersburg, 2003), edited by R. Koch and S. Lebedev, volume 27A, pages P–1.132, Geneva, 2003, EPS.

[54] G. Van Oost, Auxiliary heating experiments with a tungsten test limiter in TEXTOR 94, in <u>Europhysics Conference Abstracts (CD-ROM, Proc. of the 22th EPS Conference on Controlled Fusion and Plasma Physics, (Bournemouth, 1995)</u>, edited by K. B. E., volume 19C, pages 345–8, Geneva, 1995, EPS.

[55] H. Takenaga, Relationship between particle and heat transport in JT-60U plasmas with internal transport barrier, in <u>Proc. of the 19th IAEA Conf. , Lyon, France, October 2002</u>, pages IAEA–CN–94/EX/C3–5Rb, Vienna, 2002, IAEA.

[56] G. P., Plasma Phys. Controlled Fusion **45**(5), 601 (2003).

[57] M. Marmar, Overview of recent Alcator C-Mod research, in <u>Proc. of the 19th IAEA Conf. , Lyon, France, October 2002</u>, pages IAEA–CN–94/OV/4–1, Vienna, 2002, IAEA.

[58] E. Speth, Rep. Prog. Phys **52**, 57 (1989).

[59] R. Fischer, E. Wolfrum, C. Fuchs, and ASDEX Upgrade Team, Integrated Density Profile Analysis in ASDEX Upgrade H-modes, in <u>Europhysics Conference Abstracts (CD-ROM, Proc. of the 35th EPS Conference on Plasma Physics, Hersonissos, Crete, 2008)</u>, edited by P. Lalousis and S. Moustaizis, volume 32D, pages P–4.010, Geneva, 2008, EPS.

[60] I. Hutchinson, <u>Principles of Plasma Diagnostics</u>, Cambridge Univ. Press, 1987.

[61] E. Wolfrum, J. Schweinzer, M. Reich, L. D. Horton, and C. F. Maggi, Review of Scientific Instruments **77**(3), 033507 (2006).

[62] Z. Pietrzyk, P. Breger, and D. Summers, Plasma Phys. Controlled Fusion **35**, 1725 (1993).

[63] J. Schweinzer, E. Wolfrum, F. Aumayr, M. Pöckl, H. Winter, et al., Plasma Phys. Controlled Fusion **34**, 1173 (1992).

[64] J. Schweinzer, D. Wutte, and H. Winter, J. Phys. B: At. Mol. Opt. Phys. **27**, 137 (1994).

[65] R. Brandenburg, . Schweinzer, J, F. Aumayr, and H. Winter, J. Phys. B: At. Mol. Opt. Phys. **31**, 2585 (1998).

[66] R. Brandenburg, J. Schweinzer, S. Fiedler, F. Aumayr, and H. Winter, Plasma Phys. Controlled Fusion **41**, 471 (1999).

[67] P. R., Thomson Scattering, in <u>European Joint Ph.D. Programme on Fusion Science and Engineering: Second advanced course on diagnostics and data acquisition (Lisbon, Portugal)</u>, Feb. 2009.

[68] H. Murmann, S. Götsch, H. Röhr, H. Salzmann, and K. Steuer, Rev. Sci. Instrum. **63**, 4941 (1992).

[69] B. Kurzan, M. Jakobi, H. Murmann, and ASDEX Upgrade Team, Plasma Physics and Controlled Fusion **46**(1), 299–317 (2004).

[70] B. Henke, E. Gullikson, and J. Davis, At. Data and Nucl. Data **54** (1993).

[71] K. Kanaya and S. Okayama, J. Phys. D: Appl. Phys. **5**(43) (1972).

Acknowledgments

After three years and a printed PhD thesis, I feel obliged to thank all those who have in one way or another helped me, driven me and accompanied me. Those who I may have unintentionally forgotten, please forgive my absent-mindedness.

First of all my direct supervisor, Dr. Rudolf Neu. Thank you for being always professional, frank and direct, I am extremely grateful for your guidance and support in these years. I have learned much from your experience and example.

My group leader, Dr. Ralph Dux. Thank you for all the knowledge you ware able to share and convey.

Prof. Dr. Hartmut Zohm for the support, the extremely interesting lectures and the always precise and constructive comments.

Dr. Thomas Pütterich, for being there to answer my infinite questions and for his great help throughout these years. I am deeply grateful.

Dr. Clemente Angioni, for being always available for explanations and discussions.

The full ASDEX Upgrade team, for the great effort and assistance in each experimental session.

All my lunch mates and friends from IPP who have refrained from talking about work during lunch break in these years: Laura, Minja, Eleonora, Sylvia, Rachael, Tilman, Arthur, Manolo (I know it was hard..), Asher, Karl, Matthias, Andreas, Felix, Fernando, Luis.

My office mates, infinitely patient with bottles, music and drumming.

My friends outside of IPP who made life in Munich a great experience up to now.

Family and friends in Italy.

Laura, for your presence and courage, your patience and confidence, your colours and all their shades.